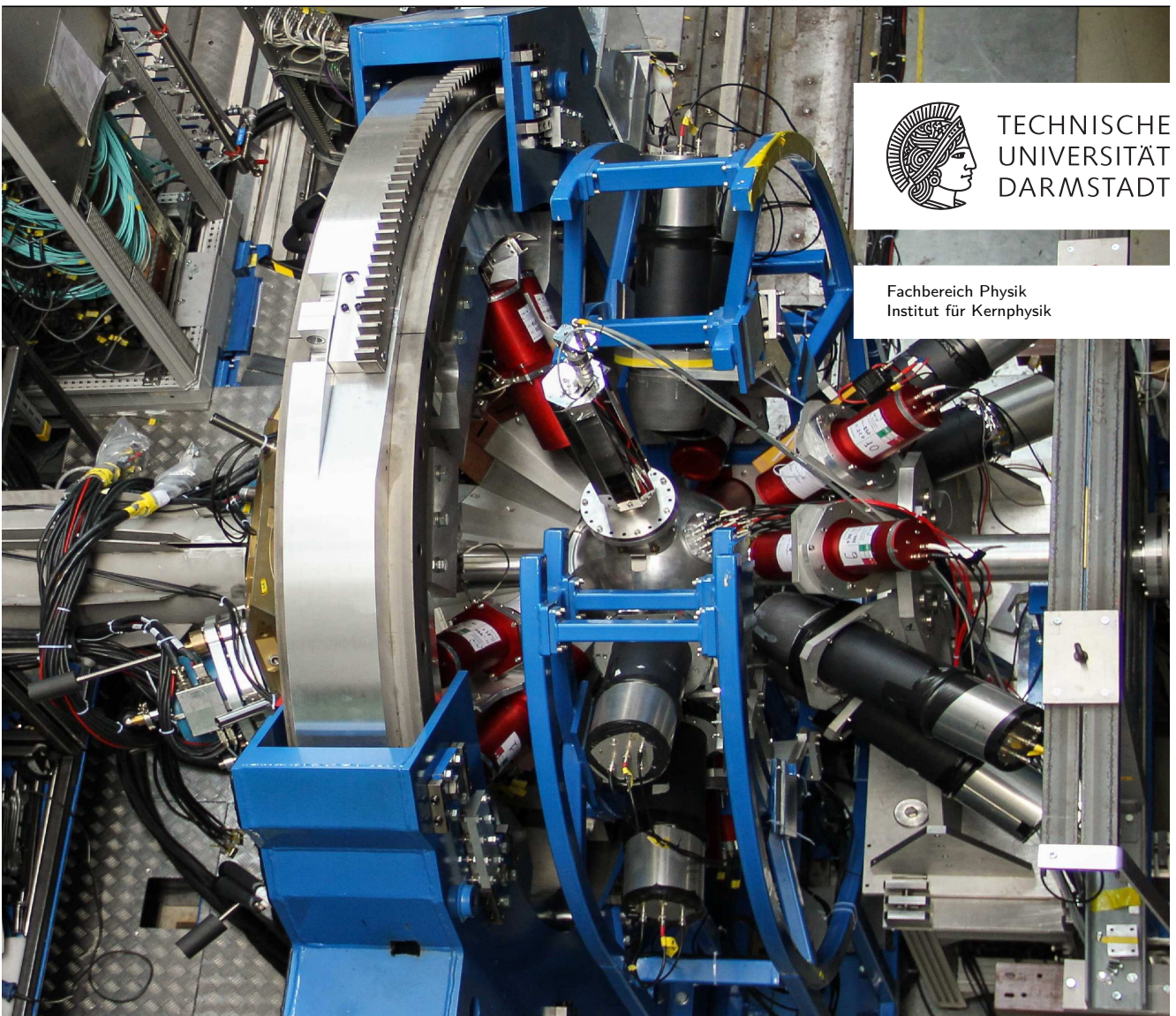


# Lifetime measurement in the mass region $A \approx 100$ with the PreSPEC-AGATA setup

Zur Erlangung des Grades eines Doktors der Naturwissenschaften (Dr. rer. nat.)  
genehmigte Dissertation von Damian Ralet M. Sc. aus Gérardmer  
Tag der Einreichung: Mai 26, 2015, Tag der Prüfung: June 24, 2015  
2015 — Darmstadt — D 17

1. Gutachten: Prof. Dr. Dr. h.c. N. Pietralla
2. Gutachten: Prof. Dr. T. Aumann



Lifetime measurement in the mass region  $A \approx 100$  with the PreSPEC-AGATA setup

Genehmigte Dissertation von Damian Ralet M. Sc. aus Gérardmer

1. Gutachten: Prof. Dr. Dr. h.c. N. Pietralla
2. Gutachten: Prof. Dr. T. Aumann

Tag der Einreichung: Mai 26, 2015

Tag der Prüfung: June 24, 2015

2015 – Darmstadt — D 17

---

## Erklärung zur Dissertation

Hiermit versichere ich, die vorliegende Dissertation ohne Hilfe Dritter nur mit den angegebenen Quellen und Hilfsmitteln angefertigt zu haben. Alle Stellen, die aus Quellen entnommen wurden, sind als solche kenntlich gemacht. Diese Arbeit hat in gleicher oder ähnlicher Form noch keiner Prüfungsbehörde vorgelegen.

Darmstadt, den August 3, 2015

---

(D. Ralet)





---

# Abstract

Mid-shell nuclei in the mass region  $A \approx 100$  show collective behavior. For instance, neutron rich even-even molybdenum isotopes are associated with a shape-phase transition. A spherical vibrator nucleus is observed for  $N=48$  neutrons, while measurements indicate a deformed rotor nucleus for  $N=64$  neutrons. In order to characterize the shape of molybdenum nuclei better, thus the shape-phase transition in molybdenum isotopes, a PreSPEC-AGATA experiment was performed at GSI. In particular, the experiment aimed at measuring the lifetime of the  $4_1^+$  excited state of  $^{108}\text{Mo}$  to deduce the decay transition rate of the  $4_1^+$  state.

The production of  $^{108}\text{Mo}$  was performed in two steps. First, the GSI Fragment-Separator (FRS) selected  $^{109}\text{Tc}$  ions produced via fission of a  $^{238}\text{U}$  beam. Then,  $^{109}\text{Tc}$  ions underwent a fragmentation reaction on a beryllium secondary target. Half-speed of light fragments produced in this second reaction were identified by the Lund-York-Cologne Calorimeter (LYCCA).  $\gamma$ -rays were detected by the AGATA array positioned around the secondary target at forward angles. A complex electronics and data-acquisition system was set up to record the coincidences between a flying ion and the  $\gamma$ -rays it emitted.

The interaction position of  $\gamma$ -rays inside an AGATA crystal is determined with good resolution. Therefore, combined with the large Doppler shift of the  $\gamma$ -ray, it provides a unique possibility to measure lifetime with the Geometrical-Doppler-Shift-Attenuation method.

From the data analysis which included several new techniques, the half-life of  $T_{1/2} = 11_{-6}^{+16}$  ps was extracted for the first  $4_1^+$  state of  $^{108}\text{Mo}$ . The statistics recorded in this experiment is relatively low which leads to a large uncertainty on this measurement.

With this large uncertainty, it is not possible to conclude on the exact behavior of the  $^{108}\text{Mo}$  nucleus, even though the comparison of our measurement with geometrical models would favor a transitional nucleus with approximate  $X(5)$  solution of the Bohr-Hamiltonian.

However, this measurement proves the possibility of lifetime determination coupling relativistic ion beams with the AGATA array. Therefore, it represents a crucial step towards more precise measurements that will be performed at HISPEC with the increased beam intensity provided by the Super-FRS at FAIR.



---

## Kurzfassung

Kerne in der Schalenmitte im Massenbereich von  $A \approx 100$  zeigen kollektive Verhaltensweisen. Zum Beispiel sind Neutronen-reiche gerade-gerade Molybdän-Isotope mit einem Gestaltphasenübergang verbunden. Für Kerne mit  $N=48$  Neutronen wurden sphärische Zustände mit Vibrationsmoden beobachtet, während experimentelle Daten auf deformierte Zustände mit Rotationsbanden bei Kernen mit  $N=64$  Neutronen hinweisen. Um die Form der Molybdänisotope besser zu charakterisieren, und damit den Phasenübergang zu beschreiben, wurde ein PreSPEC-AGATA Experiment an der GSI durchgeführt. Dieses Experiment zielte insbesondere darauf ab, die Lebensdauer des angeregten  $4_1^+$  Zustands von  $^{108}\text{Mo}$  zu messen und daraus die Übergangsrate abzuleiten.

Die Produktion von  $^{108}\text{Mo}$  Kernen wurde in zwei Schritten durchgeführt. Zuerst werden mit Hilfe des GSI Fragment-Separators (FRS)  $^{109}\text{Tc}$  Ionen, welche durch Kernspaltung eines  $^{238}\text{U}$  Strahls erzeugt wurden, selektiert. An einem zweiten Target aus Beryllium werden die  $^{109}\text{Tc}$  Ionen fragmentiert. In dieser Reaktion bei halber Lichtgeschwindigkeit erzeugte Rückstoss-Fragmente wurden mittels des Lund-York-Cologne-CALorimeter (LYCCA) identifiziert. Die  $\gamma$ -Strahlen wurden von dem um das sekundäre Target in Vorwärtswinkeln angeordneten AGATA Array detektiert. Um Koinzidenzen zwischen einem fliegenden Ion und von ihm emittierten  $\gamma$ -Strahlen zu messen, wurde komplexe Elektronik und eine aufwändige Datenaufnahme entwickelt.

Da die Wechselwirkung der  $\gamma$ -Strahlung innerhalb eines AGATA Kristalls sehr gut beschrieben ist, und die Dopplerverschiebung sehr gross ist, bietet das Experiment eine einzigartige Möglichkeit, Lebensdauern mit der Geometrical-Doppler-Shift-Attenuation Methode zu messen.

Nach einer detaillierten Datenanalyse, welche mehrere neue Techniken umfasst, konnte für den ersten  $4_1^+$  Zustand von  $^{108}\text{Mo}$  eine Halbwertszeit von  $T_{1/2} = 11_{-6}^{+16}$  ps bestimmt werden. Die in diesem Experiment aufgenommene Statistik ist relativ niedrig, wodurch die Messung mit grossen Unsicherheiten behaftet ist.

Mit dieser grossen Unsicherheit ist es nicht möglich, genaue Rückschlüsse auf die Eigenschaften des  $^{108}\text{Mo}$  Kerns zu ziehen. Dennoch würde ein Vergleich unserer Messung mit dem geometrischen Modell eine Beschreibung der Kern nahe der  $X(5)$  Lösung favorisieren.

Die Messung bestätigt die prinzipielle Möglichkeit der Lebensdauerbestimmung mithilfe von relativistischen Ionenstrahlen und dem AGATA Array. Daher ist diese Arbeit grundlegend für genauere Messungen, die bei HISPEC mit erhöhter Strahlintensität am Super-FRS bei FAIR durchgeführt werden sollen.



---

# Acknowledgements

This work was supported by the BMBF under Nos. 05P09RDFN4, 05P12RDFN8, and by the LOEWE center HIC for FAIR.

I would like to thank Prof. Dr. Dr. h.c. Norbert Pietralla for allowing me to do my PhD in his group at the Technische Universität Darmstadt.

I am grateful to Dr. Jürgen Gerl, the  $\gamma$ -spectroscopy group leader, that welcomed me in his group and also that supervised this work. I would like to thank him for the patience, understanding and help he provided over these years and especially toward the end of the thesis.

I would like to thank Dr. Stéphane Pietri for following closely and supervising this work. I am grateful in particular for the time he spent explaining me the GSI data acquisition system MBS and for his helpful discussions on the data analysis. Without him, the thesis would not have the same completeness.

I am grateful to Dr. Gilbert Duchêne, my PhD thesis co-supervisor, for being able to follow this work closely from Strasbourg. His supports and advices have been of great help for the fulfillment of this thesis.

I am grateful to Dr. Hans-Jürgen Wollersheim for the usefull discussions we had on the physics phenomena occurring in the region mass  $A \approx 100$ .

This work would not have been possible without the help of all the collaborators of both AGATA and PreSPEC collaborations. Among those, I would like to thank three person in particular. Dr. Dirk Rudolph, for the help he provided me to correct and improve the manuscript of the data acquisition paper. Dr. Dino Bazzacco and Dr. Caterina Michelagnoli, for the help they provided during the set up of the AGATA array at GSI and for the useful discussions we had on the AGATA data analysis.

During these years at GSI, I have met many colleague that became friends. Among those, I would like to mention my office mate, Natasa, with whom it was always possible to discuss data-analysis questions, but also private topics. Christian, for the numerous and helpful discussions on lifetime measurements. Frederic, a close friend that has always helped me during these years.

Aside from GSI, I would like to thank Vladimir, Thomas, Javier for being great friends and climbing partners. It has been a great honor to be climbing regularly with so strong climbers. Morgan, an old friend that is always ready to climb and to share his knowledge on Bayesian data-treatment. I am grateful to Evegni and Phillip for the unconditional help and support on the slopes of the Elbrus mountain.

I am thankful to my family.

“Merci a mes parents, Eve et Damien, pour leurs soutien qui a été sans relâche pendant toutes ces années”.

At last but not least, this thesis would not have been possible without Giulia, my life partner. She helped me on so many aspects over these three and a half years of PhD that it is impossible to mention them all.

---

# Contents

1	Nuclear structure studies in the mass region $A \approx 100$	17
1.1	Deformation formalism	18
1.2	Geometrical models	21
1.2.1	Bohr Hamiltonian	21
1.2.2	Nuclear collectivity	22
1.2.3	Summary of the collective modes	24
1.3	Useful observables for nuclear structure studies	25
1.3.1	Selection rules	25
1.3.2	Transition probabilities	25
1.3.3	Units and conversions	26
1.3.4	Relation between the quadrupole moment and the $B(E2)$ value	26
1.4	Mass region $A \approx 100$	27
1.4.1	Shape-phase transition	27
1.4.2	Triaxiality	28
1.4.3	Particularity of Mo isotopes	28
2	Experimental setup	31
2.1	The GSI fragment separator	32
2.1.1	The $B\rho - \Delta E - B\rho$ method	32
2.1.2	In flight identification of the ions in the FRS	33
2.2	The Lund York Cologne Calorimeter	36
2.2.1	DSSSD tracking detectors	36
2.2.2	Energy loss measurement	36
2.2.3	Total kinetic energy measurement	37
2.2.4	Time of flight determination	38
2.2.5	Reaction chamber	38
2.3	AGATA	40
2.3.1	The AGATA array	40
2.3.2	Interaction position determination of $\gamma$ rays using segmented germanium detectors	41
2.3.3	Forward tracking of Compton scattered $\gamma$ ray	41
2.3.4	AGATA at GSI	45
2.4	HECTOR+	48
2.5	Lifetime measurements at intermediate energies	49
2.5.1	Lifetime measurement methods	49
2.5.2	The geometrical-DSAM method	49
3	The Data Acquisition system for PreSPEC-AGATA	53
3.1	Introduction	54
3.2	Description of the PreSPEC DAQ	55
3.2.1	The FRS sub-system	56
3.2.2	The LYCCA sub-system	56
3.2.3	The GAMMA sub-system	57
3.3	The AGATA data flow at GSI	58
3.3.1	Pre-processing stage of the AGATA data flow	58
3.3.2	The Global Trigger and Synchronisation System	58
3.3.3	Data flow handling with NARVAL	60



3.4	Triggering the system . . . . .	61
3.4.1	Generation of the trigger request signals . . . . .	61
3.4.2	Description of the trigger logic . . . . .	61
3.5	Coupling of the DAQ systems . . . . .	63
3.5.1	Principle . . . . .	63
3.5.2	System integrity check . . . . .	63
3.6	Conclusion . . . . .	65
4	Data analysis . . . . .	67
4.1	Identification of the fragments with the FRS . . . . .	68
4.1.1	Isotope identification . . . . .	68
4.1.2	Useful contaminants inside the FRS settings . . . . .	70
4.1.3	Maximization of the number of identified ions . . . . .	70
4.2	LYCCA data analysis . . . . .	71
4.2.1	ToF calibration . . . . .	71
4.2.2	DSSSD modules calibration . . . . .	72
4.2.3	CsI(TI) energy calibration . . . . .	73
4.2.4	Absolute energy calibration of the LYCCA Wall . . . . .	74
4.2.5	Identification of the fragments in LYCCA . . . . .	75
4.3	Target positioning with the uranium X rays . . . . .	79
4.3.1	Bayesian approach to fitting a model . . . . .	79
4.3.2	One dimensional Model . . . . .	80
4.3.3	MCMC minimization procedure . . . . .	83
4.3.4	Result on the target position . . . . .	84
4.3.5	Conclusion . . . . .	85
4.4	AGATA data analysis . . . . .	86
4.4.1	Energy calibration of AGATA detectors . . . . .	86
4.4.2	Time calibration of AGATA detectors . . . . .	87
4.4.3	Optimal particle- $\gamma$ time . . . . .	89
4.4.4	PSA hit distribution . . . . .	90
4.4.5	Influence of the data replay . . . . .	91
4.4.6	Tracking of the data . . . . .	92
4.5	Peak-to-total ration optimizations . . . . .	94
4.5.1	Influence on the single particle hit . . . . .	94
4.5.2	Influence of the particle- $\gamma$ time . . . . .	94
4.5.3	Influence of the depth of the hits . . . . .	95
4.5.4	Influence of the $\gamma$ -ray multiplicity . . . . .	95
4.5.5	Optimum $\gamma$ -ray spectrum . . . . .	95
5	Lifetime determination . . . . .	97
5.1	Adjustment of Monte-Carlo simulations for lifetime determination . . . . .	98
5.1.1	Presentation of the Monte-Carlo simulations . . . . .	98
5.1.2	Determination of the beam velocity . . . . .	99
5.1.3	Determination of the unknown parameters of the MC simulations . . . . .	100
5.1.4	Verification of the model in view of previously measured lifetime . . . . .	103
5.2	Lifetime determination in the $^{108}\text{Mo}$ isotopes . . . . .	104
5.3	Conclusion . . . . .	105
5.4	Interpretation of the lifetime with the geometrical models . . . . .	106
5.4.1	Energy predictions . . . . .	106
5.4.2	Comparison of transition rates . . . . .	106
6	Conclusions and perspectives . . . . .	109
7	Appendix . . . . .	111
7.1	Relative distances . . . . .	111
7.2	Definition of the Euler angles . . . . .	112
7.3	Change of frame of reference change . . . . .	113
7.4	Spherical harmonics . . . . .	114

---

7.5	Control of the convergence of the fit . . . . .	115
7.6	$\gamma$ -ray spectra for the even-even molybdenum isotopes . . . . .	117
7.6.1	$^{100}\text{Mo}$ . . . . .	118
7.6.2	$^{102}\text{Mo}$ . . . . .	118
7.6.3	$^{104}\text{Mo}$ . . . . .	119
7.6.4	$^{106}\text{Mo}$ . . . . .	119
7.6.5	$^{108}\text{Mo}$ . . . . .	120
7.7	Systematic determination of the centroid . . . . .	121
7.7.1	$^{100}\text{Mo}$ . . . . .	121
7.7.2	$^{102}\text{Mo}$ . . . . .	121
7.7.3	$^{104}\text{Mo}$ . . . . .	122
7.7.4	$^{106}\text{Mo}$ . . . . .	122
7.7.5	$^{108}\text{Mo}$ . . . . .	123

---

## List of Figures

1.1	Shape predictions for the nuclei in the nuclear chart. . . . .	17
1.2	Shape of a nucleus for the first deformation orders. . . . .	18
1.3	Shape of a nucleus as a function of the two deformation parameter $\beta$ and $\gamma$ . . . . .	19
1.4	Schematic drawing of a deformed nucleus. . . . .	23
1.5	Representation of the nucleus collective behavior. . . . .	24
1.6	Plot of the systematics of the first $2_1^+$ energy in the mass region $A \approx 100$ . . . . .	27
1.7	$R_{4/2}$ ratios in the mass region $A \approx 100$ . . . . .	28
1.8	Systematics of the molybdenum isotopic chain. . . . .	29
2.1	Schematic view of the experimental setup used to produce the radioactive molybdenum isotopes. . . . .	31
2.2	Schematic view of the FRS. . . . .	32
2.3	Selection of an isotope with the FRS. . . . .	33
2.4	Achromatic versus mono-energetic mode of the FRS. . . . .	34
2.5	Schematic view of the LYCCA calorimeter. . . . .	36
2.6	Photograph of the <i>DSSSD target</i> detector. . . . .	37
2.7	Position of the LYCCA modules inside the wall of the calorimeter. . . . .	37
2.8	Representation of a LYCCA wall module. . . . .	38
2.9	Picture of the <i>ToF</i> membrane. . . . .	39
2.10	Photograph of the reaction chamber. . . . .	39
2.11	Geodesic geometry for the $4\pi$ solid angle coverage and dimensions of the three AGATA detectors types. . . . .	40
2.12	Schematic view of a segmented AGATA crystal. . . . .	41
2.13	CAD drawing of the AGATA array at GSI. . . . .	42
2.14	Induced charge on the electrode of a coaxial detector. . . . .	43
2.15	Induced charges in an electrically segmented germanium detector. . . . .	43
2.16	Interaction cross section of a $\gamma$ ray in germanium. . . . .	44
2.17	Compton scattering scheme. . . . .	44
2.18	Cluster identification of the interaction position in a $4\pi$ germanium shell. . . . .	45
2.19	Doppler broadening due to uncertainties on beam velocity and emission angle. . . . .	46
2.20	CAD drawing of the AGATA and HECTOR+ $\gamma$ -ray detectors array. . . . .	48
2.21	Lifetime measurement techniques. . . . .	49
2.22	Simulation of the Doppler shifted energy as a function of the observation angle. . . . .	50
2.23	Schematic view of both slow-down and geometrical effect. . . . .	50
2.24	Simulation of both DSAM and geometrical effect. . . . .	51
3.1	Schematic view of the location of the MBS DAQ system . . . . .	55
3.2	GTS coupling scheme. . . . .	58
3.3	Coupling scheme of the MBS and NARVAL data-flow. . . . .	59
3.4	Trigger generation, and time alignment of the request. . . . .	61
3.5	Comparison of the core energy in both MBS and AGATA DAQ system. . . . .	63
3.6	Time energy histogram of the $^{109}\text{Rh}$ isomer. . . . .	64
3.7	Doppler corrected X-rays energy as a function of its emission angle. . . . .	64
4.1	Superposition of FRS settings that allows with isomer tagging method the identification of all species. . . . .	68
4.2	Energy-vs-time histograms of the isomeric decay of $^{109}\text{Rh}$ and $^{109}\text{Ru}$ . . . . .	69
4.3	Identification plot for FRS setting with $^{107}\text{Nb}$ centered at the final focal plane. . . . .	70
4.4	Intrinsic PMT time of one of the 32 PMTs of the LYCCA start plastic. . . . .	71
4.5	Mean time difference of the LYCCA membrannes. . . . .	72
4.6	Determination of the time of flight offset with uranium beam. . . . .	73

4.7	Target and wall DSSSD calibrated with the automatic calibration procedure. . . . .	73
4.8	LYCCA identification histogram obtained after energy calibration. . . . .	74
4.9	$Z$ identification of the fragments with LYCCA. . . . .	75
4.10	$\gamma$ -ray spectra for the Mo isotopes observed from the fragmentation of $^{109}\text{Tc}$ FRS beam. . . . .	76
4.11	Calibration of the mass in the LYCCA calorimeter. . . . .	78
4.12	Definition of the geometry. . . . .	81
4.13	Width of the Doppler corrected X-rays after optimization of the target position. . . . .	83
4.14	Optimum target positioning with uranium X rays. . . . .	84
4.15	Projection for the minimum width of the two K X-rays of uranium. . . . .	84
4.16	Verification of the calibration of detector 06A. . . . .	86
4.17	Cross talk effect and correction for detector 01C. . . . .	87
4.18	Time determination from a net charge. . . . .	89
4.19	Effect of the walk correction using the time information extracted from AGATA traces. . . . .	90
4.20	Beam induced background reduced with a time condition. . . . .	92
4.21	Hits distribution inside a AGATA crystal. . . . .	92
4.22	AGATA hit distribution view from the target position. . . . .	93
4.23	Influence of the AGATA data replay on the data quality. . . . .	93
4.24	Influence of the time selection of the peak-to-total. . . . .	94
4.25	Influence of the time selection of the peak-to-total ratio. . . . .	95
4.26	Influence of the multiplicity condition on the peak-to-total ratio. . . . .	96
4.27	Optimum $\gamma$ -ray histogram obtained after several conditions. . . . .	96
5.1	Determination of the beam velocity. . . . .	100
5.2	Relation between the beam $\beta$ after the target with the incoming beam energy. . . . .	101
5.3	Determination of the geometrical offset. . . . .	102
5.4	Verification of the MC simulations with a set of experimental data points. . . . .	103
5.5	Lifetime determination of the $4_1^+$ state of $^{108}\text{Mo}$ . . . . .	104
5.6	Comparison of the energy ratios in neutron-rich molybdenum isotopes. . . . .	106
5.7	Comparison of the $B(E2)$ value with the geometrical model. . . . .	107
7.1	Orientation of a rigid body with the Euler angles. . . . .	112
7.2	Progression of the chains. . . . .	115
7.3	Fit result of the uranium X-ray transition. . . . .	115
7.4	Gated $\gamma$ -ray spectrum for the $^{100}\text{Mo}$ nucleus. . . . .	118
7.5	Gated $\gamma$ -ray spectrum for the $^{102}\text{Mo}$ nucleus. . . . .	118
7.6	Gated $\gamma$ -ray spectrum for the $^{104}\text{Mo}$ nucleus. . . . .	119
7.7	Gated $\gamma$ -ray spectrum for the $^{106}\text{Mo}$ nucleus. . . . .	119
7.8	Gated $\gamma$ -ray spectrum for the $^{108}\text{Mo}$ nucleus. . . . .	120
7.9	Fit of the $^{100}\text{Mo}$ $4_1^+$ to $2_1^+$ transition. . . . .	121
7.10	Fit of the $^{102}\text{Mo}$ $4_1^+$ to $2_1^+$ transition. . . . .	121
7.11	Fit of the $^{104}\text{Mo}$ $4_1^+$ to $2_1^+$ transition. . . . .	122
7.12	Fit of the $^{106}\text{Mo}$ $4_1^+$ to $2_1^+$ transition. . . . .	122
7.13	Fit of the $^{108}\text{Mo}$ $4_1^+$ to $2_1^+$ transition. . . . .	123

---

## List of Tables

3.1	Gate generation for the different triggers. . . . .	62
4.1	Summary of the three FRS settings. . . . .	69
4.2	Summary of the observed transition energies. . . . .	77
4.3	Energy resolution of the AGATA detectors . . . . .	88
4.4	Time resolution of the AGATA detectors. . . . .	91
5.1	Doppler-shifted energy of the $2_1^+$ to $0_1^+$ transition of $^{102}\text{Mo}$ . . . . .	99
5.2	Summary of the energy centroids of the observed $\gamma$ -ray transitions. . . . .	101
5.3	Simulations influence on the half-life determination of the $4_1^+$ state of $^{108}\text{Mo}$ . . . . .	104
7.1	First order spherical harmonics . . . . .	114





---

# Introduction

Protons and neutrons are arranged inside a nucleus by several forces that come into play. In order to have a deeper understanding of these forces, nuclear structure studies investigate nuclei outside the valley of stability. One of the facilities in the world that allows to experimentally access these nuclei is the FRagments Separator (FRS) [1] at GSI.

The nuclear structure physics program conducted with the FRS at GSI and planned with the Super-FRS at FAIR is organised within the NUclear-STRucture, Astrophysics and Reactions (NUSTAR) [2] collaboration. One of the sub-collaborations of NUSTAR is the HIgh-Resolution In-flight SPEctroscopy (HISPEC) collaboration [3]. The precursor of HISPEC, PreSPEC, aims at finding instrumentation solutions, at developing methodologies and at performing  $\gamma$ -ray spectroscopy experiments at the FRS.

From 2012 to 2014, the  $\gamma$ -spectroscopy group of GSI was operating the Advanced GAMMA Tracking Array (AGATA) [4] for a two years experimental campaign called the PreSPEC-AGATA campaign. The experimental setup was coupling the FRS, the Lund York Cologne CALorimeter (LYCCA) [5] and the High Energy  $\gamma$  deteCTOR (HECTOR+) [6] with AGATA.

The PreSPEC-AGATA campaign addressed nuclear structure topics about closed-shell nuclei, dipole responses and collective phenomena, with in total seven large-scale experiments [7–9]. One of these experiments, named “S428”, studied the nuclear collective behavior in the mass region  $A \approx 100$  via lifetime measurements [10] and it is the subject of this thesis.

In the first chapter of this thesis, I introduce the notion of the collective phenomena that occurs in the mass region  $A \approx 100$ . In order to explain the physics phenomena at play in this region, I first describe the deformation formalism and then I briefly review nuclear structure geometrical models.

In the following chapter, I describe the experimental setup of the PreSPEC-AGATA campaign. In this chapter, the complexity of large-scale  $\gamma$ -ray spectroscopy experiments is presented together with the advantages it provides in terms of lifetime measurements.

A complex experimental setup implies, on the other hand, a large number of electronic channels. Therefore, I detail in Chapter 3 the coupling of the data acquisition system of the AGATA detectors with the FRS-LYCCA-HECTOR+ detectors (that allowed the data-taking). This technical chapter answers to the three following questions:

- How to couple a digital with an analog system?
- How to optimize the data-taking?
- How to ensure proper data correlation between all the detectors?

Chapter 4 provides the data analysis procedure I developed and applied to observe the  $\gamma$ -ray transitions of the “S428” experiment.

The determination of the lifetime of the excited state is based on a Monte-Carlo simulations that are described in Chapter 5. In addition to the lifetime determination, an interpretation in terms of Geometrical models is provided in this chapter.

At last, in Chapter 6, I provide a conclusion and perspectives of this work.



# Chapter 1: Nuclear structure studies in the mass region $A \approx 100$

The mass region  $A \approx 100$  corresponds to nuclei with a number of neutrons between the magic numbers 50 and 82 and with a number of protons between the magic numbers 28 and 50. On the nuclear chart shown in Fig. 1.1, this mass region is circled in green.

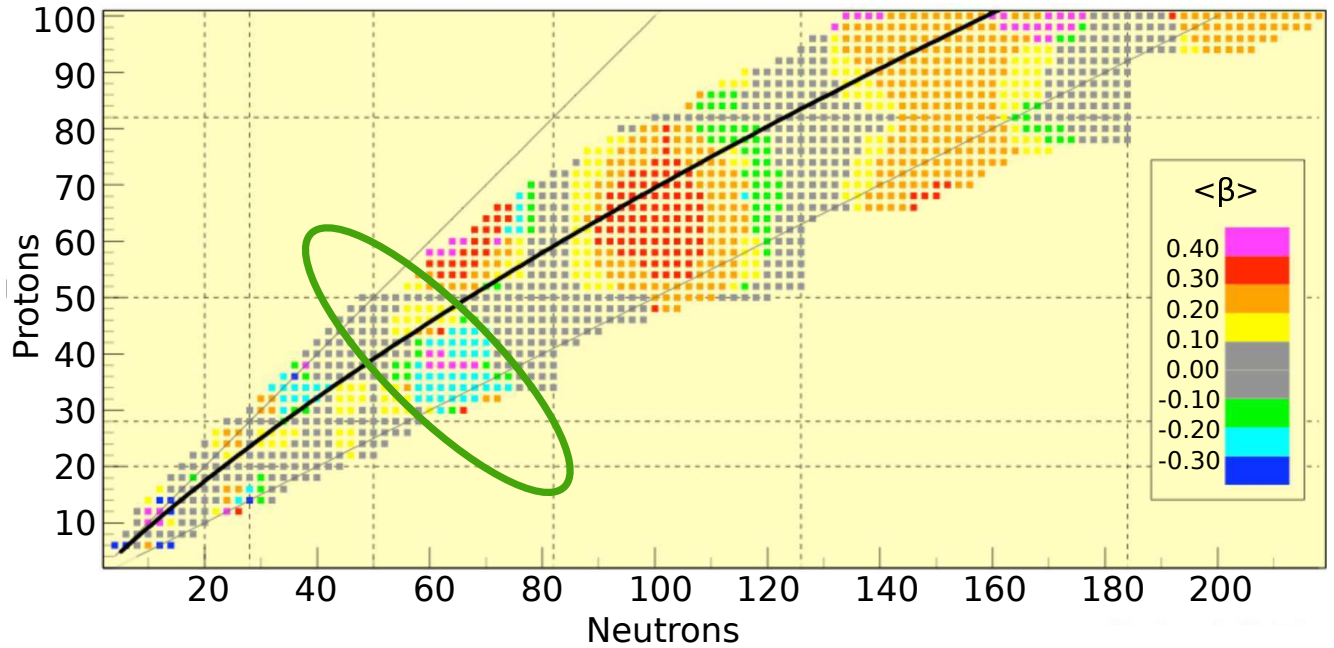


**Figure 1.1:** Shape predictions for the nuclei in the nuclear chart. The color code provides the deformation of each nucleus of the chart. The value of the deformation parameter ( $\beta$ ) is obtained with Hartree-Fock-Bogoliubov calculations [11]. The area circled in green corresponds to the mass region  $A \approx 100$  which is the subject of this thesis. The dashed lines indicate the nuclear magic numbers at stability. The black line corresponds to the valley of stability. The figure is adapted from [12].

From the color code, which indicates the predicted level of deformation, we can notice that the mass region of interest is subject to nuclear deformation. This region is interesting for additional collective phenomena such as rapid-shape changes, shape-coexistence, triaxiality and exotic shapes. In order to have a deeper understanding of the phenomena that occurs in this region, the measurement of both energies and lifetimes of excited states is required.

In Section 1.1, the formalism needed to parametrize the shape of a nucleus is described. Section 1.2 contains a discussion of the geometrical models applied to even-even nuclei. In Section 1.3, the nuclear structure observables use for these nuclear studies are discussed. In Section 1.4, I conclude this chapter with a status on the measurements that has been performed in the mass region  $A \approx 100$ .

## 1.1 Deformation formalism

In order to derive an Hamiltonian that describes a deformed nucleus, the shape of the nucleus need to be parametrised. The nuclear surface, noted  $R(\theta, \phi)$ , describes the nuclear shape in the spherical coordinate system:  $\theta$  is the polar angle with respect to the  $z$  axis and  $\phi$  is the azimuthal angle. We expand the nuclear surface  $R$  in terms of spherical harmonics:

$$R(\theta, \phi) = R_0 \left( 1 + \sum_{\lambda, \mu} \alpha_{\lambda, \mu} Y_{\lambda, \mu}(\theta, \phi) \right), \quad (1.1)$$

where  $R_0$  is the radius of a spherical nucleus with the same volume. The function  $Y_{\lambda, \mu}$  is the spherical harmonic of order  $\lambda, \mu$  (see Annexe 7.4 for a definition of the spherical harmonics). The expansion coefficients  $\alpha_{\lambda, \mu}$  describe the deformation of the nuclear surface. Since the nuclear surface  $R$  is a physical property of the nucleus, it has to be a real number. Thus we have  $\alpha_{\lambda, \mu} = (-1)^\mu \alpha_{\lambda, \nu}^*$ .

The orders  $\lambda = 0$  and  $\lambda = 1$  correspond to a spherical nucleus and to its translation respectively. The second order ( $\lambda = 2$ ) describes the quadrupole deformation of the nuclear shape. The third order ( $\lambda = 3$ ) corresponds to an octupole deformed nucleus. A schematic view of the different nuclear shapes for the first deformation orders is shown in Fig. 1.2.

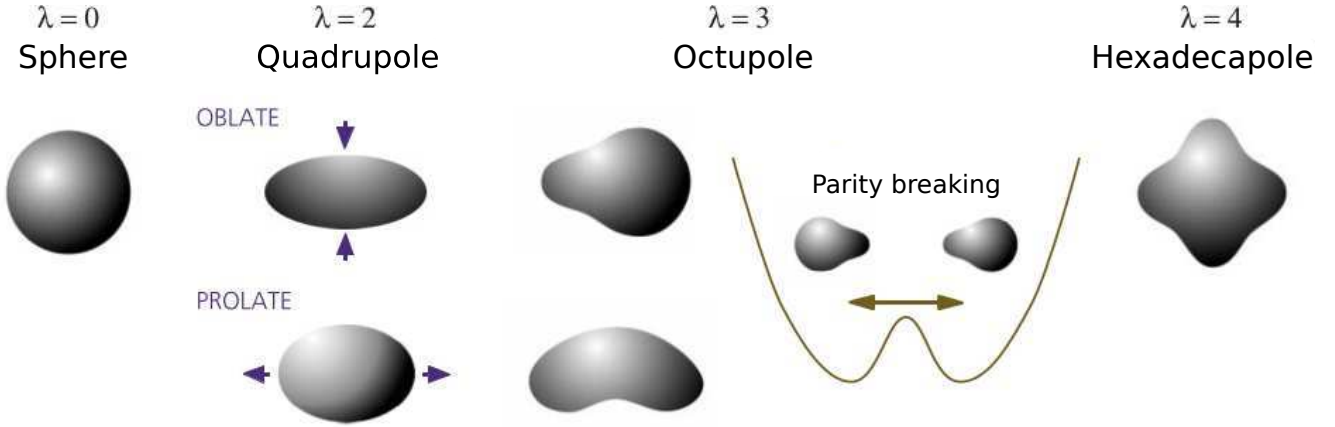


**Figure 1.2:** Representation of the nuclear shapes for the first deformation orders. The order  $\lambda = 1$  is not represented here since it corresponds to a translation of the nucleus. The figure is adapted from [13].

In this work, we consider only quadrupole deformation  $\lambda = 2$ , hence the shape of a nucleus is assumed to be an ellipsoid (see Fig. 1.2). In this case, five deformation coefficients, the  $\alpha_{2, \mu}$  variables, are needed to characterize the shape of a nucleus.

The spherical harmonics expansion given in Equation 1.1 describes the nuclear surface in the laboratory reference system  $\mathcal{K}$ . In order to match the deformation axis of the ellipsoid with the axis of the reference system, we rotate the laboratory reference system  $\mathcal{K}$  with three Euler angles<sup>1</sup>.

After the rotation, the nucleus is described in its frame of reference that we note  $\mathcal{K}'$ . In the nucleus frame of reference  $\mathcal{K}'$ , we note  $a_{2, \nu}$  the five deformation parameters. The judicious choice of the axis of the frame of reference  $\mathcal{K}'$  with the principal axis of deformation of the nucleus reduces the number of parameters needed to describe the shape of the nucleus. Indeed, the axial symmetry induces that non-diagonal moments of inertia are null, thus the relations [14]:

$$\begin{aligned} a_{2,2} &= a_{2,-2} \\ a_{2,1} &= a_{2,-1} = 0 \end{aligned}$$

In order to simplify the notations, we adopt the variable substitution as suggested by Hill and Wheeler [15]:

$$\begin{aligned} a_0 &= \beta \cos(\gamma) \\ a_2 = a_{-2} &= \frac{1}{\sqrt{2}} \beta \sin(\gamma), \end{aligned} \quad (1.2)$$

<sup>1</sup> The definition of the Euler angles together with the frame of rotation are given in Annexes 7.2 and 7.3 respectively.

where  $\beta$  corresponds to a measurement of the elongation parameter of the nucleus and  $\gamma$  corresponds to the degree of axial asymmetry, *i.e.*,  $\gamma$  is a variable that describes how much the deformation of a nucleus diverges from the axial symmetry.

In order to express the surface  $R(\theta, \phi)$  of a quadrupole ( $\lambda = 2$ ) deformed nucleus in its frame of reference, we substitute the variable  $a_0$ ,  $a_2$  and  $a_{-2}$  into Equation 1.1. Thus, the following equation results for the nuclear surface:

$$R(\theta, \phi) = R_0 \left[ 1 + \beta \sqrt{\frac{5}{16\pi}} \left( \cos(\gamma) \cdot (3 \cos^2(\theta) + 1) + \sqrt{2} \sin(\gamma) \cdot \sin^2(\theta) \cdot \cos(2\phi) \right) \right], \quad (1.3)$$

where the dependency on trigonometric functions of the angle  $\theta$  and  $\phi$  arises from the expression of the first order spherical harmonic (given in Annexe 7.4).

The nuclear radius can be also expressed along the axis of the nucleus' frame of reference [16]. Thus, an equation simpler than Equation 1.3 is derived:

$$R_k = R_0 \left[ 1 + \sqrt{\frac{5}{4\pi}} \beta \cos\left(\gamma - \frac{2}{3}\pi k\right) \right], \quad (1.4)$$

where  $k = 1, 2, 3$  denotes the index of the frame of reference axis.

A deformation parameter couple  $(\beta, \gamma)$  is associated with different nuclear shape. The scheme in Fig. 1.3 shows the different nuclear shapes inside the plane defined by the deformation parameters  $(\beta, \gamma)$ .

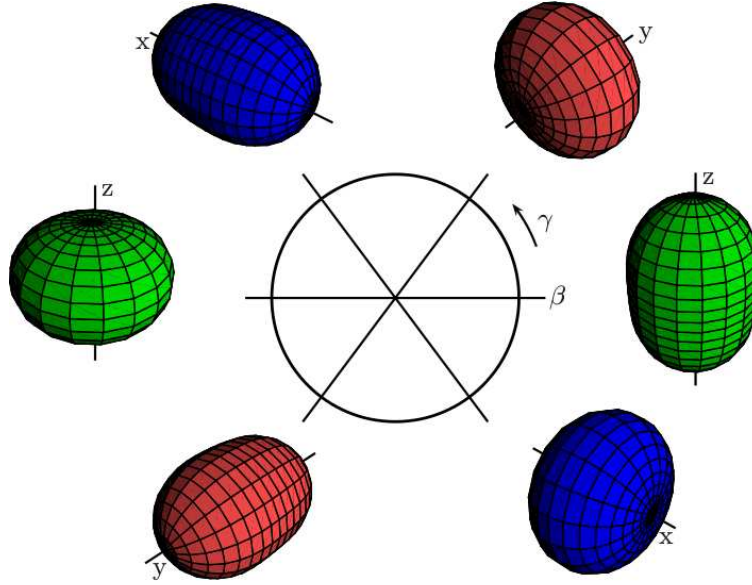


**Figure 1.3:** The shape of the nucleus is represented by a function of the two deformation parameters  $\beta$  and  $\gamma$ .  $(x, y, z)$  corresponds to the axis of the frame of reference  $K'$  of the nucleus. The color code highlights the deformation axis: green for  $z$ , red for  $y$  and blue for  $x$ . The figure is taken from [17].

The nucleus has a spherical shape for  $\beta = 0$ . The nuclear shapes described with an axial asymmetry parameter  $\gamma = 30^\circ$  have a maximum axial asymmetry.

In the plot shown in Fig. 1.3, the Lund convention in which the elongation parameter  $\beta \geq 0$  is adopted. With this convention, the nucleus is axially deformed for  $\gamma$  multiple of  $\pi/3$ . In this way, the parametrization by  $(\beta, \gamma)$  of the nuclear shapes have a “rotational symmetry” in  $\gamma = k \cdot (\pi/3)$  for  $k \in [1, 2, 3, 4, 5, 6]$ .

- A symmetrically deformed nucleus with  $\gamma = 2k \cdot (\pi/3)$  is oblate, which corresponds to a nucleus that is deformed along the major axis  $z$  of the ellipsoid.
- A symmetrically deformed nucleus with  $\gamma = (2k + 1) \cdot (\pi/3)$  is prolate, which corresponds to a nucleus that is deformed along the minor axis  $x$  or  $y$  of the ellipsoid.

An other convention used in Fig. 1.1 put a limit to the deformation space to  $\gamma \in [0, \pi/3]$ . With this convention:

- 
- the shape of the nucleus is oblate deformed for  $\beta > 0$ ;
  - the shape of the nucleus is prolate deformed for  $\beta < 0$ .

The symmetries present in the  $(\beta, \gamma)$  shape parametrization of the nuclear shape need to be fixed by a convention. We chose to limit the region of interest of the  $(\beta, \gamma)$  deformation space to  $\gamma \in [0^\circ, 60^\circ]$ , with the elongation parameter  $\beta > 0$ . In this case, the oblate deformed nuclei are obtained in  $\gamma = 0^\circ$  and the prolate deformed nuclei have  $\gamma = 60^\circ$ . A nucleus with an elongation parameter  $\beta \sim 0.3$  has a pronounced deformation. A nucleus is instead named “super-deformed” with a  $\beta \sim 0.6$ .

To summarize this section, the potentially quadrupole-deformed shape of the nucleus in the laboratory frame of reference can be described by five parameters: three Euler angles used for the orientation of the nucleus and the two deformation parameters ( $\beta$  and  $\gamma$ ). These latter describe the shape of a nucleus.

In the next paragraph, the collective behaviors of a nucleus are approached with this formalism and with the help of the geometrical models.



---

## 1.2 Geometrical models

---

### 1.2.1 Bohr Hamiltonian

---

The quantum mechanics of a deformed nucleus can be described by the so called ‘‘Bohr Hamiltonian’’ that was first derived by A. Bohr in 1952 [16]. In general, the Hamiltonian is expressed as the sum of the kinetic energy  $T$  and the potential energy  $V$  of the system hence:

$$H = T + V. \quad (1.5)$$

The two energies terms can be expressed in terms of nuclear surface coordinates (cf. Equation 1.1) by the following relations:

$$V = \frac{1}{2} \sum_{\lambda,\mu} C_\lambda |\alpha_{\lambda,\mu}|^2 \quad (1.6)$$

and

$$T = \frac{1}{2} \sum_{\lambda,\nu} B_\lambda |\alpha_{\lambda,\mu}|^2, \quad (1.7)$$

where  $C_\lambda$  and  $B_\lambda$  are quantities that depend on the nuclear matter properties. These are described in more details in reference [16].

In the previous paragraph, we have seen the coordinate transformation of the coefficient  $\alpha_{\lambda=2,\mu}$  in terms of the deformation parameters  $\beta, \gamma$  that belongs to the frame of reference  $\mathcal{K}'$ . Thus, after a time derivation of the  $\alpha_{\lambda,\mu}$  coefficients in terms of the deformation parameters (details of the calculation are given in both references [14] and [16]), the Bohr Hamiltonian can be expressed as a sum of three energy terms:

$$H = T_{vib} + T_{rot} + V. \quad (1.8)$$

$T_{vib}$  is the vibrational energy term:

$$T_{vib} = -\frac{\hbar^2}{2B} \left\{ \frac{1}{\beta^4} \frac{\partial}{\partial \beta} \beta^4 \frac{\partial}{\partial \beta} + \frac{1}{\beta^2} \frac{1}{\sin(3\gamma)} \frac{\partial}{\partial \gamma} \sin(3\gamma) \frac{\partial}{\partial \gamma} \right\}, \quad (1.9)$$

where  $B$  is the value of the quantity  $B_{\lambda=2}$  from Equation 1.7. Its expression is  $B = \frac{1}{2} \rho_0 R_0^5$ , with  $\rho_0$  the charge density and  $R_0$  the radius of the nucleus. The  $(\beta, \gamma)$  variables are the deformation parameters and  $\hbar$  the Planck constant.

The term  $T_{rot}$  is the rotational energy term defined by:

$$T_{rot} = \sum_{k=1}^3 \frac{\hbar^2}{2\mathcal{I}_k} J_k^2, \quad (1.10)$$

where  $\mathcal{I}_k$  are the moments of inertia of the nucleus and  $J_k$  is the orbital angular momentum of the nucleus. The summation over  $k$ , the axis of deformation, arises from the change of coordinate system, *i.e.*, from the laboratory to the nucleus coordinate system. The moment of inertia  $\mathcal{I}_k$  is expressed in terms of deformation parameters of the nucleus by:

$$\mathcal{I}_k = 4B \beta^2 \sin^2\left(\gamma - k \frac{2\pi}{3}\right); \quad k = 1, 2, 3. \quad (1.11)$$

The last term in Equation 1.8 is the potential energy and is given by a generic function [17] of the two deformation parameters  $\beta$  and  $\gamma$ :

$$V = V(\beta, \gamma). \quad (1.12)$$

At this point the terms and the equations required to describe the different collective behaviours in a nucleus are described. The Bohr Hamiltonian of Equation 1.8 provides a description of the nucleus in terms of nuclear vibrations, rotations and coupling of the two. Nevertheless, the solution of the Schroedinger equation with the Bohr-Hamiltonian from Equation 1.8 is rather complex. To overcome this, we provide simplified descriptions of the nucleus in the following paragraphs. Simplified models are obtained applying different conditions on the deformation parameters  $\beta, \gamma$  and on the potential  $V(\beta, \gamma)$ .

Moreover, the geometrical models are commonly compared and interchanged with the Interacting Boson Models<sup>2</sup> (IBM) [18]. Contrary to the geometrical models, where the nucleus is described collectively with the Bohr Hamiltonian, the IBM models for even-even nuclei are based on fermions couples described in terms of effective bosons. Each boson can have an angular momentum 0 (*s* type) or 2 (*d* type). The IBM models consist of one dimension for the boson *s* and five dimensions for the boson *d*, therefore have a group structure with six dimensions. In this group, one can construct three sub-groups, named  $U(5)$ ,  $O(6)$  and  $SU(3)$ . Each of the sub-groups provides a description of the nucleus with large similarities with the corresponding cases of the geometrical models [19].

The geometric models for different collective behaviors and the corresponding IBM sub-groups are the following:

- spherical vibrator –  $U(5)$
- axially deformed rotor –  $SU(3)$
- $\gamma$ -soft or  $\gamma$ -unstable rotor–  $O(6)$

In addition to these three limiting case, it exists: (*i*) shape-phase transitional critical points that can be described by the  $E(5)$  and  $X(5)$  analytical solution of the Bohr-Hamiltonian; (*ii*) transitional situations.

---

## 1.2.2 Nuclear collectivity

---

### Spherical vibrator

---

The vibration modes are related to a closely spherical nucleus that have surface oscillations. The harmonic spherical vibrator is obtained with the potential  $V(\beta, \gamma)$  with a dependence in  $\beta^2$  given by

$$V = \frac{1}{2}C^2\beta^2. \quad (1.13)$$

where  $C$  is the quantity  $C_\lambda$  from Equation 1.6 for  $\lambda = 2$ .

Under this condition on the energy potential, *i.e.*,  $V$  depends only on the deformation parameter  $\beta$ , it is possible to separate the Bohr Hamiltonian into two parts [17]: one depending only on  $\beta$  and one depending only on  $\gamma$ . With this method, we can derive the vibrational energies for a spherical harmonic vibrator [17]:

$$E_{vib} = (N + \frac{5}{2})\hbar\omega \quad (1.14)$$

with  $\omega = \sqrt{\frac{C}{B}}$  and  $N$  corresponding to the excitation level or phonon state. For example, the first phonon state  $N = 1$  corresponds to the first  $2_1^+$  excited state in a pure vibrator. Similarly to the case of a rigid rotor, we can calculate the energy ratio of the first  $4_1^+$  excited state over the energy of the first excited  $2_1^+$ :

$$R_{4/2} = E_4/E_2 \sim 2.0. \quad (1.15)$$

---

### Axially deformed rotor

---

Before describing the axially deformed rotor, a simplified theoretical case of a rigid rotor is considered. This case will help us in the forthcoming explanation of a general axially deformed rotor. Moreover, the Bohr Hamiltonian for a rigid rotor is very simple and an easy analytical solution can be obtained.

Since we assume a rigid rotor, there is no variation of the deformation parameter  $\beta$ , thus  $\frac{\partial}{\partial\beta} = 0$ . Moreover, as we assume that the deformation occurs only along the axis of the ellipsoid, therefore the parameter of axial asymmetry is null:  $\gamma = 0$ . Under these assumptions, only the rotation term  $T_{rot}$  remains in the Bohr Hamiltonian of Equation 1.8. Thus, our system is described by the following Hamiltonian

$$T_{rot} = \frac{\hbar^2}{2\mathcal{I}}\mathbf{R}^2, \quad (1.16)$$

where  $\mathbf{R}$  is the rotational angular momentum that consists of both intrinsic excitation and nuclear rotation.  $\mathcal{I}$  is the moment of inertia of the nucleus. For a small deformation parameter  $\beta$ , assuming an homogeneous rigid body and neglecting the pairing [19], the moment of inertia is expressed as

$$\mathcal{I} = \frac{2}{5} A M R_0^2 (1 + 0.31\beta), \quad (1.17)$$

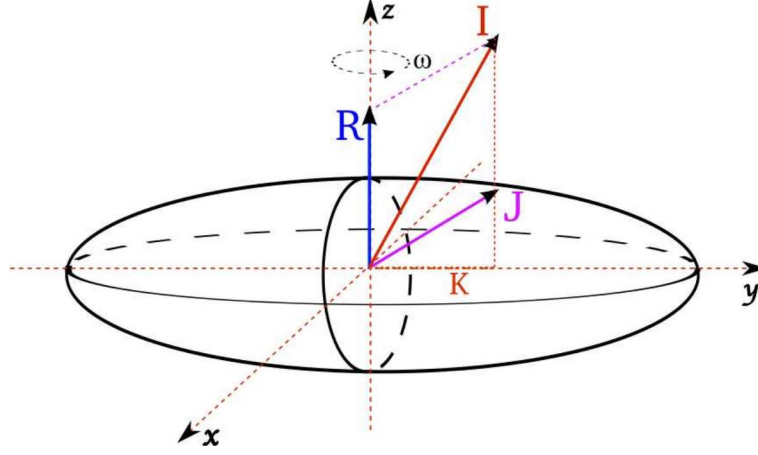


**Figure 1.4:** Schematic drawing of a deformed rotating nucleus. The nucleus rotates along the  $z$  axis, perpendicular to the symmetry axis  $y$ . The total spin of the nucleus is  $\mathbf{I} = \mathbf{R} + \mathbf{J}$  with  $\mathbf{R}$  the rotation vector and  $\mathbf{J}$  the intrinsic excitation spin.  $K$  indicates the projection of the intrinsic excitation on the symmetry axis. The figure is taken from [20].

with  $A$  the number of nucleons in the nucleus,  $M$  the mass of the nucleus and  $R_0$  the hypothetical radius of a spheric nucleus with the same volume. A schematic view of a deformed nucleus with its quantization axis  $y$  and rotational axis  $z$  is shown in Fig. 1.4.

For a nucleus in the ground state, the intrinsic spin is  $J^\pi = 0^+$  and the projection of the intrinsic excitation is  $K = 0$ . In this case, the rotational angular momentum is equal to the angular momentum [19]:  $\mathbf{R} = \mathbf{J}$ . The solution of the Schrodinger equation for a rigid rotor [21] provides the rotational energy as a function of the total angular momentum  $J$ :

$$E_{rot} = \frac{\hbar}{2\mathcal{I}} J(J+1). \quad (1.18)$$

The rotational energy  $E_{rot}$  depends only on the total angular momentum of the state  $J$  and on the structure parameter: the moment of inertia. The energy ratio of the first excited  $4_1^+$  state over the energy of the first excited  $2_1^+$  state is in this case

$$R_{4/2} = E_4/E_2 \sim 3.33. \quad (1.19)$$

When an intrinsic excitation occurs, the total angular momentum takes the value of the projection  $K$  of the intrinsic angular momentum  $\mathbf{J}$  and we obtain [19] the following rotational energy:

$$E_{rot} = \frac{\hbar}{2\mathcal{I}} [J(J+1) - K(K+1)]. \quad (1.20)$$

The construction of the axially deformed rotor comes now relatively simply from the coupling of a rigid rotor with a spherical vibrator. In this case, the nucleus is deformed and it can have phonon vibrations.

Two types of excitations arise. The first one, the  $\beta$  vibration, where the phonon excitation is along the deformation axis, with  $K = 0$  and the phonon excitation can induce change of the quadrupole deformation  $\beta$ . The second one, the  $\gamma$  vibration, which corresponds to an excitation with  $K = 2$  perpendicular to the deformation axis and in which the axial symmetry is broken.

---

### Axially asymmetric rotors

---

It is possible to distinguish two asymmetric rotors. The first one has the potential  $V(\gamma)$  with a steep and deep minima at a given  $\gamma$  value. This case is called “rigid triaxial rotor”. The second one, similar to the  $O(6)$  solution of the IBM, is the  $\gamma$ -soft rotor, which corresponds to a potential  $V(\gamma)$  completely flat in  $\gamma$  degree of freedom. In this case, the nucleus can oscillate freely in  $\gamma$  with a mean value  $\langle \gamma \rangle = 30^\circ$ . Due to the independence on  $\gamma$  of the nuclear potential, a similar energy spacing as in the rotor case can be derived [19]. The energy ratio in this case [19] is given by:

$$R_{4/2} = E_4/E_2 \sim 2.5. \quad (1.21)$$

---

<sup>2</sup> The interacting boson models are sometimes referred to algebraic models.

### 1.2.3 Summary of the collective modes

The discussions held above on the three collective nuclear behavior are summarized in one diagram shown in Fig. 1.5. In the figure are also shown the typical  $\gamma$ -ray cascades, the energy ratios  $R_{4/2}$  and the reduced transitions strengths implied by these limiting cases.

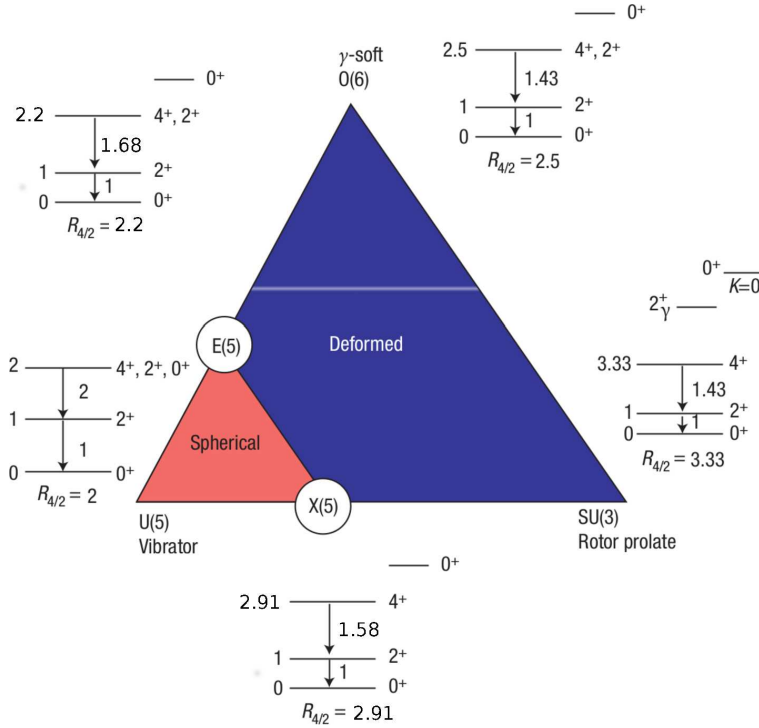


**Figure 1.5:** Representation of the collective behaviors of the nucleus. The correspondence of the collective geometrical models with the IBM models is indicated at the corners of the triangle. Typical  $\gamma$ -ray cascades obtained in these limits are shown in the figure together with the energy ratios between the first  $4^+_{11}$  and  $2^+_{11}$  state. The reduced transition strengths normalized to one are indicated on the right hand side of the arrows. The figure is adapted from [22].

Moreover, we can notice two circled areas:  $X(5)$  and  $E(5)$  that correspond to critical points, that provide a description for shape-phase transitional nuclei. They both have an analytical solution of the Bohr Hamiltonian that can be associated with a sub-group of the IBM models (thus their names).

In the case of  $E(5)$ , the transition from vibrator to  $\gamma$ -soft rotor is described. The details of the calculation are given in Reference [23]. The  $X(5)$  case corresponds to the shape-phase transition between a vibrator and a rotor, as explained in Reference [24]. Analytical solutions that approximate the Bohr-Hamiltonian between  $X(5)$  and  $SU(3)$  and between  $E(5)$  and  $O(6)$  are described in References [25] and [26] respectively.

In this paragraph, we have described the nuclear collectivity behavior with three limiting cases of the geometrical models and more particularly the assumptions –on the deformation parameters  $\beta$  and  $\gamma$  and on the energy potential of the Bohr Hamiltonian  $V(\beta, \gamma)$ – that are implied by these limiting cases. These models help us to understand the type of nuclei we are dealing with in the mid-shell region  $A \approx 100$ .

Aside the geometrical models, more sophisticated models exists such as the one based on mean-field theories [27].

Before providing a brief overview of the measurements in this particular mass region, we describe the nuclear observables that are of particular interest for the description of the mass region  $A \approx 100$ .

---

### 1.3 Useful observables for nuclear structure studies

---

In the previous paragraph, we mentioned the importance of the energy ratio between the first  $4_1^+$  and  $2_1^+$  excited level of the nucleus as a method to characterize its collective behavior: rotational, vibrational or  $\gamma$ -soft. We can obtain more detailed information on these behaviors by measuring the lifetime of excited levels. Indeed, the lifetime of an excited state is related to its transition probability, thus to the matrix element that allows a sensitive comparison between measurements and models.

In the following paragraph, before developing the formalism on the transition probabilities and their typical units, we first remind the selection rules of electromagnetic transitions.

---

#### 1.3.1 Selection rules

---

Let us consider an excited state with spin and parity  $J_i^{\pi_i}$  that decays to a lower state with spin parity  $J_f^{\pi_f}$ . The decay can occur via emission of a  $\gamma$ -ray with an energy  $E_\gamma = E_i - E_f$ , where  $E_i$  and  $E_f$  are the energy of the initial and final state respectively. The electromagnetic decay is characterized by its multipole order  $L$  and by its character: Electric ( $E$ ) or Magnetic ( $M$ ). The decay can occur if the photon of multipole order  $L$  follows the quantum mechanical selection rules on angular momentum and parity conservation [28]:

$$|J_i + J_f| \geq L \geq |J_i - J_f|. \quad (1.22)$$

The parity of a transition of order  $L$  is

- $\pi = \pi_i \cdot \pi_f = (-1)^{L+1}$  for magnetic decay
- $\pi = \pi_i \cdot \pi_f = (-1)^L$  for electric decay.

---

#### 1.3.2 Transition probabilities

---

In the case of multipole transitions of order  $L$  and character  $\lambda$ , the transition rate is given by [21]:

$$T_{if} = \frac{8\pi(L+1)}{\hbar((2L+1)!!)^2} \left(\frac{E_\gamma}{\hbar c}\right)^{2\lambda+1} B(\Pi\lambda; J_i \rightarrow J_f), \quad (1.23)$$

where  $B(\Pi\lambda; J_i \rightarrow J_f)$  is the transition strength between the state  $i$  and  $f$ . It is defined by:

$$B(\Pi\lambda; J_i \rightarrow J_f) = \frac{1}{2J_i + 1} \left| \langle \psi_f | \mathcal{O}_{\Pi,\lambda} | \psi_i \rangle \right|^2, \quad (1.24)$$

where  $\mathcal{O}_{\Pi,\lambda}$  is the electromagnetic operator (a description of the operator can be found in [29]) and  $\psi_i$  ( $\psi_f$ ) corresponds to the wave-functions of the state with spin  $J_i$  ( $J_f$ ). For example, in the case of electric dipole transition ( $E2$ ), Equation 1.24 is expressed as:

$$B(E2; J_i \rightarrow J_f) = \frac{1}{2J_i + 1} \left| \langle \psi_f | E2 | \psi_i \rangle \right|^2, \quad (1.25)$$

and it is commonly called  $B(E2)$  value.

The transition rate is linked to the lifetime  $\tau$  of a state  $i$  by the equation:

$$T_{if} = \frac{1}{\tau}. \quad (1.26)$$

The reduced matrix element depends on the wave-function of the initial and final state, therefore the lifetime of an excited state is an ideal observable to compare experimental observation with model predictions.

---

### 1.3.3 Units and conversions

---

The unit of the reduced transition strength, in the case of an  $E2$  transition is  $e^2\text{fm}^4$ , where  $e = 1.6 \cdot 10^{-19}$  C and  $1 \text{ fm} = 10^{-15}$  m. For a transition with an energy  $E_\gamma$  in MeV and a lifetime in second, we have the following relation [29]:

$$T(E2) = \frac{1}{\tau} = 1.223 \cdot 10^9 \cdot E_\gamma^5 \cdot B(E2) \quad (1.27)$$

An other commonly used unit for the  $B(E2)$  value is the Weisskopf unit (W.u.). It is defined by [19]:

$$1\text{W.u.} = 0.0594 \cdot A^{4/3} e^2\text{fm}^4, \quad (1.28)$$

where  $A$  is the mass number.

The advantage of the Weisskopf unit compare to the  $e^2\text{fm}^4$  unit lies in the description of the collectivity: the W.u. highlights the single particle contributing to the deformation. A value larger than one W.u. is associated with a collective behavior.

Moreover, the Grodzins relation [30] states that the  $B(E2)$  value is inversely proportional to the energy of the first  $2_1^+$  state. Thus, the measurement of the energy of the first excited state in a nucleus provides an indication of the  $B(E2; 2_1^+, 0_1^+)$  value. A generalisation of the Grodzins relation for higher spin state can be derived from the Bohr-Hamiltonian and is provided in Reference [31].

---

### 1.3.4 Relation between the quadrupole moment and the $B(E2)$ value

---

The measurement of the lifetime of an excited state is useful to characterize the charge distribution, or quadrupole moment, inside the nucleus. Indeed, from the parametrization of the surface of the nucleus given in Equation 1.1, we can derive [21] the intrinsic quadrupole moment in second order in the deformation parameter  $\beta$ :

$$\mathcal{Q}_0 = \frac{3}{\sqrt{5}\pi} Z R_0^2 \beta (1 + 0.16\beta), \quad (1.29)$$

with  $Z$  is the proton number of the nucleus.

We cannot observe experimentally the intrinsic quadrupole moment of the nucleus which is expressed in the reference frame ( $\mathcal{X}'$ ) of the nucleus, but the spectroscopic quadrupole moment, noted  $\mathcal{Q}$ , which is related to the measurement in the laboratory frame ( $\mathcal{X}$ ). The relation between the two is given by [19]:

$$\mathcal{Q} = \mathcal{Q}_0 \frac{3K^2 - J(J+1)}{(J+1)(2J+3)}. \quad (1.30)$$

In the limiting case of a rigid rotor with  $R_{4/2} = 3.33$ , the relation between the quadrupole moment and the  $B(E2)$  value is [21]:

$$B(E2; J_i \rightarrow J_f) = \frac{5}{16\pi} e^2 \mathcal{Q}_0^2 \left| \langle J_i K 20 | J_f K \rangle \right|^2 \quad (1.31)$$

where  $\langle J_i K 20 | J_f K \rangle$  is a Clebsh-Gordan coefficient connecting the state of spin  $J_i$  and  $J_f$ . A more general relation between the  $B(E2)$  values and intrinsic quadrupole moments for axially deformed nuclei with  $R_{4/2} < 3.33$  is given in Reference [32].

To summarize, if we measure the lifetime of an excited state that decays via  $E2$  transition, we can estimate its reduced matrix element from Equations 1.27 and introduce the value into Equation 1.31 in order to calculate the quadrupole moment. We can also introduce the quadrupole moment into Equation 1.29 and 1.30 in order to determine the deformation parameter  $\beta$  of a nucleus with the help of the geometrical models.



The inverse of the energy of the first  $2_1^+$  is plotted in Fig. 1.6 for the even-even nuclei with  $Z \in [36, 50]$ . The nuclear

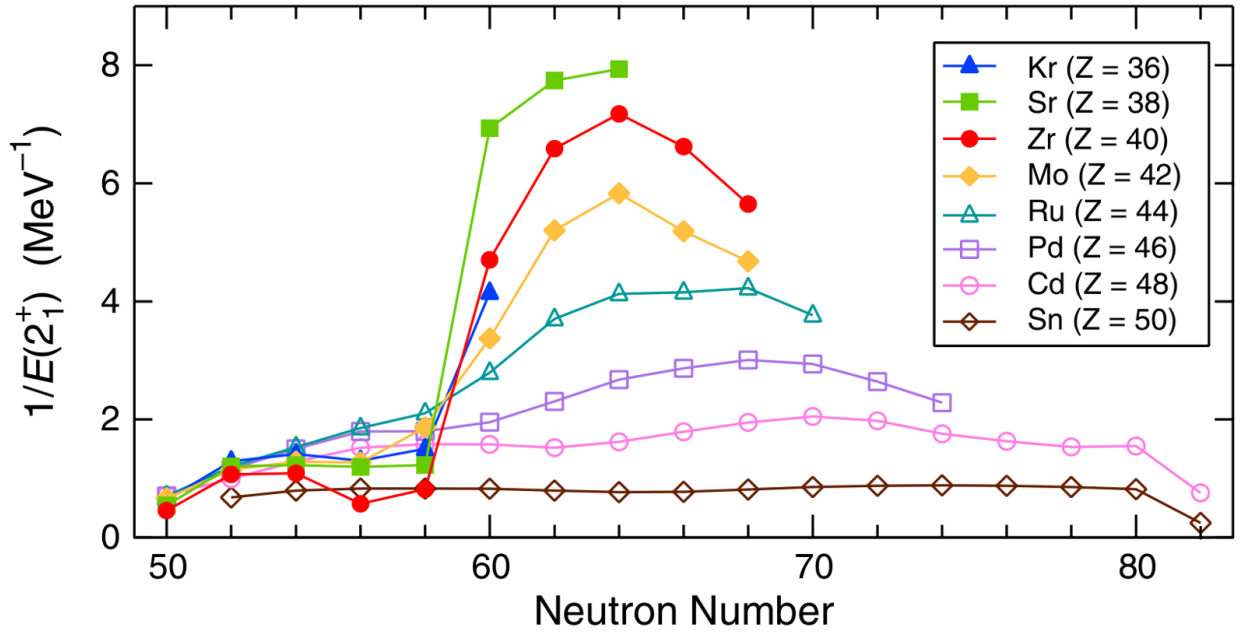


**Figure 1.6:** Plot of the systematics of the first  $2_1^+$  energy in the mass region  $A \approx 100$ . The color code, given in the insert, is related to the different isotopic chains. The energy values plotted here are the adopted ones from Reference [33]. The figure is taken from [34].

structure in the mass region  $A \approx 100$  is therefore highlighted. The number of protons of the tin ( $_{50}\text{Sn}$ ) isotopes is a magic number. The energy of its first  $2_1^+$  state is close to one and constant along the isotopic chain. Thus, according to the Grodzins relation, the  $B(E2)$  values are closed to one and tin isotopes have a spherical shape. If we remove protons from the tin isotopes and keep constant the neutron number, we observed a decrease of the first  $2_1^+$  energy, which is an indication of a collective excitation behavior. If we now focus on a mid shell isotope, e.g. zirconium ( $_{40}\text{Zr}$ ), we can notice that for 58 neutrons the energy of the first  $2_1^+$  is high. While adding neutrons to  $^{98}\text{Zr}$ , we observe a fast decrease of the first  $2_1^+$  state energy. This energy change occurs only by adding two neutrons and is therefore called “rapid” shape transition from a spherical to a deformed nucleus. We observe a similar rapid shape transition also in other isotopes in the region, e.g. krypton ( $_{36}\text{Kr}$ ), strontium ( $_{38}\text{Sr}$ ) and molybdenum ( $_{42}\text{Mo}$ ). To conclude, this plot shows the importance of the energy of the first  $2_1^+$  state in relation to the collective behavior observed in the mass region  $A \approx 100$ .

#### 1.4.1 Shape-phase transition

If we consider on the zirconium isotopic chain, we notice that a lot of theoretical efforts have been put into explaining the rapid shape transition. For example, Hartree-Fock-Bogoliubov (HFB) calculations using a DS1 Gogny interaction [11] predict that the zirconium isotopes with  $N \geq 60$  are deformed with a prolate and oblate minimum very close in energy. A calculation from Xu et al. [35] predicts a stable oblate shape for  $N \geq 70$ , using both cranked and configuration-constrained shell models. The work of Schunck et al. [36] predicts a spherical potential for  $^{106}\text{Zr}$  and a tetrahedral ground state for  $^{108,110}\text{Zr}$  nuclei.

One can notice from the previous examples that the theoretical works in the zirconium isotopes do not fully agree and predict different shapes and shape-phase transitions. Moreover, the predicted number of neutrons for which the shape-phase transition occurs is different depending on the model that we consider.

Similar behavior is expected in the strontium, molybdenum and ruthenium isotopes. For example, in a recent lifetime measurement by A.G. Smith et al. [37], the competition between oblate-prolate shapes for various isotopes in the mass region  $A \approx 100$  is highlighted. For nuclei with a higher  $Z$ , we can quote the work of A. M. Bruce et al. [38], in which the measurement of the lifetime of the first  $2_1^+$  state in  $^{112,113}\text{Tc}$  isotopes suggests an oblate ground state.

The systematics of energy ratios  $R_{4/2}$  in the mass region  $A \approx 100$  depicted in Fig. 1.7 shows, for the zirconium and molybdenum isotopes, a shape transition from a spherical nucleus at  $N \sim 58$  to a deformed nucleus at  $N \sim 62$ .

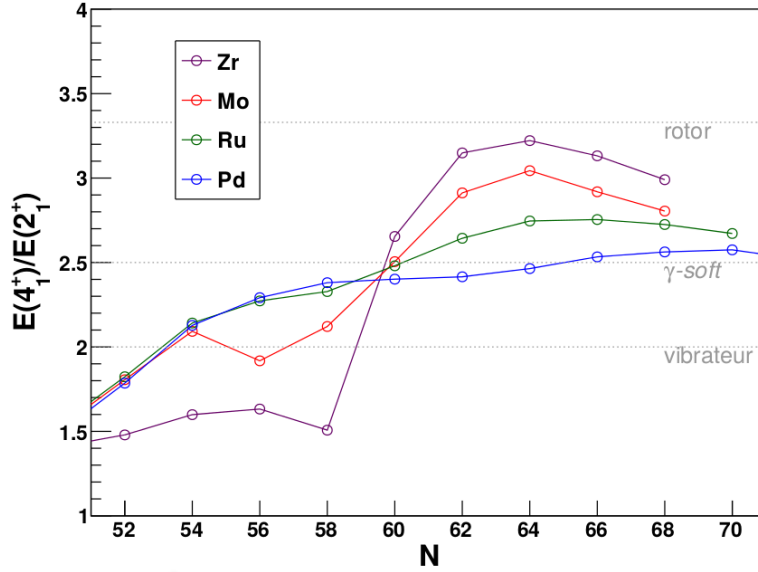


**Figure 1.7:** Systematics of the energy ratio of the first  $4_1^+$  over the first  $2_1^+$ . The color code, given in the insert is related to the different isotopic chains. The energies values are the adopted ones from Reference [33]. The dotted grey lines indicate the energy ratios for the three limiting case mentioned in Paragraph 1.2.2. The figure is taken from [12].

#### 1.4.2 Triaxiality

In the mass region  $A \approx 100$ , triaxial behavior is also expected. For instance, in the recent work of P.-A. Söderström et al. [39] the question of triaxiality is raised for the  $^{116,118}\text{Ru}$  nuclei. Furthermore, it is in the even-odd molybdenum isotopes that triaxial behavior is most often observed, e.g. J.A. Pinston et al. [40] obtained a triaxial deformation parameter  $\gamma \approx 17^\circ$  for  $^{105,107}\text{Mo}$ .

#### 1.4.3 Particularity of Mo isotopes

In the previous paragraphs, we discussed the importance of deformation in the understanding of the nuclear structure in the mass region  $A \approx 100$ . The present work concerns the molybdenum isotopic chain and in particular  $^{108}\text{Mo}$ . The adopted energy values of the ground state band (up to spin 6) of molybdenum isotopes is plotted in Fig. 1.8. The lifetime of the excited states are given inside the green box.

The measurement of Hutter et al. [41] is of particular interest for the present work. Indeed, it provides a systematic measurement of the  $B(E2)$  values up to spin  $10^+$  of the  $^{104,106}\text{Mo}$  nuclei. Furthermore, Hutter et al. compared his results with the critical point symmetry  $X(5)$ . Their results favor a rotational interpretation of  $^{104,106}\text{Mo}$ . Nevertheless, in the search for a critical point symmetry  $X(5)$  suggested by Caprio et al. [42], the neutron rich molybdenum isotopes remain good candidates.

In this Chapter, we presented the collective behavior that occurs in the mass region  $A \approx 100$ . Moreover, we discussed the importance of the collective models in order to understand the nuclear structure in these nuclei. Furthermore, we stressed the importance of the lifetime measurement focussing our discussion onto the lifetime of the excited  $^{108}\text{Mo}$ , the subject of the present work.

In order to further test the possibility of a critical point-symmetry, we need to measure the lifetime of the first  $4_1^+$  excited state of  $^{108}\text{Mo}$ . From the comparison between the half-life of the first  $4_1^+$  excited state of both  $^{104}\text{Mo}$  and  $^{106}\text{Mo}$  isotopes, we can expect a half-life value of the  $4_1^+$  state of  $^{108}\text{Mo}$  to be close to  $\sim 25$  ps. The present work is focussed on the determination of this specific half-life.

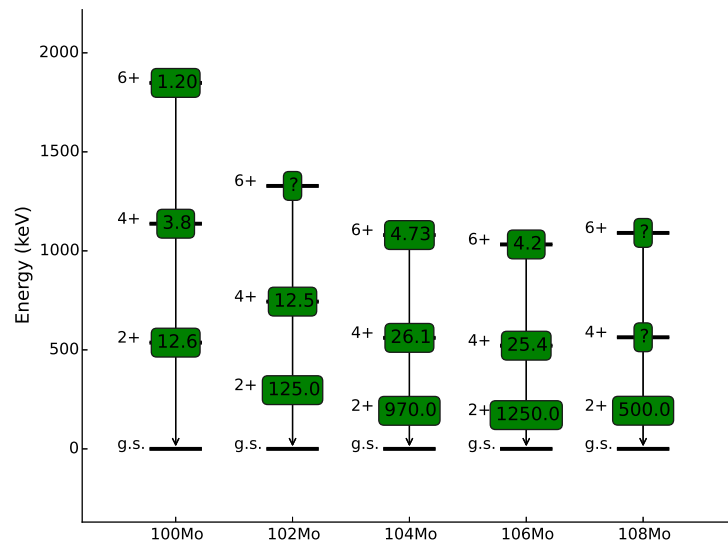


**Figure 1.8:** Energy of the excited levels of the ground state band of the molybdenum isotopes up to spin 6. The lifetime values given in the green boxes are expressed in ps. They are the adopted values taken from the ENSDF database [33]. The unknown values are marked with a question mark.



## Chapter 2: Experimental setup

The production of the molybdenum isotopes was performed in a multi-stage process depicted in Fig. 2.1.

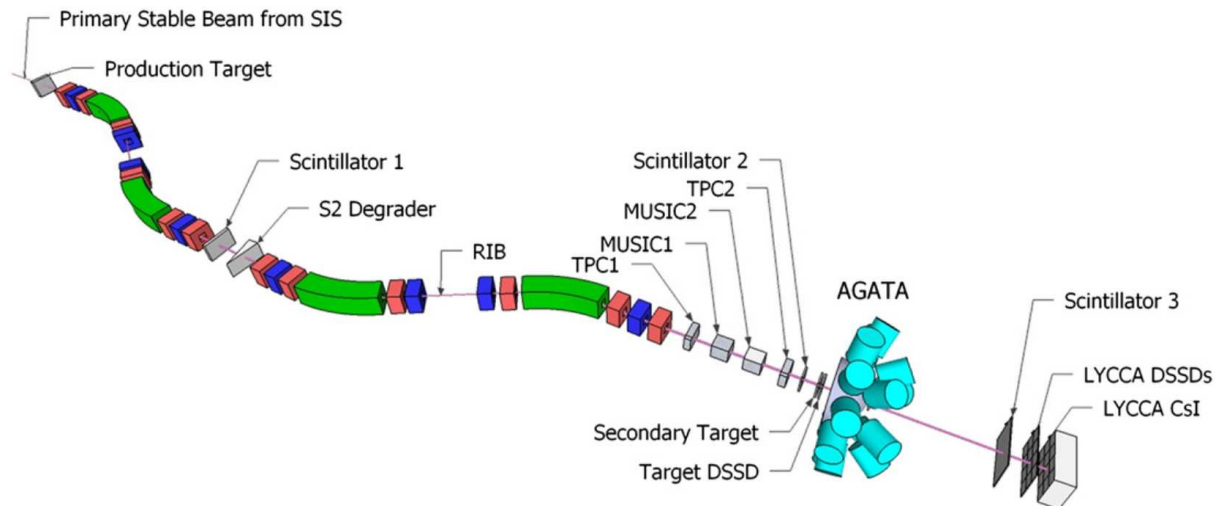


**Figure 2.1:** Schematic view of the experimental setup used to produce the radioactive molybdenum isotopes. The figure is taken from [43].

At first, the UNiversal LINear ACcelerator (UNILAC) pre-accelerated an uranium beam that was injected in the SIS-18 synchrotron [44]. The uranium was further accelerated by the SIS-18 synchrotron up to an energy of 600 MeV/u. The extraction of the uranium beam out of the SIS-18 was taking about one second. Thus, at this stage, the extracted beam from the SIS-18 had a specific time structure in bunches (or spills) with a typical one second extraction and three seconds ramping time. The beam was then transmitted to the FRagment Separator (FRS) [1]. Here the SEETRAM<sup>1</sup> measured a beam intensity up to  $2 \cdot 10^9$  particles per spill.

The uranium beam underwent a fission reaction on a  $1033 \text{ mg/cm}^2$  thick beryllium target positioned at the entrance of the FRS, the primary target of the FRS.  $^{109}\text{Tc}$  fission fragments were selected by the FRS set in mono-energetic mode<sup>2</sup>. The FRS provided, in addition, identification and tracking of all species passing through it. It is worth noting that, at the final focal plane of the FRS, three species were identified and centered:  $^{107}\text{Nb}$ ,  $^{108}\text{Mo}$  and  $^{109}\text{Tc}$ . The total beam intensity measured by a plastic scintillator positioned at the last focal plane of the FRS was 1900 particles per spill.

This multi-species beam, with an energy  $\sim 150 \text{ MeV/u}$ , was sent to a  $700 \text{ mg/cm}^2$  thick beryllium secondary target. The fragments of the second-step fragmentation were tracked and identified by the Lund York Cologne CAlorimeter (LYCCA) [5]. The secondary target was surrounded by two types of  $\gamma$ -ray detectors: the Advanced GAMMA Tracking Array (AGATA) [4] and the High Energy  $\gamma$ -ray deteCTOR (HECTOR+) [6]. The  $^{109}\text{Tc}$  beam underwent a fragmentation onto the secondary target to produce, e.g.  $^{108}\text{Mo}$  in a 1-proton knockout reaction.

The data were written onto disk for events in which a  $\gamma$ -ray was detected in coincidence with a particle passing through the FRS and LYCCA. The number of coincidence trigger reached up to 320 Hz.

In this chapter, I describe each of the apparatus above mentioned. I start in Section 2.1 with the FRS. It is followed by a description of the LYCCA calorimeter in Section 2.2. I explain the  $\gamma$ -ray detector AGATA in Section 2.3 and HECTOR+ in Section 2.4.

In the last Section of this chapter I describe the experimental methods that are used for lifetime measurements and I detail the one that can be applied with our experimental setup.

<sup>1</sup> SEETRAM stands for SEcondary Electron TRAnsmision Monitor [45].

<sup>2</sup> We further explain the reason and the advantages/disadvantages of this mode in Paragraph 2.1.1.

## 2.1 The GSI fragment separator

The relativistic ion beam delivered by the SIS is transported to the entrance of the FRS where it undergoes fission or fragmentation reactions on a primary target. After the primary target, the four dipole magnets of the FRS select reaction products of interest using the  $B\rho - \Delta E - B\rho$  method explained in Paragraph 2.1.1. After each dipole, slits can be inserted into the beam line in order to cut contaminants. Optimal beam quality and focussing are obtained with a series of quadrupole and sextupole magnet before and after each dipole magnet.

The identification of the fragments is performed by the FRS standard detectors described in Paragraph 2.1.2.

### 2.1.1 The $B\rho - \Delta E - B\rho$ method

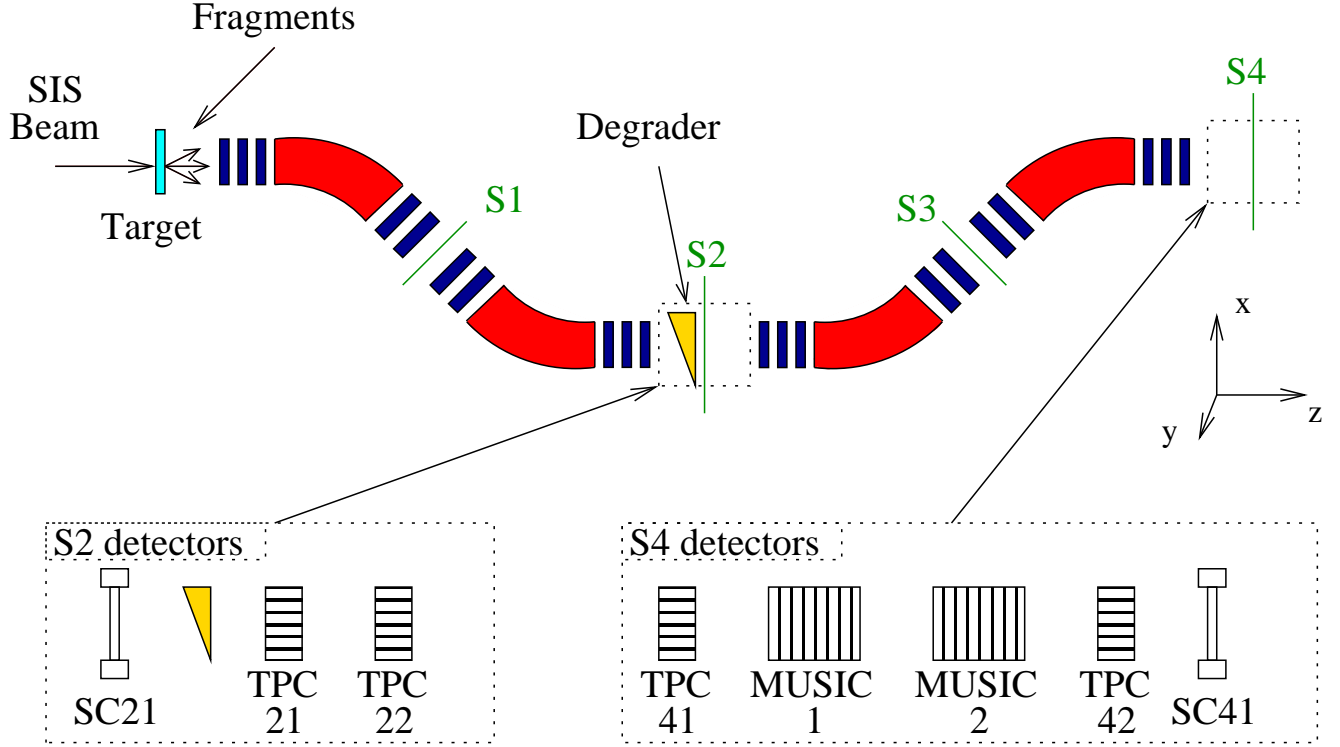


**Figure 2.2:** Schematic view of the FRS. The four dipoles are drawn in red and the quadrupoles in blue. The sextupoles are not drawn here. A fragment from the beam cocktail produced at the target level is selected by the four dipoles of the FRS. The boxes in the lower part of the drawing show the FRS detectors needed for the full identification and tracking of the fragments. The detector positions are not to scale but their relative positions are respected. The distances are given in Annexe 7.1. The drawing is inspired from [46].

The selection of a fragment of interest  $\frac{A}{Z}X$  with a momentum  $p_0$  is performed in three steps. In the first part of the FRS, the first two dipoles of Fig. 2.2, select an ion according to its magnetic rigidity:  $B\rho_0$  where  $B$  is the magnetic field and  $\rho_0$  is the bending radius of the ion trajectory. Indeed, the homogeneous magnetic field  $\vec{B}$  of a dipole magnet induces a Lorentz force to a moving charge  $Qe$  ( $e$  the electron charge) with mass  $Au$  ( $u$  is the atomic mass unit) [47]:

$$\vec{F}_{Lorentz} = Qe \cdot \vec{v} \times \vec{B}, \quad (2.1)$$

where  $\vec{v}$  is the velocity of the ion. Since  $\vec{B}$  and  $\vec{v}$  are perpendicular, the Lorentz force is centripetal and its norm can be written as follows:

$$|\vec{F}_{Lorentz}| = \frac{mv^2}{\rho_0}. \quad (2.2)$$

The combination of Equations 2.1 and 2.2 provides the following equation showing the explicit dependence of the  $\frac{A}{Q}$  ( $AoQ$ ) of the fragment with the  $B\rho_0$ :

$$B\rho_0 = \beta\gamma c \frac{A}{Q} \frac{u}{e}, \quad (2.3)$$

where  $\beta = \frac{v}{c}$ , with  $c$  the speed of light in vacuum and  $\gamma$  the Lorentz factor. Therefore, each fragment with a different  $AoQ$  ratio has a different bending radius  $\rho$  and the first selection stage make use of this relation to select all species with similar  $AoQ$ . The momentum acceptance of the first FRS dipole determines the number of species passing around the selected  $AoQ$ . A representation of the selection through the momentum acceptance of the dipole of the species is shown in red in Fig. 2.3.

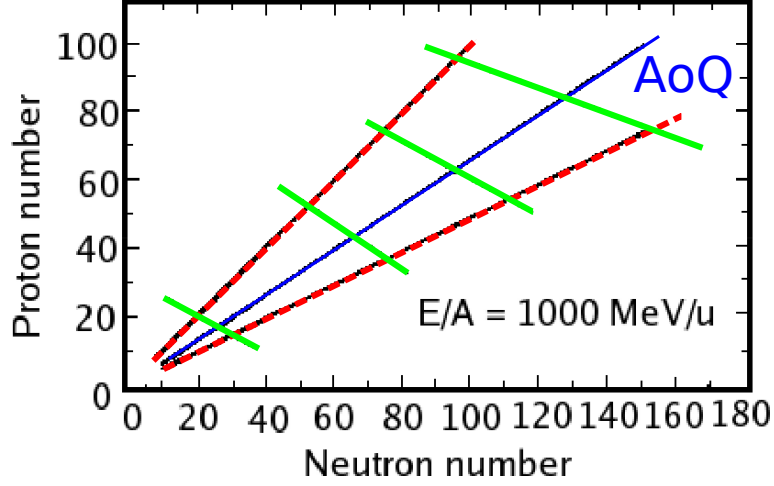


**Figure 2.3:** Selection of an isotope with the FRS. The slits permit to reduce the transmission of a given section, thus allowing to narrow the space between the “green lines” or the “red/blue” lines. The first selection after the first two dipoles is between the two red lines. The impact of the middle focal plane degrader followed by a second  $B\rho$  selection is illustrated by the area between two green lines. The figure is adapted from [46].

As different species can have similar  $AoQ$  ratios, in order to suppress unwanted isotopes after the second dipole, a wedge shaped degrader is positioned at the intermediate focal plane. The energy loss by a charged particle inside a unit of matter ( $\frac{dE}{dx}$ ) follows the Bethe and Bloch equation [48]:

$$\frac{dE}{dx} = f(\beta)Z^2, \quad (2.4)$$

with  $Z$  the atomic number of the ion and  $f(\beta)$  a function depending on the material and on the beam velocity. The different energy loss of different species in the degrader provides a momentum spread of the beam cocktail. A specific  $B\rho$  value applied to the last two FRS dipoles shown in Fig. 2.2 selects the isotope of interest. This second selection is schematically illustrated in Fig. 2.3.

Employing a wedge shaped degrader, the angle of the wedge can be chosen to set the FRS in achromatic mode, *i.e.*, the position of a specie at the final focal plane has a narrow spatial distribution, independent of the particle momentum. This provides a good transmission efficiency for a given specie and contaminants arriving at different positions can be easily removed with slits. The shape of the wedge degrader can also be adjusted to correct the position dependence of momentum at the middle focal plane of the FRS. After the degrader all ions of the centered species have the same momentum and the FRS optics make that they come broad on the target at the final focal plane of the FRS. This FRS mode is called mono-energetic [49]. This affects the transmission efficiency but assures a narrow velocity distribution at the final focal plane of the FRS (Fig. 2.4).

### 2.1.2 In flight identification of the ions in the FRS

All the ions reaching the final focal plane of the FRS need to be identified. In order to achieve ion identification, meaning determination of both charge ( $Q$ ) and mass ( $A$ ), their velocity, positions and charge or proton number ( $Z$ ) must be measured. For the ions at 400 MeV/u considered in this experiments ( $Z \sim 40$ ), the ions are assumed to be fully stripped in the FRS( $Q = Z$ ) [51].

The ion velocity is obtained by measuring the Time of Flight ( $ToF$ ) between the middle focal plane (S2) and the final focal plane (S4) with the help of plastic scintillator detectors (Sc21 at S2 and Sc41 at S4). The time signal in each scintillator is measured by two Photo-Multiplier Tubes (PMTs), one on the left ( $T_{Sc21L}$  and  $T_{Sc41L}$ ), and one on the

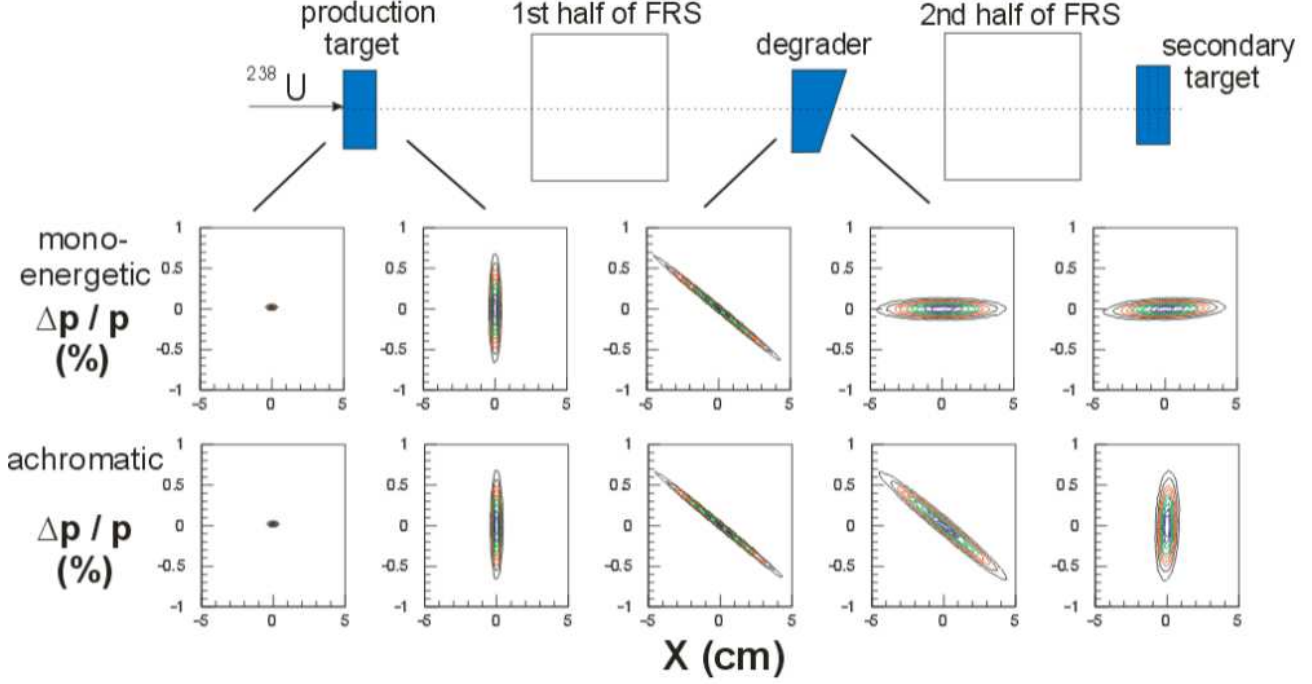


**Figure 2.4:** Representation of the particle spreading in momentum  $p$  ( $y$  axis) and position ( $x$  axis) of the particles in different stages of the FRS. The mode of the spectrometer is selected by setting different wedge angles of the S2 degrader. The figure is adapted from [50].

right side ( $T_{Sc21R}$  and  $T_{Sc41R}$ ) of the rectangular scintillators. The  $ToF$  of an ion can then be calculated using the following relation:

$$ToF = (T_{Sc41L} + T_{Sc41R}) - (T_{Sc21L} + T_{Sc21R}). \quad (2.5)$$

This allows a time-of-flight measurement independently of the position of particles at the S2 and S4 focal planes. The velocity  $\beta = \frac{v}{c}$  of an ion can easily be deduced knowing the distance  $D$  between the two scintillators<sup>3</sup>:

$$\beta = \frac{D}{ToF} \frac{1}{c}. \quad (2.6)$$

Time Proportional Chambers (TPC) are used to determine the beam-particle positions. The FRS TPCs [52] are  $CH_4$  gas detectors operated at normal pressure and room temperature. Charged particle passing through the TPC ionise the gas and in the presence of an uniform electric field, electrons are collected by the anode, and positive charges are deposit on the cathode. The position along the dispersive plane of the dipoles ( $x$  axis –the axis are represented in Fig. 2.2–), *i.e.*, along the anode, is given by a delay line. The position in the  $y$  axis is obtained by measuring the drift time of the charges inside the TPC detector. The angle of the particles is obtained combining information of two TPCs in one focal plane.

Once positions are determined, it is possible to calculate the magnetic rigidity of a fragment for both sections of the FRS according to the equations:

$$B\rho_2 = (B\rho_0)_2 \left(1 + \frac{x_2}{D_2}\right) \quad (2.7)$$

and

$$B\rho_4 = (B\rho_0)_4 \left(1 + \frac{x_4 - M \cdot x_2}{D_4}\right), \quad (2.8)$$

where  $(B\rho_0)_2$  and  $(B\rho_0)_4$  are the magnetic rigidities of the fragments for a central trajectory at the middle focal plane (S2) and final focal plane (S4). The measured positions are  $x_2$  for the middle focal plane and  $x_4$  for the final focal plane.

<sup>3</sup> In the experiment presented in this work, the distance between the middle and the final focal planes was  $\sim 34$  m.



The dispersion in a section is  $D_2$  for the first part of the FRS and  $D_4$  for the second part of the FRS and  $M$  is the magnification between the intermediate and the final focal plane. The magnetic field  $B$  inside each dipole is measured by calibrated Hall probes.

Introducing  $B\rho$  and  $\beta$  in Equation 2.3 provides the  $AoQ$  of the ions:

$$AoQ = \frac{A}{Q} = \frac{B\rho e}{\beta\gamma c u}. \quad (2.9)$$

The  $Z$  of the ions are obtained with a MUlti Sampling Ionisation Chamber (MUSIC) [53]. The  $CF_4$  gas of the chamber gets ionised by the particle passing through the detector. The energy loss inside the gas is proportional to  $Z^2$  of the particle (see the Bethe-Bloch equation 2.4). The detector drift space is subdivided in eight sub-volumes. For each of them, charges are independently collected at the anode. The averaging of the eight anode energy deposits allows a better energy resolution than what would be reached using a single drift space. The  $Z$  of an ion is obtained by including a correction for the velocity dependence function  $f(\beta)$  in the Bethe-Bloch relation:

$$Z = \sqrt{\frac{\Delta E}{f(\beta)}}. \quad (2.10)$$

## 2.2 The Lund York Cologne Calorimeter

The Lund York Cologne Calorimeter (LYCCA), positioned after the last plastic scintillator of the FRS (labelled SC41 in Fig. 2.2), allows both identification and tracking of the fragments produced by the reaction in the secondary target. The detectors composing the LYCCA calorimeter are sketched in Fig. 2.5.

The position of the ion on the secondary target and its outgoing angle, is determined with Double-Sided-Strip-Silicon Detectors (DSSSD) described in Paragraph 2.2.1

The identification of the reaction products is based on the measurement of three quantities: energy loss ( $\Delta E$ ), Total Kinetic Energy ( $TKE$ ) and time of flight ( $ToF$ ) on an event-by-event basis. The  $Z$  of a fragment is determined with the measurement of both  $\Delta E$  and  $TKE$  [5]. For a given  $Z$ , the different isotopes are identified combining the  $TKE$  measure with the velocity of the ion [5]. Paragraph 2.2.2 describes the  $\Delta E$  measurement with DSSSDs. The Cesium Iodide (CsI(Tl)) crystals described in Paragraph 2.2.3 provide the measurement of the ion remaining energy,  $E(CsI)$ . The total kinetic energy of the ion is computed by summing the energy loss  $\Delta E$  with the ion energy  $E(CsI)$ . The fragment velocity, which is needed for both ion identification and Doppler correction of the  $\gamma$ -ray emitted in-flight, is obtained with the Time-of-Flight ( $ToF$ ) measurement explained in Paragraph 2.2.4. In Paragraph 2.2.5 details on the target positions and on the reaction chamber are given.

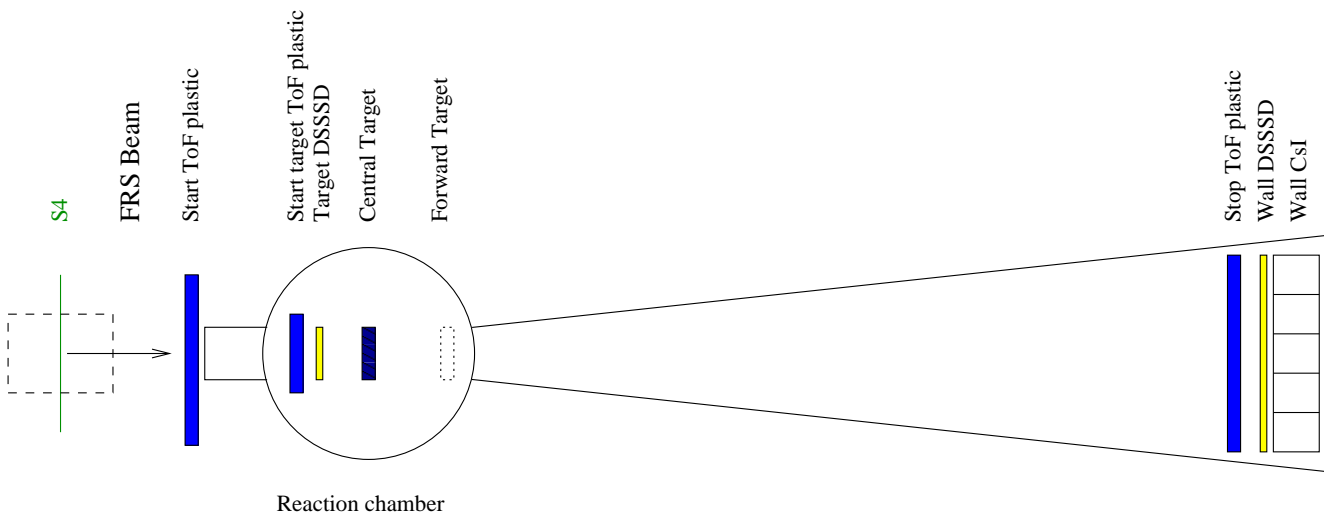


**Figure 2.5:** Schematic representation of the LYCCA calorimeter that provides identification and tracking of the reaction products after the secondary target. The distances between all the elements shown in the figure can be found in Annexe 7.1. The FRS final focal plane detectors are not represented here.

### 2.2.1 DSSSD tracking detectors

Each DSSSD detector module is a squared Silicon wafer with an active area of  $5.8 \times 5.8 \text{ cm}^2$ . The thickness is  $\sim 300 \mu\text{m}$ . Both N and P side of the semiconductor are subdivided in 32 strips ( $\sim 1.83 \text{ mm}$  width each) read out individually for the *DSSSD* and two by two for the *wall DSSSD*. The position of the ion provided by the device is extracted considering the strip with the maximum deposited energy. The DSSSD detector called *DSSSD target* provides the position at the secondary target (see LYCCA schematic view in Fig. 2.5). A picture of the *DSSSD target* mounted on its Printed Circuit Board (PCB) is shown in Fig. 2.6. The *wall DSSSD* detector is made of 16 DSSSD modules. It is used to extract the positions of the ions  $\sim 3 \text{ m}$  behind the target. Positions measured by the *DSSSD target* and the *wall DSSSD* provide the outgoing angle after reaction in the target and therefore, in combination with the angle measured by the TPC detectors it provides a measurement of the scattering angle of the ions. The positions covered by the 16 DSSSD detectors is shown in Fig. 2.7.

### 2.2.2 Energy loss measurement

The energy loss is obtained from the *Wall DSSSD* detector positioned after the *Stop plastic* (see Fig. 2.5). This detector has the same characteristics as the *target DSSSD*, but, in order to reduce the large number of channels present



**Figure 2.6:** Photograph of the *DSSSD target* detector mounted on its PCB frame [5].

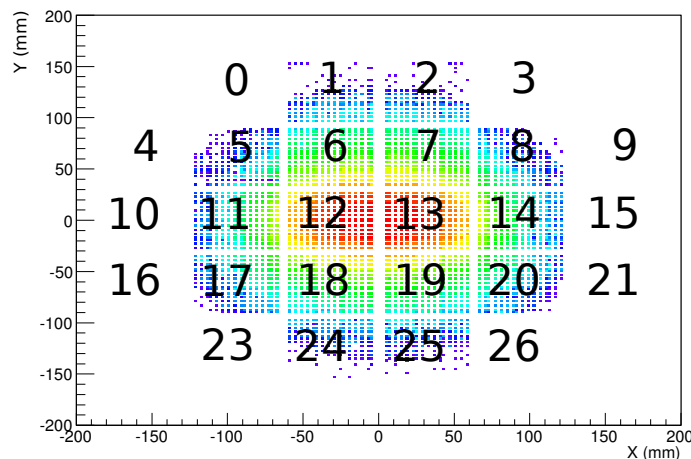


**Figure 2.7:** Position of the sixteen LYCCA modules as used in the 2012 experimental campaign. The labelling is given in the optic of twenty-six modules needed for the full construction of the *LYCCA wall*.

in the *LYCCA Wall*, the DSSSD strips on both N and P side are connected to the preamplifier (and shaper) two by two. Therefore only  $2 \times 16$  strips per DSSSD detectors are read out, providing a strip width of  $\sim 4$  mm [5].

---

### 2.2.3 Total kinetic energy measurement

---

The remaining energy of the ions is measured with Cesium Iodide (CsI(Tl)) crystal scintillators. The light of each scintillator element is collected by a photodiode which is connected to an amplifier followed by a shaper read out by an Amplitude to Digital Converter (ADC) [5]. One CsI(Tl) crystal has a dimension of  $19.4 \times 19.4$  mm<sup>2</sup> with a length of 33 mm. They are mounted on a 7.0 mm pyramidal light guide matching the  $10.4 \times 10.4$  mm<sup>2</sup> dimension of the photodiodes [5]. In order to ease the mounting of the LYCCA chamber, nine CsI(Tl) crystal and one DSSSD detector are combined together in a module sketched in Fig. 2.8. In total, sixteen modules of CsI(Tl)-DSSSD compose the *LYCCA Wall* and their labels are shown in Fig. 2.7. In the experiment of the present work, the modules in position 1, 2, 24, and 25 were equipped with CsI(Tl) crystals with a length of 10 mm with a pyramidal light guide of 5 mm, thus the crystal had a different length than the other one.

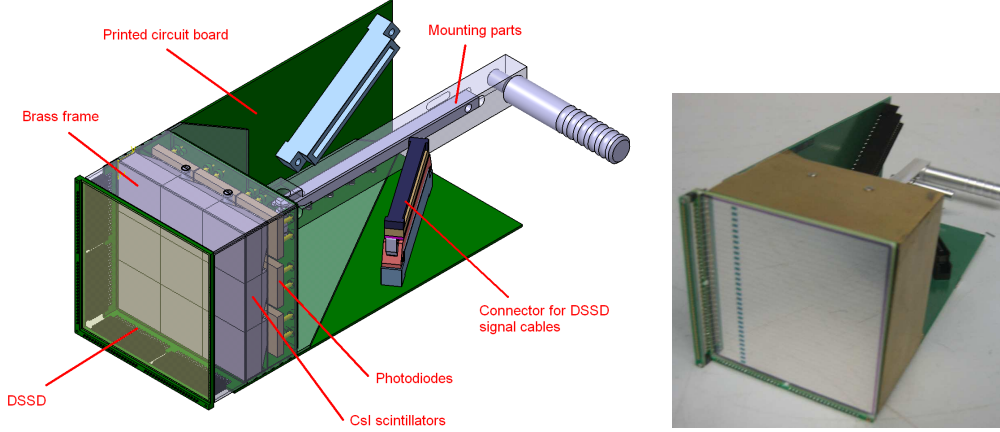


**Figure 2.8:** Representation of one LYCCA wall module. A picture of the DSSSD detector is shown on the right. The left drawing shows the assembly of both DSSSD and CsI(Ti) in one module unit. Figures are taken from [54].

---

## 2.2.4 Time of flight determination

---

The time difference between the two circular plastic scintillator membranes the *Start ToF plastic* and the *Stop ToF plastic* (drawn in the scheme in Fig. 2.5), provides the  $ToF$  of the ions. In order to reduce statistical uncertainties and to improve the  $ToF$  resolution [55], the 27 cm diameter *Start plastic* and *Stop plastic* membranes are surrounded by 32 PMTs. The average time over the multiple time readout allows an improvement of the intrinsic time resolution of the membrane by a factor of  $\frac{1}{\sqrt{32}}$  [55]. A smaller version of the *Start ToF plastic* (called *Start target ToF plastic*) is present in the setup. It has 12 PMTs and a diameter of 7.3 cm. Its smaller diameter make it possible to put it inside the reaction chamber of the PreSPEC-AGATA setup and therefore, it is closer to the target. The *Start target ToF plastic* is assumed to have a similar time resolution [5] and should give a more precise velocity since it provides the  $ToF$  of the fragment from the target position to the LYCCA wall. For the present work, the *Start ToF plastic* was kept inside the setup to test the performance of both start detectors. A picture of the membranes and their dimension is shown in Fig. 2.9. Each membrane offers the possibility to determine the position of the incident particle via the time difference of the light collection between one PMT and the average time [56].

---

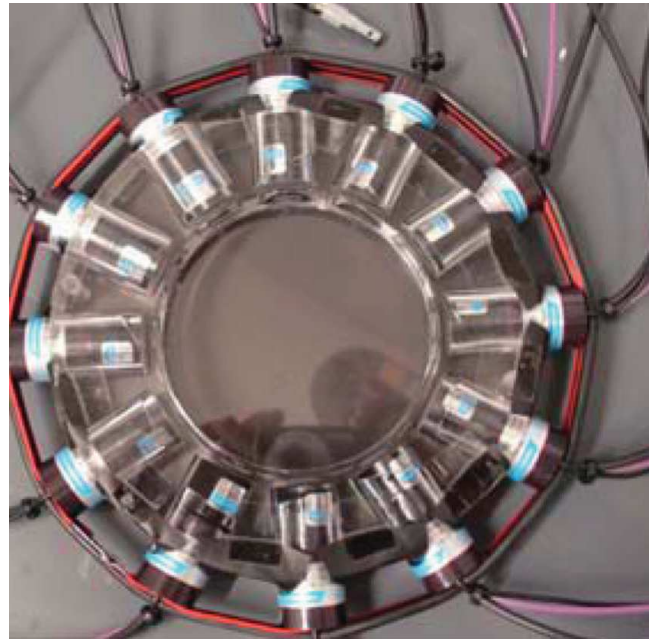
## 2.2.5 Reaction chamber

---

The aluminium reaction chamber has a diameter of  $\sim 33$  cm and it is put in vacuum at  $10^{-6}$  mbar. Inside the reaction chamber, shown in Fig. 2.10, two target positions are available: a central and a forward one. The central target position is at a nominal distance of 23.5 cm from the AGATA- $\gamma$ -ray detectors. The forward position is 15 cm downstream closer to the AGATA- $\gamma$ -ray detectors. The forward position provides a higher efficiency at rest [43]. Nevertheless, for in-flight emitted  $\gamma$ -ray at a velocity  $\beta \simeq 0.5$ , the decay of a nanosecond excited state might occur several centimeters after the target, worsening the efficiency. Therefore, the experiment described here was performed with the target at the central position. The forward position was used only during the preparation of the FRS. In this case, a plastic plate is placed in this position in order to stop the beam and observe the decay of isomeric states, as explained in Section 4.1. Otherwise, for the rest of the time, the forward target position was left empty.



(a) Picture of the *Stop ToF plastic* taken from [55].



(b) Picture of the *Start target ToF plastic* taken from [5].

**Figure 2.9:** Picture of the *ToF* membrane of the LYCCA calorimeter. On the left hand side, the picture of the 32 PMTs, 27 cm diameter membrane is shown. Similar membranes are used for both the *Start* and *Stop plastic*. On the right, a smaller version with 12 PMTs and 7.7 cm diameter placed inside the target chamber is shown.

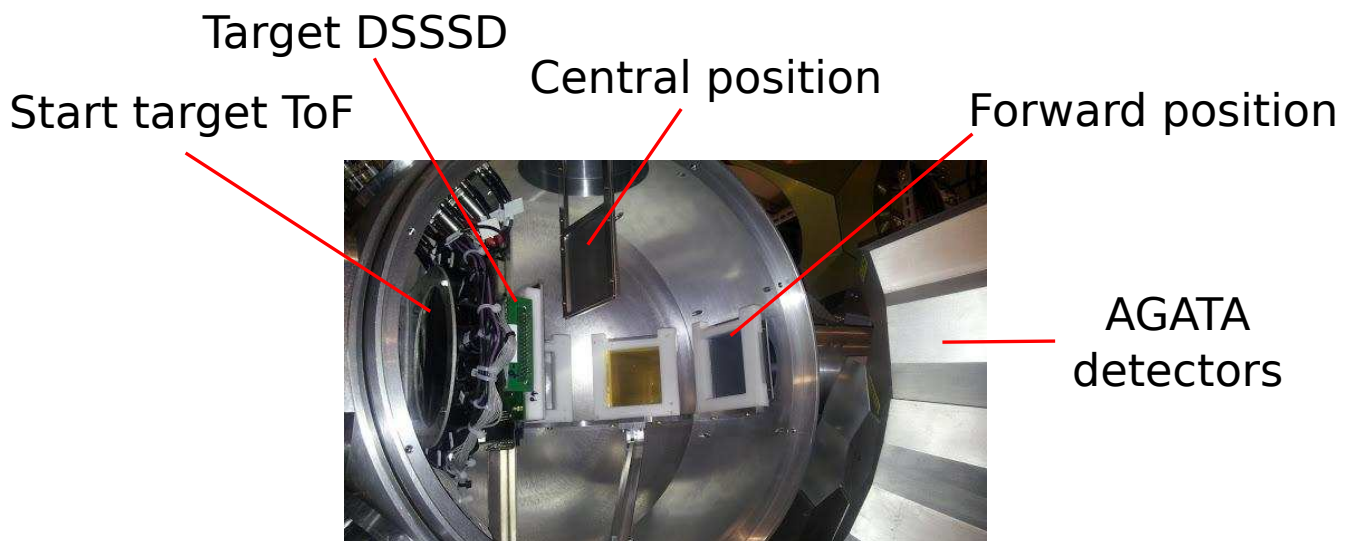


**Figure 2.10:** Photograph of the reaction chamber. The labels central and forward position indicate the two possible target positions.

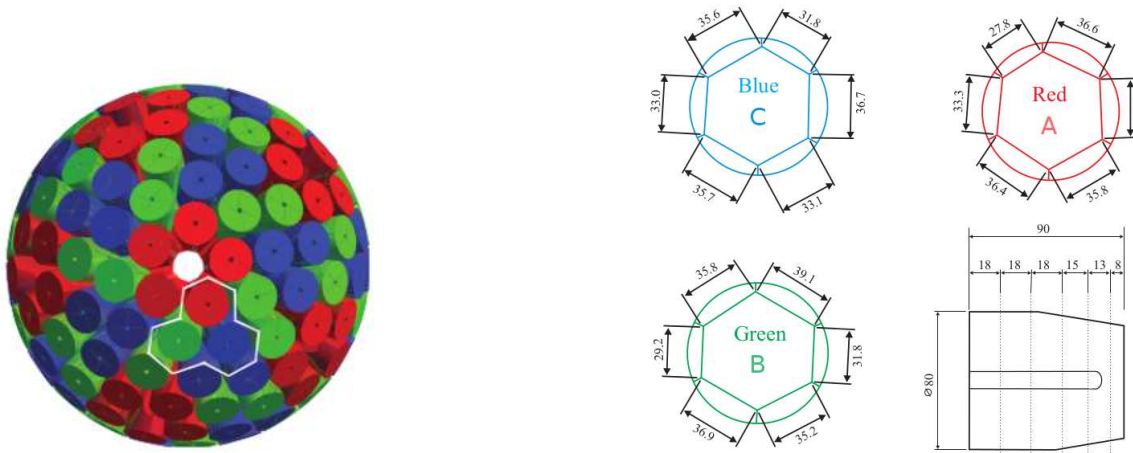
## 2.3 AGATA

The Advanced GAMMA Tracking Array (AGATA) is a project supported mainly by founding agencies of several European countries. The main line of the project is to build an array composed of  $\gamma$ -ray detectors made of high-purity segmented germanium semiconductor [4]. The strength of the project is the segmentation of each detector, which allows first to determine the interaction position of the  $\gamma$ -ray with the measured signal shapes and then to reconstruct the path of a Compton scattered  $\gamma$ -ray inside the array. Employing Pulse Shape Analysis (PSA) [57] algorithm, a 5 mm position resolution of the  $\gamma$ -ray interaction is achieved [58]. This resolution allows to determine precisely the angle of emission of the  $\gamma$  ray. Therefore, the AGATA project provides an efficient array for the Doppler correction of  $\gamma$ -rays emitted in flight.

Paragraph 2.3.1 describes the detector configuration together with the detector shape. Paragraph 2.3.2 explains how the interaction positions of the  $\gamma$ -rays are determined with the PSA algorithm. The underlying idea of the tracking algorithm is reported in Paragraph 2.3.3. At last, Paragraph 2.3.4 compares the gain provided by the AGATA array with respect to conventional, *i.e.*, not segmented, high purity germanium detectors.

### 2.3.1 The AGATA array

The AGATA project aims at reaching a  $4\pi$  solid angle coverage in order to assure a high  $\gamma$ -ray detection efficiency and full tracking of Compton scattered  $\gamma$ -rays. A geodesic geometry shown in Fig. 2.11a with 180 detectors has been chosen to minimise dead material [4]. The array is built from units of three germanium crystal with different hexagonal shapes. The dimensions of the three types labelled A,B,C are given in Fig. 2.11b. One of each detector type is mounted inside a triple-cryostat.



(a) Geodesic geometry for the  $4\pi$  solid angle coverage.

(b) Dimensions of the three types (A,B,C) of the AGATA asymmetric detectors.

**Figure 2.11:** AGATA technical drawings. The figures are adapted from [4].

An AGATA crystal is made of n-type closed coaxial high purity electrically segmented germanium material. By segmentation of the outer contact, each detector is divided in 36 areas identified by a letter (from A to F) and a number (from 1 to 6). A view of the AGATA detector labelling is shown in Fig. 2.12.

Since the GSI beam spot is typically 6 cm wide (FHMW), the standard arrangement of AGATA with a small pentagonal hole for the beam is not suitable. For this reason, the triple cryostat of the detectors close to the beam line was modified to a double cryostat structure. Since the detectors close to the beam line are type A detectors (drawn in red in Fig. 2.11a) the double cryostats are made of crystal types B and C.

During the 2012 AGATA campaign at GSI, nineteen AGATA crystals<sup>4</sup> were arranged in three double cryostats and five triple cryostats<sup>5</sup>. A Computer Aided Design (CAD) of the AGATA detector positions is shown in Fig. 2.13. Each crystal is labelled according to the cryostat position inside the array shown in Fig. 2.13 and its crystal type. For example, detector 12A corresponds to a crystal type A in the cryostat in position 12.

<sup>4</sup> The detector in 07A although present inside the triple cryostat during the 2012 campaign was not operational and it is not counted here.

<sup>5</sup> In order to increase the total number of crystals, one of the triple cryostats was filled with only two crystals. The type A detector was missing.



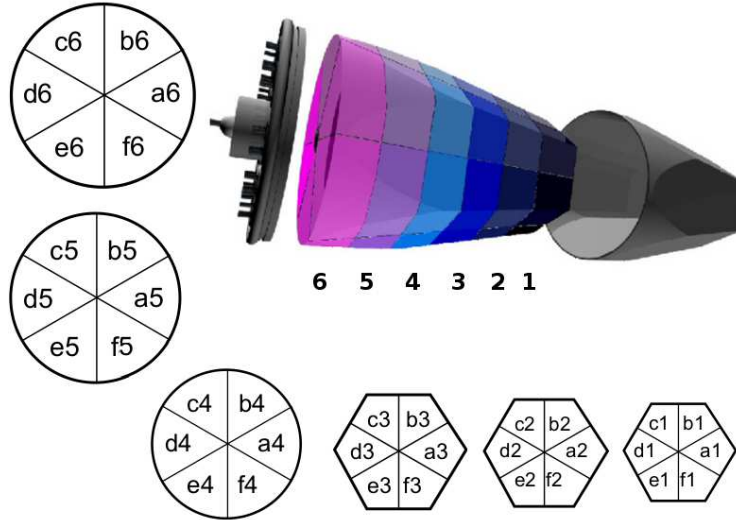


**Figure 2.12:** Schematic view of a segmented AGATA crystal. The 36 segments are identified with a number for each layer along the depth axis and a letter for the sectors in the perpendicular plane. The figure is adapted from [4].

The target used in this experiment was positioned in the center of the array at the nominal distance of 23.5 cm. A picture of the detector positioned around the reaction chamber is shown in Fig. 2.10.

---

### 2.3.2 Interaction position determination of $\gamma$ rays using segmented germanium detectors

---

In a coaxial germanium detector, the shape of the charge collection signal as a function of the time depends on the distance between the position of  $\gamma$ -ray interaction and the electrode which collects the charges. A schematic representation of the time-dependant charge collection for different distances is shown in Fig. 2.14. Indeed, the charge induced on the electrode by moving charge carriers (electrons and holes) in a coaxial germanium detector depends on the interaction position [60]. Consequently, the pulse shape analysis allows a radial determination of the position of the  $\gamma$  ray.

In the case of an electrically segmented detector, charges are induced on the neighbouring electrodes, called mirror charges, as shown in Fig. 2.15. In this example, the segment B4 where the charge is positive and presents a plateau corresponds to the segment where the  $\gamma$ -ray interacted and created electron-hole pairs. This is called the segment with a *net charge*. The segment pulse shape recall the one of a coaxial detector in Fig. 2.14. Moreover, the moving charges induce signals in the neighbouring electrodes. An induced signal is called a *transient charge*. As illustrated in Fig. 2.15, the shape of net and transient charges depends on the interaction position of the  $\gamma$ -ray. The center of the segment with the net charge gives an idea of the interaction position, but using the transient charge information a better position resolution can be achieved.

The Pulse Shape Analysis [57] (PSA) algorithm compares a database of signal shape (each of the AGATA crystals has its own database) with the net and transient charge signal of a  $\gamma$ -ray interaction to deduce the interaction position. The PSA provides a position resolution of about 5 mm (FWHM) for the first interaction hit of 1 MeV  $\gamma$  rays [58, 62].

The net and transient charge signals for each position can be measured with the use of a scanning table [63–65] in order to build a database where known positions are associated with the pulse shapes. In practice, this process needs a three dimensional grid of 1 mm side, which with the Liverpool scanning table [63], takes two or three months of data taking per detector [4]. Therefore, only a few key positions are scanned per detector and the AGATA basis is built relying on AGATA Data Library (ADL) electric-field simulations [4, 66].

---

### 2.3.3 Forward tracking of Compton scattered $\gamma$ ray

---

A  $\gamma$ -ray can interact with matter via four different processes:

- Photoelectric: the incoming  $\gamma$  ray is absorbed by the atom and its energy is transmitted to an electron that is then ejected.

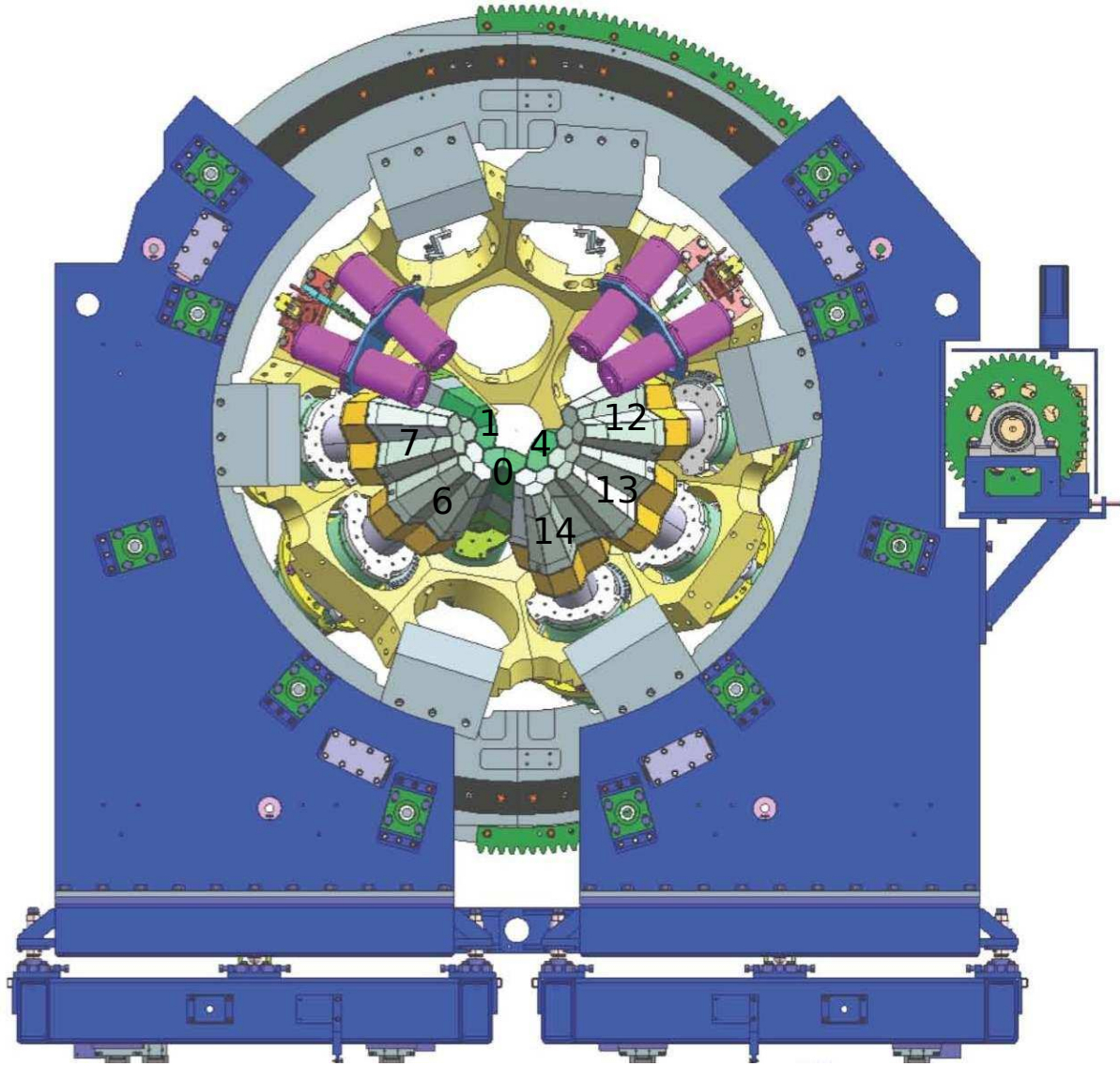


**Figure 2.13:** CAD of the AGATA detectors inside the holding structure. The green detectors are detectors mounted in double cryostat and the grey ones are mounted in a triple cryostat. The labels are used to refer the position inside the AGATA holding structure, shown in light yellow. The purple detectors are  $LaBr_3$  from the HECTOR+ array. Courtesy: Milano group [59].

- Rayleigh scattering: the incoming  $\gamma$  ray scatters on a bound electron of the atom. No energy is transferred to the electron.
- Compton scattering: the incoming  $\gamma$  ray scatters on a free (or quasi free) electron. The photon is deflected by an angle  $\theta$  and transfers a part of its energy to the electron.
- Pair production: if the energy of the incoming  $\gamma$  ray is larger than 1.022 MeV, it is energetically possible to produce a electron-positron pair. The photon is annihilated and its energy excess is transferred to the electron-positron pair as kinetic energy.

The cross section for these processes in the germanium as a function of the  $\gamma$ -ray energy is shown in Fig. 2.16.

In nuclear structure experiments, the detected  $\gamma$ -ray energies are typically in a range from tenth of keV to few MeV, which implies that the interaction of the photon in the germanium is dominated by Compton scattering. As previously mentioned, the Compton scattered photon with an energy  $E_0 = h\nu$  transfers part of its energy to the recoil electron. The resulting energy  $E'_0 = h\nu'$  of the gamma is [60]:

$$h\nu' = \frac{h\nu}{1 + \frac{h\nu}{m_0c^2}(1 - \cos(\theta))}, \quad (2.11)$$



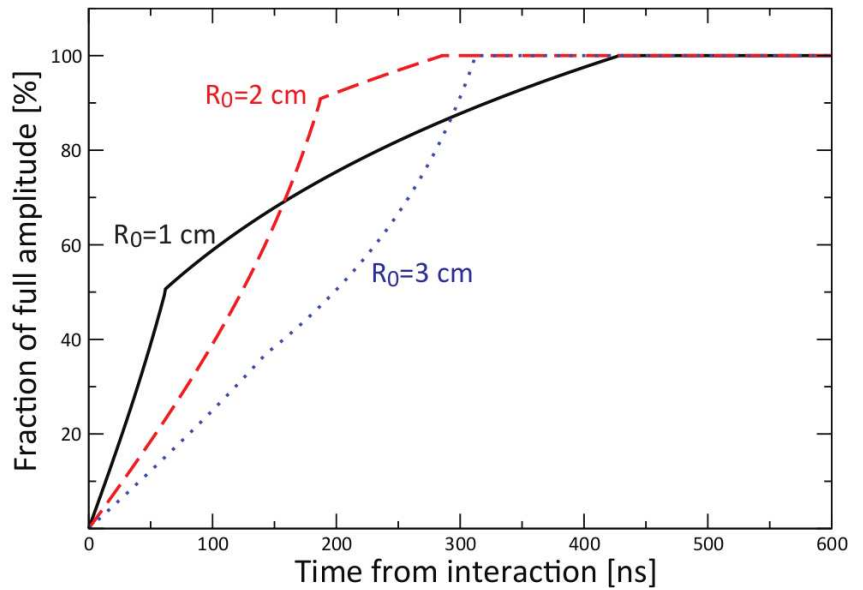
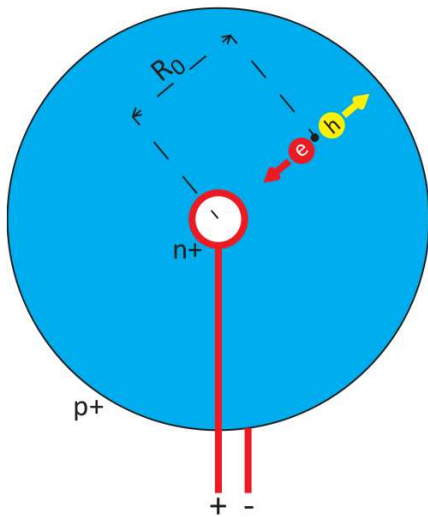


**Figure 2.14:** On the left is shown a schematic view of the moving electron-hole pairs inside a coaxial detector. On the right, the amplitude of the induced charge is drawn as a function of the radial distance. The model used here is described in Chapter 12 of Reference [60]. The figure is taken from [61].

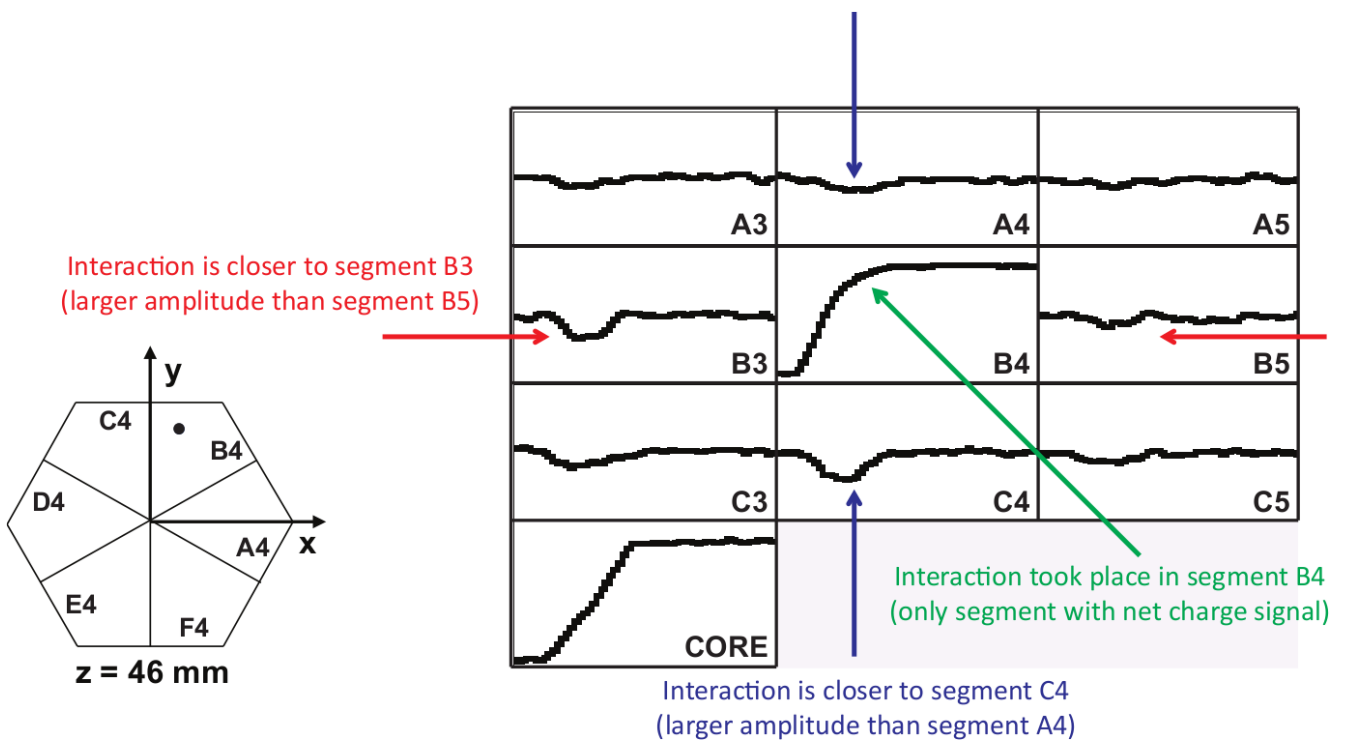


**Figure 2.15:** Induced charges in an electrically segmented HPGe detector. In this example, the net charge is observed in segment B4. Transient charges are observed in the neighbouring segments and their relative amplitudes indicate the azimuthal position. The figure is taken from [61].

with the mass of the electron at rest  $m_0c^2 = 0.511$  MeV and  $\theta$  the angle between the incoming and the scattered  $\gamma$  ray.

The energy deposited by the photon inside the finite volume of the detector can be different from the incoming photon energy. Moreover, a  $\gamma$  ray of 1 MeV can do multiple Compton scattering before it deposits all its energy. Thus, a Compton-scattered  $\gamma$  ray can escape the detector volume. Some germanium arrays are using Compton shields to reject events with a Compton-scattered  $\gamma$  ray escaping from the germanium volume, but this solution affects the  $\gamma$ -ray detection

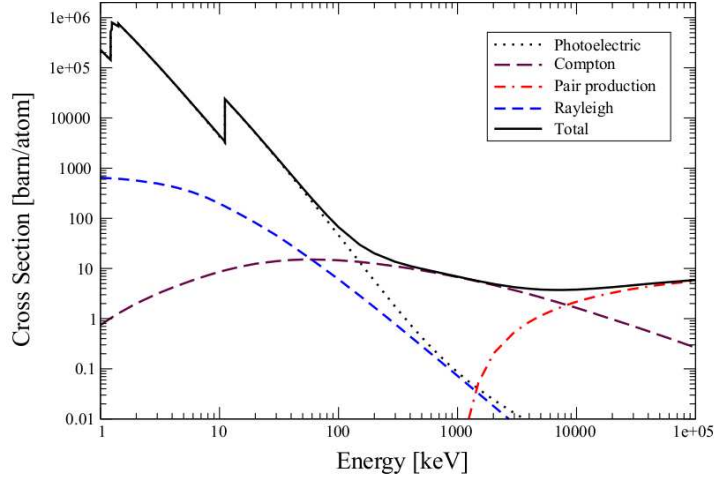


**Figure 2.16:** Cross section of the  $\gamma$ -ray interaction in germanium as a function of its energy for the main interaction processes.

efficiency. Therefore, another solution is to bring each germanium detector close to each other and to add the energy deposit in neighbouring crystals with an add-back procedure. The solution developed by the AGATA project has in addition segmented detectors that allow to reconstruct the full energy of a Compton-scattered  $\gamma$  ray.

To give a simplified representation, the following explanations are limited to the case of the forward tracking in a  $4\pi$  germanium shell without dead-material. For one event, each hit that occurred in the germanium shell is considered. With a hit  $i$  is associated an energy  $E_{\gamma_i}$  and position  $(x_i, y_i, z_i)$ . The source (or vertex) position is also known in order to calculate the Compton scattering angles between incoming and scattered  $\gamma$  ray. Equation 2.11 is then expressed as a relation between the incident  $\gamma$ -ray energy  $E_{\gamma_{i-1}}$  and the Compton scattered  $\gamma$ -ray energy  $E_{\gamma_i}$ :

$$E_{\gamma_i} = \frac{E_{\gamma_{i-1}}}{1 + \frac{E_{\gamma_{i-1}}}{m_0 c^2} (1 - \cos(\theta_i))} \quad (2.12)$$

with notations given in Fig. 2.17 for  $i = 1, 2$ . The energy  $e_i$  transferred to the electron during the Compton-scattering process is given by:

$$e_i = E_{\gamma_{i-1}} - E_{\gamma_i} \quad (2.13)$$

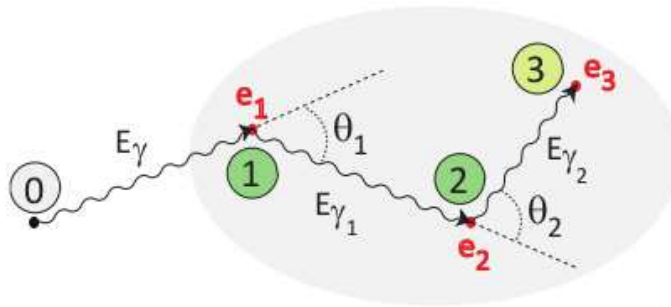


**Figure 2.17:** Multiple Compton scattering of a  $\gamma$  ray with an energy  $E_{\gamma}$  coming from position zero (the target) and that Compton scattered twice before full absorption of its energy in position three. The figure is taken from [67].

Assuming that the total energy of the incoming  $\gamma$  ray is known, we can calculate the probability to have a given Compton scattering sequence. The  $\gamma$  ray has no mass, it travels in the germanium at the speed of light, therefore the

time between two Compton-scattered  $\gamma$ -ray hits cannot be measured<sup>6</sup>. As a consequence, hits are not time ordered and a probability has to be assigned for all permutations of hit sequences. The procedure to fix the initial assumption, *i.e.*, that we know the total energy of the  $\gamma$  ray, is to consider all possible cluster ( $\gamma$ -ray interaction hits are grouped together if they are close to each other, shown in Fig. 2.18) in the germanium shell and to assign to each cluster a probability based on Equation 2.12. Once all possible clusters are taken into account, a probability for all the permutations for every cluster is calculated. The clusters with a probability higher than a given value (parameter of the tracking algorithm) are

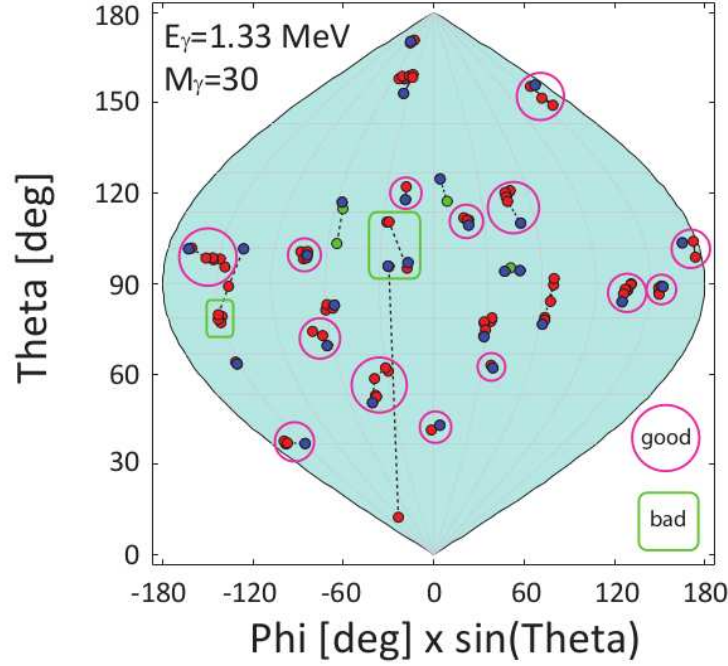


**Figure 2.18:** Interaction positions and cluster identification in a  $4\pi$  germanium shell as considered by the tracking algorithm. Figure taken from [68].

accepted. Other clusters are rejected and this provides to the AGATA tracking array the possibility to discard  $\gamma$ -ray with a Compton-scattered  $\gamma$ -ray escaping the germanium volume and therefore provides an equivalent to a Compton-shield.

There are some issues inherent to this method. The PSA is assuming one hit per segments, which in case of two hits would have an impact on the angle calculation. Second, the tracking algorithm does not take into account the fact that the interaction position differs from the assigned position (scattered electron). At last, the tracking principle is based on the Compton scattering equation and cannot take into account a modification of the  $\gamma$ -ray angle without any energy deposit, *i.e.*, a Rayleigh scattered  $\gamma$  ray.

### 2.3.4 AGATA at GSI

The velocity of the ions reaching the secondary target is typically in the order of  $\beta \sim 0.5$ . At such velocities, the energy shift due to the Doppler effect must be taken into account. In the nucleus frame, moving at a velocity  $\beta$ , the emitted  $\gamma$  ray energy is noted  $E_0$ . A detector positioned at an angle  $\theta$  measures the Doppler shifted energy noted  $E_{Lab}$  given by the equation:

$$E_{Lab} = E_0 \frac{\sqrt{1 - \beta^2}}{1 - \beta \cos(\theta)}, \quad (2.14)$$

which can also be written as:

$$E_0 = E_{Lab} \frac{1 - \beta \cos(\theta)}{\sqrt{1 - \beta^2}}. \quad (2.15)$$

<sup>6</sup> The time resolution of a germanium detector is  $\sim 20$ ns. In order to distinguish two Compton scattered  $\gamma$ -rays separated by  $\sim 5$  cm (mean free path of a 1 MeV  $\gamma$  ray) a time resolution of at most 160 ps would be needed.

We note  $\Delta E_0$  the uncertainty of the energy  $E_0$  after Doppler correction. It depends on the measurement accuracy of the three variables present in Equation 2.15:  $E_{Lab}$ ,  $\theta$  and  $\beta$ . We can express the uncertainty  $\Delta E_0$  by:

$$\Delta E_0 = \sqrt{\Delta E_{lab} \frac{\partial E_0}{\partial E_{lab}} + \Delta \theta \frac{\partial E_0}{\partial \theta} + \Delta \beta \frac{\partial E_0}{\partial \beta}}, \quad (2.16)$$

with an obvious notation for the measurement accuracy  $\Delta E_{Lab}$ ,  $\Delta \theta$  and  $\Delta \beta$ . The principal origin of the measurement accuracies are:

- $\Delta E_{lab}$ : the energy resolution of the  $\gamma$ -ray detector
- $\Delta \theta$ : the resolution, or opening angle of the  $\gamma$ -ray detector
- $\Delta \beta$ : the resolution achieved by the LYCCA *ToF* system

The partial derivative of Equation 2.15 as a function of the angle  $\theta$  provides the Doppler broadening due to the opening angle of the detector:

$$\frac{\Delta E_\theta}{E_0} \stackrel{\text{def}}{=} \frac{1}{E_0} \frac{\partial E_0}{\partial \theta} \Delta \theta = \frac{\sin(\theta)}{1 - \beta \cos(\theta)} \Delta \theta. \quad (2.17)$$

The Doppler broadening effect due to an uncertainty on the velocity measurement – drawn in red in Fig. 2.19 – is given in the following equation:

$$\frac{\Delta E_\beta}{E_0} \stackrel{\text{def}}{=} \frac{1}{E_0} \frac{\partial E_0}{\partial \beta} \Delta \beta = \frac{\beta - \cos(\theta)}{(1 - \beta^2)(1 - \beta \cos(\theta))} \Delta \beta. \quad (2.18)$$

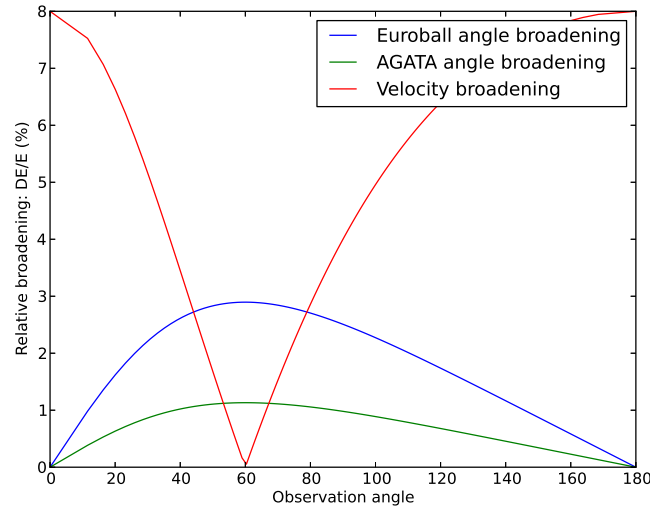


**Figure 2.19:** The Doppler broadening of a segmented detector with a 5 mm position resolution considering  $\beta = 0.5$  and a distance detector-source of 23,5 cm is shown in green. The blue line highlights the Doppler broadening effect for a Euroball cluster germanium detector positioned at 70 cm from the source. The red curve shows the energy broadening due to an uncertainty on the velocity of the ion of  $\Delta \beta = 6\%$ .

The previous  $\gamma$ -ray detector array used for the PreSPEC-RISING fast beam campaign [69] has a larger opening angle, that broadened the  $\gamma$ -ray resolution after Doppler correction. To compensate this effect, the germanium crystals were installed relatively far from the target (70 cm), reducing the  $\gamma$ -ray detection efficiency [69]. The segmentation of an AGATA crystal provides the interaction position for the first interaction point of a 1 MeV  $\gamma$  ray with a resolution in the order of 5 mm (FWHM). The Doppler broadening impact due to the uncertainty on the velocity measurement as a function of the observation angle is drawn with a red line in the graph in Fig. 2.19. The blue and green curves in the figure, represent the Doppler broadening due to the opening angle of the detector as a function of the angle of observation. The green curves drawn in the figure assumes an AGATA segmented detector having a 5 mm position resolution. The blue curve is plotted for a Euroball cluster assuming the condition of Reference [69]. From the plot in the figure, a clear gain in resolution is obtained using segmented germanium detectors.

---

The reduction of the Doppler broadening allows a distance target-detector of 23,5 cm and therefore a good  $\gamma$ -ray detection efficiency of 3.3% calculated in the calorimetric<sup>7</sup> mode [70]. Furthermore, the AGATA detectors are positioned at forward angle which is favorable for an increase of efficiency due to the Lorentz boost. For the discussed experiment, a factor two increase of efficiency is expected [43]. Those improvements make the AGATA array a state-of-the-art detector for  $\gamma$ -ray spectroscopy with relativistic ion beams.

---

<sup>7</sup> The calorimetric mode is not taking the tracking algorithm into account and is simply summing the central contact energy together for every event. The first interaction hit is chosen as the hit with the highest energy.

## 2.4 HECTOR+

In addition to the germanium detectors, scintillator detectors of the High Energy DeteCTOR (HECTOR+) array [6] are positioned around the secondary target. Two different scintillator types are used:

- $BaF_2$  crystals with an excellent timing response (slightly better than 1 ns) and an energy resolution of 10% at 1.3 MeV [69].
- $LaBr_3:Ce$  3.5"x8" crystals, which achieve an energy resolution of  $\sim 2.4\%$  at 1.3 MeV and  $\sim 1\%$  at 10 MeV at FWHM. The intrinsic time resolution is measured at 880 ps as FWHM [6].

Four  $LaBr_3 : Ce$  are positioned at forward angles inside the AGATA array, while the other 10  $LaBr_3$  and 8  $BaF_2$  are at  $90^\circ$  and at backward angles. A schematic drawing of the positions for both  $LaBr_3 : Ce$  and  $BaF_2$  in the experimental setup is shown in Fig. 2.20.

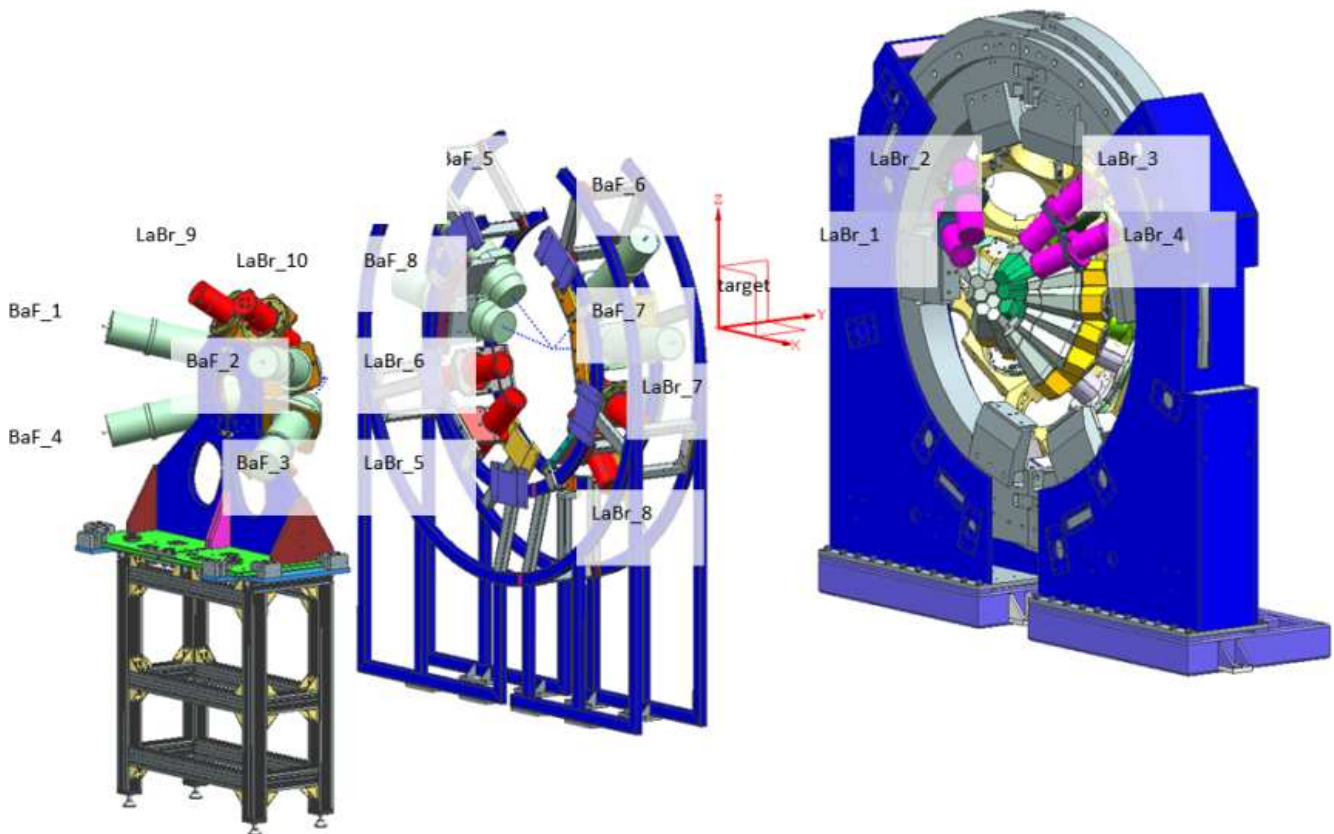


**Figure 2.20:** CAD drawing of the AGATA and HECTOR+ array. The detectors are held in three structures: AGATA structure for forward angle, the former Miniball structure for the  $90^\circ$  angle and a dedicated structure at backward angles. Courtesy: Milano group [59].

The HECTOR+ detector array is complementary to the AGATA array, increasing the solid-angle coverage for the  $\gamma$ -ray detection, allowing measurement of higher-energy  $\gamma$  ray and providing a possibility for neutron- $\gamma$  discrimination. In addition, detectors with an excellent timing resolution can be used for beam-induced background investigations.

---

## 2.5 Lifetime measurements at intermediate energies

---

In the work of this experiment, we are interested to measure the lifetime of the first excited  $4_1^+$  state of  $^{108}\text{Mo}$ . The physics discussion of the Chapter 1 provides an estimation of the expected lifetime of  $\tau = 25$  ps. In this section, I now focus the discussion on the experimental methods that can be used in order to measure a  $\sim 25$  ps lifetime.

In the first paragraph of this section, I discuss the “standard” method used in experimental nuclear structure to measure lifetimes of an excited level. In the following paragraph, I explain a newly developed lifetime method applicable for this experiment.

---

### 2.5.1 Lifetime measurement methods

---

The lifetime of an excited state can be measured with different methods according to the expected lifetime value.

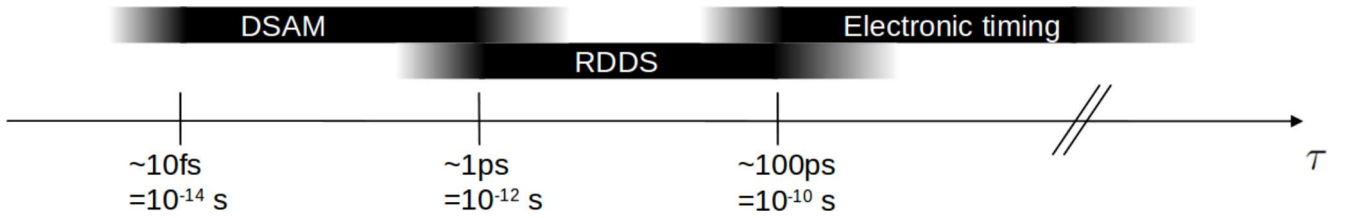


**Figure 2.21:** Lifetime ranges for which the three most common lifetime techniques can be used. The figure is taken from [71].

The three commonly used methods are summarized in the diagram shown in Fig. 2.21. Each of these methods are used to measure excited transitions in a given lifetime range and can be summarized as follows:

- A lifetime longer than  $\sim 100$  ps is measured via the electronic timing method. For a given transition energy the number of  $\gamma$  rays per unit of time is registered. The time unit is defined by the sensitivity of both the electronic and the detectors. Thus, this method allows a direct measurement of the excited level decay curve as a function of time. In this case, the  $\gamma$  rays need to be emitted at rest.
- For intermediate lifetimes, ( $\sim 1$  ps to 100 ps), the Recoil Distance Doppler Shift<sup>8</sup> (RDDS) method can be used. This method uses the velocity dependence of the Doppler shifted energy. For a nucleus at a velocity  $\beta = v/c$ , the energy of the detected  $\gamma$ -ray under an angle  $\theta$  is shifted according to the Doppler shift Equation 2.19. Inserting a velocity degrader at a distance  $d$  from the target, the excited level can decay before the degrader with a velocity  $\beta$  or after the degrader with a velocity  $\beta' < \beta$ . Therefore, the  $\gamma$  rays observed under an angle  $\theta$  can have two distinct energies. The ratio of the number of counts between these two energies provides an indirect measurement of the lifetime.
- The Doppler-Shift Attenuation Method (DSAM) allows to measure the lifetime of excited states ranging from  $\sim 10$  fs to  $\sim 1$  ps. As in the case of the RDDS method, the DSAM method use the velocity dependence of the Doppler shifted energy. In this case, the excited nuclei of the beam are slow down inside a degrader. The nuclei that decay before the stopper have a significant shift in energy. The nuclei that decay during the slow-down process have a Doppler shifted energy that depends on its velocity (related to the slow-down process) at their decay position, thus on the lifetime of the  $\gamma$  ray transition.

---

### 2.5.2 The geometrical-DSAM method

---

Before describing the method used for the experiment of this work, we first remind the Doppler shift equation:

$$E_{shift} = E_0 \frac{\sqrt{1 - \beta^2}}{1 - \beta \cos \theta} \quad (2.19)$$

where  $\beta = v/c$  is the beam velocity,  $\theta$  the emission angle and  $E_0$  the rest energy of the  $\gamma$  ray transition.

In the PreSPEC-AGATA campaign, the AGATA  $\gamma$ -ray detectors were covering angles from  $18^\circ$  to  $65^\circ$ . Thus, at the velocity  $\beta \sim 0.5$ , the Doppler shifted energy of a  $\gamma$  ray emitted at the rest energy of  $E_0 = 360$  keV has a range between 600 and 400 keV. The result of a simulation of the Doppler shift energy as a function of the emission angle can be found



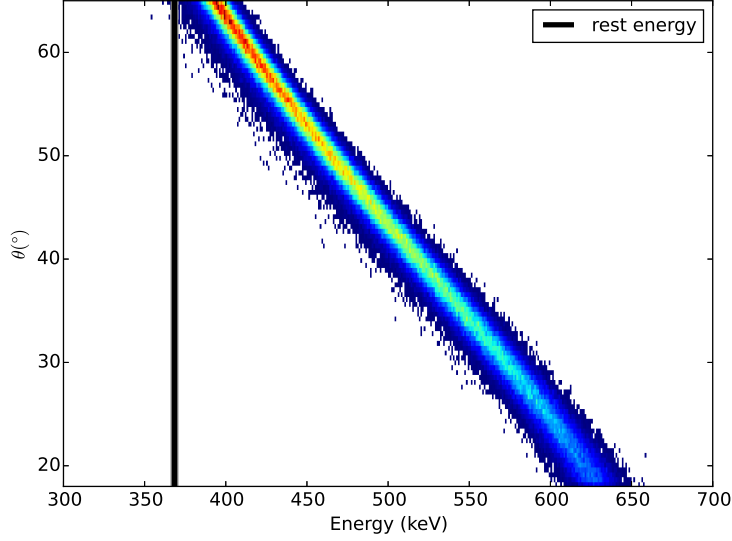


**Figure 2.22:** Simulated Doppler shifted  $\gamma$ -ray energy as a function of the observation angle  $\theta$ . The black straight line indicates the rest energy of the  $\gamma$  ray.

in Fig. 2.22. Over this large energy shift, a really high statistics is needed in order to see the transitions as a function of the angle. Therefore, it is common to Doppler correct the energy by the following equation:

$$E_0 = E_{shift} \frac{1 - \beta \cos \theta}{\sqrt{1 - \beta^2}} \quad (2.20)$$

where, this time,  $\beta$  and  $\theta$  are the measured velocity and the observation angle under which is measured the energy  $E_{shift}$ .

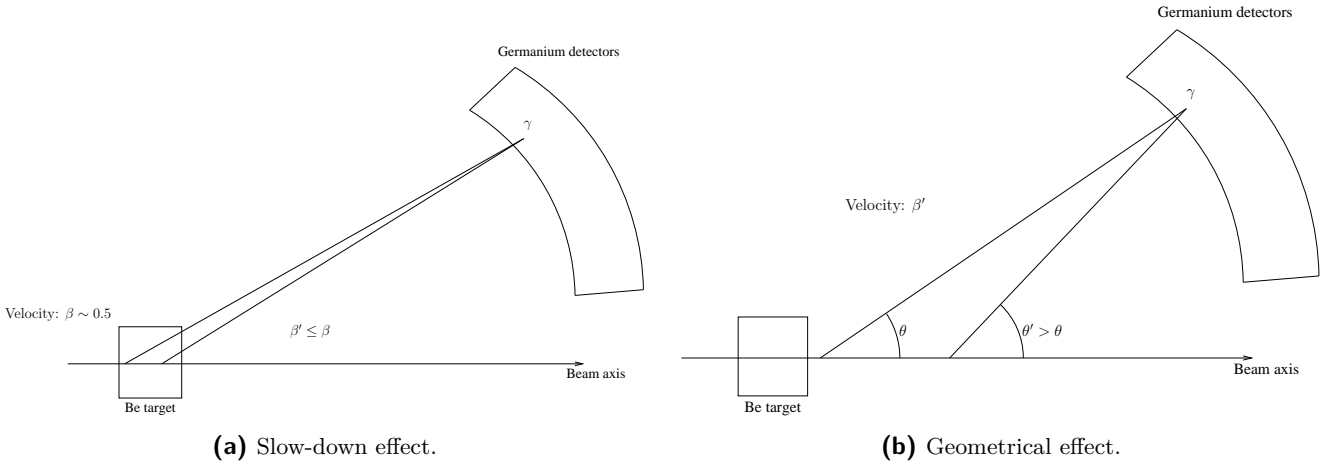


**Figure 2.23:** Schematic view of both slow-down and geometrical effect. These two effects can be observed if the beam is passing through the target with a high velocity, in our case  $\beta \sim 0.5$ .

In the experiment presented in this work, the beam velocity at the target level is  $\beta \sim 0.5$ , thus the flight time of the nuclei through the target is  $\sim 25$  ps. As this time is very short and many nuclei can decay behind the target, we can separate two Doppler shift effects according to their decay position:

- for the nuclei that decay inside the target we have the “slow-down effect”,
- for the nuclei that decay behind the target, we have a “geometrical effect” .

<sup>8</sup> Also known as plunger measurement.



The “slow-down effect” is the one exploited in DSAM techniques. A schematic representation of the “slow-down effect” is drawn in Fig. 2.23a. Since only the average velocity  $\beta$  can be accessed experimentally, we cannot access the exact velocity of the beam at the de-excitation moment. Therefore, the energy of the transitions after the Doppler correction (given by Equation 2.20) is wrongly corrected for the events in which the  $\gamma$  ray is emitted at a different velocity than the measured one. These wrongly Doppler corrected  $\gamma$  rays affect the shape of the observed  $\gamma$  ray transition. For instance, if we correct the Doppler shifted energy with the velocity after the target we would observe a tail at higher energies. The simulation of this effect is shown in Fig. 2.24a. The tail, thus the shape of the Doppler corrected transition, is related to the beam velocity at the moment of emission and therefore to the lifetime of the transition.

The “geometrical effect” is predominant on the slow-down process when the half-life of the transition is  $\sim 40$  ps as we shall see in Chapter 5. When a nucleus decays at a distance  $d'$  after the target, the emission angle  $\theta'$  of the  $\gamma$  ray is larger<sup>9</sup> than the emission angle for a decay at a distance  $d < d'$ . A schematic view of the difference between the decay angle is drawn in Fig. 2.23b. Once more, we cannot access experimentally the decay position of the emitted  $\gamma$  ray, thus we need to assume that its decay occurs at the target position. Therefore, when we perform the Doppler correction, we have an error on the angle, which shifts the energy of the centroid of the transition as shown, for a simulated case in Fig. 2.24b. The shift with respect to the rest energy is directly related to the error we make on the angle of emission thus to the lifetime.

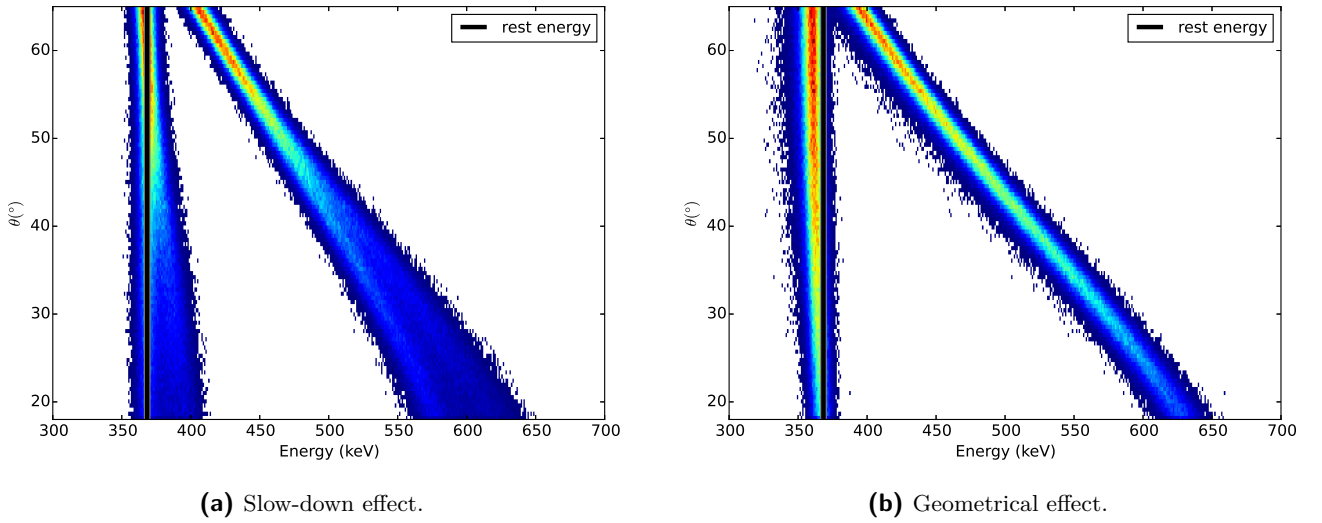


**Figure 2.24:** Simulation of both the slow-down and the geometrical effect. In order to distinguish the two effects, we simulate here separately the two effect, thus the  $y$  axis in the left picture is the emission angle while it is the observation angle in the picture on the left. The beam velocity that we used to correct for the Doppler shift is the beam velocity after the target. The tilted line is the Doppler shifted energy, while the straight one is the Doppler corrected energy. The black line represents the rest energy of the  $\gamma$  ray.

In reality, both effects are present at the same time, thus the line-shape depends on both slow-down and geometrical effect.

To conclude, in the case of a beam at half speed of light, with a target of finite thickness, the lifetime of an excited state can be extracted only after the proper characterisation of the tail of the transition and of the energy of its centroid. Moreover, compared to a previous lifetime measurement performed with the Euroball cluster [72], the position resolution of the AGATA detectors provides a higher sensitivity to the lifetime effect on the line-shape observed after Doppler correction.

<sup>9</sup> This is valid only with this experimental setup where the  $\gamma$ -ray detectors are positioned at forward angles.



---

## Chapter 3: The Data Acquisition system for PreSPEC-AGATA

In this chapter, I provide a detailed description of the PreSPEC-AGATA data acquisition system. This chapter was submitted and accepted in the journal “Nuclear Instruments and Methods in Physics Research Section A: Accelerators, Spectrometers, Detectors and Associated Equipment” [73].

The following paragraph is the abstract of the article.

The PreSPEC setup for high-resolution  $\gamma$ -ray spectroscopy using radioactive ion beams was employed for experimental campaigns in 2012 and 2014. The setup consisted of the state of the art Advanced GAMMA Tracking Array (AGATA) and the High Energy  $\gamma$  deteCTOR (HECTOR+) positioned around a secondary target at the final focal plane of the GSI FRagment Separator (FRS) to perform in-beam  $\gamma$ -ray spectroscopy of exotic nuclei. The Lund York Cologne CALorimeter (LYCCA) was used to identify the reaction products. In this paper we report on the trigger scheme used during the campaigns. The data-flow coupling between the Multi-Branch System (MBS) based Data AcQuisition (DAQ) used for FRS-LYCCA and the “Nouvelle Acquisition temps Réel Version 1.2 Avec Linux” (NARVAL) based acquisition system used for AGATA are also described.

---

## 3.1 Introduction

---

Within the NUClear STructure, Astrophysics and Reactions (NUSTAR) [2] physics program of the Facility for Antiproton and Ion Research (FAIR) [74], physics goal of the HIgh-Resolution In-flight SPEctroscopy (HISPEC) [3] collaboration is to perform high resolution in-beam  $\gamma$ -ray spectroscopy at the final focal plane of the Super-FRS [75] with the AGATA [4] array in conjunction with complementary instrumentation. Similarly, the DEcay SPEctroscopy (DESPEC) [3] collaboration aims at performing stopped-beam experiments employing a wide variety of detectors for comprehensive nuclear decay studies. The two mentioned collaborations will provide detectors built with their own custom-made hardware and Data AcQuisition (DAQ) systems. The PreSPEC collaboration [3] is the precursor of the two above mentioned collaborations, and on top of its own physics program, the task of the PreSPEC collaboration at GSI is also to test the equipment and future technical solutions for HISPEC/DESPEC in view of the challenges associated with FAIR. In this context, the coupling of the conventional in-house “trigger-driven” electronics and DAQ system of the FRS [1], LYCCA [5] and HECTOR+ [6, 76] with the “digital trigger” based electronics and DAQ of the AGATA [4] detector is a proof of concept for NUSTAR at FAIR.

All experiments performed during the PreSPEC-AGATA campaign followed a similar principle [7]. The SIS-18 synchrotron accelerated a primary heavy-ion beam up to 1 GeV/u. The accelerated heavy ions were extracted from the SIS-18 synchrotron in spills of time intervals lasting typically from 1 s to 10 s. The radioactive beams entering the FRS were produced via nuclear reactions on a thick (few g/cm<sup>2</sup>) primary target. The event-by-event-identified radioactive ion-beam particles were impinging on a secondary target placed at the last focal plane (S4) of the FRS. At this point, the produced radioactive ions underwent Coulomb excitation on a gold target or secondary fragmentation on a beryllium target. The  $\gamma$ -ray detectors AGATA and HECTOR+ surrounded the secondary target to obtain nuclear-structure information. Behind the secondary target, the reaction products were identified with LYCCA [5]. The GSI DAQ system MBS [77] recorded the data coming from the FRS, LYCCA, and HECTOR+ detectors, and is described in Section 3.2. The AGATA [4] germanium-detector array was read out by fully digital electronics synchronised through the Global Trigger and Synchronisation system (GTS) [78]. The AGATA data-flow system including the GTS and the NARVAL [79] DAQ system is presented in Section 3.3. In Section 3.4 the trigger coupling scheme is discussed. A demonstration of the performance of the coupled system is given in Section 3.5, prior to a conclusion in Section 3.6.

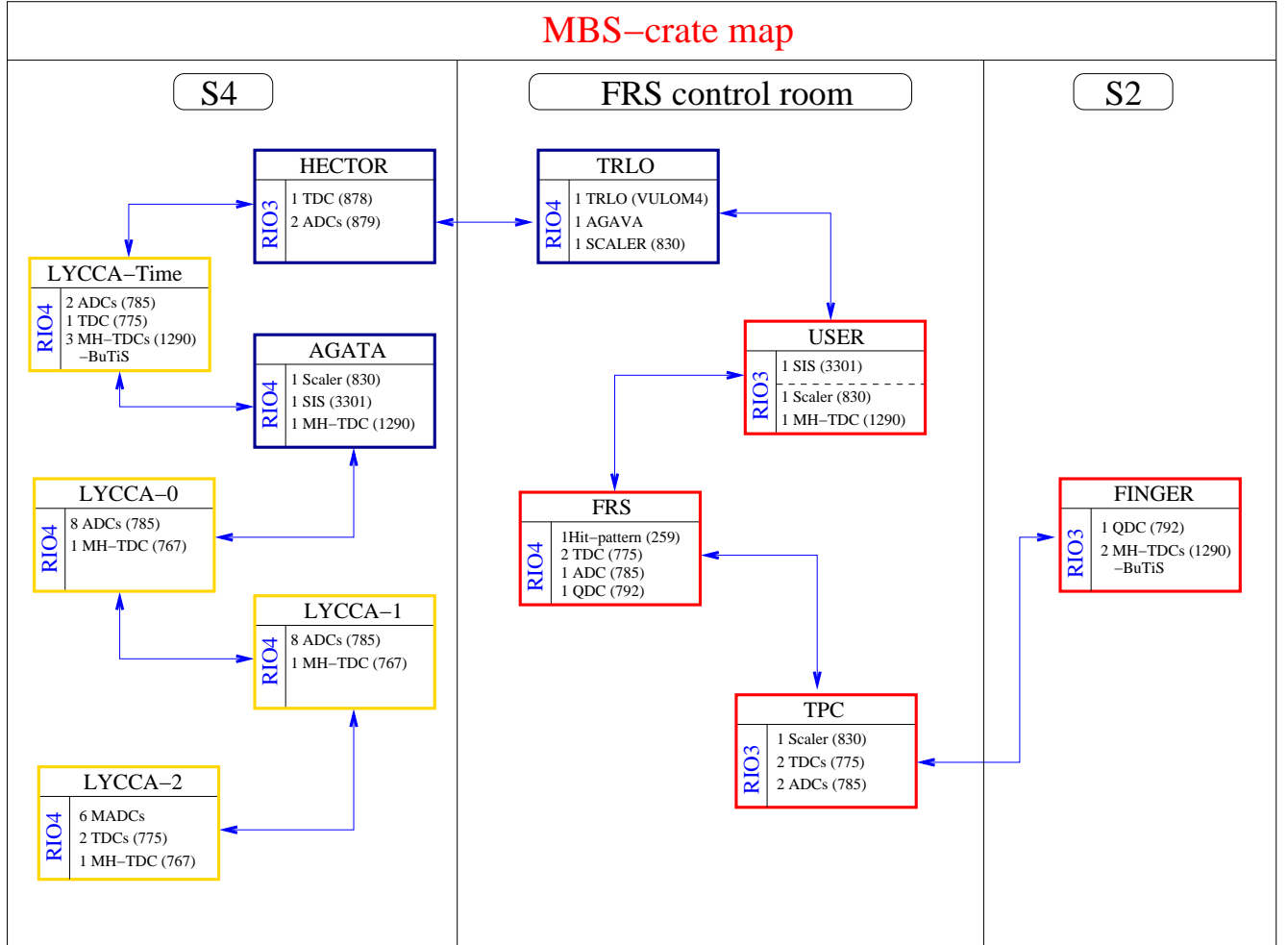


**Figure 3.1:** Schematic view of the location of the complex and widely distributed MBS DAQ system of the PreSPEC-AGATA campaign. Each of the eleven VME crates was linked with the trigger bus connection represented by the blue arrow. Each box represents a crate. Red contours denote the FRS sub-system, yellow the LYCCA sub-system and blue the AGATA sub-system. The BuTiS sign means that the MH-TDCs of the crates were synchronised with an external clock. Modules in each crate are listed according to their abbreviations (see text for details).

The PreSPEC DAQ system running MBS was responsible for the trigger logic and data collection of the full setup except AGATA. Eleven MBS branches were used, each consisting of a single VME crate controlled with a RIO3 or RIO4 processor [80]. As in a standard MBS system, each crate contained, in addition to the controller, a TRIVA trigger module [81]. The TRIVA modules were linked together via their trigger bus making sure that the system operated synchronously on an event-by-event basis. In such a synchronous system, the data acquisition runs at the speed of its slowest component. The eleven VME crates were positioned between the FRS middle focal point area (S2), the FRS end focal point area (S4) and the FRS control room as shown in Fig. 3.1. The PreSPEC DAQ was sub-divided into three sub-systems: FRS, LYCCA, and GAMMA. Each sub-system consisted of a sub-set of crates and electronics modules which are described hereafter.

In each sub-system of the setup Time to Digital Converter with Multi-Hit (MH-TDCs) capabilities were used for time measurement. Contrary to a standard TDC, the MH-TDCs record the time of all hits within a time window. For any event, a few microseconds of the associated memory buffer were written to disk. In such case, often several hits per trigger were present. To select the “proper hit”, *i.e.*, the one corresponding to the triggering particle, an external time reference was fed into four MH-TDC channels. Only one timing signal from the last focal plane scintillator would have been sufficient, but for redundancy, both left and right scintillator timing signals from the middle and from the final FRS focal plane were chosen.

---

### 3.2.1 The FRS sub-system

---

The FRS identification was based on the  $B\rho - \Delta E - B\rho$  method which required the determination of the magnetic rigidity ( $B\rho$ , with  $B$  denoting the magnetic field of a given FRS dipole, and  $\rho$  the bending radius of the magnet [47]) through position determination at the middle and final focal planes and Time of Flight (ToF) measurement of the ion in order to deduce its corresponding  $A/Q$  ratio. Here  $A$  is the mass number of the ion and  $Q$  its charge. An energy loss “ $\Delta E$ ” measurement for the determination of the atomic number  $Z$  of the nucleus [82] was performed at the final focal plane [1]. Four VME crates were dedicated to the read out of the FRS detectors.

The position at each focal plane was determined by Time Proportional Chambers (TPC) [52] all read out by the same crate (cf. Fig. 3.1). Positions in the dispersive plane of the FRS were determined with TPC delay lines connected to a Time to Digital Converter (TDC, Caen V775). Positions in the vertical plane were given by a measurement of the drift time of the ionized gas with another TDC. In addition, the *TPC crate* hosted two Amplitude to Digit Converters (ADCs, Caen V785) to measure the charge of the TPC electrodes and a scaler module (Caen V820) for monitoring purposes.

The  $\Delta E$  measurement was done with two MUlti-Sampling Ionization Counters (MUSIC) [53] positioned at the S4 final focal plane. The anode signals of the MUSIC detector were amplified and connected to one ADC (Caen V785) of the *FRS crate*. The ToF measurement was performed with conventional plastic detectors at the middle and final focal plane of the FRS followed by CFDs (Constant Fraction Discriminators) and TACs (Time to Amplitude Converters). Photomultiplier signals of the plastics and TAC signals were sent to the *FRS crate* hosting one Charge to Digital Converter, (QDC, Caen V792) and one ADC. In addition, two TDCs were foreseen for the read out of beam monitoring detectors at other focal points. They were not used during PreSPEC-AGATA data taking. The *FRS crate* hosted also a hit pattern (Caen V259) module, which received all logic signals from each subsystem to allow either a consistency check with the standard triggering (see below) or, in case of a normalization trigger, to measure redundantly trigger probabilities.

A third crate (called the *USER crate*) was used to assure proper FRS identification in case of high beam intensities. This is relevant for intensities  $\gtrsim 5 \times 10^4$  particles per second at the final focal plane, or in case of an inhomogeneous spill structure. The *USER crate* comprised a ADC-digitizer module (SIS3301) [83] with pile-up disentanglement capabilities for the readout of one of the two MUSICS. In parallel all timing signals (TPCs, scintillators S2/S4, and triggers) were sent to a Caen V1290 TDC, which has multi-hit capabilities. It was used to perform pile-up determination and served as a backup for the TOF measurement in case the analog chains exhibited problems. The *USER crate* hosted as well one V830 Caen scaler module that monitored counting rates of various detectors of the experiment as well as the dead time of the full MBS system.

The particle rates at the middle focal plane was much higher than at the last focal plane. For this reason the “finger” detector [84], a plastic detector segmented into 32 strips, was used allowing a ToF measurement at higher rates than the standard middle-focal-plane scintillator. The signals coming from the photo-multiplier tubes (PMT) of the “finger” detector were split to send one of them to a CFD followed by a MH-TDC for timing purpose, and the other one to a QDC in order to extract charge information related to the strip that fired. Two MH-TDCs (Caen V1290) and one QDC (Caen V792) were hosted inside the *FINGER crate* located in the middle focal plane area. The clock of the MH-TDCs was synchronised with the one placed at the last focal plane area using the BuTiS [85].

---

### 3.2.2 The LYCCA sub-system

---

The particle identification in LYCCA was based on a  $E$ -ToF (mass  $A$ ) and  $E - \Delta E$  (charge  $Z$ ) measurement [5]. In addition, LYCCA provided tracking of the reaction products after the secondary target. Circular membrane plastic scintillators [55] with multiple PMT readout, were used as start and stop for the ToF measurement. Two start plastic detectors were available, one with 32 PMTs (diameter 27 cm) located  $\sim 1.0$  m in front of the secondary target, and a second one, the target ToF, with 12 PMTs (diameter 7.3 cm) at about 10 cm before the secondary target. The stop plastic had 32 PMTs and was located  $\sim 3.0$  m behind the secondary target. The time signals from the PMTs were read out with 3 MH-TDCs (Caen V1290) located in the *LYCCA-time crate*. The clock of the MH-TDCs were synchronised with the one of the *FINGER crate* via BuTiS [85]. In addition, the *LYCCA-time crate* hosted two ADCs (Caen V785) to record the energy signals of all 32x32 strips of the target Double Sided Silicon Strip Detector (DSSSD) which provided the interaction position on the target [5]. An extra TDC in common stop (Caen V775) was located in this crate for the target DSSSD timing signals used for hit distinction during experiments with high S4 rate.

The  $E - \Delta E$  measurement was obtained from the LYCCA wall that consisted of 16 telescopes. Their front part made of 32x32 strips DSSSD detectors for  $\Delta E$  and position measurement were attached to a stack of nine CsI crystals (CsI) for the total energy measurement [5]. The strips of the DSSSD wall modules were connected in pairs and fed into STM-16+ Mesytec shapers [86]. 16 ADCs (Caen V785) and two MH-TDC (Caen V767) in both the *LYCCA-0 crate* and *LYCCA-1 crate* received the energy and the time outputs of the shapers, respectively.

---

The CsI signals went into MSCF-16 shapers and further to six Mesytec ADC (MADC-32). Their timing signals were processed by one MH-TDC (Caen V767) and two TDCs (Caen V775). These nine modules were hosted in the *LYCCA-2 crate*.

---

### 3.2.3 The GAMMA sub-system

---

The HECTOR+ detector array was composed of ten large volume LaBr<sub>3</sub>:Ce scintillators and eight large volume BaF<sub>2</sub> scintillators. The readout and acquisition of HECTOR+ signals was done with the *HECTOR crate*. In this crate, two ADCs (Caen V879) and one TDC (Caen V878) were present. They recorded two dynamic ranges for the LaBr<sub>3</sub>:Ce scintillators in order to cover low and high energy  $\gamma$ -rays, and their time. In addition, two time components (slow and fast) of the BaF<sub>2</sub> detectors were recorded in order to allow neutron- $\gamma$  discrimination and to fully use their good intrinsic time resolution. The energy read-out of the BaF<sub>2</sub> scintillators had only one range.

The *AGATA crate* consisted of one MH-TDC (Caen V1290) and one scaler module (Caen V830) in which each germanium core signal was sent after passing through a Timing Filter Amplifier (TFA) and CFD. In addition, the crate hosted a flash-ADC module (SIS-3301) in which seven core energy signals were read out. This crate was set mainly for monitoring of the  $\gamma$ -part of the trigger (Section 3.4) and for consistency checks of the data coupling (see Section 3.5).

The master crate in the setup was called *TRLO crate*. It assured the synchronous read out of all the crates for a given Master trigger. Master triggers were generated by the TRigger LOGic (TRLO) firmware [87–89] (Section 3.4) installed on a VULOM4 [90] that handled dead-time locking and read-out decisions taken according to the user-defined scheme (Section 3.5).

In addition, the *TRLO crate* included an AGAta VME Adaptateur (AGAVA) [4] that provided the possibility to couple VME-based system to the AGATA system and the GTS time-stamp information for any MBS event (Section 3.3).

### 3.3 The AGATA data flow at GSI

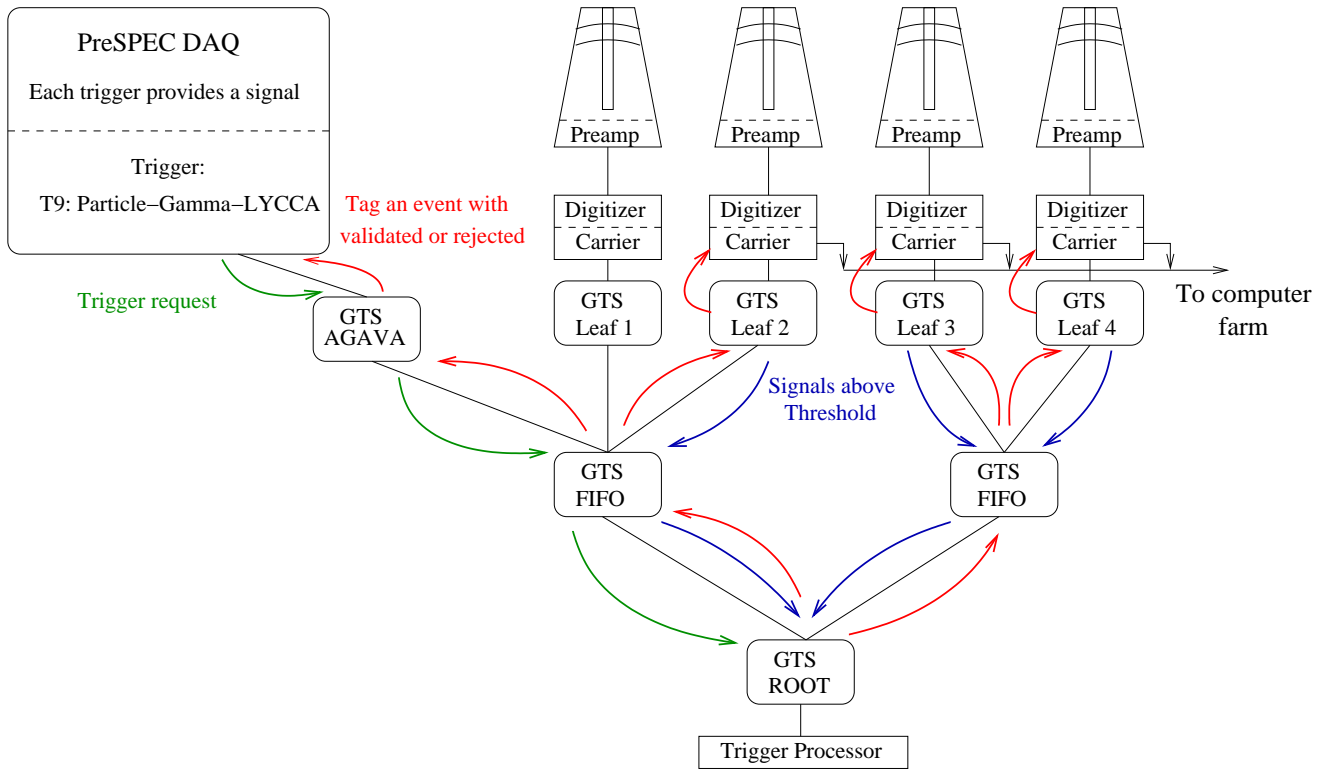


**Figure 3.2:** The core output of each crystal was connected to a GTS configured as leaf of the GTS tree (see text for details). Every time a core had a signal above threshold, a request was sent to the root of the tree connected to the trigger processor (blue arrows). One other leaf (GTS AGAVA) represented the complementary detectors of the PreSPEC setup. It sent a request to the trigger processor for each validated MBS trigger (green arrows). The trigger processor performed the coincidence, and validated  $\gamma$ -ray events in coincidence with PreSPEC ancillary detectors (red arrows). Validated events were read by the computer farm.

#### 3.3.1 Pre-processing stage of the AGATA data flow

The 36 segments and two core signals (two gains for each core were available during the GSI experiments: 5 MeV and 30 MeV full range) coming from the pre-amplifiers of each segmented HPGe detectors were sampled by 100 MHz, 14-bit flash-ADCs of the digitizers. They were running with a common clock received by the GTS. The 38 digitized signals were sent via optical fibers to the pre-processing stage. The latter was composed of mezzanine cards hosted on ATCA carriers boards [4]. Mezzanines processed the data, *i.e.*, extracted the energy information via a digital trapezoidal filter, or a Moving Window Deconvolution (MWD) algorithm [91]. Timing information was extracted using a leading-edge algorithm. For any core signal above noise level, time, energy, and trace (100 samples) of the core and segment digital signals (pulse shape) were stored inside the mezzanine memory. The GTS system assured the time-stamping of this data on a 48-bit stamp with a step of 10 ns. The mezzanines stored the data until a decision from the trigger processor (see next paragraph) was received to either validate or discard the events. In the case of event validation, all the mezzanines sent their data to their carrier. The latter built and pushed the event to the computer farm.

#### 3.3.2 The Global Trigger and Synchronisation System

The AGATA triggering system, called GTS, was built as a tree, where each germanium detector corresponds to a leaf. In the tree philosophy, each leaf was sending a trigger request to the trigger processor unit connected to the root of the tree (see illustration in Fig. 3.2).

In the preprocessing electronics, the threshold was set slightly above noise level to allow a good base-line determination in the MWD process, assuring the best possible energy resolution. Each crystal that had its core signal crossing this



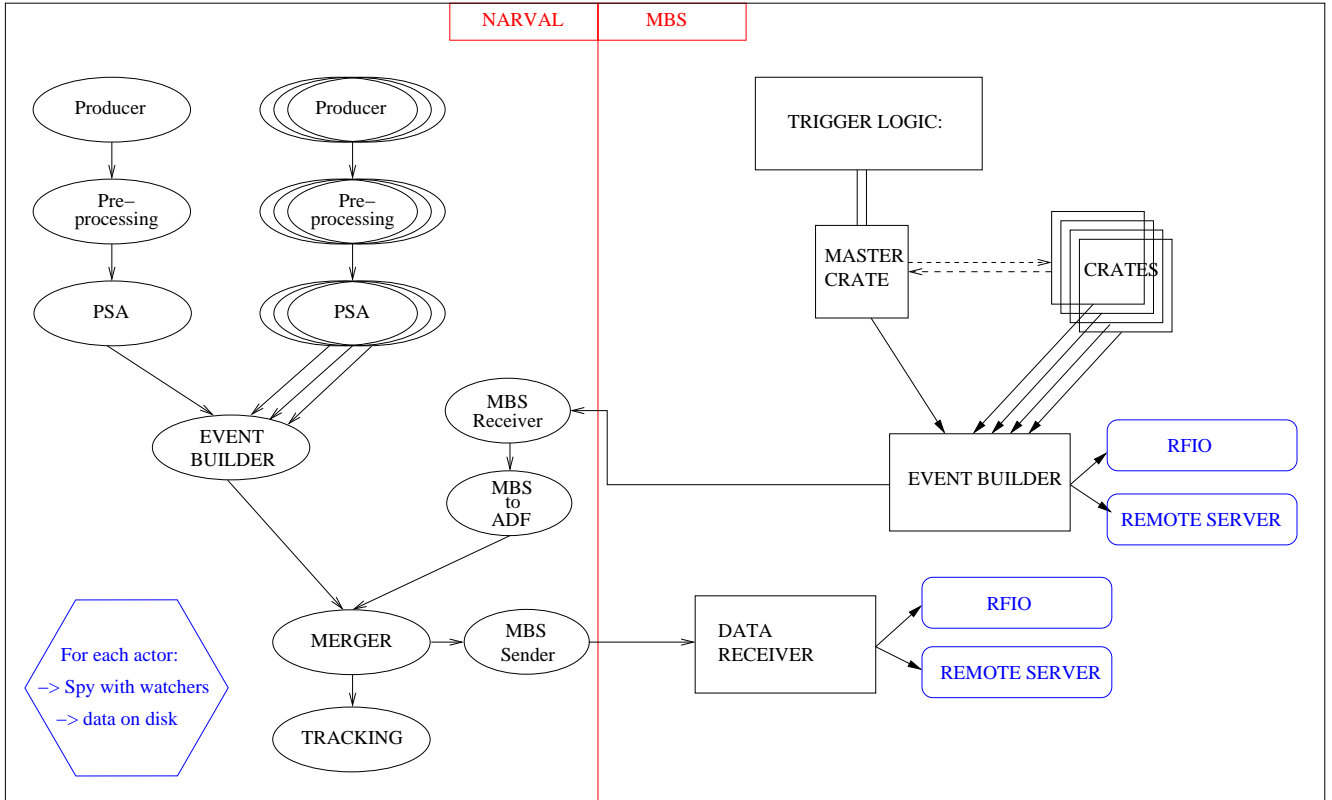


**Figure 3.3:** Scheme of the data flow coupling for the AGATA and MBS DAQ system. On the left hand side are shown the different actors of NARVAL that were needed to process the data flow. The right hand side depicts the MBS DAQ systems, with the different crates reading out the data of the PreSPEC ancillary detectors, together with the MBS data flow (see text in Section 3.2 for details).

threshold provided a trigger request to the GTS tree that forwarded the request to the root GTS connected to the trigger processor [78]. The latter either validated or rejected the trigger request. It sent the decision via the tree to the requesting GTS, and the associated event was either read by the computer farm or discarded. A reduced scheme of the GTS tree configuration as used for the experiments is shown in Fig. 3.2. The GTS decision to validate or reject depended on the trigger processor configuration. In the “standard” PreSPEC configuration two partitions were set: one containing all the germanium detectors, and the other one containing the trigger request from the particle detector, or ancillary detector. Each partition that had at least one request set the partition “up” for  $1 \mu\text{s}$ . A coincidence between the two partitions was set if both of them were “up” for  $6 \mu\text{s}$  with the coincidence window set to  $-/+ 3 \mu\text{s}$  around the ancillary request. Each GTS-leaf (detectors or ancillary leaf) that had a request in the coincidence window was validated. With this trigger processor configuration, the full system got validated by the VME-based electronics. This solution was chosen in order to be able to couple an analog system with a fully digital one. The trigger decision inside the GTS system was taking at least  $10 \mu\text{s}$  and it was not possible to wait that long in the PreSPEC analog branch before processing the event. Consequently the read-out of the coupled system was controlled by the trigger decision from the TRLO firmware. This solution was devised also to allow to have a different threshold for the particle- $\gamma$  coincidence regardless of any effect on the MWD filter applied in the pre-processing stage. We operated usually with higher  $\gamma$ -ray thresholds for the coincidence, cutting most of the Lorentz boosted X-rays generated by the slowing down process of the incoming beam in the detectors and target material. This feature proved to be invaluable for heavy  $Z$  beam on high  $Z$  target, where the particle- $\gamma$  trigger would have otherwise been drowned in background.

The GTS system had also the possibility to be used in an “isomer tagging” configuration in order to measure the decay of an isomeric state of an ion stopped by a catcher in front of the AGATA detectors. In that case, the ancillary partition was set with a window of  $1 \mu\text{s}$ , the germanium partition with a window of  $10 \mu\text{s}$  and the coincidence window was set to  $-11/+2 \mu\text{s}$ . If a prompt photon is emitted with the beam implantation, the system was recording all consecutive  $\gamma$ -ray decays during the next  $10 \mu\text{s}$  of the “up”  $\gamma$  partition. With no prompt  $\gamma$ -ray, the system would record an isomer decaying in the following  $11 \mu\text{s}$  after implantation due to the coincidence window. As a consequence, this configuration allowed the measurement of isomers, with a lifetime between a few hundred nanoseconds and several microseconds. The implantation rate had to be limited to a few kilohertz in order to avoid the  $\gamma$  partition to be set “up” continuously, *i.e.*,

---

until the next implanted ion, and because the minimum bias trigger was used as main trigger to operate the MBS DAQ with limited dead-time.

---

### 3.3.3 Data flow handling with NARVAL

---

Each event, as validated by the GTS, comprised energy, time-stamp and traces from the 36 segments and the core of each germanium crystal. This information was processed in computer farms with the so-called “actors” of NARVAL [70]. As shown on the left side of the scheme in Fig. 3.3, the topology (or set of actors) for each crystal consisted of three main elements. The first actor, *Producer*, collected the data from the carriers. The second actor, *Pre-Processing*, performed the time and energy calibration of the core and each segment with a hit. Then a third actor, the Pulse Shape Analysis *PSA*, extracted from the pulse shapes the interaction positions of each detected  $\gamma$  ray using a grid-search algorithm [57]. Afterwards, an actor *Event-Builder* built the event according to related time-stamps, *i.e.*, constructed an event with data coming from different crystals. A second building stage, the *Merger*, allowed the merging of the PreSPEC detector data with the AGATA data flow as explained in Section 3.5. The positions and energies of each interaction point of all  $\gamma$  rays were used by the *Tracking actor* [92] in order to reconstruct the full energy of a Compton scattered  $\gamma$  ray from all associated interaction points.

Each actor had the possibility to write data encoded with the AGATA Data Format (ADF) [93] on disk. During all the GSI experiments, data were written at the level of the actor *Producer* in order to allow a “replay” of the data if post-experiment calibrations were needed. The data after the PSA algorithm were written for on-line and off-line analysis after *Event Builder*, *Event Merging* and *Tracking*. In addition, the data flow was monitored by Watchers [93] that spied each NARVAL actor.



addition, it depended only on the particle detection efficiency of a single detector. Therefore, it was the minimum bias trigger. It was used with a selectable reduction factor as a normalization trigger. Trigger 10 was also used without reduction during isomer measurements (isomer tagging configuration). Physics triggers (6-9) required a coincidence with a particle (SC41 signal), a LYCCA signal and with a  $\gamma$ -ray detected in AGATA (trigger 9) or in HECTOR (trigger 8). Trigger 7 and 6 were the same as trigger 9 and 8 respectively, without the coincidence with the LYCCA signal. Trigger 5 was a generic FRS trigger. It was used during the set up of the FRS, and could be switched to any FRS detector. Triggers from 2 to 4 were calibration triggers used for the calibration of HECTOR (trigger 4), AGATA (trigger 3), and LYCCA (trigger 2). Trigger 1 was a scaler readout trigger. It ran at 10 Hz, and was always validated (it stayed pending until the dead time was released).

Triggers with higher number took priority, e.g. trigger 10 had a higher priority than trigger 9.

This trigger scheme was implemented on a Field Programmable Gate Array (FPGA) in a module developed at GSI, the VULOM4 [90], with the help of the TRLO firmware. Trigger request signals were stretched to 150 ns, time aligned and sent to a logic unit that continuously evaluated the coincidences. A trigger was generated if all associated signals were present at one clock cycle. The TRLO logic waited for 100 ns and during that time assigned the trigger number according to the coincidence scheme. The trigger was accepted if the PreSPEC DAQ system was not processing another event. The timing of the different trigger requests for a part of the configuration can be seen in Fig. 3.4.

Gates were generated and were sent to the different modules of the crates according to the trigger number as shown in Table 3.1. In addition, all triggers latched all scaler modules in any of the eleven VME crates.

**Table 3.1:** Gate generation for the different triggers. The gates were sent to all the modules of FRS, HECTOR, AGATA, and LYCCA crates.

Trigger	FRS	AGATA	HECTOR	AGATA	LYCCA	Scalers
1		X				X
2		X			X	X
3	X	X		X		X
4		X	X			X
5	X	X			X	X
6, 7, 8, 9, 10	X	X	X	X	X	X
12, 13	X	X				X

For any accepted trigger, a gate to the AGATA (as shown in Table 3.1) was sent. This gate triggered the GTS system setting the ancillary partition to “up” (Section 3.3). Inside any MBS event a tag (validated or rejected) from the AGATA, *i.e.*, the GTS system, was written in addition to the GTS time-stamp. For both GTS tags, MBS data were written on disk. It assured the data to be recorded for a trigger 8, where a clear of the MBS event in case of a GTS rejection flag would have discarded an event with a  $\gamma$  ray detected by HECTOR.

---

## 3.5 Coupling of the DAQ systems

---

### 3.5.1 Principle

---

As mentioned above, the MBS system was based on several branches, connected to each other via a trigger bus, which assured the synchronisation of the data. For each TRIVA validated trigger, the data words of each crate were read out by the VME crate backplanes (sub-event), and were sent via network to an event builder. The data were written on disk at the level of the event builder. A schematic view of the MBS data flow structure can be found on the right hand side of the scheme in Fig. 3.3.

The “built” data from MBS was sent to the AGATA computer farm via an Ethernet connection received by a specific NARVAL actor called *MBS Receiver*. The actor *MBS to ADF* encapsulated the MBS data in an ADF format. Each MBS event had a GTS time-stamp (Section 3.4) and was written on disk in the ADF format to allow off-line data merging (in case of re-calibration needs for AGATA). The MBS data were merged with the AGATA “built” data by the actor *Merger* using the GTS time-stamps. In Fig. 3.3 the scheme of the full data flow including the MBS event building, the AGATA data processing, and the coupling of MBS and AGATA data flow is illustrated.

The last NARVAL actor (Fig. 3.3), the actor *MBS Sender*, and its associated MBS receiver were sending back all information in the MBS data format. This enabled a simpler online analysis.

---

### 3.5.2 System integrity check

---

The first verification was performed by an MBS process, the *Time Sorter*, that performed a one to one data analysis. It checked that any event sent to NARVAL was built and properly sent back to the MBS receiver. No missing events were seen.

As explained before, any MBS event got a tag from the GTS system through the AGAVA in order to indicate if the event was accepted or rejected by the GTS. The tagging information showed that in case of a trigger 9, *i.e.*, *Particle- $\gamma$ <sub>AGATA-LYCCA</sub>*, more than 99.9% of the events were accepted by the GTS system.

In order to be able to verify the proper synchronisation between MBS and the AGATA data flow, seven AGATA core signals were digitized within the MBS DAQ (see Section 3.2). The two-dimensional histogram in Fig. 3.5 proves the correlation between data coming from AGATA itself (*y*-axis) and the one generated within MBS (*x*-axis). The diagonal line shows proper correlation of the data after data-merging. The MWD algorithms used with the SIS module and AGATA electronic had different parameters which can explain most of the events with different energies seen outside the diagonal.

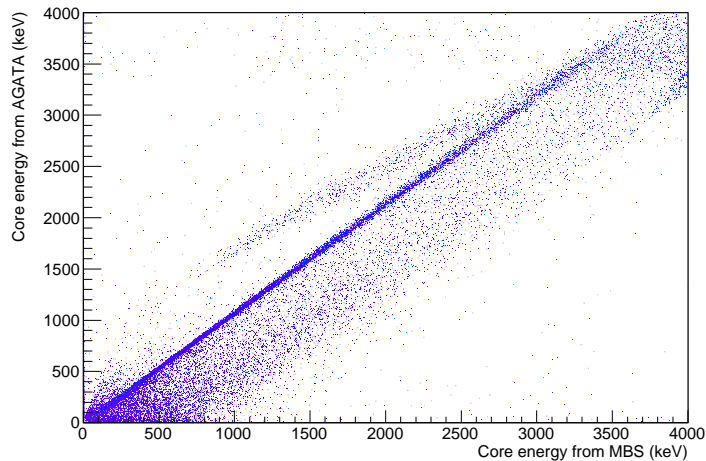


**Figure 3.5:** Core energy of one crystal in the MBS data acquisition digitized by the SIS module as a function of the core energy obtained with the AGATA electronics and computer farm.

A good behaviour of the system was seen as well with the isomer setting (see Section 3.3), when both data from PreSPEC ancillary detectors and from AGATA had to be present and correlated. The time information is also needed to see the  $\gamma$ -ray decay occurring from 100 ns to a few  $\mu$ s after the implantation. A time versus energy  $\gamma$ -ray spectrum is shown in Fig. 3.6, with the observation of the decay of the  $^{109}\text{Rh}$  isomeric state that has a half life of  $T_{1/2} = 1.66(4) \mu\text{s}$  [94].

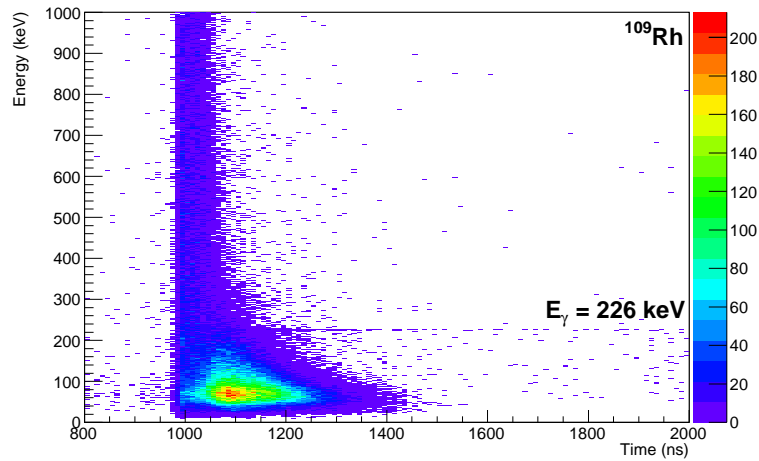


**Figure 3.6:** Time versus energy spectrum for an isomeric state of  $^{109}\text{Rh}$ . The transition at  $E_\gamma = 226 \text{ keV}$  belongs to the decay of a  $T_{1/2} = 1.66(4) \mu\text{s}$  isomeric state [94].

A last validation test for the system correlation was performed using in flight emitted X-rays, which have a large production cross-section. The data correlation is essential in order to be able to see the angular dependence of the X-rays after Doppler correction as shown in Fig. 3.7. The two  $K_\alpha$  X-rays of uranium at 94.6 keV and 98.4 keV were clearly identified and proved that both MBS and AGATA data sets were correlated.

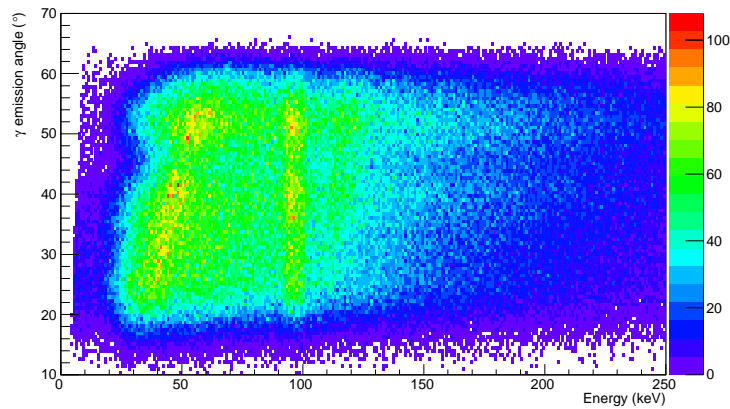


**Figure 3.7:** Angle of the  $\gamma$ -ray emission in AGATA as a function of the Doppler-corrected  $\gamma$ -ray energy. The straight vertical line slightly below 100 keV corresponds to a superposition of the two  $K_\alpha$  X-rays of  $^{238}\text{U}$  ions after Doppler correction using the outgoing velocity and tracking information from LYCCA. This proved the correlation between AGATA and MBS data.

---

## 3.6 Conclusion

---

The coupling of the data flow, triggered by the analog MBS system and the digital GTS, showed good results and provided a proof of principle of the flexibility of MBS and AGATA. Indeed, the data taken by both AGATA and MBS were consistent, and proper analysis on an event-by-event basis is possible. The data integrity was confirmed with test cases such as isomers and particle-X-ray correlations. An additional integrity test was performed using an MBS *Time Sorter* where any MBS event was correlated to the same event after passing the NARVAL system.

The coupled DAQ at GSI was used for eight experiments in 2012 and 2014, and produced almost 200 TB of data including calibrations. The system was pushed up to 3 kHz of event data for MBS, and around 3 kHz of validated events per AGATA crystal. Up to 22 working AGATA crystals were in the setup.

The limiting factor of the system was its dead time. The total number of events recorded on disk per second was in standard utilisation limited to few kilohertz. The dead time mainly originated from the RIO3 VME controller used for the TPC crate. Therefore a RIO4 exchange has been foreseen for future experiments. In addition, the spill structure due to the slow extraction from the SIS-18 synchrotron was affecting the total throughput. Diagnostic tools in the TRLO firmware were readily used to help beam operators optimize beam settings.

A possible improvement could be performed on the particle- $\gamma$  coincidence. A huge contribution of the recorded events came from high energy events: charged particles passing through the AGATA detectors. An anti-coincidence on an upper  $\gamma$ -ray threshold could be applied to improve the ratio of interesting events over background. Adding an energy loss condition from the MUSIC detectors inside the trigger can help to remove contributions from charged particles lighter than the ones of interest thus also improve the maximal throughput of the system.





---

## Chapter 4: Data analysis

In order to investigate the nuclear structure of an exotic nucleus, two nuclear reactions are involved. The first one occurs at the entrance of the FRS (as mentioned in the previous section), where a nucleus of interest is produced. It is selected by the FRS and at the end of the FRS it undergoes the second nuclear reaction. In the experiment described here, a fragmentation occurs on a secondary Beryllium target surrounded by the AGATA detectors.

The analysis performed to identify fragments in the FRS is presented in Section 4.1. The reaction products, after the Beryllium target are identified by the LYCCA calorimeter array. Since the  $\gamma$ -rays are emitted in flight, they are strongly Doppler shifted and the outgoing velocity need to be precisely measured.

In order to disentangle different reaction channels, an accurate calibration of all the detectors of the LYCCA array is needed. The different calibration steps are presented in Section 4.2.  $K_{\alpha}$  X-rays of Uranium primary beam are used to calibrate the LYCCA ToF and to determine a possible shift of the position of the target. This analysis, based on Bayesian analysis methods, is explained in Section 4.3. The AGATA detector calibration is performed at its best in order to minimize uncertainties on the position provided by the Pulse Shape Algorithm (PSA). This procedure is described in Section 4.4.

## 4.1 Identification of the fragments with the FRS

The fission of the 600 MeV/u  $^{238}\text{U}$  primary beam from SIS produced many isotopes that were selected and identified by the FRS. Two FRS production settings were used during the experiment: one with  $^{108}\text{Mo}$  isotopes and one with  $^{107}\text{Nb}$  isotopes centered at the final focal plane of the FRS. Both settings were in mono-energetic mode (see Section 2.1), which implied a narrow velocity spread of the fragments at the secondary target and the drawbacks of spread in positions and loss in the transmission efficiency. However, a narrow velocity distribution at the secondary target level facilitates DSAM methods and should ease mass identification with LYCCA.

### 4.1.1 Isotope identification

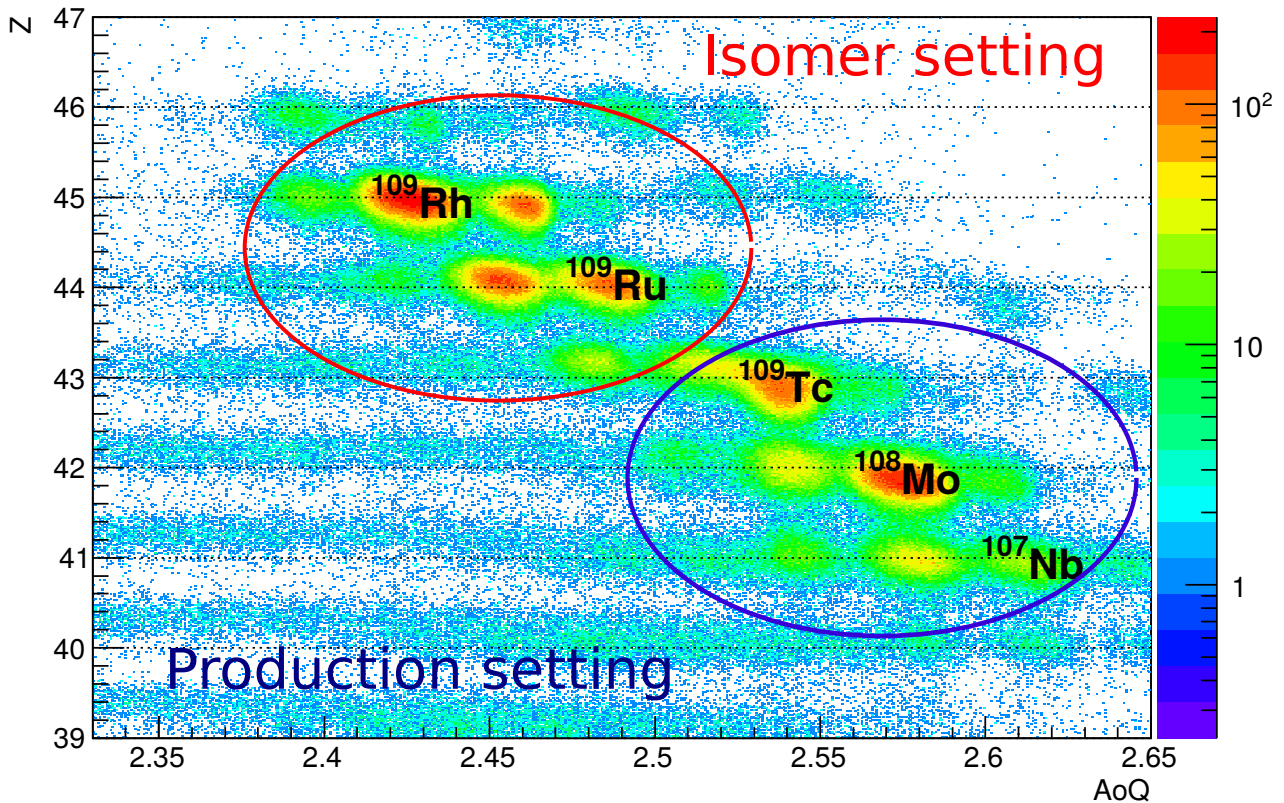


**Figure 4.1:** Superposition of the identification plots for the  $^{108}\text{Mo}$  and  $^{107}\text{Nb}$  production settings and for the  $^{109}\text{Rh}$  isomer setting. This plot provides the identification of all the produced and transmitted species in the FRS during the experiment. The red circle highlights the FRS setting where the  $^{109}\text{Rh}$  and  $^{109}\text{Ru}$  isomeric transitions are observed, while the blue circle highlights the superposition of the two production settings. Species identification is obtained with the isomer tagging method.

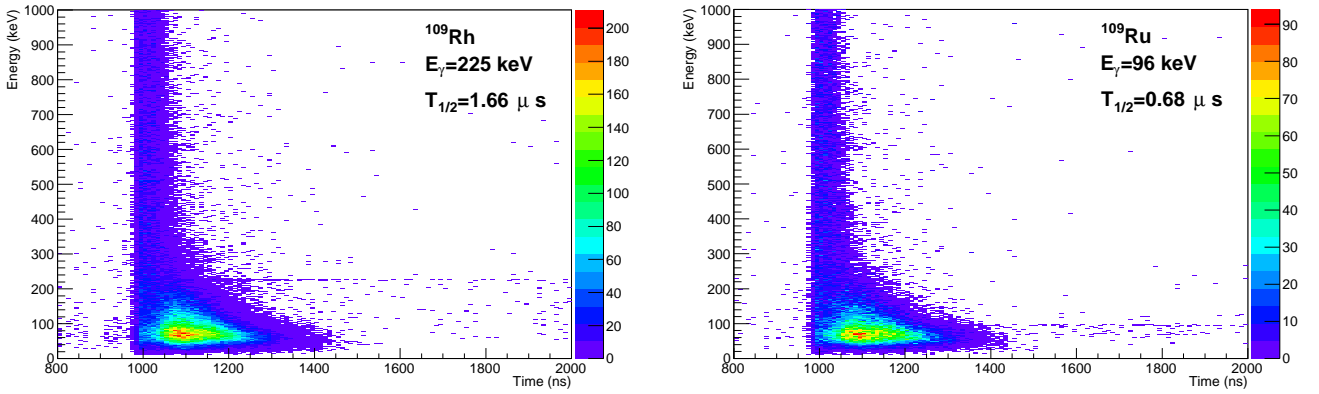
During the preparation of the FRS, the fragments produced by the relativistic fission of  $^{238}\text{U}$  beam were selected by a series of  $B\rho$  values for the FRS dipoles. A set of  $B\rho$  value is commonly called a “FRS setting”. One FRS setting is simulated using the LISE++ software. Nevertheless, the exact amount of matter in the beam line cannot be predicted. Therefore, a different (or effective)  $B\rho$  from the simulated value can be needed to select the aimed specie. Moreover, the amplitude of the signal between the uranium and e.g. molybdenum ions can be significant enough and enter a non-linear regime of the CFD used for the time-of-flight and positions determination (walk effect). Thus, a “jump” in  $Z$  from 92 to  $\sim 40$  induces uncertainties in  $AoQ$  and  $Z$  of the identified ions.

The procedure to determine without ambiguity the species produced within a FRS setting is the observation a  $\gamma$ -ray decay of an isomeric state. This latter is an excited level of a nucleus that has a lifetime of at least 200 ns that can therefore “survive” the flight time in the FRS. These excited nuclei are implanted in a thick plastic, positioned inside the reaction chamber, 15 cm further downstream from the secondary target. The decay of the excited level occurs at rest and can easily be observed inside the AGATA detectors. This method is called “isomer tagging” [95]. Usually, one or

two FRS settings are needed before an isomeric nucleus is found. Without the isomer tagging method, a scan the nuclear chart from uranium primary beam down to our mass region would be needed, which takes many intermediate settings. Thus, the isomer tagging is quick and it allows physics measurement after a few hours of beam.

The bi-dimensional identification histogram ( $AoQ-Z$ ) for three FRS settings – the “isomer setting” and two “production settings” – is shown in Fig. 4.1. Each area with high number of counts (in red) in the ( $AoQ-Z$ ) histogram corresponds to one mass identified by the FRS.

When the FRS is set on the “isomer setting” decays of isomeric states with different lifetimes are observed. Two energy-vs-time histograms, shown in Fig. 4.2, allow to name two nuclei:  $^{109}\text{Rh}$  and  $^{109}\text{Ru}$ . The different energies of the observed  $\gamma$ -ray transitions for these two nuclei provide an unambiguous determination of all ions passing through the FRS with this “isomer setting”. An overlap in the identification histogram between the “isomer setting” and the “production settings” allows a full identification of all nuclei passing in the FRS during the experiment.  $^{109}\text{Tc}$ ,  $^{108}\text{Mo}$ , and  $^{107}\text{Nb}$  are by this procedure confirmed to be produced and selected by the FRS with the “production settings”.



(a) Observed decay of a 225 keV isomeric transition of  $^{109}\text{Rh}$  with a lifetime of:  $T_{1/2}=1.66(4) \mu\text{s}$  [94]. (b) Observed decay of a 96 keV isomeric transition of  $^{109}\text{Ru}$  with a lifetime of:  $T_{1/2}=0.68(3) \mu\text{s}$  [96].

**Figure 4.2:** Bi-dimensional histograms energy-vs-time that highlights the decay of two isomeric states and allows their assignment to previously measured isomers. The number of counts per bin is indicated by the color bar on the right-hand side.

This experiments contains three main FRS settings: the “isomer setting” and two “production settings”. One is centered on the  $^{108}\text{Mo}$  isotope and the other one is centered on the  $^{107}\text{Nb}$  isotope. A summary of the main species selected in the FRS for the three settings is given in Table 4.1.

**Table 4.1:** Summary of the three FRS settings used during the experiment. The Ratio refers to the number of counts for one identified ion over the total number of identified species. In the ( $AoQ-Z$ ) histogram shown in Fig. 4.1, more species are identified than the one mentioned in this table. For this reason the sum of all ratios does not reach 100%. The positions at the final focal plane of the FRS (S4) are measured with the two last FRS TPCs.

Settings	Main isotopes in the setting		Ratio (%)		Mean of S4 positions (mm)	
Isomer	$^{109}\text{Rh}$	$^{110}\text{Rh}$	27.7	9.90	-2.1	22.3
	$^{108}\text{Ru}$	$^{109}\text{Ru}$	16.1	13.1	-14.2	11.5
	$^{107}\text{Tc}$	$^{108}\text{Tc}$	2.79	4.17	-21.7	5.06
$^{108}\text{Mo}$	$^{108}\text{Tc}$	$^{109}\text{Tc}$	3.95	33.0	-25.6	1.7
	$^{107}\text{Mo}$	$^{108}\text{Mo}$	14.1	10.8	-9.54	2.6
	$^{106}\text{Nb}$	$^{107}\text{Nb}$	3.31	1.46	-11.9	-3.1
$^{107}\text{Nb}$	–	$^{109}\text{Tc}$	–	7.72	–	7.72
	$^{107}\text{Mo}$	$^{108}\text{Mo}$	6.47	41.7	-10.3	-0.44
	$^{106}\text{Nb}$	$^{107}\text{Nb}$	12.3	7.1	-3.4	1.0

#### 4.1.2 Useful contaminants inside the FRS settings

With a production setting not only the aimed nuclei are passing through the FRS dipoles and are centered at the final focal plane of the FRS. For example, the positions at the final focal plane of the FRS reported in Table 4.1 proves that also  $^{109}\text{Tc}$  is centered at S4 when the FRS setting is on  $^{108}\text{Mo}$ . They represent 33% of the total amount of particles reaching the S4 scintillator and identified by the FRS. This situation is even more pronounced with the  $^{107}\text{Nb}$  setting, in which  $^{108}\text{Mo}$  is the dominant specie and it is also the most centered one. The “contamination” by other species is a consequence of the mono-energetic mode of the FRS and it is advantageous for the experiment. Indeed, the primary goal of the experiment is to populate  $^{106}\text{Zr}$  isotopes via secondary fragmentation of the  $^{107}\text{Nb}$  ions at the secondary target. The large proportion of  $^{108}\text{Mo}$  isotopes centered at the S4 target produces also  $^{106}\text{Zr}$  ions via the two proton knockout reaction channel and therefore, it increases the yield of the wanted isotopes. In addition, the neutron removal in  $^{108}\text{Mo}$  produces  $^{100-107}\text{Mo}$  isotopes, whose lifetime of the even-even nuclei are known. This provides the possibility to test the sensitivity of the lifetime measurement method [97].

#### 4.1.3 Maximization of the number of identified ions

The TPC detectors loose efficiency when the rate is high, e.g. a rate of  $\sim 300$  kHz at the middle focal plane of the FRS [98]. Moreover, the position information given by the S2 scintillator is missing probably due to a wrong setting up of the TAC. For this reason, the identification histogram ( $AoQ-Z$ ) in Fig. 4.1 have a low number of counts with respect to the total number of events recorded. Nevertheless, it is possible, due to the fact that the FRS is set in mono-energetic mode, to identify the nuclei via their velocity  $\beta = v/c$ ; which in some extend, prove a proper working ToF measurement in the experiment. This method provides a factor three increase in the number of identified ions at S4 than with the AoQ value. The FRS identification histogram using the  $\beta$  and  $Z$  of the particles is shown in Fig. 4.3.

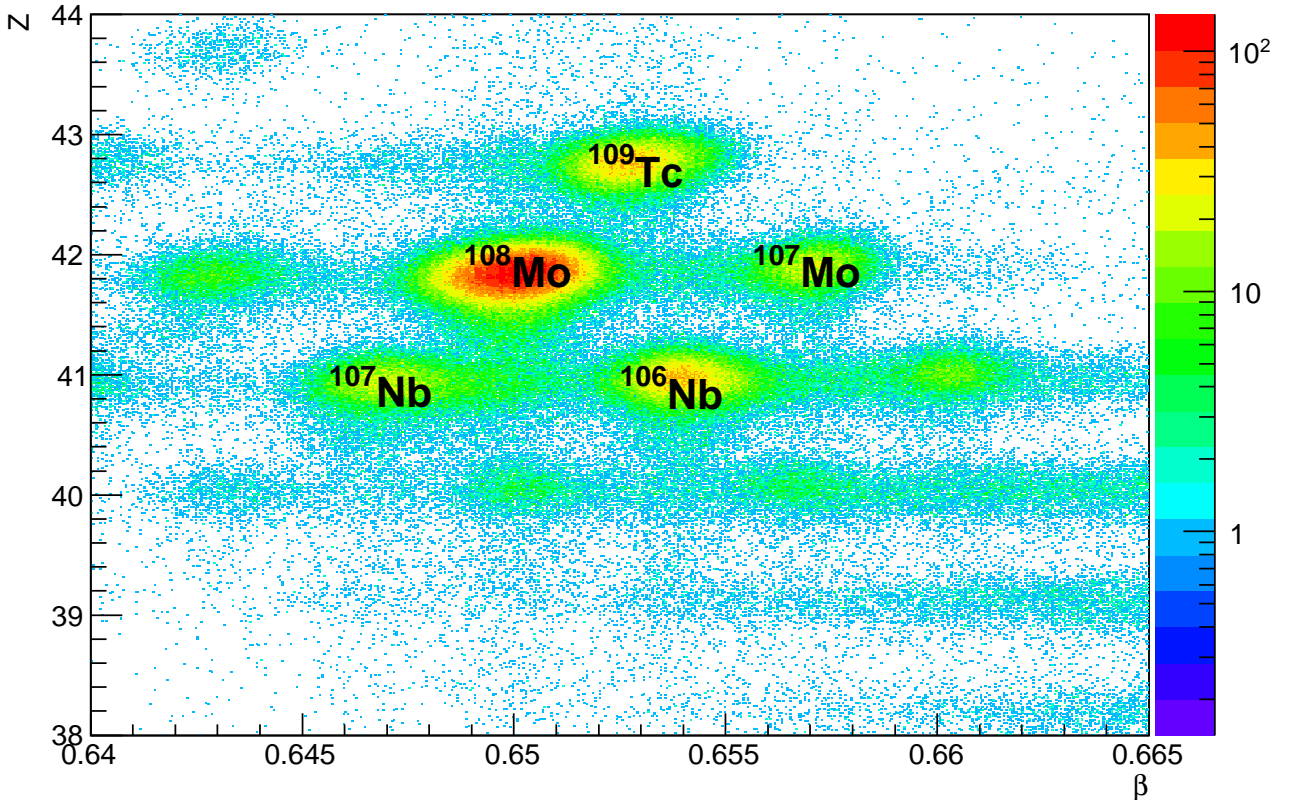


**Figure 4.3:** Identification plot for a FRS setting with  $^{107}\text{Nb}$  centered at the final focal plane.  $\beta$  and  $Z$  of the ions are used for a species identification due to the mono-energetic mode of the FRS. The most intense species (with  $Z = 42$ ) is the  $^{108}\text{Mo}$  isotope.

## 4.2 LYCCA data analysis

The LYCCA calorimeter is designed to identify fragments up to mass 100 at energies around 100-300 MeV [5]. In the present experiment, the masses of the isotopes of interest are higher. In order to achieve an optimum calibration for the ToF, the calibration procedure is performed for each run, *i.e.*, 2 GB data files, corresponding roughly to one hour of beam time. This procedure is described in Section 4.2.1.

The main idea for energy calibration of the LYCCA Wall modules is to combine an empty target (technically, empty frame) with a target run. These two runs provide two energies for the ions reaching the LYCCA wall thus two different energy losses in the wall detectors. These two calibration points are used for gain matching and absolute energy calibration of the total kinetic energy calibration relying on ATIMA [99] simulations. The details on the calibration method used for the DSSSD and CsI(Tl) are described in Section 4.2.2 and Section 4.2.3 respectively.

The determination of the velocity of the outgoing fragment and mass determination of the fragments is presented in Section 4.2.5 using the Doppler corrected  $\gamma$ -ray spectra (minimizing the FWHM of known transitions).

### 4.2.1 ToF calibration

The time needed to collect the light emitted when a particle hits the membrane depends on the distance between the particle hit and the PMTs. The PMT time, or intrinsic PMT time, is given with respect to the average<sup>1</sup> of left and right PMT time signals of the plastic scintillator at the final focal plane of the FRS. The correlation between the time to collect the light ( $time_{raw}$ ) and the distance from the emission to the PMT ( $distance_{PMT-HIT}$ ) is shown in Fig. 4.4a for one PMT. The corrected time measurement ( $time_{cor}$ ) is obtained according to the following equation:

$$time_{cor} = time_{raw} + distance_{PMT-HIT} \times slope \quad (4.1)$$

A time shift inside a PMT due to temperature dependence of the PMT gain affects all the positions in the same way. This justifies a unique *slope* coefficient per PMT for the whole experiment. The *slope* of each PMT is obtained with a fit of the ellipsoid in the time versus distance of interaction plot. The positions of the interactions at the LYCCA start scintillator are extrapolated from the S4 TPCs and interpolated between Target DSSSD and Wall DSSSD for the LYCCA stop scintillator. The effect of the correction is observed in Fig. 4.4b.

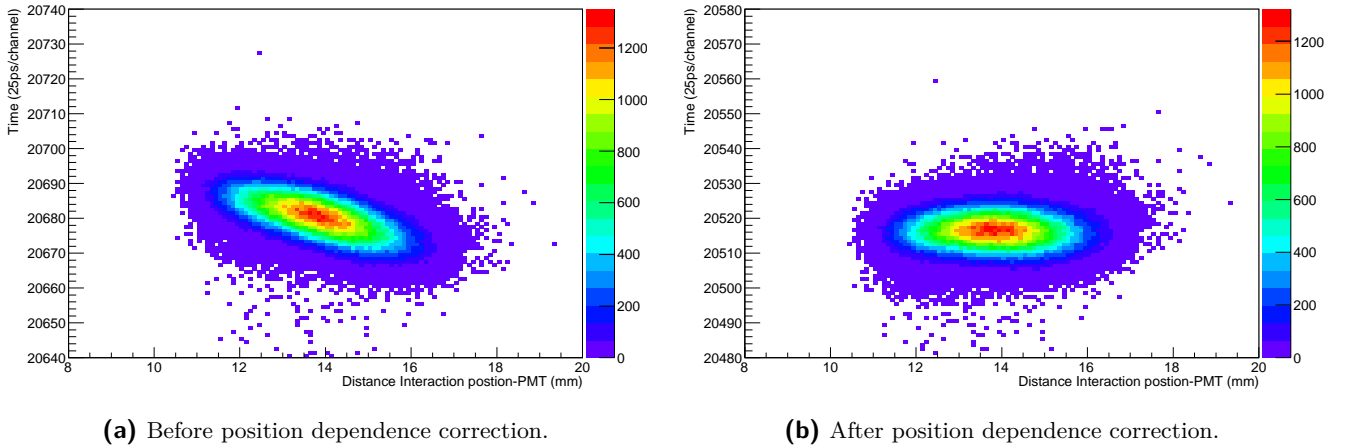


**Figure 4.4:** Intrinsic time of the First PMT of the start plastic scintillator as a function of the distance between the PMT and the interaction position of the ion in the membrane.

The time of each PMT is aligned to the mean time between the time of all PMTs. This process has to be done run by run to take into account individual PMT time shifts between consecutive runs. Indeed, up to 50 ps shift between two consecutive runs of an hour has been observed. The time resolution obtained after an event by event correction is 88 ps for the start membrane, while for the stop membrane is 193 ps.

In order to cancel potential drift of the time reference (here the scintillator at the final focal plane of the FRS), we calculate the average over all PMT times of the start and the stop membrane and compute the difference. The systematic variations of this time difference are shown in the plots in Fig. 4.5.

<sup>1</sup> The time average provides a time reference that is independent of the position of the light emission inside the last focal plane scintillator.

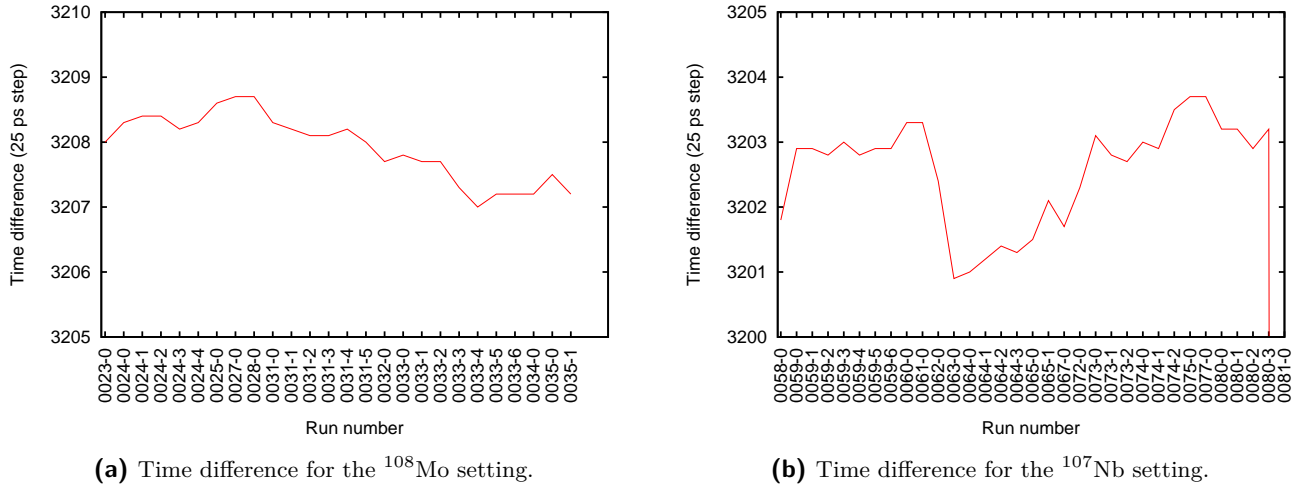


**Figure 4.5:** Systematic variations of the mean time difference between the start membrane and the stop membrane scintillator. The  $x$ -axis is labelled with the run number. Each run corresponds to  $\sim$  one hour of data.

An offset has to be applied to the mean time difference in order to obtain the correct velocity of the outgoing ions. We compute an “artificial” offset to the time difference shown in Fig. 4.5 in order to compensate the variations. The origin of this shift is not clearly understood, except for the drastic change at run labeled 0063\_0} (see Fig. 4.5b) which corresponds to a change in the PMT voltage that was done at this stage of the experiment.

The correction of the time for the interaction position and adjusting the measurement stability of the mean time is not sufficient to measure the time-of-flight of the ions. Indeed an offset needs to be added to the measured time difference to have the proper reference. This offset depends on the cable length between the two membranes that can hardly be measured. Therefore, we used the technique described hereafter. The uranium primary beam was sent through the FRS, with minimal matter and it reacted in a  $700 \text{ mg/cm}^2$  thick beryllium target. Even if the atomic number of the beryllium is low, it can excite the uranium ions and provoke the emission of  $K_\alpha$  X-ray at 94 keV and 98 keV. These are emitted in flight and therefore their energies need to be Doppler corrected with the proper beam velocity. A scan over a range of “realistic” time of flight offsets is performed in order to determine the value that minimizes the width of the X-rays transitions. More details on the Doppler correction and its influence on the width of the transitions can be found in Section 4.3.

The matrix showing the uranium Doppler corrected X-rays energy as a function of the time of flight offset is shown in Fig. 4.6a. The 1000 offsets values are applied to the ToF which ranged from  $31 \cdot 10^{-9}$  to  $60 \cdot 10^{-9}$  s. The velocity  $\beta[i]$ , with  $i \in [0, 999]$ , used for the Doppler correction is calculated according to the following equation:

$$\beta[i] = \frac{Dist}{time_{diff} + i \cdot offset} \quad (4.2)$$

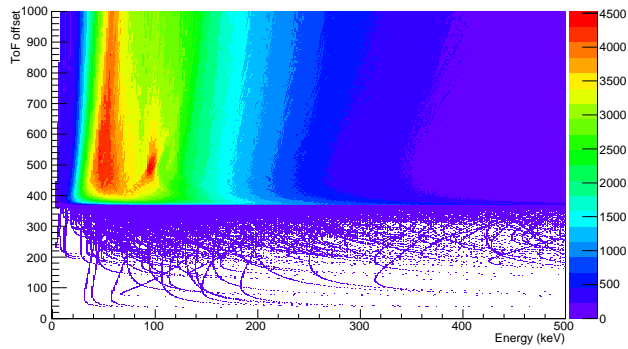
where  $time_{diff}$  is the calibrated time difference between the start and stop membrane of LYCCA (see Equation. 4.1) and  $Dist$  is the distance between the start and the stop membrane given in Annexe 7.1).

The energy projection for the time of flight offset that minimizes the width of the X-rays is presented in Fig. 4.6b. The resolution obtained allows hardly to identify two X-ray transitions as observed during the commissioning experiment [7]. The main source of uncertainty that worsens the resolution comes from the velocity spread in the thick beryllium target.

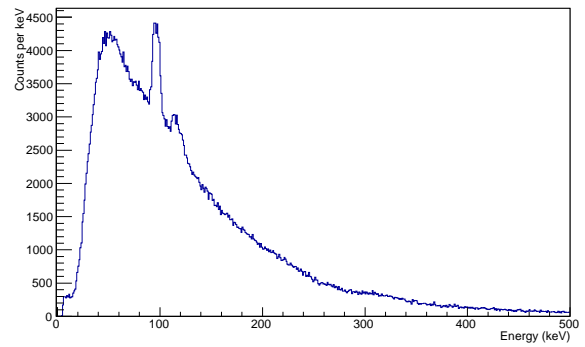
#### 4.2.2 DSSSD modules calibration

DSSSDs are used for both position measurement and energy loss measurement. Both N- and P-side of the DSSSDs are read out and stored in the data flow. The energy calibration can be done in a semi-automatic method. Assuming that the energy deposit measured by the N-side is equal to the one measured by the P-side, it is possible to gain match all the strips with respect to each other and to have all the strips of each DSSSD calibrated. Details of the method can be found in Reference [100]. The result of the calibration for the target DSSSD module and for all modules of the LYCCA wall is shown in Fig. 4.7.

The second step is to gain match all the modules with respect to each other. This is performed using the different fragments passing in a given setting. Indeed, under the assumption that the energy loss inside the DSSSD wall is not

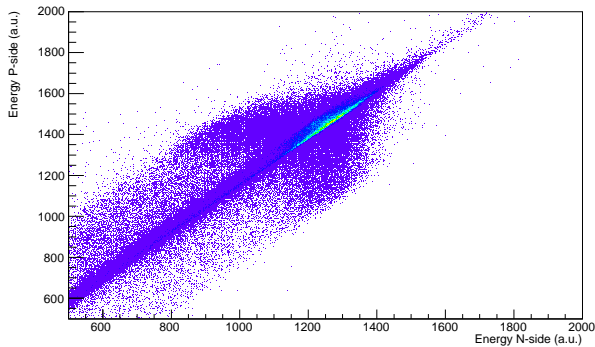


(a) Bi-dimensional histogram of the Doppler corrected energy vs the ToF offsets.

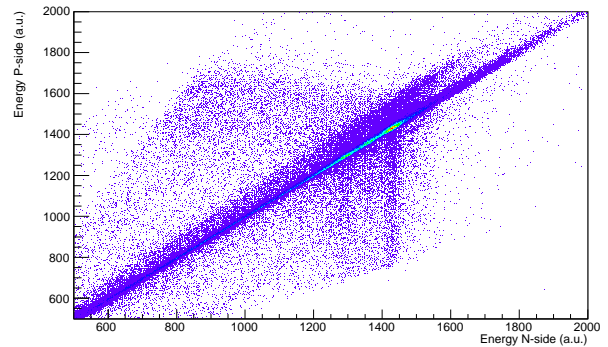


(b) Energy projection for the optimum velocity offset.

**Figure 4.6:** Determination of the Time of Flight offset scanning over a range of offsets ( $y$ -axis of the bi-dimensional histogram). The offset is chosen to be the one minimizing the FWHM of the transitions. The projection for the optimum offset is shown on the right hand side. The two main transitions being the K X rays of uranium are superimposed.



(a) Target DSSSD module.



(b) Wall DSSSD modules.

**Figure 4.7:** Self calibration of both N and P side. The straight line provides an indication of a properly working calibration, with each strip on the N side being gain matched to all the strips of the P-side.

depending on the angle of the particle<sup>2</sup>, the energy deposit by each incoming fragment depends only on its  $Z$ . A limitation of this method is that only the most central modules can be calibrated. The external one do not have enough counts to employ this method. Nevertheless, this aspect has in practice a small impact on the total detection efficiency.

### 4.2.3 CsI(Tl) energy calibration

A good energy resolution for the Total Kinetic Energy (TKE) measurement is needed in order to be able to distinguish masses around 100, which is at the limit of LYCCA capabilities. The calibration is performed using a similar principle as the gain matching method of the DSSSD modules.

In order to determine the gain of the different CsI(Tl) modules, at least two calibration points are needed. Therefore, we use two runs: one with the 700 mg/cm<sup>2</sup> thick beryllium target and the other one without any target. For both runs, we consider different incoming FRS fragments present within the setting, since each fragment deposits a different energy in the CsI(Tl). Thus, we reduced measurement uncertainties. As in the case of the calibration of the DSSSDs, this calibration method is limited by statistics and only central modules coefficients can reliably be calculated.

<sup>2</sup> The angle of the incoming ion inside the detector adds an uncertainty to the energy measurement. For small angle, the error on the energy measurement is well below the energy resolution of the DSSSD thus, the 2 mm thickness of the DSSSD does not play a role.

#### 4.2.4 Absolute energy calibration of the LYCCA Wall

Once the channels of the CsI(Tl) and DSSSD detectors are gain matched, it is possible to obtain an absolute energy calibration for both  $E$  and  $\Delta E$ . The LISE++ simulations<sup>3</sup> of the experimental setup provide the total kinetic energy and energy lost at the LYCCA wall for all the species that pass through the secondary target without undergoing fragmentation or nuclear reactions. Two calibration points were obtained combining both empty target and beryllium target run. The following equation was obtained for the energy loss calibration:

$$\Delta E = Strip_N \times 0.719 - 650 \text{ (MeV)}, \quad (4.3)$$

where  $Strip_N$  is the N-side gain matched energy of the strip hit by a particle. The calibration of the energy measured by the CsI(Tl) crystal is given instead by:

$$E(CsI) = CsI_{Raw} \times 11.4 + 11600 \text{ (MeV)}, \quad (4.4)$$

where  $CsI_{Raw}$  is the gain matched energy deposit in the CsI(Tl) module hit by an ion. Adding up the two, we obtain the total kinetic energy deposit by the ion inside the LYCCA Wall:

$$TKE = \Delta E + E(CsI) \text{ (MeV)}. \quad (4.5)$$

These calibration coefficients allow to obtain a TKE-DE identification histogram such as the one shown in Fig. 4.8. The latter is gated on an incoming  $^{109}\text{Tc}$  FRS beam. The central area with higher number of counts in the histogram of Fig. 4.8 corresponds to the FRS beam which kept the same number of protons and neutrons. This area is linked toward the left to a “banana” shape area that corresponds to nuclei with the same number of protons as  $^{109}\text{Tc}$  and with less neutrons. The “banana” area just below corresponds to  $_{42}\text{Mo}$  isotopes.

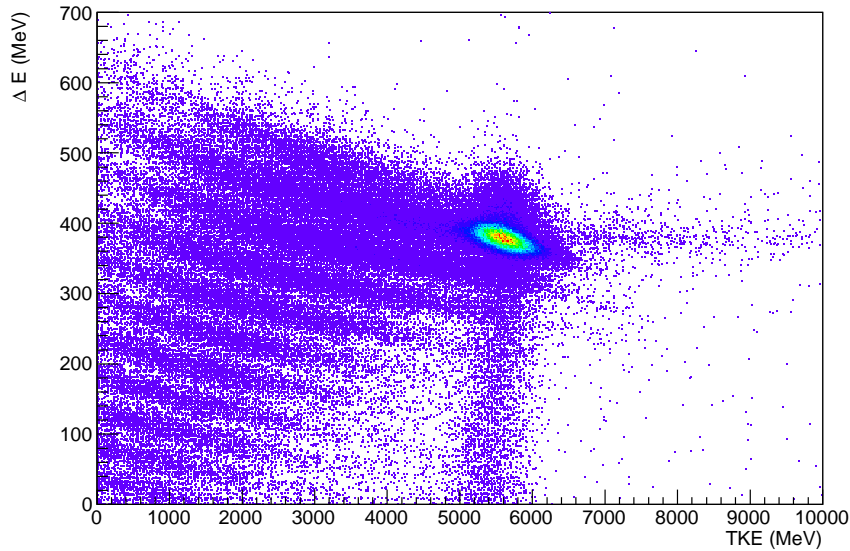


**Figure 4.8:** LYCCA identification histogram obtained after energy calibration of the LYCCA wall. It is produced with a gate on an incoming FRS beam of  $^{109}\text{Tc}$ . The area with most of the statistics, here in yellow-red, corresponds to fragments that passed through the target without undergoing nuclear reactions. The “banana” shape area with a lower energy loss corresponds to proton removal channels.

We have 85% of the overall events hitting the modules labelled 6, 7, 12, 13, 18, 19 (labels are given in Fig. 2.7). These modules are the ones that have a reliable calibration therefore, in the rest of this work, only these six central LYCCA modules are used.

<sup>3</sup> LISE++ is a simulation program [101] that includes beam transport code, reaction mechanisms and energy loss calculations of the beam passing through matter.



---

## 4.2.5 Identification of the fragments in LYCCA

---

The LYCCA calorimeter provides both  $Z$  and  $A$  of the fragments, thus it allows us to determine the reaction channel of the reaction. Nevertheless, even if determination of the proton number is obvious –meaning that we can determine the proton number with a simple bi-dimensional histogram–, the determination of the neutron number required additional treatment of the data. Therefore, in the following paragraph, we detail the procedure developed in order to obtain a neutron number of the fragments.

---

### Determination of the proton number

---

We mentioned in Paragraph 4.2.4 that each “banana” like structure of the  $E - \Delta E$  histogram in Fig. 4.8 corresponds to an isotopic chain.

Projecting the  $E - \Delta E$  histogram along the  $\Delta E$  axis for an energy range of 400 MeV, we obtain the histogram shown in Fig. 4.9. This procedure allows us to estimate the  $Z$  resolution obtained in our experiment as:

$$\frac{\Delta Z}{Z} = 0.018. \quad (4.6)$$

This value is without correction of the velocity dependence and therefore it is an upper limit. Anyway, it is comparable to the  $Z$  resolution  $\frac{\Delta Z}{Z} \leq 0.015$  ( $Z \leq 36$ ) obtained during the LYCCA commissioning [5].

To conclude, we have an unambiguous proton-number determination for  $Z \sim 40$ .

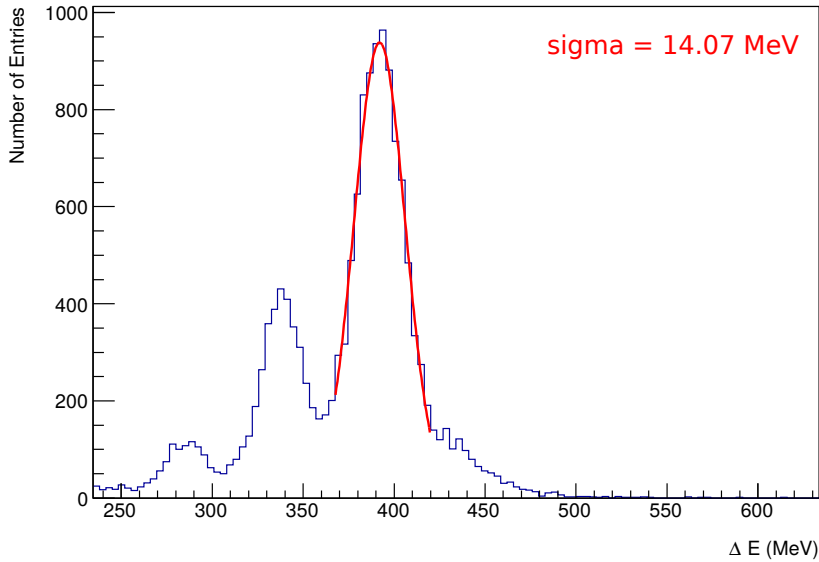


**Figure 4.9:**  $Z$  identification of the fragments with LYCCA. This histogram is a projection of the bi-dimensional histogram shown in Fig. 4.8 for an CsI(Tl) energy range of 4600 to 5000 MeV.

---

### Determination of the neutron number

---

For nuclei lighter than the one produced in this experiment, it is possible to obtain a mass identification of the fragments with the LYCCA calorimeter. For example, the PreSPEC-AGATA commissioning experiment identified the masses of  $^{78,80}\text{Kr}$  and  $^{74}\text{Se}$  [7]. Nevertheless, the mass resolution achieved in this experiment is not sufficient to clearly distinguish mass around  $A \sim 100$ . Therefore, we have to use an indirect method to find the mass number of the fragments.

The relation between the mass  $A$ , the velocity  $\beta$  and the total kinetic energy  $TKE$  of the fragment is defined by:

$$A \propto Mass_{au} = (TKE + K) \times \frac{\sqrt{1 - \beta^2}}{1 - \sqrt{1 - \beta^2}}, \quad (4.7)$$

with  $K$  being an offset to be determined. The simulation from M.J. Taylor [102] shows a linear dependence between the total kinetic energy and velocity of the fragments. Therefore, we determine our offset  $K$  such that the  $Mass_{au}$  variable is independent of  $\beta$  and  $TKE$ .

In order to determine the mass precisely, we need to look at the  $\gamma$ -ray transitions. We scan all the possible masses until we observe the  $\gamma$ -ray transitions, that we assign to the different molybdenum isotopes. The histograms of the observed  $\gamma$ -ray transitions for several mass selection, thus molybdenum isotopes, are shown in Fig. 4.10. In order to optimize the peak-to-total, we plot the histogram under two conditions. First, only  $\gamma$ -ray events within 30 ns after the passage of the ions are considered. Second, a  $\gamma$ -ray multiplicity condition is applied to select events with a maximum of four germanium crystals that triggers. Additional details on the “optimal” conditions can be found in Paragraph 4.5.

The energy of the centroids are reported in the fifth column of Table 4.2. They are similar to the rest energy given in the third column of the same table.

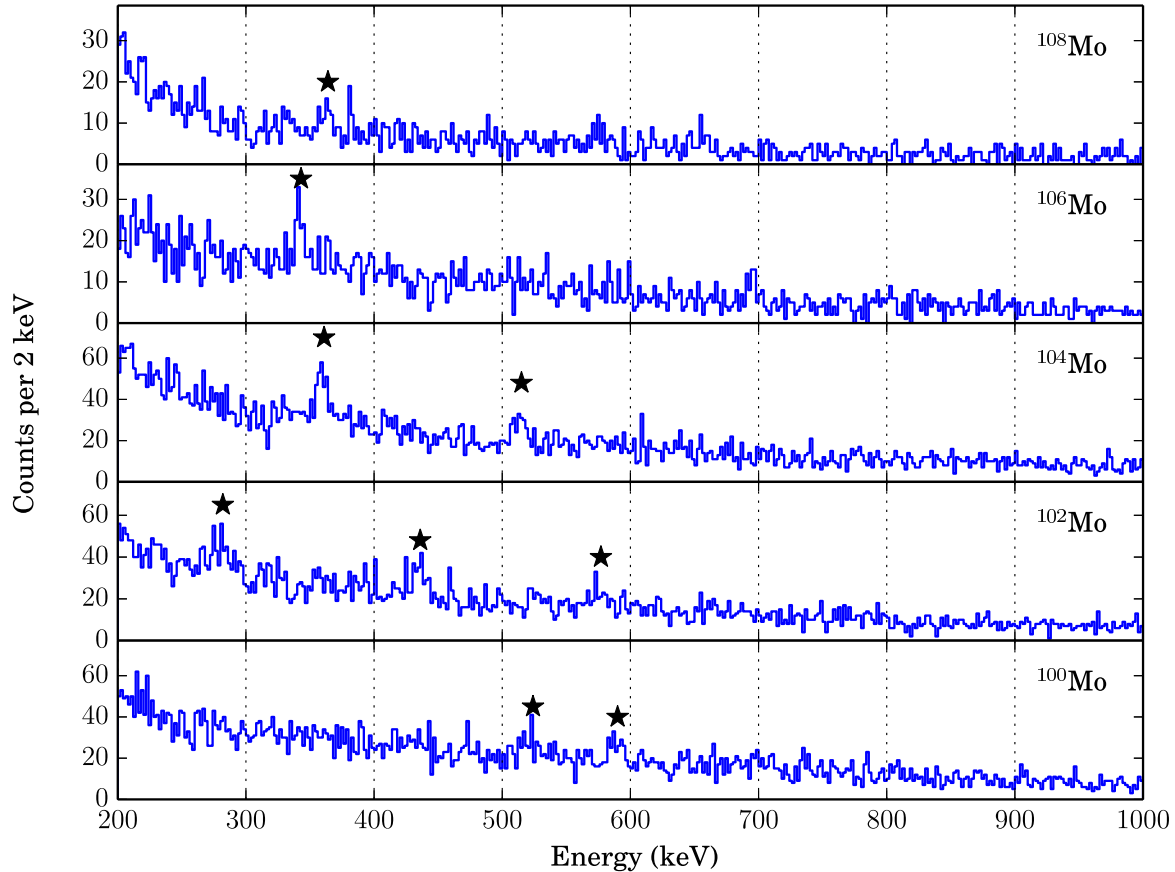


**Figure 4.10:** List of the  $\gamma$ -ray transitions that are observed inside the Mo isotopic chain. From top to bottom, the  $\gamma$ -ray spectra associated with the even-even nuclei from  $^{108}\text{Mo}$  to  $^{100}\text{Mo}$ . The observed transitions are indicated by stars. In addition to a mass selection, a 30 ns gate on the particle-gamma time is applied together with a multiplicity condition (a maximum number of four germanium detectors triggered).

Even if the observed transition energies are close to the rest energies, we need to assess that the observed  $\gamma$ -ray decays correspond indeed to the assigned molybdenum isotopes and not, e.g., to the even-odd molybdenum isotopes. Thus, we provide the following justifications:

- The  $4_1^+$  to  $2_1^+$  transition energies of  $^{108}\text{Mo}$ ,  $^{106}\text{Mo}$  and  $^{104}\text{Mo}$  are separated by more than 15 keV, which is enough<sup>4</sup> to distinguish them by the  $\gamma$ -ray energy for the three isotopes.
- For the  $^{106,104,102}\text{Mo}$  nuclei, the  $4_1^+$  to  $2_1^+$  transitions are observed with a systematic energy shift of  $\sim 10$  keV and we expect a shift due to the lifetime as it will be demonstrated in Section 5.

<sup>4</sup> We expect in an optimum case an energy resolution after Doppler correction of 5 to 10 keV at FWHM (Paragraph 4.3.5).

**Table 4.2:** Summary of the transition energies in the nuclei populated in the experiment. In addition to the adopted energies and lifetimes [33], we report in this table the energies of the observed transitions that are used to confirm our isotope identification.

Nucleus	Transition	Tabulated energy (keV) [33]	Half-life (ns)	Observed energy (keV)
$^{108}\text{Mo}$	$2_1^+ \rightarrow 0_1^+$	192.7	500	–
	$4_1^+ \rightarrow 2_1^+$	370.9	?	364
	$6_1^+ \rightarrow 4_1^+$	527.0	?	–
	$8_1^+ \rightarrow 6_1^+$	662.0	?	–
$^{106}\text{Mo}$	$2_1^+ \rightarrow 0_1^+$	170.5	1250	–
	$4_1^+ \rightarrow 2_1^+$	350.7	25.4	343
	$6_1^+ \rightarrow 4_1^+$	511.2	4.2	–
	$8_1^+ \rightarrow 6_1^+$	654.9	1.77	–
$^{104}\text{Mo}$	$2_1^+ \rightarrow 0_1^+$	192.2	970	–
	$4_1^+ \rightarrow 2_1^+$	368.4	26.1	361
	$6_1^+ \rightarrow 4_1^+$	519.2	4.73	515
	$8_1^+ \rightarrow 6_1^+$	641.7	2.21	–
$^{102}\text{Mo}$	$2_1^+ \rightarrow 0_1^+$	296.6	125	282
	$4_1^+ \rightarrow 2_1^+$	447.1	12.5	436
	$6_1^+ \rightarrow 4_1^+$	584.2	?	577
	$8_1^+ \rightarrow 6_1^+$	690.9	1.8	–
$^{100}\text{Mo}$	$2_1^+ \rightarrow 0_1^+$	535.6	12.6	524
	$4_1^+ \rightarrow 2_1^+$	600.5	3.8	590
	$6_1^+ \rightarrow 4_1^+$	711.0	1.20	–
	$8_1^+ \rightarrow 6_1^+$	780.0	0.58	–

- For  $^{102}\text{Mo}$  and  $^{104}\text{Mo}$  isotopes, higher spin states are populated. For example we observe a weak line for the  $6_1^+$  to  $4_1^+$  transition in  $^{104}\text{Mo}$ . This is consistent with the Goldhaber model [103] stating that in fragmentation reactions the attainable angular momentum of the fragments depends on the number of nucleons removed.
- The  $\gamma$ -ray spectra in the lower panel of Fig. 4.10 is assigned to  $^{100}\text{Mo}$ . It is the first lighter nucleus starting from  $^{108}\text{Mo}$  with only a  $2_1^+$  to  $0_1^+$  transition at  $\sim 500$  keV, without any transitions at  $\sim 350$  keV. We observed in the  $\gamma$ -ray spectra of this nucleus higher energies peaks that can be assigned to the energies of  $6_1^+$  to  $4_1^+$  and  $4_1^+$  to  $2_1^+$  transitions.
- The even-odd molybdenum isotopes have a higher number of excited states. Therefore, when an even-odd nucleus is produced in an excited state, it can decay via multiple  $\gamma$ -ray cascades thus, each of the  $\gamma$ -ray transitions has a weak intensity. As a consequence, we do not clearly observe these transitions on top of the radiation background present in the  $\gamma$ -ray spectra.

The observed transitions are required to assign a  $Mass_{au}$  region for each even-even nucleus observed in the experiment. Nevertheless, we need to determine the overlap between too consecutive masses and potentially the contribution of the even-odd nuclei in our  $\gamma$ -ray spectra.

In order to determine the contribution of neighbouring reaction channels in our  $\gamma$ -ray spectra, we define the ratio of the number of observed  $\gamma$ -ray at the energy  $E_0$  over the number of  $\gamma$ -ray observed from<sup>5</sup> 200 to 1000 keV.

If we chose  $E_0$  to match the observed  $\gamma$ -ray transition energy of a nucleus (e.g. 343 keV), we observe an enhancement of the ratio at the  $Mass_{au}$  (corresponding to e.g.  $^{106}\text{Mo}$ ). Since the  $^{106,104,102,100}\text{Mo}$  nuclei have a somehow abundant statistics, the previously defined ratio is plotted as a function of the mass of the fragments in Fig. 4.11. The width of the enhancement yield for a given  $\gamma$ -ray transition provides a measured for the mass gate.

<sup>5</sup> The lower limit of the range is chosen to reduce the contribution of atomic radiation (beam induced background). The upper limit is set to include all the observed transitions.

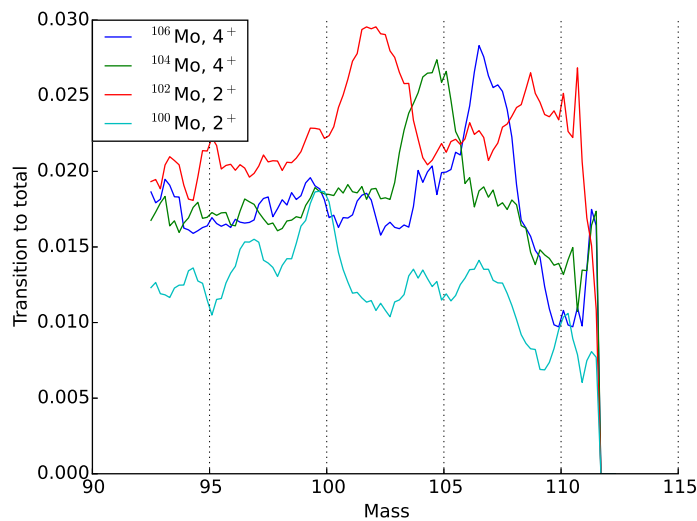


**Figure 4.11:** Calibration of the mass in the LYCCA calorimeter. The  $y$  axis is the ratio of the number of counts inside an energy range over the total number of  $\gamma$ -rays observed in the spectrum. The energy range is chosen according to the energy of the observed  $\gamma$ -ray transition. In the plot, each line corresponds to a different  $\gamma$ -ray energy. The color code is given in the plot insert. The ratio is enhanced for the nucleus with the selected transition.

---

### 4.3 Target positioning with the uranium X rays

---

Despite that the target position was measured using a laser before the experiment, uncertainties persist. The actual position of the target might be slightly shifted with respect to the measured position. However, Doppler shifts are significantly large when doing experiments with relativistic beams, especially when measuring  $\gamma$ -ray transitions. Therefore it is critical to know the target position as precisely as possible and it is important to understand and characterize the position uncertainties. In the following, we develop a procedure that uses the two K- $\alpha$  x-rays of the uranium primary beam in order to calibrate the target position. The reason to use the primary beam is that the atomic radiations have a larger production cross section compared to nuclear reactions and it allows to perform this calibration using only a few minutes of beam time.

The calibration we designed is based on a 1D model that considers two Gaussian features on top of an exponential continuum in the X-Ray spectrum. In addition, we also include a third feature to model the noise from contaminants. Given the importance of the calibration uncertainties in our experiment, we moved away from the traditional techniques and switched to Bayesian analysis which states the calibration in terms of probabilities. Thus, we fit this multi-component model to the data from the calibration phase using a Markov-Chain Monte-Carlo (MCMC) technique.

In this section, I detail the model and explain the origin of its different components. Then I present the fitting technique, which produce the final calibration as well as its uncertainties. However, I first need to introduce briefly the Bayesian analysis background needed to understand the fitting technique.

---

#### 4.3.1 Bayesian approach to fitting a model

---

To avoid further confusion, we adopt some conventional definitions and terminology throughout this chapter.

We call “data” anything that refers to what we want to describe with a model. This can be for instance number of counts per unit of energy measured under a given angle by the AGATA detectors. In particular, we refer mostly to measurements associated with uncertainties. Moreover, one must keep in mind that any measurement only represents one realisation of the true underlying physics. In other words, what we measure is a noisy view of an intrinsic property, which could sometimes be far from the expected average.

However, we want to understand and characterize the physics itself from whatever dataset we can get. This paradigm is the origin of the Bayesian inference.

---

#### Bayesian Principle

---

The Bayes principle (first reference in 1763 [104]) expresses the probability of a *Model* given some *Data*, by relating it to the probability that the same *Data* can be generated from this *Model* and some *prior* knowledge about the model of interest. This translates into the commonly used equation of conditional probability (or Bayes’ theorem):

$$p(\text{Model} | \text{Data}) = p(\text{Data} | \text{Model}) \frac{p(\text{Model})}{p(\text{Data})}, \quad (4.8)$$

where  $p(\text{Data} | \text{Model})$  is called the *likelihood* of *Data*.  $p(\text{Model})$  is called the *prior* probability distribution of the model, which encodes our beliefs in the originate from the model (for instance one parameter must be within a given range of values).  $p(\text{Data})$  is called the evidence, which strictly encodes the belief in *Data*.  $p(\text{data})$  is often considered as a “simple” normalization factor that we can explicit by:

$$Z = \int p(\text{Model} | \text{Data}) d\text{Model}. \quad (4.9)$$

Finally,  $p(\text{Model} | \text{Data})$  is called the *posterior* probability distribution function (PDF) of the model given the data. It reflects the inference that we make on the model given a set of data.

---

#### Likelihood definition

---

In the context of our calibration problem, we need to define our likelihood function  $p(\text{Data} | \text{Model})$ . We consider a uni dimensional model<sup>6</sup> from a mixture of 3 Gaussian features – two transitions of interest and a contaminant corresponding to an unknown process<sup>7</sup> – and an exponential continuum in the X-ray spectrum. This model is parametric, so we can

---

<sup>6</sup> We consider only the Doppler corrected energy detected over all angle as a variable.

<sup>7</sup> The model we construct here is generic, therefore a  $\gamma$ -ray transition from an unknown physics process is treated in the same way as a transition with known physics origin.

explicit its notation as  $Model(\vec{E}; \vec{\Pi})$ , where  $\vec{E}$  is for this study the set of energies at which we evaluate the model and  $\vec{\Pi}$  a set of parameters for the model. We detail the model itself in Section 4.3.2.

The Likelihood  $p(Data(E)|Model(E, \vec{\Pi}))$  quantify the similarity between  $Data$  and the model predictions, given the parameters  $\vec{\Pi}$ . Hence the best set of parameters for this particular model is the set  $\vec{\Pi}$  for which the likelihood is maximum. Implicitly, this supposes a notion of distance between the observed X-ray spectrum and the spectrum predicted from the model (given a set of parameters). Although there are many possibilities to define our “distance” metric in general, we must consider the statistical properties of an observed spectrum to best compare with our model.

A spectrum is a series of discrete events, *i.e.*, a captured photon in the detector, for a given energy. In our spectrum, the probability to record an event at a given energy is independent of the energy of the previously measured events. Therefore, the probability to measure an event at a given energy follows a Poisson statistics. We recall that in the calibration phase, we measured atomic transitions, which means that the number of events, or counts, per bin of energy is important. Therefore, we can approximate the Poisson distribution of counts in an energy range as being Gaussian<sup>8</sup>.

Thus, once we have a model that predicts the counts of transitions at an energy  $E$ , the Likelihood function is expressed as a Gaussian distribution<sup>9</sup>. We note the observed counts at an energy  $E$ ,  $N_{obs}(E)$  and the model prediction at this energy  $N_{pred}(E, \vec{\Pi})$ :

$$p(N_{obs}(E) | N_{pred}(E, \vec{\Pi})) = \frac{1}{\sqrt{2\pi N_{pred}(E, \vec{\Pi})}} \exp\left(-\frac{1}{2} \frac{(N_{obs}(E) - N_{pred}(E, \vec{\Pi}))^2}{N_{pred}(E, \vec{\Pi})}\right). \quad (4.10)$$

Finally, we can estimate the posterior PDF of the model from Equations 4.8 and 4.9, more specifically  $p(\vec{\Pi}|N_{obs})$ , the posterior PDF of the parameters of our model,  $\vec{\Pi}$ , to describe an observed spectrum. Exploring the values of  $\vec{\Pi}$  allows us to find the best set  $\vec{\Pi}_{best}$  to calibrate our experiment properly. In addition, if one can fully characterize this posterior PDF, one can fully characterize the uncertainties of the calibration. In Section 4.3.3, we describe the method we used to explore the parameter space and to construct the posterior PDF of  $\vec{\Pi}$ . We first explicit our model in the following section.

---

### 4.3.2 One dimensional Model

---

Before describing the different parts of the model, we need to explain the origin and the problem we want to solve. The uranium primary beam impinged on a 700 mg/cm<sup>2</sup> thick beryllium target at around half the velocity of the light. Inside the target, the uranium ions get excited decaying by emission of two X rays at the energy of 94.6 and 98.4 keV. The decay occurs in flight and the observed energy in the laboratory referential has a large Doppler shift. For clarity, we remind the Doppler shift equation:

$$E_{Lab} = E_0 \frac{\sqrt{1 - \beta^2}}{1 - \beta \cos(\theta)}, \quad (4.11)$$

where  $E_0$  is the emitted energy in the frame attached to the ion and  $E_{Lab}$  the observed energy in our germanium detector (see Section 2.3). We note  $\beta$  the recoil velocity and  $\theta$  the angle between the recoil ion trajectory and the direction of the emitted X-ray. The angle  $\theta$  is measured experimentally combining positions measured in three detectors: the DSSSD target, the wall DSSSD and AGATA with the PSA algorithm. A schematic view of the problem and the adopted notation is shown in Fig. 4.12.

We determine the interaction position of the beam on the target assuming the distance between the target DSSSD and the target to be small. The angle of the incoming ions (vector  $V_{in}$ ) is small therefore, we assume that the interaction position of the beam in the target  $(x_t, y_t, z_t)$  is the same as the measured position by the target DSSSD  $(x_m, y_m, z_m)$ . This assumption is valid only with the target positioned at the central position of the chamber since the distance between the target DSSSD and the target is  $\sim 5$  cm (see photograph in Fig. 2.10). The direction of the outgoing velocity,  $V_{out}$  is determined with both the target DSSSD and wall DSSSD positions  $(x_w, y_w, z_w)$ . The position of interaction of the  $\gamma$  ray  $(x_a, y_a, z_a)$  is determined with the PSA algorithm. We chose the first interaction hit by selecting the hit in the AGATA crystal with the highest energy deposit.

The  $\gamma$ -ray emission angle  $\theta$  depends on the positions mentioned in this paragraph and an offset in the positioning of the detector leads to a systematic error in the Doppler correction of the  $\gamma$ -ray. This error increases the transition width after Doppler correction. Nevertheless, we can revert the problem and determine the offset of the target position that minimizes the width. This position is in fact the real target position.

---

<sup>8</sup> This is the so called “law of large number”.

<sup>9</sup> A.k.a. Normal distribution.

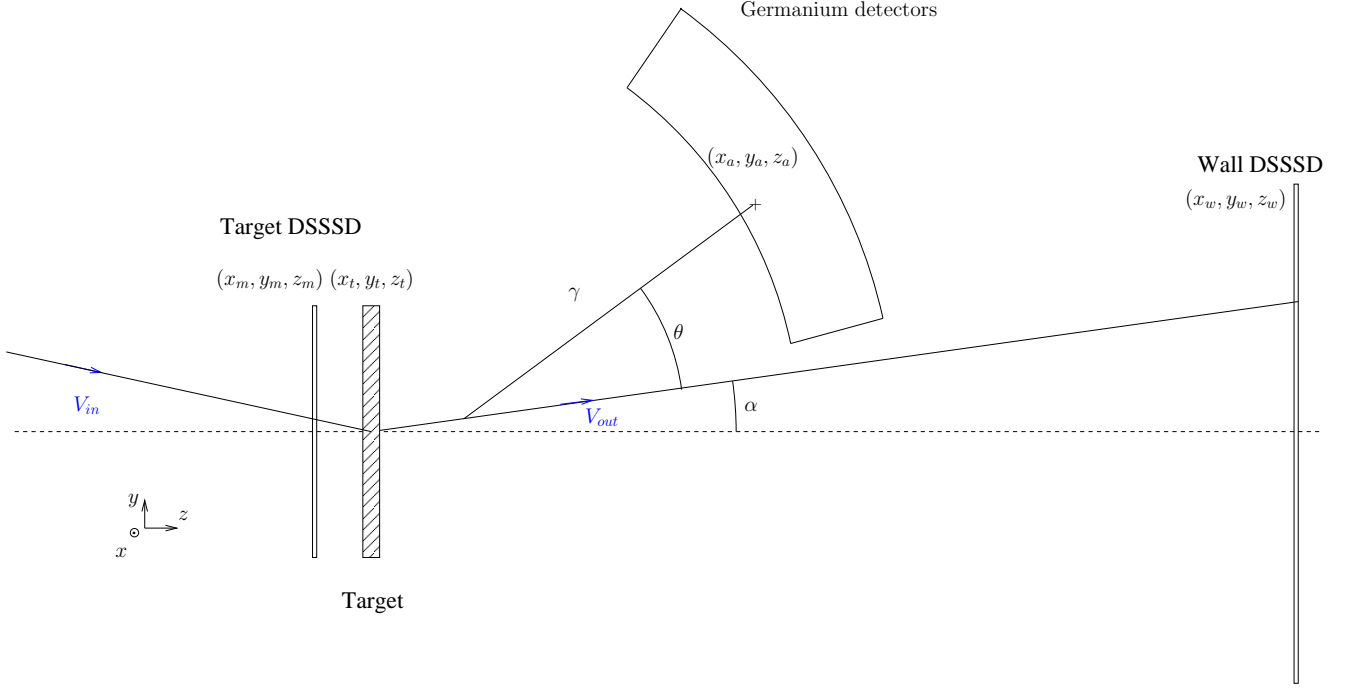


**Figure 4.12:** Geometry definition for the determination of the angle  $\theta$ . We draw on the scheme three detectors from which we extract the position information that we use to determine the angles.

#### Offset consideration

In a first approximation, we consider only the offset in the plane  $(x, y)$  perpendicular to the beam axis. We define a mesh of possible offset with a 1 mm resolution, which corresponds to the resolution achieved to determine the ion position on the target. At each position offset of the mesh, we Doppler correct the X-rays with their re-calculated angle of emissions as explained in the previous paragraph.

#### Formalism for binned data

In the case of in-flight emitted X rays, we measure the energy under a given angle  $\theta_{obs}$ . However, the finite precision of both energy and angle imposes that we bin the measurements, in other words, that we consider the bi-dimensional histogram of the measured energy as a function of the observation angle. The number of counts in a bin is therefore defined as:

$$dN(E_{lab}, \theta_{obs}, \beta),$$

where  $E$  is the energy of the detected photon, observed under an angle  $\theta_{obs}$  and  $\beta = v/c$  the velocity at which the photon is emitted in flight.

We then correct this histogram for Doppler effects. Finally, we obtain a distribution of Energy as function of angles such as the one presented in Fig. 3.7. Similarly to the initial, non-corrected distribution, it is possible to define the corrected number of counts in an energy-angle bin as:

$$dN'(E_0, \theta_{obs}, \beta = v/c),$$

where  $E_0 = f(E_{lab}, \theta_{obs}, \beta)$  is the Doppler-corrected energy, for which the correction function  $f$  is given by Eq. 2.15. At last, the bi-dimensional Doppler-corrected distribution is projected on the energy axis to obtain the energy spectrum of interest:

$$N_{proj}(E'_0, \beta) = \int_{\theta_{obs}} dN'(E'_0, \theta_{obs}, \beta) d\theta_{obs}$$

In this section, we establish our model to describe the energy spectrum we presented above. This model is general and can apply to more than the case of the uranium X-rays.

This model must take into account multiple characteristics of our experiment:

- a set of  $n$  spectral lines corresponding to  $n$  transitions. In the case of the uranium experiment, we only consider  $n = 2$ .
- a spectral continuum or background that comes from the room,
- similarly a continuum component coming with the beam,
- and the instrument response, *i.e.*, the energy efficiency of the array.

The calibration problem usually consists of extracting the energies of the  $n$  transitions of interest. However, the proper treatment must include the other *nuisance* components to fully capture these transitions, especially when the noise is important. At this point, hypotheses which are part of our model have to be chosen. A change in the hypothesis is considered a model change.

### Spectral lines

We first assume that each of the  $n$  transitions generates a Gaussian line in the energy spectrum. Thus, we have three parameters to describe each line: for the  $i$ -th: the count amplitude  $A_i$ , the mean energy  $\mu_i$  and the energy variance  $\sigma_i^2$ . It is defined by:

$$g_i(E; A_i, \mu_i, \sigma_i) = \frac{A_i}{\sqrt{2\pi\sigma_i^2}} \exp\left(-\frac{(E - \mu_i)^2}{2\sigma_i^2}\right) \quad (4.12)$$

with  $E$  the energy, at which the model is evaluated.

### Background continuum

The background in our case represents a source of noise to find our transitions in the spectra. This noise is mostly induced by the beam and we can model this component with a unique exponential decay function:

$$noise(E) = A \cdot \lambda \exp(-\lambda E), \quad (4.13)$$

with  $A$  the amplitude and  $\lambda$  the decay parameter.

In principle, we should also account for the continuum generated by the room background. However, the room continuum is low in comparison with the beam, because the measurements are performed using coincidence technique (described in Section 3.4.2). Therefore, it is valid to neglect the room as an independent source of noise and consider a single component from the beam.

### Mixture model

Once we have defined the transition features and the noise, we can combine the different components, as the sum of all the transitions on top of the continuum:

$$M(E; \Pi) = \sum_{i=1}^n g_i(E; E_i, \sigma_i, A_i) + noise(E; A, \lambda), \quad (4.14)$$

where  $\Pi$  is the vector of all the parameters:  $\Pi = \{(E_i, \sigma_i, A_i)\}_{i \in [1..n]} + (A, \lambda)$ .

### Instrument response

We do not account for the detector response (efficiency) in this present model. The extra calibration step to the detector should account for most of the effects. The residual effects should only affect the relative amplitudes of the transition lines but we do not expect strong impact on finding their centroids and widths.



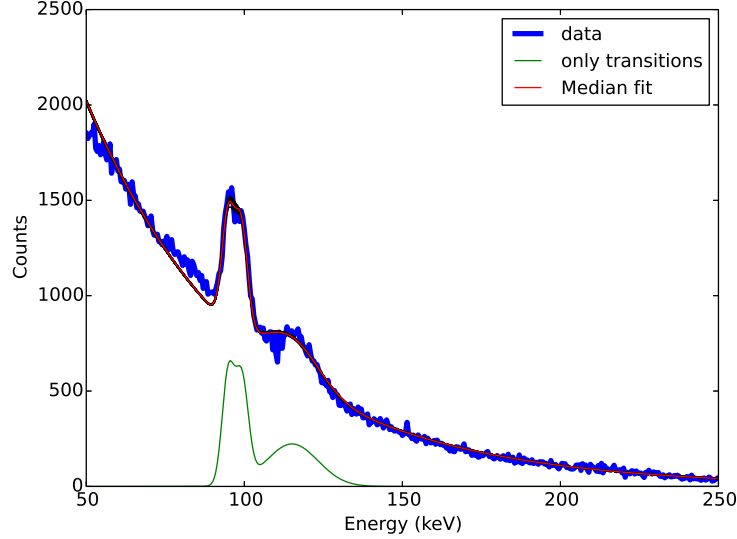


**Figure 4.13:** Doppler corrected histogram of the uranium X-ray transitions is plotted in the figure together with the fit. The blue curve is the observed dataset, while the red line indicates our “best-fit” model. The green curve shows only the transition components of our model.

#### Bayesian Priors

The model we built above is very general and thus can apply to X-ray transitions as well as to  $\gamma$ -ray transition. However, we must focus on the uranium case that we study to define explicitly our priors required in equations 4.8. From the literature, the two K- $\alpha$  X-rays energies of uranium have energies of 94.6 and 98.4 keV, respectively.

Figure 4.13 shows the energy spectrum (Doppler corrected) of the uranium X-rays. The two X-ray transitions are superposing to each other and generate the feature visible below 100 keV. We observe on this spectrum a second transition-like feature at an energy of  $\sim 115$  keV. This energy is too high to be X-rays of uranium emitted in the target. There are two possible explanations to generate this feature. The first one would be electronic-radiative-capture (REC) [105], but only simulations could confirm this hypothesis [106]. A second possible explanation would be X-rays emitted from the uranium beam before the target thus, produced in the target DSSSD or in the start plastic. The feature lies at different energies than expected for the uranium radiations as we assumed all particles emitted within the target during the Doppler correction phase. The energy of this secondary feature in Figure 4.13 would correspond to uranium emissions 10 cm before the target. This position matches with previously mentioned detectors: *Start target ToF*. Because this is not a feature of interest, hereafter, we refer to it as unknown transition.

From the above discussion, we can surely fix the number of transitions of interests to two and the addition of one unknown transition, so that a total of  $n = 3$  transitions is in our model. Even if we have strong expectations on the energy of these features, we do not impose a strict value and instead let them free in our model. In particular, the values we can infer during the fitting procedure provide a good validation of our method if the energies we infer agree. However, we impose that the first two transition lines must be at least 3 keV apart from each. We add this condition in order to constrain the fit procedure to take into account two transitions instead a single wider transition. In total, we have 11 parameters in our model.

---

#### 4.3.3 MCMC minimization procedure

---

At this stage of the discussion, we have defined all the equations and formalism to address our problem. Nevertheless, we still need a procedure to explore the 11 dimensional parameter space. The method we adopted here is based on Markov Chain Monte-Carlo (MCMC) techniques [107].

We sample our parameter space with a large (compare to the dimension of the parameter space) number of chains [107]. A chain is, in a simplistic view a succession of points belonging to the parameter space. One chain is exploring the parameter space based on Markov chain principle, *i.e.*, the choice of one point of the chain depends only on the posterior probability (define in Equation 4.8) of the previously calculated point of the chain.

The MCMC implementation chosen in the analysis is the one from Foreman-Mackey et al. [108]. Within this implementation, the convergence is assured with a few simple checks described in Annexe 7.5.

#### 4.3.4 Result on the target position

With the MCMC method, we determine at each point of the mesh, the optimum set of parameters  $\Pi$  and therefore optimum width of the two X-ray transitions. The plot of the width of the transition as a function of the offset in both  $x$  and  $y$  direction is shown in Fig. 4.14.

The product of the transition width is minimum at a position offset of  $(x, y) = (-1, -4)$  mm. The curve in red in Fig. 4.13 corresponds to our model evaluated for the median value of our set of parameters  $\bar{\Pi}$ , with the optimum target offset.

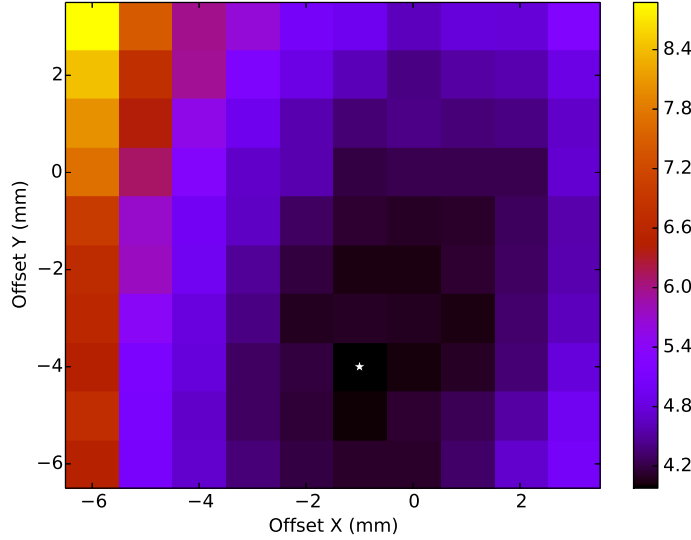


**Figure 4.14:** Each  $(x, y)$  bin corresponds to an offset applied to the measured target position. We weight each bin by the product of the two X-ray median widths. The white star highlights the minimum obtained in an offset  $(x, y) = (-1, -4)$  mm. The X-Ray median widths are indicated by the color bar on the right-hand side.

The width of the transition determined from a fit has uncertainties and the result on the position offset is reliable only if the width of the transitions are determined with good precisions. The bi-dimensional histogram with a 1 mm spacing is projected over both  $x$  and  $y$  axis for the minimum value of the product of the width of the two transitions. Figure 4.15 shows the result of this projection, with symmetric error-bar at the FWHM. At each point of the mesh, we have low statistical fluctuation (with small error). Therefore we conclude that our result is valid.

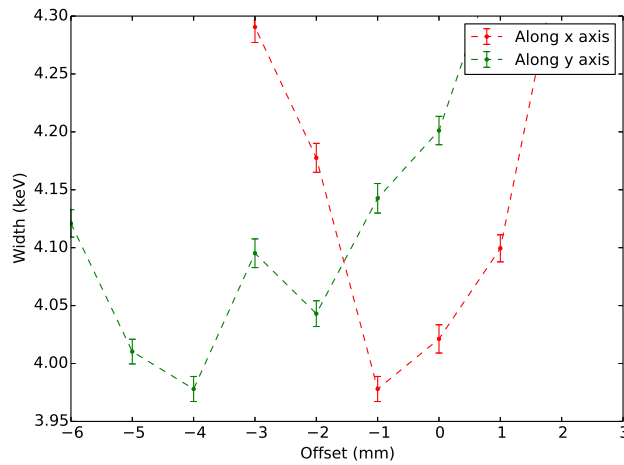


**Figure 4.15:** Projection of the bi-dimensional histogram shown in Fig. 4.14 for the minimum width of the two K X-rays of uranium along the  $x$  and  $y$  offset. The symmetric error-bar shown here are given at FWHM.

---

### 4.3.5 Conclusion

---

The model we describe in this section, along with the introduction of a Bayesian data analysis technique allows us to determine the optimum target position for the PreSPEC-AGATA experiment. This newly determined position improves the energy resolution obtained after Doppler correction. Indeed the width of the 94.6 keV X-ray transition pass from  $\sigma = 1.99_{-0.09}^{+0.10}$  keV for the measured target position to  $\sigma = 1.92_{-0.08}^{+0.09}$  keV after the target shift<sup>10</sup>.

The thick target (700 mg/cm<sup>2</sup> beryllium) implies a large velocity spread therefore, a substantial Doppler broadening. It becomes necessary to include the latter into the model. Moreover, we need to consider the angle of emission of the X-rays to further increase the precision and accuracy of the calibration.

The model is applied only to determine an offset in the  $(x, y)$  plane, but could be also used to determine a potential offset along the beam axis  $z$ . Moreover, instead of considering the projection over all the measurement angles, we could perform a bi-dimensional fit, which would further increase our sensitivity. At last, this model could be further improved in order to include the target position offset within our model. In such case, we would not be limited by our mesh and would in addition obtain the correlation between the  $x$  and  $y$  offset<sup>11</sup>.

---

<sup>10</sup> The error on the width values are given by the 16th and 84th percentile.

<sup>11</sup> This method was not chosen in this work since it require a lot of power computing time.

---

## 4.4 AGATA data analysis

---

In this section, the different calibration steps and corrections that are needed to optimize the performance of the AGATA array are presented. The energy calibration procedure of the segments and of the traces and the effect of a cross-talk correction is highlighted in Paragraph 4.4.1.

The time calibration procedure is presented in Paragraph 4.4.2. The strategy performed to obtain an optimum time resolution for the particle- $\gamma$  time is explained in Paragraph 4.4.3.

All these steps are essential in order to reduce uncertainties on the position determination of the  $\gamma$ -ray hits inside the detectors by the PSA. The gain on the position resolution is hard to quantify, but some visible effects are presented in Section 4.4.4. In Paragraph 4.4.5, the PSA capacity is highlighted together with a comparison of the energy resolution we obtained after re-calibration of the AGATA detectors. At last, in Paragraph 4.4.6, we discuss the possibilities to use the tracking algorithm for this experiment.

---

### 4.4.1 Energy calibration of AGATA detectors

---

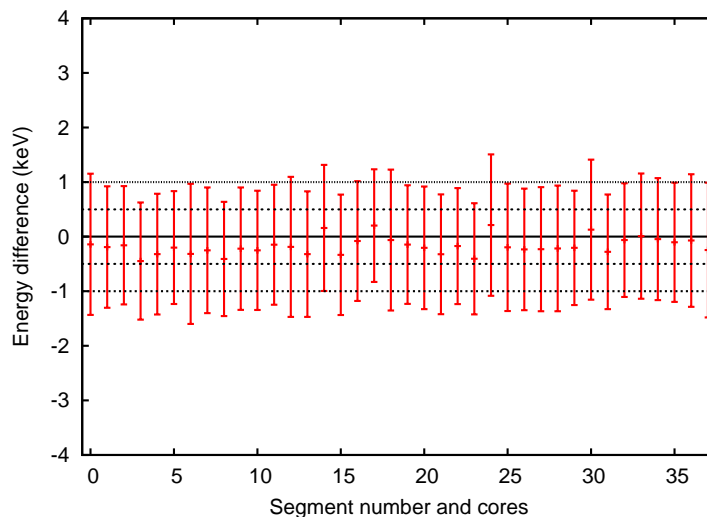


**Figure 4.16:** The channels 36 and 37 of the  $x$  axis correspond respectively to high and low gain of the central contact. The channels 0 to 35 of the  $x$  axis are the segments. The  $y$  axis is the energy difference between the measured energy of the 1332.5 keV transition of  $^{60}\text{Co}$  and the tabulated value. The dotted lines indicate a shift of 0.5 keV, the full one a shift of 1 keV. The error bars correspond to the energy resolution of the segment (or central contact) at FWHM. This figure is for detector 06A.

The energy calibration has two impacts on the quality of the final result: the lifetime of a transition. The first impact of a precise energy calibration is an energy resolution that is minimal thus optimum. The other impact is on the  $\gamma$ -ray position resolution computed by the PSA algorithm which relies on the energy calibration of the traces. The position resolution of the first  $\gamma$ -ray interaction point inside the germanium detector impacts the Doppler correction and as a consequence the shape of the transition used for the lifetime determination of the transition. Thus, for the experiment presented in this work, it is essential to have a precise energy calibration over the whole experiment.

The energy calibration of the AGATA detectors is performed with an automatic procedure that uses a peak-search algorithm and Gaussian fits [109]. A cobalt ( $^{60}\text{Co}$ ) source emits two  $\gamma$ -rays with energies of 1173.2 keV and 1332.5 keV. The two  $\gamma$  rays of this source are in the same energy range as the aimed  $\gamma$  ray of the experiment and therefore is used to get a set of 38 calibration coefficients for each detectors. Only the gain (slope) of the energy calibration is used for the amplitude calibration of the traces. The relation between the coefficient to calibrate the trace amplitude and the energy-calibration coefficient is determined with the parameters of the MWD filter of the pre-processing electronic [109].

A detector is considered properly calibrated if the energy of its central contact with high gain matches the energy of the  $^{60}\text{Co}$  lines. A shift of 0.5 keV to 1 keV is acceptable for the segments and should not influence the  $\gamma$ -ray interaction positions determined by the PSA algorithm [110]. The energy of all segments is in any case “forced” to match the central contact energy after PSA algorithm. The on-line calibration coefficients showed some shift between the segment energies and the expected 1332.5 keV line of the  $^{60}\text{Co}$  source bigger than 1 keV for most of the detectors. Therefore, a recalibration of all the 19 detectors was needed. In Fig. 4.16, the energy shift between one calibrated detector and the 1332.5 keV

$^{60}\text{Co}$   $\gamma$ -ray transition is plotted for all the 36 segments and the two central contacts. This plot shows the result of the calibration and allows to check if the automatic calibration procedure works properly, detector by detector.

In segmented detectors electronic cross talk effects are observed [111, 112] lowering the sum of all segment energies measured as the segment multiplicity increased. Thus, in addition to a good energy calibration, a cross talk correction has to be applied. This correction allows to recover the sum of hit energies when segment multiplicity up to 4-5 occurs and to increase the energy resolution [112]. Its origin can be explained by a capacitive coupling between the core and segments via the bulk of germanium material [4]. In Fig. 4.17, the energy shift between the  $^{60}\text{Co}$  source line at 1332.5 keV and the sum of measured-segment energies is plotted as a function of the segment multiplicity. The red line describes the lowered energy due to cross talk. The green line, labelled “online Xtalk”, corresponds to a cross-talk correction that is not generated for the proper detector<sup>12</sup>. The blue curve is an example of what can be achieved with the cross-talk correction: an energy shift lower than  $\sim 1$  keV for a segment multiplicity four.

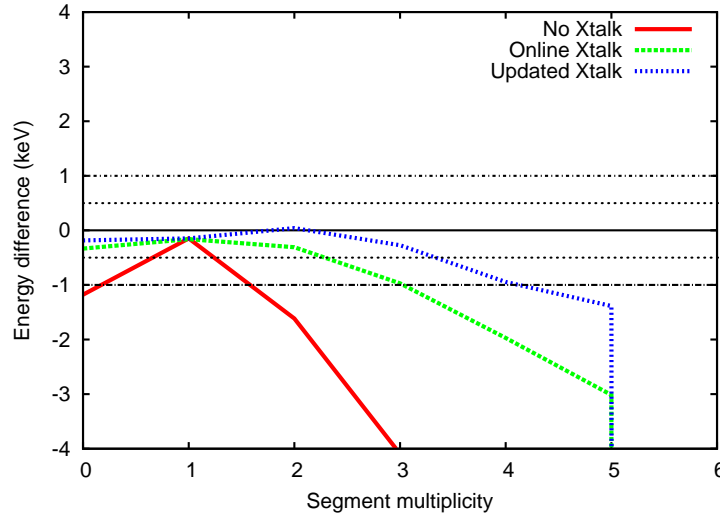


**Figure 4.17:** Cross talk influence and correction for detector 01C. Segment multiplicity labelled 0 on the  $x$  axis corresponds to the sum of all multiplicities. The energy of the sum of the segment energies is compared to the expected energy of 1332.5 keV.

Some of the AGATA detectors may have missing, broken or unstable segments. A broken segment means that the charge is not collected e.g. due to a broken cable between the segment and the pre-amplifier. The charges are in that particular case collected by neighbouring segments. In this case, the segment is missing in the data flow. A possible explanation is a faulty connection between the crystal pre-amplifier and the digitizer. An unstable segment provides an energy signal, but its gain shifts in time. If only one segment is having an issue, it can generally be recovered, or removed with minor impact on the PSA algorithm [110].

In the experiment described in the present work, detector 14B has a missing segment. In this particular case, the cross-talk matrix is generated assuming that the missing energy of the sum of segment energies should be equal to the one measured by the core. More details on the procedure can be found in [61]. Detectors 7C and 13A have one broken segment. Therefore, the cross-talk coefficients are generated accordingly, but the broken segment energy is not recovered.

Detector 04B is having six segments with unstable gain and therefore is removed for the analysis. Detector 13C has three missing segments, thus is not considered for this work. Detector 14A is not included in the analysis since the energy resolution for the core is larger than 10 keV at FWHM.

To summarize, out of the 19 detectors present inside the setup in 2012, only 16 detectors can be used for proper data analysis. A summary of the detector resolutions is given for the working detectors in Table 4.3.

#### 4.4.2 Time calibration of AGATA detectors

The time of the  $\gamma$ -ray hit is measured with respect to a reference which in AGATA is given by the crystal trigger. The AGATA system is triggered with a leading edge discriminator on the central contact of the crystal. A leading edge is used instead of a constant fraction discriminator (CFD) in order to trigger on small energy events. As a consequence, an energy dependence of the triggering time is observed (walk effect).

<sup>12</sup> This rough cross talk correction was performed during the data taking in 2012. 16 out of the 19 detectors did not have their own cross-talk correction due to lack of time during the experiment preparation.

**Table 4.3:** Energy resolution of the AGATA detectors. Detectors 04B, 13C and 14A are not working properly (see text for details). Therefore their energy resolution are not reported in the table. The crystal ID column corresponds to the position label of the crystal in the AGATA holding structure and it is given in this table for completeness.

Detector	Crystal ID	FWHM of the core (keV)	Average segment FWHM (keV)
00B	1	2.6	2.2
00C	2	2.4	2.1
01B	4	2.3	2.2
01C	5	2.3	2.2
04B	13	—	—
04C	14	2.3	3.3
06A	18	2.4	2.3
06B	19	2.5	2.1
07B	22	2.4	2.7
07C	23	2.7	2.0
12A	36	2.6	2.1
12B	37	2.4	2.7
12C	38	5.0	2.5
13A	39	2.5	2.5
13B	40	2.5	2.1
13C	41	—	—
14A	42	—	—
14B	43	2.5	2.4
14C	44	2.5	2.1

In practice, all the segment and core signals are digitalised and recorded for each trigger. Each recorded pulse shape, or signal trace, consists of 100 samples: 40 before and 60 after the triggering point. Thus, the pulse shape provides a  $1 \mu\text{s}$  snapshot of the charge collection inside the crystal. The time of a segment net charge (or of the core) with respect to the triggering point is obtained with a software CFD applied on the recorded signal trace. A schematic view of the time determination is shown in in Fig. 4.18

The PSA algorithm determines the position of the interaction of the  $\gamma$  ray comparing the pulse shapes of the net charge and transient signals with a database. Inside the database, known interaction positions are assigned to a set of pulse shapes. The PSA comparison is reliable if the time of all the segments are aligned to the core time. This time alignment consist of the first time calibration step performed on the data-set.

We can notice in Fig. 2.15 that the signal of the central contact has a concave shape while the signal of the segment with net charge has a convex shape. Thus, the leading-edge timing of the net charge segment is different than the one on the central contact, the “real”  $\gamma$ -ray time being in between. Therefore, a new time reference [109], called  $TZero$ , is chosen as the sum of the net charge time and the core time. This time provides a better time resolution than the time determined by the leading-edge on the core signal. Nevertheless this required a precise time calibration of the net charge segment signals, thus the first calibration step (time alignment of the segment times to the core time) is crucial for a good time resolution.

In order to obtain the best result, meaning determining the most accurate interaction position, the PSA algorithm tries different time shifts of the traces around the  $TZero$  time reference. As a consequence, this time reference can slightly shift depending on the crystal PSA database. Hence, the crystal time references are aligned to each other after the PSA algorithm. This time alignment is the second time calibration step.

The last time calibration step occurs at the global level where all the crystal data are built together. In a case of  $N$  detectors, a time dispersion matrix  $M$  with dimension  $N \times N$  is built with all pair detectors time. The matrix element of index  $(i, j)$  is defined as:

$$M(i, j) = TZero_i - TZero_j \quad (4.15)$$

with obvious notations. A set of  $N$  time coefficients is obtained minimizing their time dispersion inside the matrix  $M$  [109].

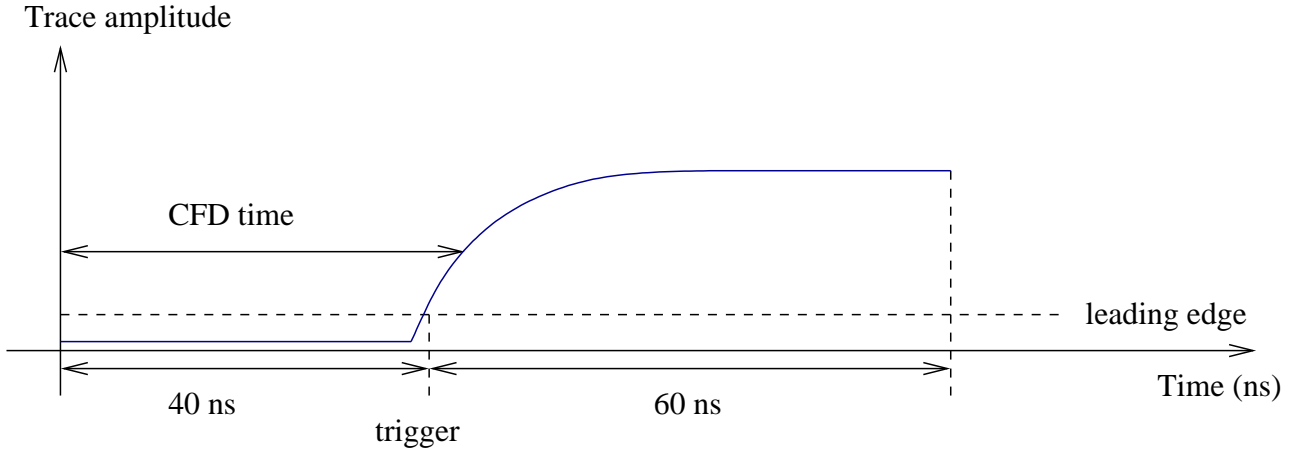


**Figure 4.18:** Schematic view of the timing of traces of a segment net charge or of the core. The leading edge triggers the trace acquisition at the level of the pre-processing electronic. The CFD time is obtained via the AGATA data analysis software (see text for details).

Applied to the triggering time, the  $TZero$  time reference allows to remove the walk effect. This procedure is detailed in the following paragraph. The  $TZero$  is determined by a CFD, therefore it has a better time resolution than the 10 ns time clock of the GTS system.

#### 4.4.3 Optimal particle- $\gamma$ time

The particle- $\gamma$  time used to reduce beam induced background in previous PreSPEC experiments with the RISING array [113, 114] needed a more elaborate treatment in the case of AGATA since it has fully digital electronics. The following paragraph details the procedure that need to be followed in order to get the most precise particle- $\gamma$  time.

The particle- $\gamma$  time  $T_{P-G}$ , *i.e.*, the time between the particle and a  $\gamma$ -ray detected in AGATA, is defined by:

$$T_{P-G} = T_{gamma} - T_{part}, \quad (4.16)$$

where  $T_{gamma}$  is the time of the  $\gamma$  ray detected inside of an AGATA detector and  $T_{part}$  is the time of the particle hitting the last FRS plastic scintillator SC41.

In the setup, there is no direct access to the time of the  $\gamma$  ray, neither to the one of the particle, without using a reference. Therefore, they are relative to the trigger of the acquisition. The trigger time should have been in theory given by the scintillator SC41, which would simplify the analysis. For practical reasons<sup>13</sup>, this is not performed inside the setup. Nevertheless, the time of the trigger is recorded inside a MH-TDC in which the scintillator time signals are also connected. Including the time of the trigger  $T_{trigger}$ , equation 4.16 is expressed as follows:

$$\begin{aligned} T_{P-G} &= (T_{gamma} - T_{trigger}) + (T_{trigger} - T_{part}) \\ &= TimeStampDiff + TimeOfTrigger, \end{aligned} \quad (4.17)$$

The particle time with respect to the trigger, called  $TimeOfTrigger$  can be calculated from the MH-TDC information. The time difference between the  $\gamma$ -ray and the trigger is given by the time-stamp difference ( $TimeStampDiff$ ) of the MBS GTS-partition (see section 3.3.2) and the  $\gamma$ -ray time-stamp present inside the key of the ADF frames [93].

$T_{gamma}$  is measured with a leading edge inside the Pre-Processing electronics as described in section 3.3.1. The signal from the leading edge is used to trigger the readout of the germanium event after validation by the GTS system and the signal time is recorded inside the data flow with a  $TimeStamp$ . The leading edge introduces a time measurement dependant on the energy of the  $\gamma$  ray. It is called walk effect. Nevertheless, the time information contained within the recorded traces is used to correct this walk effect and to improve the time resolution for the particle- $\gamma$  time. The correction is applied to the  $TimeStamp$  according to the following expression:

$$T_{gamma} = TimeStamp + TZero, \quad (4.18)$$

where  $TZero$  is the walk correction determined from the traces. Its calculation is explained in Section 4.4.2.

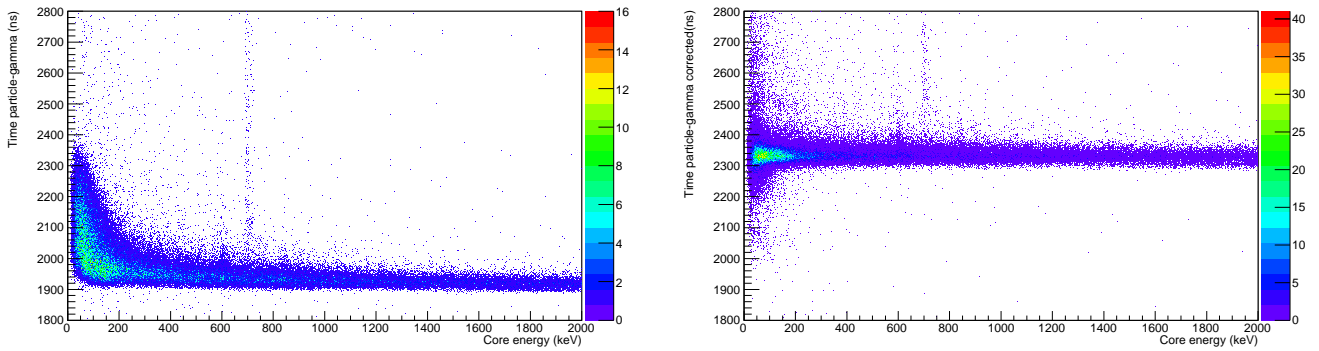
<sup>13</sup> The triggering of the acquisition is performed inside a FPGA (as explained in section 3.4.2) which may have a time jitter in the order of the clock of the FPGA (tens of ns).

The  $TimeStampDiff$  in Eq. 4.17 is now defined as:

$$TimeStampDiff = T_{\gamma} + T_{Zero} - T_{trigger}. \quad (4.19)$$

At the stage of the data analysis, the time calibration performed in paragraph 4.4.2 cannot be improved anymore. Nevertheless, time shifts around 11 ns are observed between the particle- $\gamma$  time of different detectors. A possible reason of this shift comes from the generation of the  $\gamma$  trigger request as explained in 3.4.1. The request is an  $OR$  of all the germanium detectors and is generated with analog electronics where different time constants (e.g. cable length) can be encountered. Thus, a final time shift is applied to the  $T_{P-G}$  time in order to align all the different crystal times with respect to each other.

An illustration of the impact of the walk correction is shown in Fig. 4.19 where bi-dimensional histograms of the particle- $\gamma$  time as a function of the energy of the  $\gamma$  ray are shown with and without walk correction. A 20 ns time shift between 100 and 1000 keV is observed in the histogram in Fig. 4.19a. This time shift gets completely corrected after the walk correction as shown in Fig. 4.19b.



(a) Time-energy histogram without walk correction.

(b) Time-energy histogram with walk correction.

**Figure 4.19:** Effect of the walk correction using the time information extracted from AGATA traces. The two dimensional histograms are time-energy plots. The  $x$  axis corresponds to the energy of the  $\gamma$  ray measured by the central contact, the  $y$  axis is the core time with respect to the particle time.

The time resolution of the AGATA detectors once all corrections are applied, is given in Table 4.4. The average particle- $\gamma$  time resolution at FWHM for all the detectors is 22.42 ns. The value is measured considering energies ranging from 500 keV to 1000 keV, the region of interest of the  $\gamma$ -ray transition of the experiment.

The correction of the walk effect and the precise time alignment of all the detectors allow an accurate time selection of the event and by consequence reduces the number of  $\gamma$  rays coming from beam induced background. The  $\gamma$ -ray energy histogram with a time gate of 30 ns on prompt events (small time value, ranging from 1910 ns to 1940 ns) is compared with the  $\gamma$ -ray energy histogram without time selection in Fig. 4.20. The number of counts in the histogram with time selection for an energy around 600 keV<sup>14</sup> is clearly smaller than the number of counts in the histogram without the time selection.

#### 4.4.4 PSA hit distribution

The hit position in a crystal is determined by the PSA algorithm and it depends on both energy calibration of the traces and on the  $TZero$  alignment of the traces. In principle, the distribution of the hits inside a crystal should be uniform. Nevertheless, it is not possible to fully suppress grouping of the hits inside the crystal as shown in Fig. 4.21. This is not due to a real physics phenomenon, since there is no reason for a  $\gamma$  ray to interact more at some given positions inside a crystal, but it is a wrong position assignment of the PSA algorithm. This wrong position assignment is under investigation by the AGATA collaboration.

The hit distribution inside the first layer or the AGATA crystals as seen from the target position, is shown in Fig. 4.22.

<sup>14</sup> The slow neutrons are captured by  $^{63}\text{Ge}$ . This reaction produces  $^{64}\text{Ge}$  in an excited level that decays with the emission of a  $\gamma$ -ray at an energy of 595.9 keV. The fast neutrons excite  $^{64}\text{Ge}$  and the same  $\gamma$ -ray is observed Doppler shifted. Thus, this decay is observed with a broad energy transition at around 600 keV.



**Table 4.4:** Time resolution of the detectors during the experiment gating from 500 keV to 1000 keV.

Detector	$\sigma$ (ns)	FWHM (ns)
00B	9.34	22.0
00C	9.57	22.5
01B	8.77	20.6
01C	7.81	18.4
04C	8.95	21.1
06A	9.39	22.1
06B	10.8	25.5
07B	9.93	23.4
07C	10.5	24.8
12A	8.83	20.8
12B	9.64	22.7
12C	9.73	22.9
13A	9.96	23.5
13B	9.00	21.2
14B	13.7	32.4
14C	10.2	24.1

---

#### 4.4.5 Influence of the data replay

---

The re-processing of the raw data (trace and energy) allows to improve the calibration of energy and time value and to correct for the cross talk effects. We call the re-processing of the data the “replay”. In addition to an improvement of the calibrations, it provides the possibility to test different replay options, thus to determine which options are the most suitable for the analysis of the experiment. For example, it is possible to deactivate the PSA algorithm and to assign the position of the  $\gamma$  ray to the center of the net charge segment. This option is called “segment center” and provides a quick check of the effects of the PSA algorithm. A second example of data replay option that has been tested in this work is the “pile-up rejection”. Normally, the energy of the core is extracted from the MWD filter in the carrier (see Section 3.3.1 for details). However, an energy value can be computed from the recorded traces (in such a case, the one microsecond trace allows an energy resolution of around eight keV at FWHM) and this should be equivalent to the energy from the electronic MWD filter. If not, the event is recognised as a pile-up and discarded. This method with two different shaping time parameters of the MWD filter is developed in more details in Reference [115].

The impact of the new calibration can be observed on the width of the background transitions for the 16 “properly-working” detectors. This allows the characterisation of the detector resolution improvement. With the “online configuration”, *i.e.*, the calibration coefficient used during the data taking, the width of the 1332.5 keV transition is measured to be 3.19(4) keV at FWHM. In the case of the “optimum calibration coefficient”, *i.e.*, obtained after the work described in this section, the width of the 1332.5 keV transition improved to 3.11(4) keV at FWHM.

Another way to characterise the influence of the data replay is to compare both the number of events of the  $4_1^+$  to  $2_1^+$  transition of a given nucleus and its width. The  $^{104}\text{Mo}$  is chosen here since it has a good statistics (the histograms displayed in Fig. 4.10 provides a hint of the statistics) and the  $4_1^+$  to  $2_1^+$  transition is sharper than the  $2_1^+$  to  $0_1^+$  transition of  $^{102}\text{Mo}$ . Moreover, the 125 ps half-life of the latter influences strongly the shape, as explained in Section 2.5. The plot drawn in Fig. 4.23 highlights the results obtained for the above mentioned data-replay options.

The main effects observed from the data replay and displayed in Fig. 4.23 are:

- The width of the “optimum calibration coefficient” is slightly higher than with the “online calibration coefficient” but due to the large uncertainties, a clear conclusion is not possible. The peak-to-total ratio increases by 2.8% for the “optimum calibration coefficient” with respect to the “online configuration”.
- The width of the transition in the case of “segment center” is 5% higher than for the “optimum calibration coefficient”.
- The “pile-up rejection” condition provide the same width of the transition but we observe a 1.6% increase of the peak-to-total ratio.

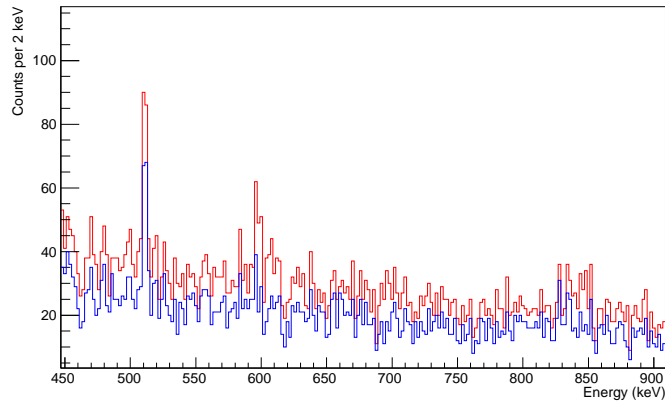


**Figure 4.20:** Influence of the particle- $\gamma$  time selection on the background. The histogram drawn in red has no time selection, the one in blue has a 40 ns time selection.

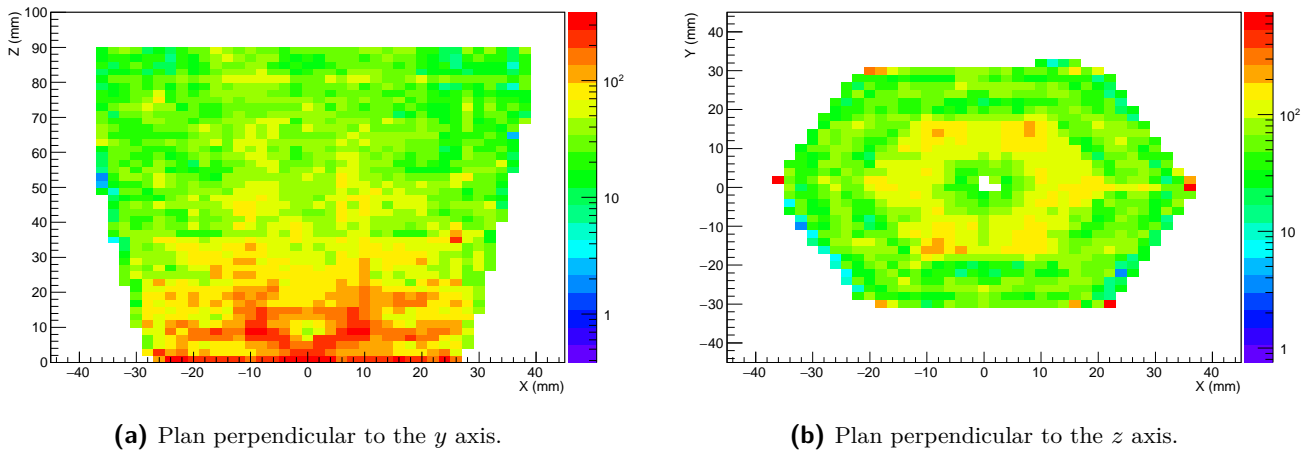


**Figure 4.21:** Hits distribution inside an AGATA crystal. The positions are determined by the PSA algorithm.

From these plots, we conclude that the PSA works as expected, producing a clear improvement of the transition width after Doppler correction. In addition, we assert that the data-replays increased the peak-to-total ratio of the  $4_1^+$  to  $2_1^+$  transition. The impact of the data-replay is more pronounced for higher energy transitions, such as the  $6_1^+$  to  $4_1^+$  transitions of  $^{104}\text{Mo}$  as we clearly see with the “optimum calibration coefficient” case. Last but not least, with an optimized time calibration of the traces, we can apply a 40 ns time selection which impact even more the peak-to-total ratio. We discuss this last point in Paragraph 4.5.

#### 4.4.6 Tracking of the data

The AGATA array power comes not only from its good position resolution but also from its tracking capabilities (see Section 2.3.3). Nevertheless, with the lifetime of the transitions we are looking for, *i.e.*, from a few tenth to hundreds of picoseconds, we need to be cautious.

Indeed, most of the decay of the excited levels of nuclei produced at the secondary target occurs more than 20 ps after the nuclear reaction (see the forth column in Table 4.2 for the lifetime of the excited levels). We have seen in Section 2.5 that the flight pass through the target is  $\sim 25$  ps; therefore, most of the  $\gamma$  rays are emitted after the target. In such case, the position of the emitter is unknown and the tracking assumes it comes from the target. Thus, the  $\gamma$  rays emitted after the target should be rejected by the tracking algorithm<sup>15</sup>. In order to avoid an effect of the tracking algorithm on the lifetime measurement of the excited levels, we do not track the data in the work presented here, but use core energy signals only. We chose the hit with the highest energy deposit as the first interaction hit of the  $\gamma$  ray.

<sup>15</sup> There are plans within the AGATA collaboration to modify the Orsay Forward Tracking algorithm [92] such that the decay position is not assumed at the target levels, but is a parameter that is included in the chi squared test of the tracking algorithm [116].

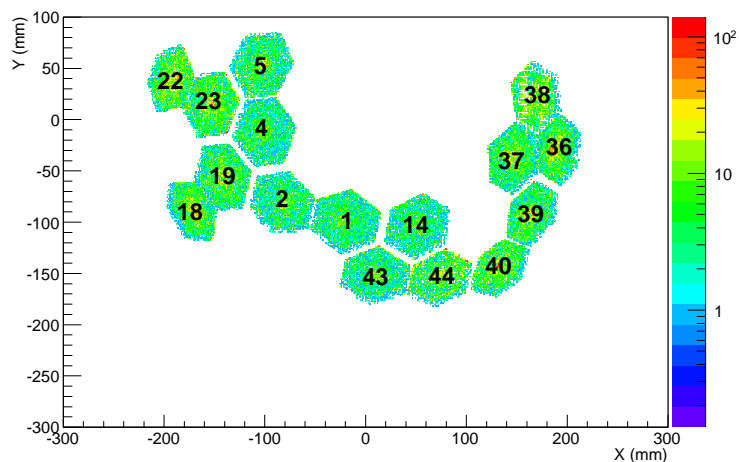
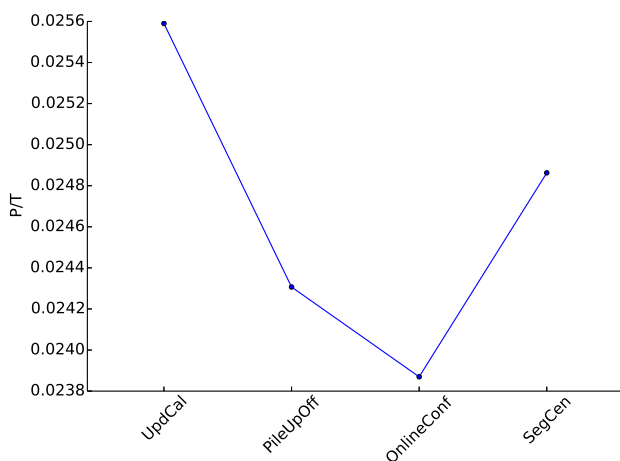
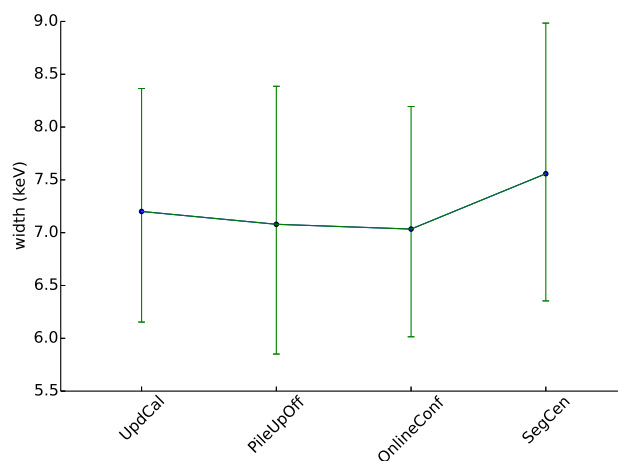


**Figure 4.22:** Hit distribution of the first detector layers view from the target position. The display for all AGATA crystals includes also the label of the crystal identification.



**(a)** Comparison of the Peak-to-Total (P/T).



**(b)** Comparison of the width of a  $\gamma$ -ray transition.

**Figure 4.23:** Results of several AGATA data replays versus the number of counts and the width of the  $4_1^+$  to  $2_1^+$  transition of  $^{104}\text{Mo}$ . The x labels refers to a replay options. “UpdCal”, “OnlineConf”, “SegCen” and “PileUpOff” are associated with “optimum calibration coefficient”, “online configuration”, “segment center” and “no pile-up rejection” respectively. See text for details.

---

## 4.5 Peak-to-total ration optimizations

---

So far, we considered the species from the one proton and some neutron removal of  $^{109}\text{Tc}$ . But the statistics is low for a systematic lifetime analysis. Therefore, in the rest of this work, we use the  $^{107}\text{Nb}$  primary beam FRS setting and select the  $^{108}\text{Mo}$  FRS ions. In the LYCCA calorimeter, we select the neutron removal reaction channel that produces the lighter molybdenum isotopes.

We can mention here that we observed in addition to neutrons removal some deep inelastic reaction of the primary beam that populates the first  $4_1^+$  excited state of  $^{108}\text{Mo}$ . Nevertheless, the  $\gamma$  ray of this transition comes with a large beam-induced background (see Fig. 7.8 in Annexe 7.6).

We saw in Paragraph 4.3.2 the influence that the determination of the target position has on the width of the observed uranium X-rays transitions. Due to the complexity of this experiment, the width, thus the peak-to-total, is influenced by each variable that is needed to Doppler correct our  $\gamma$ -ray transitions. Therefore, we saw how measurement errors influence the resolving power, *i.e.*, the capacity we have to see  $\gamma$ -ray transitions on top of a strong radiative background. In the following paragraphs, the influence of applied “gates”, *i.e.*, conditions applied on the data, are presented as a function of the peak-to-total ( $P/T$ ) ratio. The peak integral is estimated with the fitting method described in Section 4.3.2. The total number of  $\gamma$  rays is calculated summing the number of  $\gamma$  rays detected in an energy interval between 200 and 1000 keV.

Only the  $P/T$  ratios of the  $4_1^+$  to  $2_1^+$  transition of  $^{104}\text{Mo}$  for different conditions are compared. The following paragraph emphasizes the influence of the particle- $\gamma$  time selection (Section 4.5.2). The impact of a depth selection of the  $\gamma$ -ray interaction positions is described in Section 4.5.3 and the influence of the  $\gamma$ -ray multiplicity on the peak-to-total in Section 4.5.4.

---

### 4.5.1 Influence on the single particle hit

---

The first analysis tests the condition of the selection of a single interaction hit in both FRS and LYCCA. This selection provides a 8% gain in  $P/T$ . The data points are plotted as reference in Fig. 4.24, 4.25 and 4.26.

---

### 4.5.2 Influence of the particle- $\gamma$ time

---

We mentioned in Section 4.4.3 that a time gate influences the background line of the non-Doppler corrected spectra. In the following we show the impact of the time selection on the peak-to-total ratio. For this analysis, we define our time 0 at 2300 ns (see histogram in Fig. 4.19b). We then compute the peak-to-total ratio for different time gates: 20, 30, 40, 50 and 60 ns. In order to have an accurate scan of the time range, we shift the time gate from 0 to 30 ns with a 5 ns step. The  $P/T$  data points for all the time conditions are plotted in Fig. 4.24. From this plot, we observe a clear gain in the peak-to-total ratio with a 40 ns time gate and with no shift with respect to time 0.

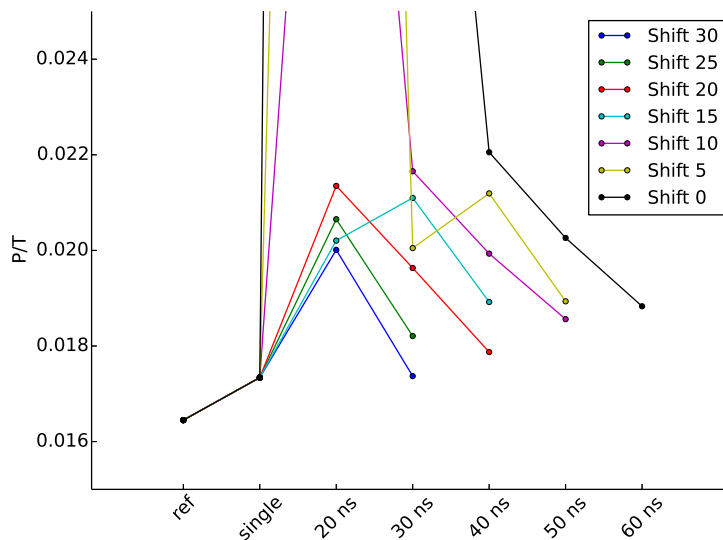


**Figure 4.24:** Systematics of the  $P/T$  ratio as a function of the width of the time gate. The  $P/T$  data point out-of-range have a non-converging fit due to the low-statistics. The color code is given in the insert.

---

### 4.5.3 Influence of the depth of the hits

---

The beam induced background consist of, e.g. bremsstrahlung radiation. The bremsstrahlung photons have low energy thus, they have a high probability to interact in the first mm of a crystal. Therefore, removing the events that have an interaction in the first few layers of the crystal could reduce the background thus, increase the  $P/T$  ratio.

With the position information of the hits in the crystal, provided by the PSA, we can select the  $\gamma$  ray events according to the depth of the first interaction hit, *i.e.*, the hit with the highest energy deposit<sup>16</sup>.

The layers considered for this analysis have a thickness of 1, 5, 10, or 15 mm. The  $P/T$  ratio for different thickness of the layer removed in the front is shown in Fig. 4.25. It can be observed that the depth selection reduces the  $P/T$  ratio, thus it is not used in the analysis.

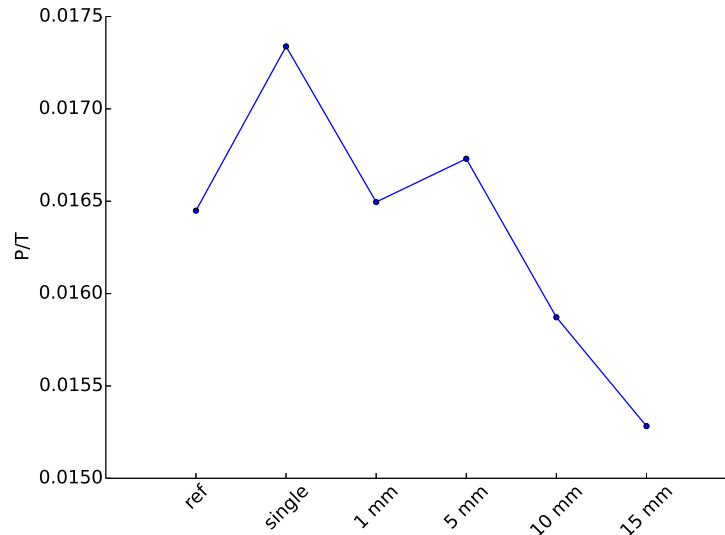


**Figure 4.25:** Systematics of the  $P/T$  ratio as a function of the thickness of the removed front layer.

---

### 4.5.4 Influence of the $\gamma$ -ray multiplicity

---

We define the  $\gamma$ -ray multiplicity as the number of AGATA crystals that has an event. In case of nuclear reactions at half speed of light, we are expecting [117] to have a low  $\gamma$ -ray multiplicity and therefore we consider in this analysis a low  $\gamma$ -ray multiplicity event. In Fig. 4.26, we plot the systematics of the  $P/T$  ratio as a function of the  $\gamma$  multiplicity. From this plot, it is clear that the optimum condition is to select events with a  $\gamma$ -ray multiplicity below four.

---

### 4.5.5 Optimum $\gamma$ -ray spectrum

---

Applying the condition of single particle hit, particle- $\gamma$  time and low multiplicity conditions that optimized as described in this paragraph, we can generate a  $\gamma$ -ray histogram as shown in Fig. 4.27 for the  $^{104}\text{Mo}$  isotope. The  $P/T$  ratio obtained is 0.032, which is 48% better than without any selection. This allows a clear observation of higher spin transitions in  $^{104}\text{Mo}$  such as the  $6_1^+$  to  $4_1^+$  transition. The other spectra for the even-even molybdenum isotopes can be found in Annexe 7.6

---

<sup>16</sup> As explained in Section 4.4.6, the tracking algorithm cannot be used in this experiment. Thus, selecting the highest energy hit as first interaction hit is the only assumption possible here.

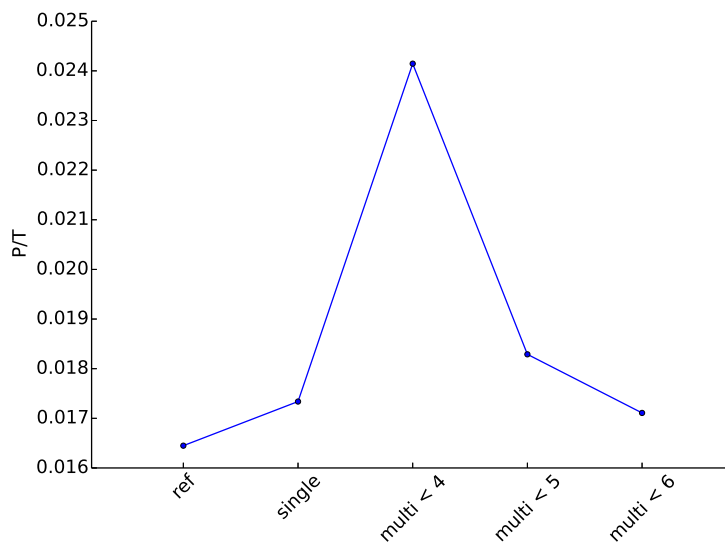


**Figure 4.26:** Influence of the multiplicity conditions on the peak to total ratio. The  $x$  axis corresponds to the event selection we apply on the data. The  $y$  axis depicts the  $P/T$  ratio.

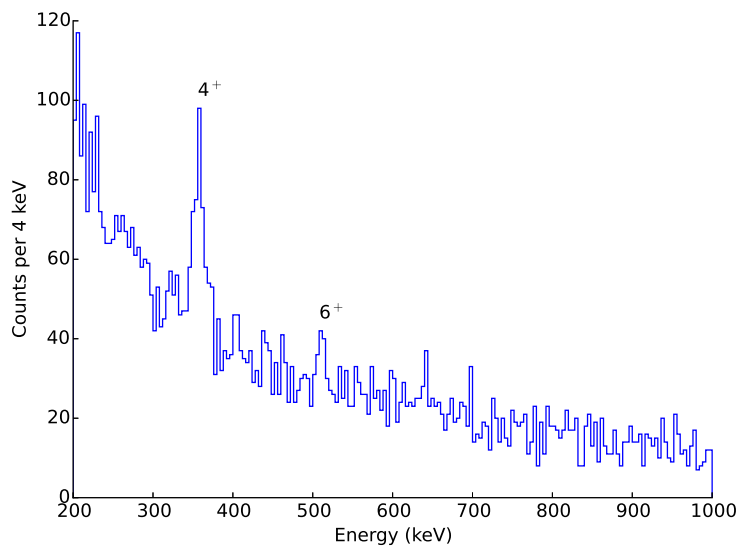


**Figure 4.27:** Optimum  $\gamma$ -ray histogram obtained after several conditions: single particle hit, 40 ns particle- $\gamma$  time selection and  $\gamma$ -ray multiplicity inferior to 4. In this histogram, we clearly identify the  $6_1^+$  to  $4_1^+$  and  $4_1^+$  to  $2_1^+$  transitions of  $^{104}\text{Mo}$  at the energies of 510 and 358 keV respectively.

---

## Chapter 5: Lifetime determination

In the previous chapters, I explained the data analysis process that lead to the  $\gamma$ -ray spectra, together with the conditions that optimize the peak-to-total ratio. Nevertheless, as I mentioned in Chapter 1, the aim of the experiment is to measure the lifetime of the  $4_1^+$  excited level of  $^{108}\text{Mo}$ . Thus, in the following chapter, I will provide the procedure that I followed for this measurement.

The procedure is a two steps process explained in Section 5.1. The first step corresponds to the “adjustment” of the Monte-Carlo (MC) simulations developed for the half-life measurement. For this adjustment, the known half-life of both the  $2_1^+$  excited level of  $^{102}\text{Mo}$  and the  $6_1^+$  excited level of  $^{104}\text{Mo}$  are used. These half-life values belongs to two separate time ranges: 4.73 ps and 125.0 ps. Thus, the MC simulations are adjusted with two distinct data points, each of them being dominated by one of the two effects of the Doppler shift (see Section 2.5 for the details on these two effects). In the second step, the known half-life values of the observed transitions are used to verify that the MC simulations are reliable for half-life measurement.

In Section 5.2, the MC simulations are used to extract a half-life value of the  $4_1^+$  excited level of  $^{108}\text{Mo}$ .

Section 5.3 provides a conclusion on the experimental technique developed in this work in order to determine the half-life of the  $4_1^+$  state of  $^{108}\text{Mo}$ . In the same section, a different approach, that could be used to reduce the systematic errors of our half-life measurement, is also discussed.

---

## 5.1 Adjustment of Monte-Carlo simulations for lifetime determination

---

The lifetime determination relies on a Monte-Carlo (MC) simulations of a part of the experimental setup: the Doppler shift of the  $\gamma$ -ray transitions at the level of the secondary target. In order to compare the MC simulations with the experiment, we simulate the Doppler correction of the shifted  $\gamma$  ray under the same assumptions as in the experiment, *i.e.*, the beam velocity after the target is used for the Doppler correction and the decay position is assumed to occur at the target position.

For the MC simulations of the experimental setup we made some hypotheses that are explained in Paragraph 5.1.1. In addition, the experimental setup described in Section 2 presents limitations that make a realistic simulations challenging. For instance, we can mention the following points:

- The beam velocity at the target level is unknown. The velocity measured experimentally by the FRS is an average velocity between the middle and last focal plane of the FRS. Moreover, the beam velocity measured by the LYCCA calorimeter is an averaged velocity between the slow-down effect and the outgoing fragment velocity after the target. Therefore, in order to have the incoming beam velocity at the target entrance for our MC simulations, we rely on the fact that at a given angle, the Doppler shifted energy of a given transition depends only on the beam velocity. The velocity determination of the beam is explained in details in Paragraph 5.1.2.
- Even if we have determined the relative position of the target for this experiment (see Section 4.3), the exact geometry is not completely known. For example, we did not take into account rotation of the AGATA frame. A rotation of the AGATA frame would affect all transitions in the same way: the observation angles have a systematic “offset”, thus the position of the energy centroid of the transitions are consistently shifted. Trying to minimize all the distances, including rotations, was performed but not conclusive. Therefore, we include a position offset in our MC simulations. The determination of this offset is explained in Paragraph 5.1.3.
- They are indications that the target of the experiment could have been mistaken with a thinner one present on the target ladder during the experiment. Therefore, to take into account this potential miss-match we parametrised the target thickness in the MC simulations. This procedure is described in Paragraph 5.1.3.

After determining the two parameters of the MC simulations, we test the reliability of these simulations by comparing them with known half-life transitions observed in the experiment of this work. The verification of the MC simulations is given in Paragraph 5.1.4.

---

### 5.1.1 Presentation of the Monte-Carlo simulations

---

The MC simulations presented in this paragraph aims at reproducing the energy shift of the transition centroids that we observed experimentally. We have explained in Section 2.5 that this shift is mainly due to the geometrical effects that can be observed for  $\gamma$  rays emitted by an ion at half speed of light. This process occurs at the target level, thus we limit the MC simulations to the processes occurring at the secondary target level. Nevertheless, we had to make assumptions in order to perform these simulations.

- The beam is point like on the target and we do not consider any angle of the outgoing fragments.
- The geometrical position of the target is the same as in the experimental setup.
- The  $\gamma$ -ray observation angles are between  $18^\circ$  to  $65^\circ$ . These limits were chosen to have the same emission angles as in the experimental setup. We assume that all the angles are uniformly covered.
- The  $\gamma$ -ray detector resolution is chosen to match the experimental value of  $\sim 3$  keV at FWHM.
- The incoming beam energy is assumed to follow a Gaussian distribution.
- The slow down process inside the 3.78 mm target is assumed to be linear in velocity.
- The reaction of the primary beam occurred at the target entrance, thus we do not take into account the reaction cross section that produced the excited nuclei.

For a  $\gamma$ -ray transition with an energy  $E_0$  and a half-life  $T_{1/2}$ , we generate an event selecting the beam energy, the  $\gamma$ -ray energy and a detection angle according to our hypotheses. For each event, we calculate the emission angle and beam velocity at the decay position to Doppler shift the  $\gamma$ -ray energy. We note  $E$  the Doppler shifted energy.



In a second step, the beam velocity after the target and the re-calculated observation angles assuming a decay at the target position are used for the Doppler correction. Thus, in order to reproduce the experimental measurement, we compute the Doppler corrected energy using a different beam velocity and angle than the one used to Doppler shift the  $\gamma$ -ray transition.

After fixing two parameters of our MC simulations, we reproduce the centroid shift observed experimentally as we shall see in Paragraphs 5.1.4. Therefore, we can say that these simulations, even if simple, are realistic.

---

### 5.1.2 Determination of the beam velocity

---

In the PreSPEC-AGATA experiments, the exact beam velocities before and after the target are not measured. From the FRS, we evaluate an average beam velocity between the middle and the last focal plane of the FRS. The beam velocity measured by the LYCCA calorimeter is an average that includes the slow down inside the target and the beam velocity after the target. Moreover, a LYCCA Time-of-Flight (ToF) offset was introduced in the analysis to minimize the transition width. Therefore, the beam velocity after the target is different than what is measured with the LYCCA calorimeter. By consequence, the determination of the beam velocity after the target need a different approach that we develop in the following discussion.

---

#### Beam velocity after the target

---

The Doppler-shift Equation 2.20 can be written in terms of the ratio of the Doppler-shifted energy over rest energy:

$$\frac{E}{E_0} = \frac{\sqrt{2 - \beta^2}}{1 - \beta \cos \theta}. \quad (5.1)$$

This equation is quadratic in  $\beta$ , thus for a given angle  $\theta$  and Doppler shifted energy  $E$ , we can solve the second order polynomial and obtain two possible beam velocities:

$$\begin{aligned} s_1 &= \frac{-U + \sqrt{U^2 - 4TV}}{2T} \\ s_2 &= \frac{-U - \sqrt{U^2 - 4TV}}{2T}, \end{aligned} \quad (5.2)$$

where  $T = 1 + (\cos \theta)^2 (E/E_0)^2$ ,  $U = -2 \cos \theta (E/E_0)^2$  and  $V = (E/E_0)^2 - 1$ .

The solution  $s_1$  is close to one, thus is not realistic and the beam velocity is computed with solution  $s_2$ .

In order to determine the beam velocity, we needed a transition with proper statistics allowing us to observe the position of the centroid of the transition under different observation angles. In addition, we needed a transition where we would not be sensitive to the slow-down effect inside the target, thus decaying mainly after the target. The  $2_1^+$  to  $0_1^+$  transition of  $^{102}\text{Mo}$  fulfills these conditions. The transition has a rest energy of 296.6 keV and the  $2_1^+$  state has a half-life of 125 ps [33]. For this ion, we have enough statistics to determine the Doppler-shifted energy at three observation angles. The energy values of the transition centroids are given in Table 5.1 together with the velocity  $\beta$  determined by solution  $s_2$  of Equation 5.2.

**Table 5.1:** Doppler-shifted energy of the  $2_1^+$  to  $0_1^+$  transition of  $^{102}\text{Mo}$  reported for three observation angles. The beam velocity  $\beta$  is determined by solution  $s_2$  of Equation 5.2.

$\theta$ ( $^\circ$ )	Doppler-shifted energy $E$ (keV)	$\beta$	Standard deviation
25	441	0.435	0.019
35	418	0.445	0.026
45	438	0.447	0.043

We plotted in red in Fig. 5.1 the determined velocity for three angle. From this figure, we notices that the data points are aligned. The weighted average over the three angles provides the beam velocity  $\beta = 0.439(14)$ .

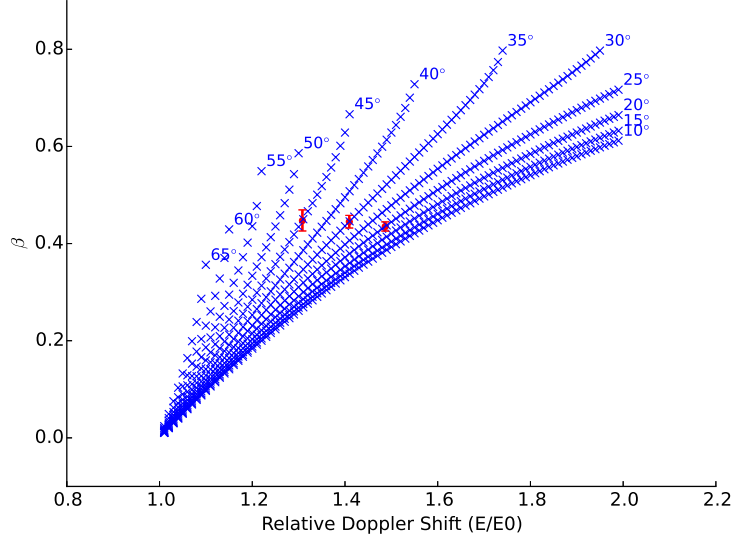


**Figure 5.1:** Determination of the beam velocity. Each set of blue data points corresponds to an angle  $\theta$  of observation. The red data points are the one reported in Table 5.1.

---

### Beam velocity before the target

---

In order to determine the beam velocity in front of the target knowing the exit velocity, we performed simulations with the LISE++ [101] code. In these simulations, the slow down process is calculated with the ATIMA [99] code.

The data points of the LISE++ simulations are plotted in Fig. 5.2 for two ions:  $^{102}\text{Mo}$  and  $^{104}\text{Mo}$ . They are produced in a knock-out reaction of the  $^{108}\text{Mo}$  FRS beam inside the  $700 \text{ mg/cm}^2$  thick beryllium secondary target.

We have obtained in the previous paragraph a beam velocity after the target of  $\beta = 0.439$ , therefore we can deduce from the curves in Fig. 5.2 that our incoming beam energy range from 160 to 170 MeV/u that corresponds to an incoming beam velocity of  $\beta = 0.521$  to  $\beta = 0.534$ .

The difference between the two  $\beta$  of two isotopes considered in the LISE++ simulations,  $^{102}\text{Mo}$  and  $^{104}\text{Mo}$ , is in the order of 4% of the measured  $\beta$  value. It is lower than the velocity resolution we can achieve with the LYCCA calorimeter thus, in the MC simulations, we assume that the reaction process does not change the beam velocity of the outgoing fragments.

In order to verify the influence of the interaction depth in the target on the beam velocity, we performed a LISE++ simulations for a hypothetical beam reaction at the entrance, at the middle, or at the exit of the target. There is 10% difference between a reaction occurring in the front of the target and one occurring at the exit of the target. In the experiment, we know that the ions have been produced, thus that the reaction occurred. Therefore, in the MC simulations, we assume that all ions are excited at the target entrance. This is affecting in a systematic way the energy of the transition centroid and is phenomenologically corrected by an effective target thickness (the determination of the effective thickness is described in the following paragraph).

---

#### 5.1.3 Determination of the unknown parameters of the MC simulations

---

In order to reproduce the energy shift of the transition centroids, the MC-simulation geometry needs to be matching the experimental one. As we shall see in the following discussion, we need to fix two parameters in the MC simulations: a geometrical offset and an effective target thickness. Before describing the method to determine these two parameters, we provide a list of the observed transitions together with the energy of their centroids.

---

#### List of the energy centroids

---

For a given transition, we determine the energy centroid assuming the transition to generate a Gaussian feature on top of the background. The fit is based on the Bayesian approach. The model that we used for the fit is similar to the one described in Paragraph 4.3.2. The only difference is that we included a second exponential decay to model the background.

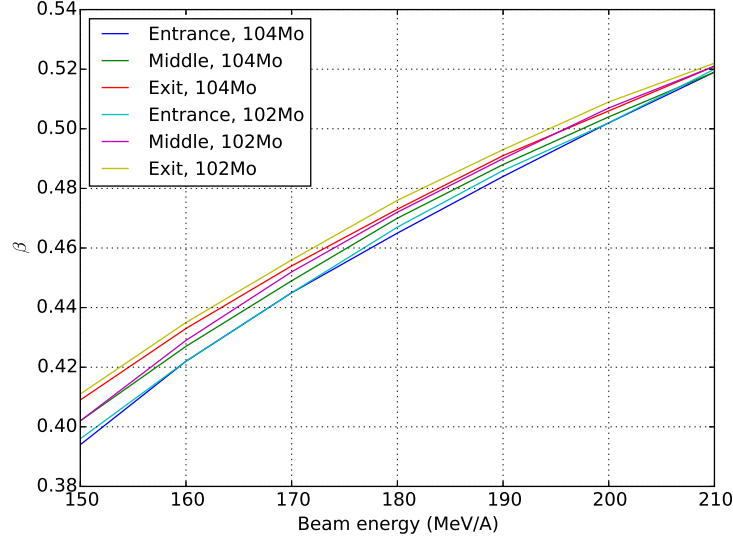


**Figure 5.2:** Determination of the beam energy at the entrance of the target ( $x$ -axis) knowing the beam velocity  $\beta$  ( $y$ -axis) of the beam after the target. The data point plotted in this figure are determined with slow-down process calculated by the ATIMA [99] code.

In order to insure consistency between the different transitions that we observed, the determination of the centroid is performed with the same methods and under the same conditions (e.g. time selection,  $\gamma$ -ray multiplicity, ...) for all the observed transitions.

The fit of the spectra for all the transitions is shown in Annexe 7.7. We reported in Table 5.2 only the energy values of the centroid for each of the observed transitions.

**Table 5.2:** Summary of the energy centroids of the observed  $\gamma$ -ray transitions. The error bars on the centroids are given by the 14th and 84th percentile. The rest energies and the half-life values reported here are the adopted values from [33].

Nucleus	Transition	Transition centroid (keV)	Rest energy $E_0$ (keV)	Half-life $T_{12}$ (ps)	$\frac{E_0 - E}{E_0}$
$^{100}\text{Mo}$	$2_1^+$ to $0_1^+$	$519.7^{+1.1}_{-1.0}$	535.6	12.6(2)	$0.0297^{+0.0019}_{-0.0021}$
$^{102}\text{Mo}$	$2_1^+$ to $0_1^+$	$279.2^{+1.4}_{-1.4}$	296.6	125(4)	$0.0587^{+0.0047}_{-0.0048}$
$^{102}\text{Mo}$	$4_1^+$ to $2_1^+$	$433.1^{+1.7}_{-1.6}$	447.1	12.5(25)	$0.0313^{+0.0035}_{-0.0038}$
$^{104}\text{Mo}$	$4_1^+$ to $2_1^+$	$356.7^{+1.1}_{-1.1}$	368.4	26.1(8)	$0.0317^{+0.0031}_{-0.0031}$
$^{104}\text{Mo}$	$6_1^+$ to $4_1^+$	$509.9^{+2.1}_{-2.9}$	519.2	4.73(15)	$0.0180^{+0.0057}_{-0.0041}$
$^{106}\text{Mo}$	$4_1^+$ to $2_1^+$	$342.7^{+1.2}_{-1.3}$	350.7	25.4 (51)	$0.0228^{+0.0036}_{-0.0035}$
$^{108}\text{Mo}$	$4_1^+$ to $2_1^+$	$361.2^{+3.3}_{-3.2}$	370.9	X	$0.0262^{+0.0086}_{-0.0089}$

### Geometrical offset

As we mentioned in Section 4.3, the target position was measured at the beginning of the beam time and we have determined in the same section the target position that minimizes the width of the uranium X ray transitions. Nevertheless, we have not considered a potential rotation of the AGATA detectors and the distance target-AGATA along the beam axis.

The energy of the uranium X rays is around 100 keV, thus the energy shift of the centroid is too small for the energy resolution we can achieve after Doppler correction. Therefore, it was tried to determine the geometry with the  $\gamma$ -ray

transitions of the molybdenum isotopes, but the statistics was too low to provide a reliable and precise determination of the geometry.

Nevertheless, in order to reproduce the experimental energy shift of the centroids with our MC simulations, we add a geometrical offset inside the MC simulations. It is straightforward to determine this offset when we know the centroid shift of the  $\gamma$ -ray transitions and the lifetime of the state from which the decay occurs.

In order to determine the geometrical offset, we need a decay that occurs mainly after the target, thus almost independent of the slow-down effect inside the target. The  $^{102}\text{Mo}$  nucleus has its  $2_1^+$  to  $0_1^+$  transition with a 125 ps half-life and is therefore the optimum candidate for the geometrical offset determination.

To determine the geometrical offset, we modified the emission angle of the  $\gamma$  ray for several geometrical offsets and compared the simulated centroid position with the one observed experimentally. The result of the relative Doppler shifted energy obtained for the different geometrical offsets is drawn in blue in Fig. 5.3. The black line in this figure highlights the experimental value of the relative Doppler shift with its error drawn in dotted lines. The crossing point between the MC-simulation line and the experimental centroid shift value corresponds to our geometrical offset.

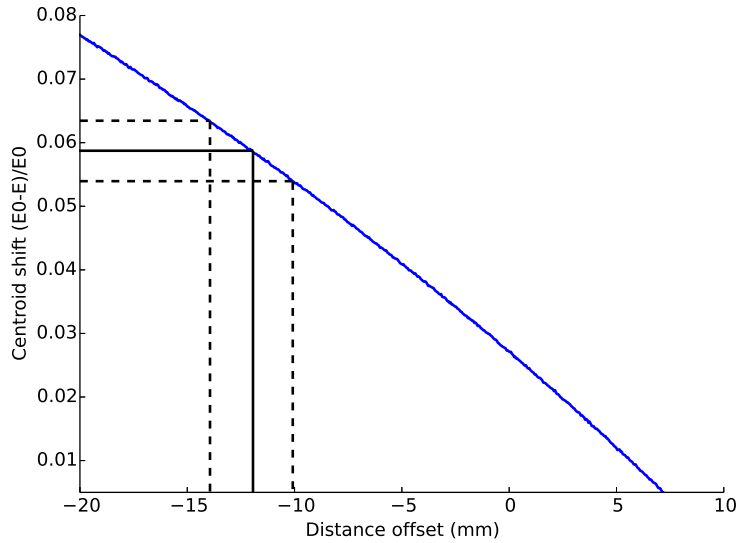


**Figure 5.3:** Determination of the geometrical offset. For each geometrical offsets, we compute the relative Doppler shift with MC simulations of the experimental setup. The black line is drawn for the observed energy shift of the centroid and corresponds to a geometrical offset of:  $-11.9^{+2.0}_{-1.9}$  mm.

With this line crossing method, we find that the geometrical offset that reproduces the centroid observed in the  $2_1^+$  to  $0_1^+$  transition of  $^{102}\text{Mo}$  is  $11.9^{+2.0}_{-1.9}$  mm.

---

### Target thickness

---

At this point, the MC simulations match the geometrical effect observed, but the deviations of the energy shift of the centroid for the transitions that decay inside the target are not reproduced. One hypothesis is that the wrong target was inserted inside the beam line. There were indeed two beryllium targets present on the central target loader and they could easily have been mistaken. In addition, the excitation position inside the target influences the impact of the slow-down effect on the centroid shift. Therefore, in the following discussion we determine an effective target thickness to reproduce the energy positions of the centroid.

The procedure applied here is similar to the one for the determination of the geometrical offset: we vary the target thickness in the MC simulations until the energy of the centroid agrees with the observed energy of the  $6_1^+$  to  $4_1^+$  transition of  $^{104}\text{Mo}$ . We selected this transition since it is the one we observed with the shortest know lifetime, thus the centroid position depends mainly on the slow-down effect. The result obtained with the line crossing method provides an effective target thickness of  $1.2^{+1.0}_{-0.4}$  mm.

The two targets inside the target loader of the experiment were a 0.81 mm and a 3.78 mm thick beryllium target. The effective thickness we have obtained suggests that the target of the experiment was rather the thin one with a 0.81 mm thickness.

In order to verify the effect of the target thickness on the half-life determination, we plotted in Fig. 5.4 the relation between the centroid shift and the half-life of the transition for the two target thicknesses. In this figure, the two red data points correspond to the one used to determine the geometric-effect (at 125 ps) and the effective thickness (at 4.73 ps). We noticed the agreement for the data point at 4.73 ps with the MC simulations that included both the effective target thickness and the geometrical offset.

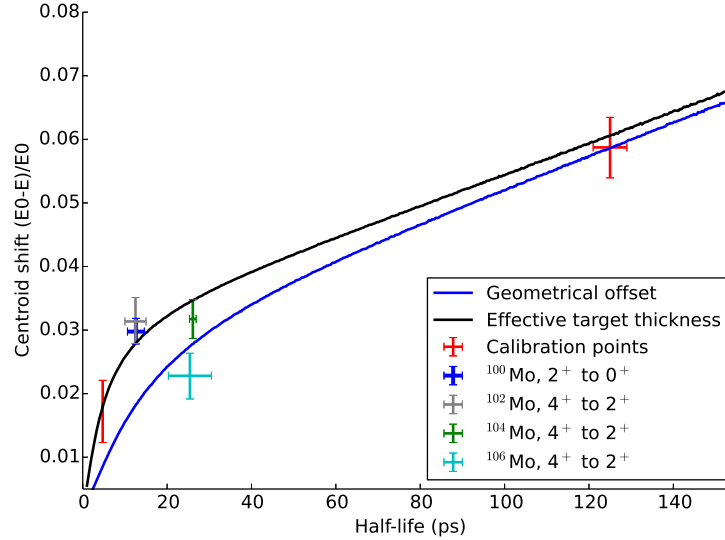


**Figure 5.4:** Verification of the MC simulations with a set of experimental data points. The blue line corresponds to the MC simulations that take into account a geometrical offset only. The black line corresponds to MC simulations in which we take into account an effective target thickness in addition to the geometrical offset. The red data points are the two experimental data points used to fix the parameters of the MC simulations. The color code for the other data points is given in the insert. The  $x$  error bars come from the error on the adopted value [33]. The  $y$  error bars are statistical errors attached with the fit of the observed transitions.

#### 5.1.4 Verification of the model in view of previously measured lifetime

Now that we fixed the two MC-simulation parameters and managed to reproduce both the geometrical and the slow-down effects on the centroid shift, we can verify that the known data points reported in Table 5.2 are agreeing with our MC simulations. We plotted the data points with a known half-life in Fig. 5.4. This plot shows a visual verification that the MC simulations are agreeing with the previous half-life measurement of the excited state of  $^{100}\text{Mo}$ ,  $^{102}\text{Mo}$  and  $^{104}\text{Mo}$ .

We can notice that the half-life of e.g. the  $2_1^+$  state of  $^{100}\text{Mo}$  agrees within one standard deviation. The same conclusion can be drawn from the half-life values of both the  $4_1^+$  state of  $^{102}\text{Mo}$  and the  $4_1^+$  state of  $^{104}\text{Mo}$ .

The  $4_1^+$  state of  $^{106}\text{Mo}$  agrees only with two and a half standard deviations with our MC simulations. We would assign its half-life to  $7.6_{-2.0}^{+3.3}$  ps, about five times smaller than the measurement performed with recoil distance method with a spontaneous fission of  $^{252}\text{Cf}$  [41]. Additional work would be needed to understand if our data point is wrong. A potential explanation is a possible contamination from even-odd molybdenum isotopes. This is supported by the fact that we do not clearly observe the  $6_1^+$  to  $4_1^+$  transition of  $^{106}\text{Mo}$  (the spectra can be seen in Fig. 7.7 of Annexe 7.6).

To conclude on the MC simulations presented in this section, we have developed a simple but realistic lifetime determination based on the centroid shift of the  $\gamma$ -ray transitions. The method was proven to provide half-life in agreement within one standard deviation of the adopted half-life values. Therefore, we can now go one step further and determine the half-life of the  $4_1^+$  excited state of  $^{108}\text{Mo}$ .

## 5.2 Lifetime determination in the $^{108}\text{Mo}$ isotopes

With the MC simulations that reproduce the relative Doppler shift as function of the half-life of a state, we can determine the lifetime of the  $4_1^+$  excited state of  $^{108}\text{Mo}$ . The intersection between the simulated curve and the relative centroid shift of the  $4^+$  to  $2^+$  transition is shown in Fig. 5.5. The value we obtained is  $11_{-6}^{+16}$  ps.

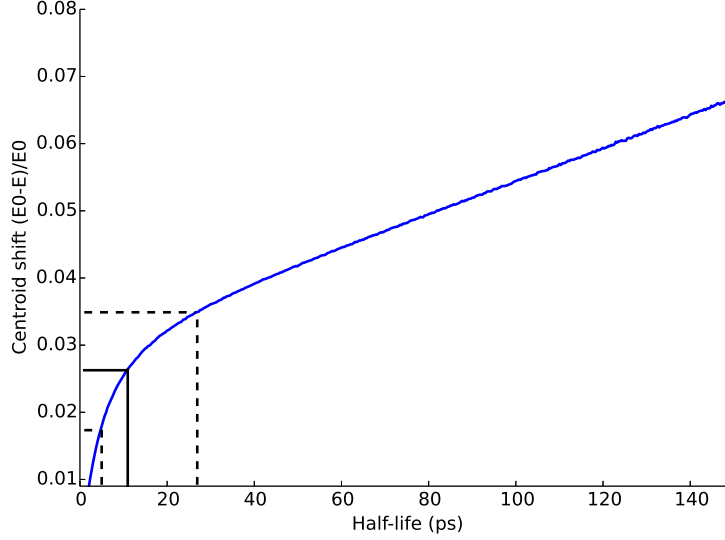


**Figure 5.5:** Lifetime determination of the  $4_1^+$  excited state of  $^{108}\text{Mo}$ . The blue curve is computed with MC simulations described in this chapter. The black line is the relative Doppler shift measured in the experiment and the dotted black line highlights our confidence interval in the determination of the centroid. The crossing of the MC-simulation line with the experimental value provides a half-life of  $11_{-6}^{+16}$  ps for the  $4_1^+$  state of  $^{108}\text{Mo}$ .

This estimation relies on the determination of the centroid of this transition with low statistics, thus the large uncertainties attached to the result.

In addition to the low statistics, this result relies on our model. We can estimate the half-life obtained if we vary the model parameters within one standard deviation. The result of this analysis of potential systematic error is given in Table 5.3. The systematic error that we have with the determination of the parameters of our MC simulations could

**Table 5.3:** Simulations influence on the half-life determination of the  $4_1^+$  state of  $^{108}\text{Mo}$ .

Geometrical offset (mm)	Effective target thickness (mm)	Half-life (ps)
12.9	1.2	$6.6_{-3.6}^{+9.0}$
10.3	1.2	$18_{-10}^{+24}$
11.9	2.2	$18_{-9}^{+18}$
11.9	0.8	$8_{-5}^{+15}$

modify our half-life determination by a factor close to two. Nevertheless, it is hard to quantify the real impact of the systematic error on our measurement due to the large statistical error.

An other half-life measurement of the  $4_1^+$  excited state of  $^{108}\text{Mo}$  was performed using prompt  $\gamma$ -ray spectroscopy of fission fragments or uranium. This half-life has not been published so far and is only available in the PhD thesis of L. Grente [12]. They found a half-life of 23.3 (5.1) ps. The value determined in this work is lower than this measurement, but agrees within one standard deviation.

---

### 5.3 Conclusion

---

To conclude on the approach we use here, we have to keep in mind that the statistical errors of our measurement are large. A different methodological approach would help to reduce systematic source of error on our measurement, but would hardly reduce statistical errors attached to this measurement.

In order to improve the measurement errors, we should include in our fit a potential tail due to the slow-down effect. Nevertheless, this would be reliable only with complex MC simulations of the experimental setup that would include:

- advanced slow down process inside the target,
- a proper determination of the beam velocity inside the target that includes the velocity spreading,
- the excitation position inside the target,
- an energy efficiency correction for the  $\gamma$ -ray detection,
- the angular distribution of the  $\gamma$  ray,
- contribution of higher spin states that “feed” the  $4_1^+$  state,

To include these features in the half-life determination, we could for example use the software called Analysis Program for Continuous-Angle DSAM (APCAD) from C. Stahl [71]. It has been recently updated by M. Lettmann in order to include geometrical effects [118] and could be used to reduce systematic sources of error attached with our measurement. Nevertheless, this simulation code relies also on a well defined geometry and it takes for each simulation (or change of geometry) around five hours. This code was tested [119], but it was not feasible to employ this code.

To conclude, the half-life of  $11_{-6}^{+16}$  ps that we have determined in this work is the best that we could have achieved considering the statistics available for the  $4_1^+$  to  $2_1^+$  transition of  $^{108}\text{Mo}$ . This measurement agrees within one standard deviation with a non-published result [12]. The limitation of the experimental setup induces significant source of systematic error, that prevents us in using more sophisticated simulation code such as the APCAD software [71].

---

## 5.4 Interpretation of the lifetime with the geometrical models

---

In Chapter 1, we discussed the nuclear structure interest of the mass region  $A \approx 100$ . For example, the neutron rich molybdenum isotopes exhibit a shape-phase transition from spherical to rotor. To describe this transition, we can use two limiting cases of the Interacting Boson Models (IBM):  $U(5)$  for vibrator and  $SU(3)$  for rotor. These two cases provide analytic formulas to predict the energies and transition rates of the excited state [19]. In addition to these two cases, the shape-phase transition from a spherical vibrator to the rotational can be described by a critical point called  $X(5)$ , for which an analytical solution can also be derived [24].

In this section, we interpret the half-life result of the first  $4_1^+$  state of  $^{108}\text{Mo}$  with a description of the shape-phase transition with the prediction of the three limiting cases of the IBM models. At first, we compare the energies of the excited levels in Paragraph 5.4.1 then, we compare the transition rates in Paragraph 5.4.2.

---

### 5.4.1 Energy predictions

---

In Fig. 5.6, we plotted the energy ratios of a level with spin  $J^+$  over the energy of the state with spin  $J^+ = 2^+$  for the vibrational and rotational limits of the IBM models. In addition, we plotted the prediction of the energy ratios of the  $X(5)$  model. In this figure, we added the systematics of the adopted energy levels of  $^{102,104,106,108}\text{Mo}$  isotopes as a function of the spin of the excited state. With the systematic drawn in this figure, we see that adding neutrons to  $^{102}\text{Mo}$

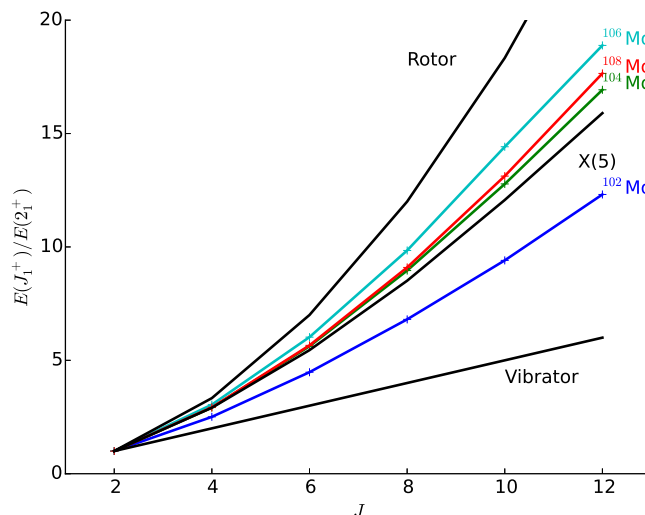


**Figure 5.6:** Comparison of the energy ratio of the excited states of  $^{102,104,106,108}\text{Mo}$  with three limiting cases of the IBM models: Rotor, Vibrator and the critical point  $X(5)$ .

induces a shape transition from vibrator like nucleus  $^{102}\text{Mo}$  to a rotor like nucleus  $^{106}\text{Mo}$ . If we add two neutrons more to  $^{106}\text{Mo}$ , the energy ratios indicate a transition towards  $X(5)$ .

In the following paragraph, we look at the transitions strength ( $B(E2)$  value) in order to refine the interpretation with the geometrical models.

---

### 5.4.2 Comparison of transition rates

---

The comparison to the geometrical models requires to normalize the transition rate of the  $4_1^+$  state with the one of the  $2_1^+$  state, thus we need to use the  $B(E2; 2_1^+ \rightarrow 0_1^+)$  value of  $^{108}\text{Mo}$  measured in an other experiment. There are two available measurements: the one of H. Penttilä et al. [120] and the one of F. Browne et al. [121]. The most recent measurement of F. Browne agrees with the one of Penttilä. Nevertheless, the exact value is not reported in Reference [121], thus even if the measurement is attached with a large error, we use the value of Reference [120] that is  $0.5(3)$  ns.

In Fig. 5.7, we report the lifetime measurement we preformed of the first  $4_1^+$  excited state of  $^{108}\text{Mo}$  normalized to the transition rate of the first  $2_1^+$  state. The measurement of this work has a  $B(E2; 4_1^+ \rightarrow 2_1^+)$  value that is between the  $X(5)$  and the vibrator prediction. Moreover, the energy of the excited states indicate a nucleus behaving between  $X(5)$



and rotor. Therefore, we could conclude that the  $^{108}\text{Mo}$  nucleus tend to be a shape-phase transitional nucleus described by the critical point  $X(5)$ .

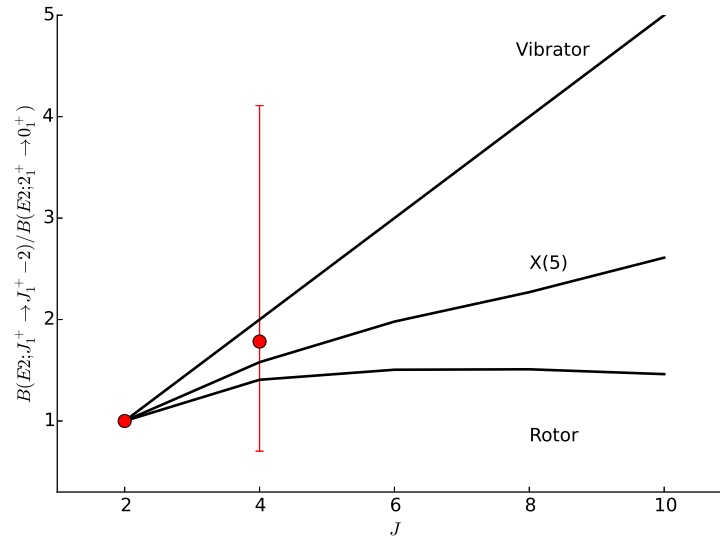


**Figure 5.7:** Comparison of the  $B(E2)$  value we obtain with the geometrical model.

Nevertheless, this conclusion need to be weighted by the large uncertainties of our measurement. Therefore, to further investigate the shape-phase transition in the molybdenum isotopes, the statistical errors need to be reduced. In addition, the measurement of transition rates for higher spin states would be of great help to conclude precisely on the shape-phase transition indicated by the energies of the excited state of the molybdenum isotopes.



---

## Chapter 6: Conclusions and perspectives

In the mid-shell nuclei, in the mass region  $A \approx 100$ , interesting collective behavior such as shape-phase transitions and triaxiality are predicted. In particular, a shape-phase transition is observed in the neutron rich molybdenum isotopic chain. Indeed  $^{100}\text{Mo}$  is spherical while the more neutron rich  $^{102,104,106,108}\text{Mo}$  are deformed nuclei.

In order to better characterize the shape of these nuclei, both excitation energies and lifetime values of the excited states need to be measured. In particular, the  $^{108}\text{Mo}$  isotope is experimentally accessible for lifetime measurement of its high-spin excited levels. Therefore, the lifetime measurements of the excited states had been tempted with the PreSPEC-AGATA experimental setup, a state-of-the-art setup in  $\gamma$ -ray spectroscopy.

The present work presented the PreSPEC-AGATA setup that was able to measure the half-life of the  $4_1^+$  excited level in  $^{108}\text{Mo}$ . A drawback of the setup is its complexity: the number of channels reached almost 2000 and represented a challenge on both data-acquisition and data-analysis side.

Within this work, I detailed the complex data-acquisition and trigger system that was set up in order to record the data in the most efficient way. The result obtained from the experiment of this work provides a proof that the system worked properly.

As an indication of the difficulties of this analysis, I can remind that the data analysis had to deal with the calibration of each electronic channel. Moreover, the Doppler correction of the  $\gamma$ -ray is highly sensitive to the geometry of the experimental setup. Since we do not simply want to observe a  $\gamma$ -ray transition but also measure its lifetime through its line-shape, the geometry had to be determined with a precision better than a millimeter.

Only after optimizing all the parameters, it has been possible to extract a half-life for the  $4_1^+$  state of  $^{108}\text{Mo}$ . The value obtained is  $11_{-6}^{+16}$  ps. The large error is due to the low statistic that remained after all the process of data-analysis. Our result, after comparison with geometrical models, indicates a nucleus that tend to correspond to the  $X(5)$  critical point, but it is difficult, with these uncertainties, to firmly establish the behavior of the  $^{108}\text{Mo}$  nucleus.

Nevertheless, the result of this measurement demonstrated the feasibility of a lifetime measurement with fission fragments at half the speed of light. This proof of principle is crucial for the HISPEC collaboration that will benefit of an increased intensity with the Super-FRS beam at FAIR which will allow to access crucial informations on the shape-phase transition in the mass region  $A \approx 100$ .



---

## Chapter 7: Appendix

---

### 7.1 Relative distances

---

The following distances were measured at the beginning of the experiment. Except if expressed, they were used for the data analysis.

```
# Detectors distances in the beam direction (in mm)

# Absolute S2 Distances from the exit window of Sc21 Degraded...
Sc21_z      -957. // Sc21 (not sure)
FocS2_z     -374. // Not measured should be checked
Finger_z    135.  // Finger
TPC3_z      286.  // TPC3
TPC4_z     1376. // TPC4

# Absolute S4 distances Relative to last quadrupole exit window
TPC5_z      91.   // TPC5 position
Music1_in_z 332.  // Music1 entrance window
Music1_out_z 782. // Music1 exit window
Music2_in_z 988.  // Music2 entrance window
Music2_out_z 1438. // Music2 exit window
TPC6_z     1518. // TPC6 position
TPC_GEM_z  1865. // not used
Sc41_z     2230.5 // Sc41 position
FocS4_z    4016. // S4 focal plane to be determined
startSci_z 2597. // Start scintillator position
startNSci_z 3901. // position of Tof target scintillator
tarDSSD_z  3958. // Target DSSD position
target1_z  4016. // Target nominal position position
target2_z  4166. // Target forward position position (variable 100 mm)
stopSci_z  7613. // Stop Scintillator position
wallDSSD_z 7628. // Wall DSSD position

# Choose secondary target position
TargetPos   0     // Which target position is used 0 Nominal, 1 Forward
```

---

## 7.2 Definition of the Euler angles

---

The Euler angles belong to the group of rotations  $SO(3)$  of the three-dimensional Euclidean space  $\mathbb{R}^3$ . Therefore, the rotation preserve the origin, euclidean distances and space orientation.

A rigid body in a three-dimensional space is orientated with respect to the reference frame by the three Euler angles  $(\alpha, \beta, \gamma) = (\phi, \theta, \psi)$ . Let us define the operator  $r(a, b)$  of angle  $a$  around the axis  $b$  which rotates the frame  $F \in \mathbb{R}^3$  to the frame  $F' \in \mathbb{R}^3$ . The referential is defined as  $(x, y, z)$ . The rigid body frame  $(X, Y, Z)$  is oriented in the referential with three consecutive rotations:

- $r(\alpha, z)$ : a rotation of angle  $\alpha$  around the  $z$  axis of the referential
- $r(\beta, N)$ : a rotation of angle  $\beta$  is the rotation around the  $N$  axis, which is the  $x$  axis after the rotation  $r(\alpha, y)$ .
- $r(\gamma, Z)$ : a rotation of angle  $\gamma$  around the axis  $Z$

The notation are given in Fig. 7.1

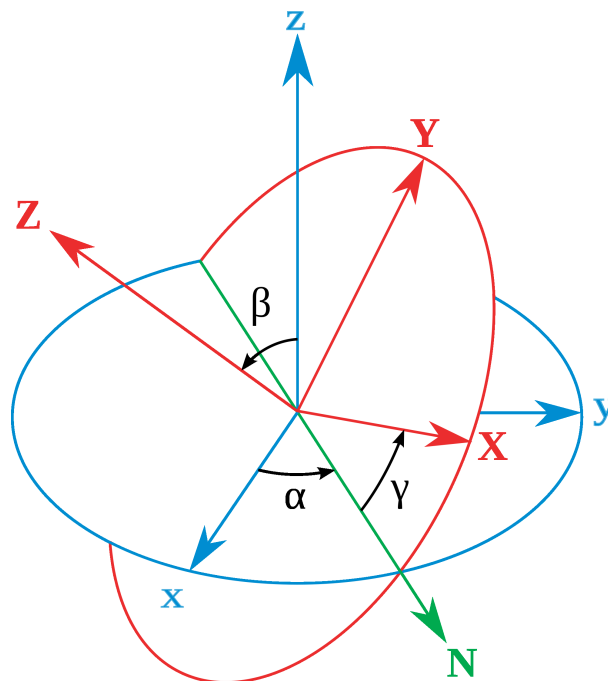


**Figure 7.1:** Orientation of a rigid body with the Euler angles. The figure is taken from the Wikipedia page [http://en.wikipedia.org/wiki/Euler\\_angles](http://en.wikipedia.org/wiki/Euler_angles).

---

### 7.3 Change of frame of reference change

---

Let us consider two coordinate system,  $K$  the reference frame, and  $K'$  the frame whose axis corresponds with the principal axis of the ellipsoid. The three Euler angles described in Annex 7.2 are commonly defined by  $(\alpha, \beta, \gamma) = (\theta_0, \theta_1, \theta_2)$ , and allow to orientate the frame  $K'$  with respect to  $K$ . The rotation of a nucleus corresponds to a rotation of the spherical harmonics of order 2. The Wigner matrix  $D_{\mu,\nu}(\theta_i)$  rotates the spherical harmonics of order  $\lambda$  by the Euler angle  $(\theta_i)$ . The coordinate change implies the transformation of the quantum number  $\mu$  of the nucleus frame to the quantum number  $\nu$  of the reference frame. A consequence of the rotation expressed as the Wigner matrix is the relation of the expansion coordinate  $\alpha_\mu$  of the reference frame with the coefficient  $a_\nu$  in the nucleus frame:

$$a_\nu = \sum_{\mu=-2}^2 \alpha_\mu D_{\mu,\nu}(\theta_i) \quad (7.1)$$

## 7.4 Spherical harmonics

The spherical harmonics  $Y_{\lambda,\mu}$  are used in quantum mechanics since they are of good quantum number  $(\lambda, \mu)$  for the orbital angular momentum  $\mathbf{L}$  and its projection along the  $z$  axis  $L_z$ :

$$\begin{aligned}\mathbf{L}Y_{\lambda,\mu} &= \lambda Y_{\lambda,\mu} \\ L_z Y_{\lambda,\mu} &= \mu Y_{\lambda,\mu}\end{aligned}\tag{7.2}$$

The spherical harmonics  $Y_{\lambda,\mu}(\theta, \phi)$  are expressed in the spherical coordinate system as:

$$Y_{\lambda,\mu}(\theta, \phi) = \exp(i\mu\phi)P_{\lambda}^{\mu}(\cos(\theta)),\tag{7.3}$$

where  $P_{\lambda}^{\mu}(\cos(\theta))$  are the Legendre polynomials.

It can be shown that the complex conjugate of the spherical harmonics are related with the spherical harmonics as

$$Y_{\lambda,\mu}(\theta, \phi)^* = (-1)^{\mu} \cdot Y_{\lambda,-\mu}(\theta, \phi)\tag{7.4}$$

The first order of spherical harmonics are given in Table 7.1.

$\lambda$	$\mu$	$Y_{\lambda,\mu}(\theta, \phi)$
0	0	$\frac{1}{2}\sqrt{\frac{1}{\pi}}$
1	-1	$\frac{1}{2}\sqrt{\frac{3}{2\pi}}\sin(\theta)\exp(-i\phi)$
	0	$\frac{1}{2}\sqrt{\frac{3}{\pi}}\cos(\theta)$
	1	$\frac{-1}{2}\sqrt{\frac{3}{\pi}}\sin(\theta)\exp(i\phi)$
2	-2	$\frac{1}{4}\sqrt{\frac{15}{2\pi}}\sin^2(\theta)\exp(-2i\phi)$
	-1	$\frac{1}{2}\sqrt{\frac{15}{2\pi}}\sin(\theta)\cos(\theta)\exp(-i\phi)$
	0	$\frac{1}{4}\sqrt{\frac{5}{\pi}}(3\cos^2(\theta) - 1)$
	1	$\frac{-1}{2}\sqrt{\frac{15}{2\pi}}\sin(\theta)\cos(\theta)\exp(i\phi)$
	2	$\frac{1}{4}\sqrt{\frac{15}{2\pi}}\sin^2(\theta)\exp(2i\phi)$

**Table 7.1:** First order spherical harmonics



## 7.5 Control of the convergence of the fit

A fit procedure is performed in two sections. The first section, the parameter space is explored to find the set that minimises the Likelihood. Each parameter is initialised with a set of walkers randomly distributed around the initial value of the parameters. The procedure will determine at each step the new value for the walkers according to the minimum of Likelihood, and determine the optimum one. The second section starts from the previously determined parameter position (walker position) and determines the error made on the parameter. Therefore, this method provides both the median value, and the error. Such as any other fit procedure, it is required to check the convergence of the result, and this even if the best result is not found. With this procedure, it is possible to observe the walkers of each parameter along the steps of the second section. If this value oscillates around one value, the convergence is obtained, otherwise, a clear divergence is observed. Figure 7.2 provides this visualisation of a set of walkers for the 11 parameters of the fit.

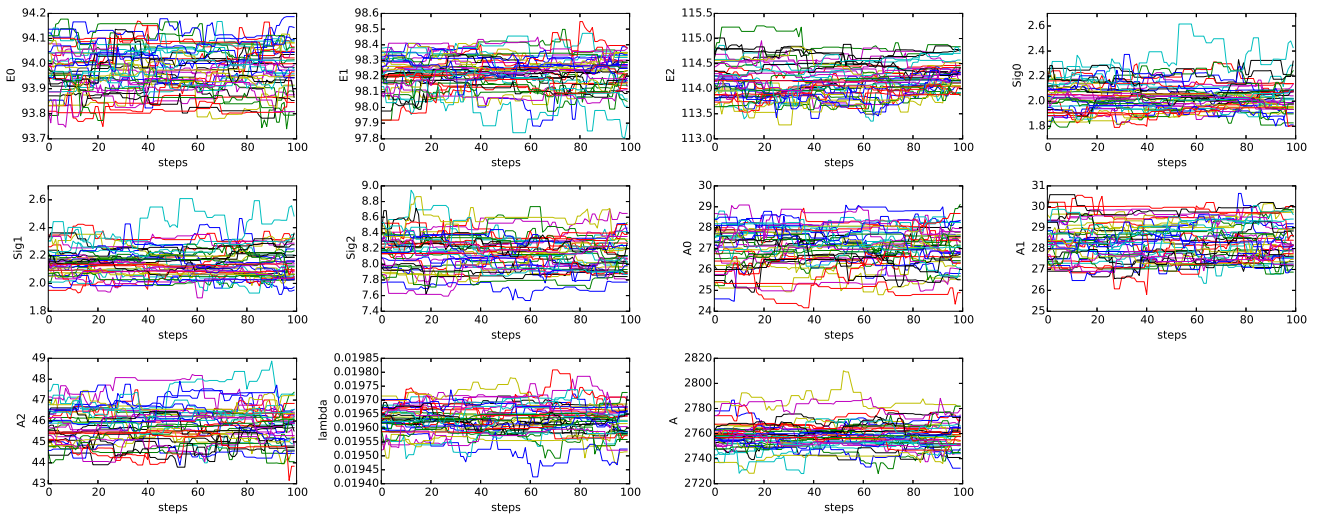


**Figure 7.2:** Progression of the chains performed to check the convergence of the fit in the case of the uranium X rays. Each of the color lines corresponds to a different chain.

An additional mean to check the convergence and the fit quality is to look at the superposition of the data with the fit result. This result is shown in Fig. 7.3, where the median value of the fit highlights the transitions without the exponential decay background.

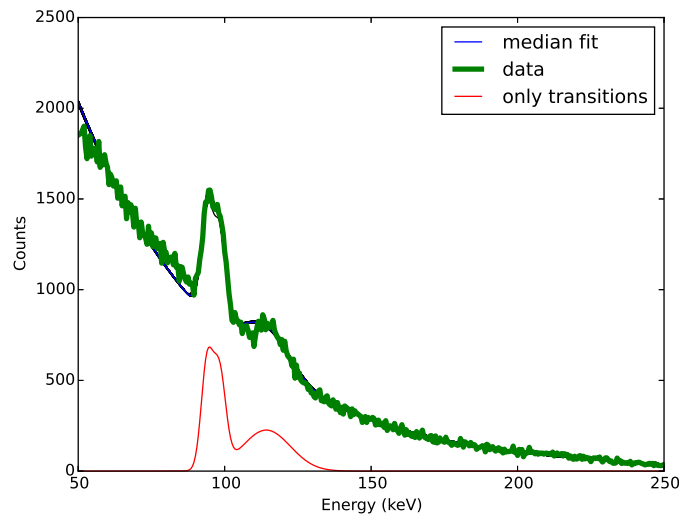


**Figure 7.3:** Result of the fitting procedure on the uranium X-ray transitions. The transitions are drawn in red without the exponential decay background.

---

In addition to its robustness, this method is quick, with a fit taking less than a minute. Therefore it is possible to performed it over an array of Doppler-corrected histogram.

---

## 7.6 $\gamma$ -ray spectra for the even-even molybdenum isotopes

---

The spectra presented in this paragraph are plotted under the optimum conditions as defined in Paragraph 4.5.

---

7.6.1  $^{100}\text{Mo}$

---

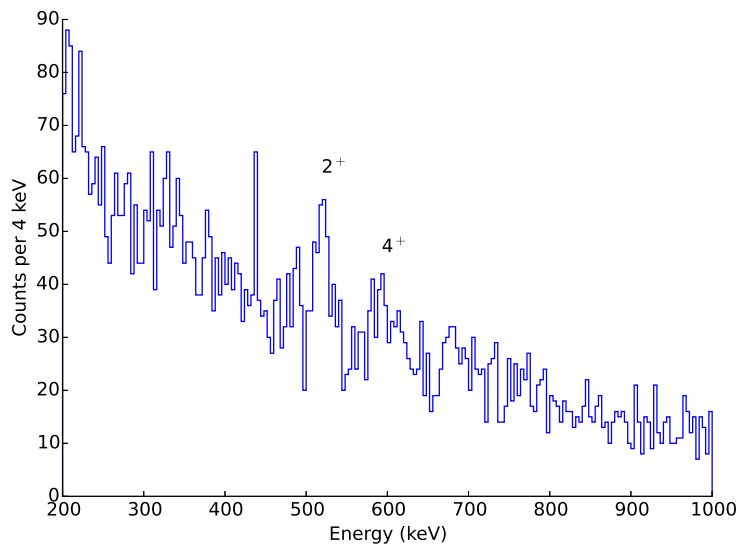


**Figure 7.4:** Gated  $\gamma$ -ray spectrum for the  $^{100}\text{Mo}$  nucleus.

---

7.6.2  $^{102}\text{Mo}$

---

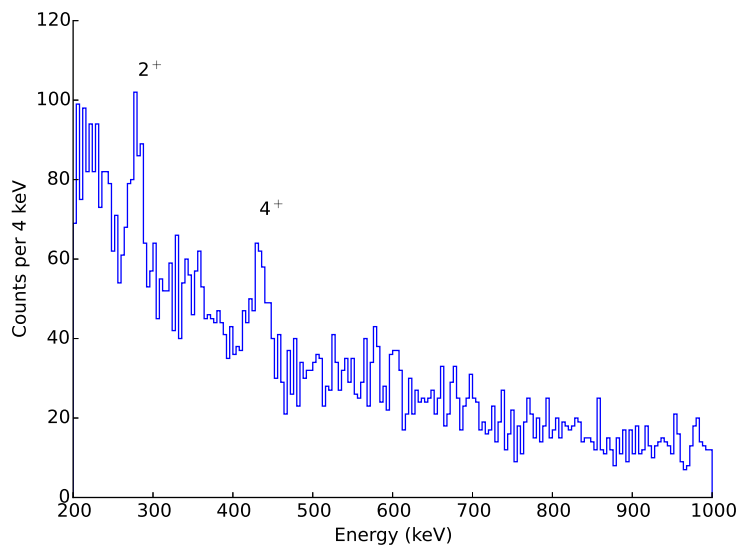


**Figure 7.5:** Gated  $\gamma$ -ray spectrum for the  $^{102}\text{Mo}$  nucleus.

---

### 7.6.3 $^{104}\text{Mo}$

---

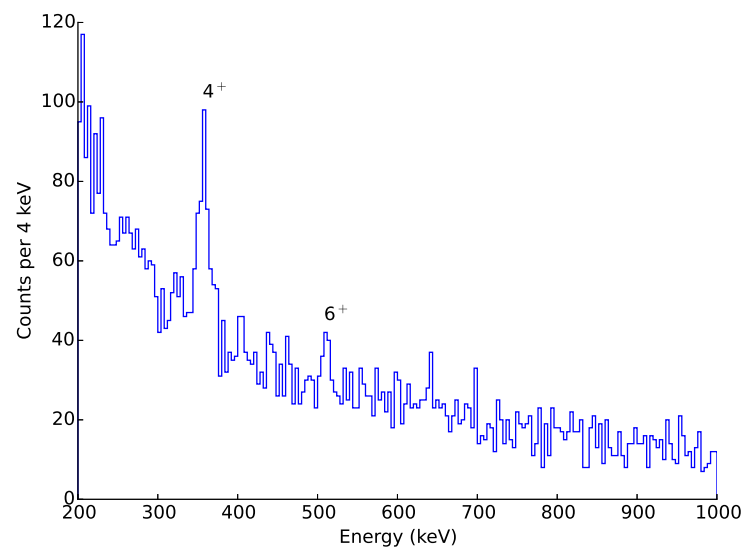


**Figure 7.6:** Gated  $\gamma$ -ray spectrum for the  $^{104}\text{Mo}$  nucleus.

---

### 7.6.4 $^{106}\text{Mo}$

---

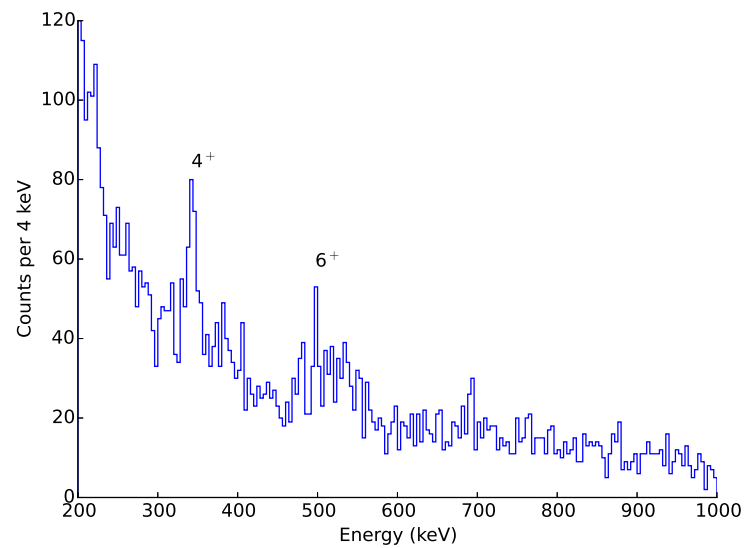


**Figure 7.7:** Gated  $\gamma$ -ray spectrum for the  $^{106}\text{Mo}$  nucleus.

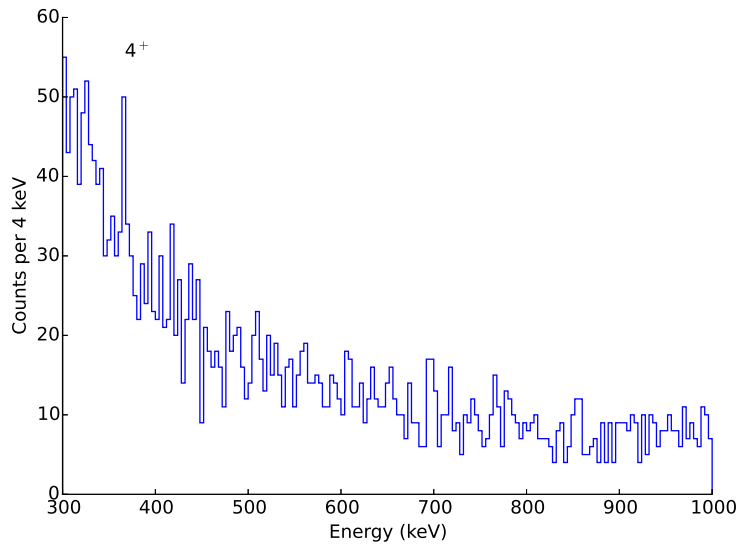


**Figure 7.8:** Gated  $\gamma$ -ray spectrum for the  $^{108}\text{Mo}$  nucleus.

---

## 7.7 Systematic determination of the centroid

---

The plots presented in this sections provide a visual verification of the fit procedure that was performed in order to determine the transition centroid in a systematic way. The model of our data is the same as presented in Section 4.3 but we took into account two decay exponential to model the background. This can be justified by the fact that there are two process that generates this background [69], thus two type of background.

---

### 7.7.1 $^{100}\text{Mo}$

---

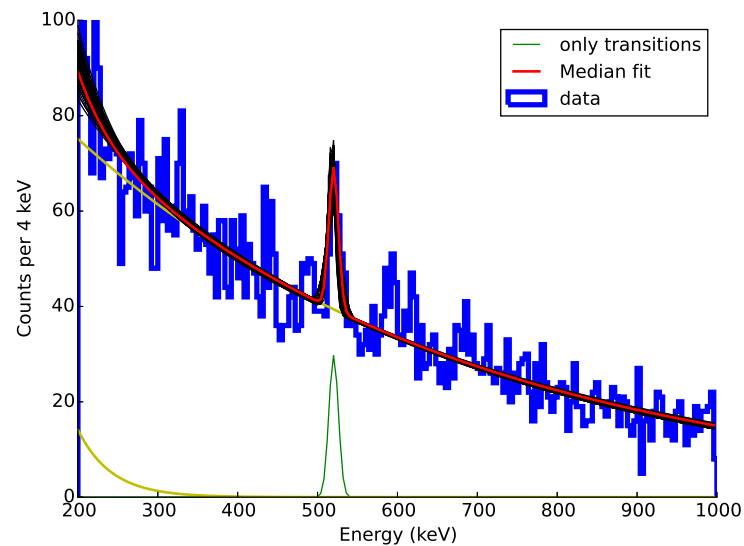


**Figure 7.9:** Fit of the  $^{100}\text{Mo}$   $4_1^+$  to  $2_1^+$  transition.

---

### 7.7.2 $^{102}\text{Mo}$

---

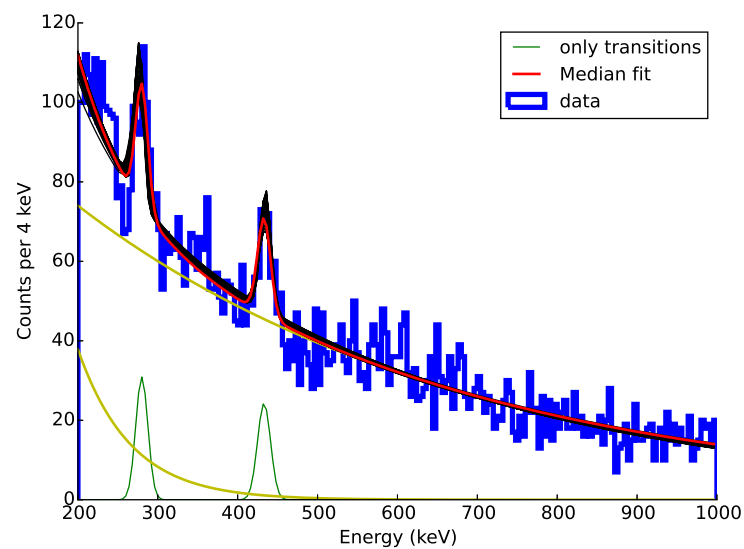


**Figure 7.10:** Fit of the  $^{102}\text{Mo}$   $4_1^+$  to  $2_1^+$  transition.

---

### 7.7.3 $^{104}\text{Mo}$

---

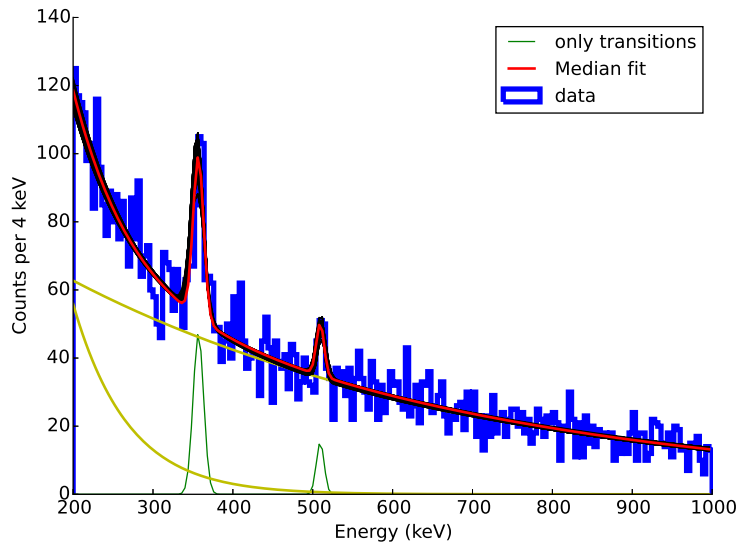


**Figure 7.11:** Fit of the  $^{104}\text{Mo}$   $4_1^+$  to  $2_1^+$  transition.

---

### 7.7.4 $^{106}\text{Mo}$

---

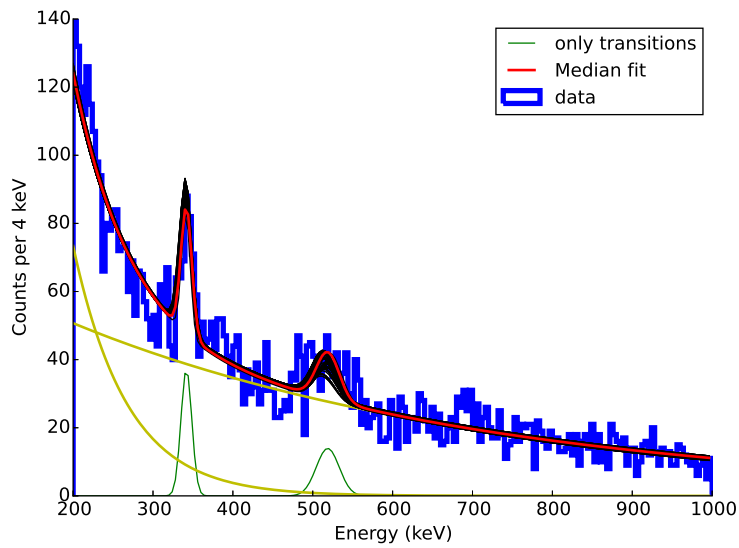


**Figure 7.12:** Fit of the  $^{106}\text{Mo}$   $4_1^+$  to  $2_1^+$  transition.



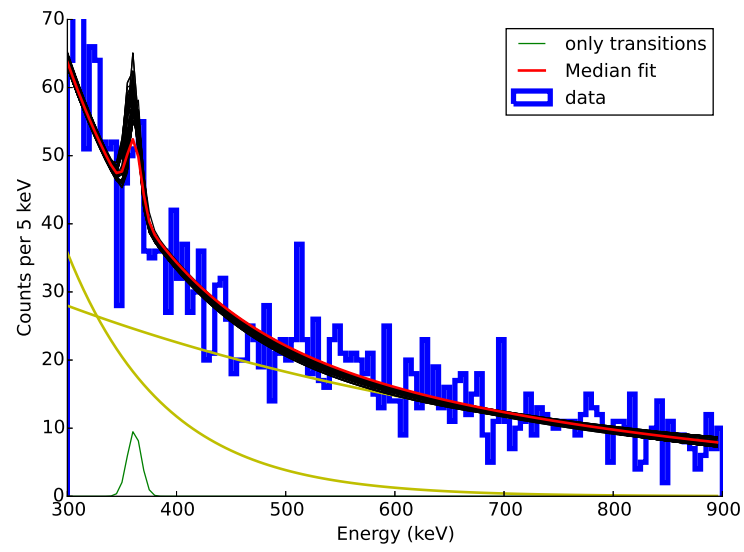


**Figure 7.13:** Fit of the  $^{108}\text{Mo}$   $4_1^+$  to  $2_1^+$  transition.



---

## Bibliography

- [1] H. Geissel, P. Armbruster, K.H. Behr, A. Brünle, K. Burkard, M. Chen, H. Folger, B. Franczak, H. Keller, O. Klepper, B. Langenbeck, F. Nickel, E. Pfeng, M. Pfützner, E. Roeckl, K. Rykaczewski, I. Schall, D. Schardt, C. Scheidenberger, K.-H. Schmidt, A. Schröter, T. Schwab, K. Sümmerer, M. Weber, G. Münzenberg, T. Brohm, H.-G. Clerc, M. Fauerbach, J.-J. Gaimard, A. Grewe, E. Hanelt, B. Knödler, M. Steiner, B. Voss, J. Weckenmann, C. Ziegler, A. Magel, H. Wollnik, J.P. Dufour, Y. Fujita, D.J. Vieira, and B. Sherrill. The {GSI} projectile fragment separator (FRS): a versatile magnetic system for relativistic heavy ions. *Nuclear Instruments and Methods in Physics Research Section B: Beam Interactions with Materials and Atoms*, 70(1–4):286 – 297, 1992. ISSN 0168-583X. doi: [http://dx.doi.org/10.1016/0168-583X\(92\)95944-M](http://dx.doi.org/10.1016/0168-583X(92)95944-M). URL: <http://www.sciencedirect.com/science/article/pii/0168583X9295944M>.
- [2] NUSTAR, -. URL: <http://www.fair-center.eu/for-users/experiments/nustar.html>.
- [3] Zsolt Podolyak. From RISING to HISPEC/DESPEC. *Nuclear Instruments and Methods in Physics Research Section B: Beam Interactions with Materials and Atoms*, 266(19-20):4589 – 4594, 2008. ISSN 0168-583X. doi: <http://dx.doi.org/10.1016/j.nimb.2008.05.106>. URL: <http://www.sciencedirect.com/science/article/pii/S0168583X08007829>. Proceedings of the {XVth} International Conference on Electromagnetic Isotope Separators and Techniques Related to their Applications.
- [4] S. Akkoyun, A. Algora, B. Alikhani, F. Ameil, G. de Angelis, L. Arnold, A. Astier, A. Ataç, Y. Aubert, C. Aufranc, A. Austin, S. Aydin, F. Azaiez, S. Badoer, D.L. Balabanski, D. Barrientos, G. Baulieu, R. Baumann, D. Bazzacco, F.A. Beck, T. Beck, P. Bednarczyk, M. Bellato, M.A. Bentley, G. Benzoni, R. Berthier, L. Berti, R. Beunard, G. Lo Bianco, B. Birkenbach, P.G. Bizzeti, A.M. Bizzeti-Sona, F. Le Blanc, J.M. Blasco, N. Blasi, D. Bloor, C. Boiano, M. Borsato, D. Bortolato, A.J. Boston, H.C. Boston, P. Bourgault, P. Boutachkov, A. Bouty, A. Bracco, S. Brambilla, I.P. Brawn, A. Brondi, S. Broussard, B. Bruyneel, D. Bucurescu, I. Burrows, A. Bürger, S. Cabaret, B. Cahan, E. Calore, F. Camera, A. Capsoni, F. Carrió, G. Casati, M. Castoldi, B. Cederwall, J.-L. Cercus, V. Chambert, M. El Chambit, R. Chapman, L. Charles, J. Chavas, E. Clément, P. Cocconi, S. Coelli, P.J. Coleman-Smith, A. Colombo, S. Colosimo, C. Commeaux, D. Conventi, R.J. Cooper, A. Corsi, A. Cortesi, L. Costa, F.C.L. Crespi, J.R. Cresswell, D.M. Cullen, D. Curien, A. Czermak, D. Delbourg, R. Depalo, T. Descombes, P. Désesquelles, P. Detistov, C. Diarra, F. Didierjean, M.R. Dimmock, Q.T. Doan, C. Domingo-Pardo, M. Doncel, F. Dorangeville, N. Dosme, Y. Drouen, G. Duchêne, B. Dulny, J. Eberth, P. Edelbruck, J. Egea, T. Engert, M.N. Erduran, S. Ertürk, C. Fanin, S. Fantinel, E. Farnea, T. Faul, M. Filliger, F. Filmer, Ch. Finck, G. de France, A. Gadea, W. Gast, A. Geraci, J. Gerl, R. Gernhäuser, A. Giannatiempo, A. Giaz, L. Gibelin, A. Givechev, N. Goel, V. González, A. Gottardo, X. Grave, J. Grebosz, R. Griffiths, A.N. Grint, P. Gros, L. Guevara, M. Gulmini, A. Görgen, H.T.M. Ha, T. Habermann, L.J. Harkness, H. Harroch, K. Hauschild, C. He, A. Hernández-Prieto, B. Hervieu, H. Hess, T. Hüyük, E. Ince, R. Isocrate, G. Jaworski, A. Johnson, J. Jolie, P. Jones, B. Jonson, P. Joshi, D.S. Judson, A. Jungclaus, M. Kaci, N. Karkour, M. Karolak, A. Kaşkaş, M. Kebbiri, R.S. Kempley, A. Khaplanov, S. Klupp, M. Kogimtzis, I. Kojouharov, A. Korichi, W. Korten, Th. Kröll, R. Krücken, N. Kurz, B.Y. Ky, M. Labiche, X. Lafay, L. Lavergne, I.H. Lazarus, S. Leboutelier, F. Lefebvre, E. Legay, L. Legeard, F. Lelli, S.M. Lenzi, S. Leoni, A. Lermitege, D. Lersch, J. Leske, S.C. Letts, S. Lhenoret, R.M. Lieder, D. Linget, J. Ljungvall, A. Lopez-Martens, A. Lotodé, S. Lunardi, A. Maj, J. van der Marel, Y. Mariette, N. Marginean, R. Marginean, G. Maron, A.R. Mather, W. Me<sub>2</sub>czyński, V. Mendéz, P. Medina, B. Melon, R. Menegazzo, D. Mengoni, E. Merchan, L. Mihailescu, C. Michelagnoli, J. Mierzejewski, L. Milechina, B. Million, K. Mitev, P. Molini, D. Montanari, S. Moon, F. Morbiducci, R. Moro, P.S. Morrall, O. Moeller, A. Nannini, D.R. Napoli, L. Nelson, M. Nespolo, V.L. Ngo, M. Nicoletto, R. Nicolini, Y. Le Noa, P.J. Nolan, M. Norman, J. Nyberg, A. Obertelli, A. Olariu, R. Orlandi, D.C. Oxley, C. Özben, M. Ozille, C. Oziol, E. Pachoud, M. Palacz, J. Palin, J. Pancin, C. Parisel, P. Pariset, G. Pascovici, R. Peghin, L. Pellegrini, A. Perego, S. Perrier, M. Petcu, P. Petkov, C. Petrache, E. Pierre, N. Pietralla, S. Pietri, M. Pignanelli, I. Piqueras, Z. Podolyak, P. Le Pouhalec, J. Pouthas, D. Pugnère, V.F.E. Pucknell, A. Pullia, B. Quintana, R. Raine, G. Rainovski, L. Ramina, G. Rampazzo, G. La Rana, M. Rebeschini,

- F. Recchia, N. Redon, M. Reese, P. Reiter, P.H. Regan, S. Riboldi, M. Richer, M. Rigato, S. Rigby, G. Ripamonti, A.P. Robinson, J. Robin, J. Roccaz, J.-A. Ropert, B. Rossé, C. Rossi Alvarez, D. Rosso, B. Rubio, D. Rudolph, F. Saillant, E. Şahin, F. Salomon, M.-D. Salsac, J. Salt, G. Salvato, J. Sampson, E. Sanchis, C. Santos, H. Schaffner, M. Schlarb, D.P. Scraggs, D. Seddon, M. Şenyiğit, M.-H. Sigward, G. Simpson, J. Simpson, M. Slee, J.F. Smith, P. Sona, B. Sowicki, P. Spolaore, C. Stahl, T. Stanios, E. Stefanova, O. Stézowski, J. Strachan, G. Suliman, P.-A. Söderstrom, J.L. Tain, S. Tanguy, S. Tashenov, Ch. Theisen, J. Thornhill, F. Tomasi, N. Toniolo, R. Touzery, B. Travers, A. Triossi, M. Tripon, K.M.M. Tun-Lanoë, M. Turcato, C. Unsworth, C.A. Ur, J.J. Valiente-Dobon, V. Vandone, E. Vardaci, R. Venturelli, F. Veronese, Ch. Veysière, E. Viscione, R. Wadsworth, P.M. Walker, N. Warr, C. Weber, D. Weisshaar, D. Wells, O. Wieland, A. Wiens, G. Wittwer, H.J. Wollersheim, F. Zocca, N.V. Zamfir, M. Ziebliński, and A. Zucchiatti. AGATA Advanced GAMMA Tracking Array. *Nuclear Instruments and Methods in Physics Research Section A: Accelerators, Spectrometers, Detectors and Associated Equipment*, 668(0): 26 – 58, 2012. ISSN 0168-9002. doi: <http://dx.doi.org/10.1016/j.nima.2011.11.081>. URL: <http://www.sciencedirect.com/science/article/pii/S0168900211021516>.
- [5] P. Golubev, A. Wendt, L. Scruton, J. Taprogge, D. Rudolph, P. Reiter, M.A. Bentley, V. Avdeichikov, P. Boutachkov, S.P. Fox, J. Gerl, Ch. Gørgen, R. Hoischen, N. Kurz, B.S. Nara Singh, G. Pascovici, S. Pietri, H. Schaffner, M.J. Taylor, S. Thiel, and H.J. Wollersheim. The Lund York Cologne Calorimeter (LYCCA): Concept, design and prototype developments for a FAIR-NUSTAR detector system to discriminate relativistic heavy-ion reaction products. *Nuclear Instruments and Methods in Physics Research Section A: Accelerators, Spectrometers, Detectors and Associated Equipment*, 723(0):55 – 66, 2013. ISSN 0168-9002. doi: <http://dx.doi.org/10.1016/j.nima.2013.04.058>. URL: <http://www.sciencedirect.com/science/article/pii/S0168900213004798>.
- [6] A. Giaz, L. Pellegrì, S. Riboldi, F. Camera, N. Blasi, C. Boiano, A. Bracco, S. Brambilla, S. Ceruti, S. Coelli, F.C.L. Crespi, M. Csatlos, S. Frega, J. Gulyàs, A. Krasznahorkay, S. Lodetti, B. Million, A. Owens, F. Quarati, L. Stuhl, and O. Wieland. Characterization of large volume 3.5" × 8" LaBr<sub>3</sub>:Ce detectors. *Nuclear Instruments and Methods in Physics Research Section A: Accelerators, Spectrometers, Detectors and Associated Equipment*, 729(0):910 – 921, 2013. ISSN 0168-9002. doi: <http://dx.doi.org/10.1016/j.nima.2013.07.084>. URL: <http://www.sciencedirect.com/science/article/pii/S016890021301111X>.
- [7] N. Pietralla, M. Reese, M.L. Cortes, F. Ameil, D. Bazzacco, M.A. Bentley, P. Boutachkov, C. Domingo-Pardo, A. Gadea, J. Gerl, N. Goel, P. Golubev, M. Górska, G. Guastalla, T. Habermann, I. Kojouharov, W. Korten, E. Merchán, S. Pietri, D. Ralet, P. Reiter, D. Rudolph, H. Schaffner, P.P. Singh, O. Wieland, and H.J. Wollersheim. On the Road to FAIR: 1st Operation of AGATA in PreSPEC at GSI. *EPJ Web of Conferences*, 66:02083, 2014. doi: 10.1051/epjconf/20146602083. URL: <http://dx.doi.org/10.1051/epjconf/20146602083>.
- [8] O. Wieland, A. Bracco, F. Camera, R. Avigo, the PRESPEC, and AGATA collaborations. Search for E1 strength in 62,64 Fe around the threshold. *Journal of Physics: Conference Series*, 580(1):012058, 2015. URL: <http://stacks.iop.org/1742-6596/580/i=1/a=012058>.
- [9] T. Alexander, Zs. Podolyák, M.L. Cortes, J. Gerl, D. Rudolph, L.G. Sarmiento, F. Ameil, T. Arici, D. Bazzacco, Ch. Bauer, M.A. Bentley, A. Blazhev, M. Bowry, P. Boutachkov, R. Carroll, C. Fahlander, A. Gadea, J. Gellanki, W. Gelletly, A. Givechev, N. Goel, P. Golubev, M. Górska, A. Gottardo, E. Gregor, G. Guastalla, T. Habermann, M. Hackstein, A. Jungclaus, I. Kojouharov, W. Korten, S. Kumar, N. Kurz, N. Lalović, M. Lettmann, C. Lizarazo, C. Louchart, S. Mandal, E. Merchán, C. Michelagnoli, Th. Möller, K. Moschner, Z. Patel, N. Pietralla, S. Pietri, D. Ralet, M. Reese, P.H. Regan, P. Reiter, H. Schaffner, P. Singh, C. Stahl, R. Stegmann, O. Stezowski, J. Taprogge, P. Thöle, P.M. Walker, O. Wieland, A. Wendt, E. Wilson, R. Wood, and H.-J. Wollersheim. Isomeric Ratios in 206Hg. *Acta Physica Polonica B*, 46, 2015. doi: DOI:10.5506/APhysPolB.46.601.
- [10] S. Pietri, J. Gerl, F. Ameil, P. Boutachkov, A. Estrade, H. Geissel, N. Goel, M. Gorska, R. Knoebel, I. Kojouharov, N. Kurz, A. Prochazka, D. Ralet, H. Schaffner, C. Scheidenberger, N. Winckler, M. Winkler, , H.J. Wollersheim, P. Boutachkov, E. Merchan, N. Pietralla, M. Reese, P. Doornenbal, W. Korten, M.D. Salsac, B. Bruyneel, L. Grete, P. Regan, Zs. Podolyak, T. Alexander, A. Bruce, F. Browne, T. Bäck, B. Cederwall, F. Ghazi Moradi, A. Johnson, A. Atac, Zs. Dombradi, Z. Elekes, D. Sohler, A. Algora, J. Agramunt, C. Domingo Pardo, D. Curien, G. Duchêne, and A. Gotardo. GSI Experimental Proposal – a PreSPEC proposal – Shape evolution in neutron-rich Zr isotopes – Spokesperson : S. Pietri, P. Doornenbal GSI contact : J. Gerl, 2011.
- [11] J. P. Delaroche, M. Girod, J. Libert, H. Goutte, S. Hilaire, S. Péru, N. Pillet, and G. F. Bertsch. Structure of even-even nuclei using a mapped collective Hamiltonian and the D1S Gogny interaction. *Phys. Rev. C*, 81:014303,

- 
- Jan 2010. doi: 10.1103/PhysRevC.81.014303. URL:  
<http://link.aps.org/doi/10.1103/PhysRevC.81.014303>.
- [12] L. Grente. *Structure des fragments de fission de masse  $A = 100 - 110$  : mesure de temps de vie et analyses en champ moyen et au-delà*. PhD thesis, Université Paris-Sud, 2014.
- [13] B. J. P. Gall. *Super et Hyper deformation du noyau atomique: du discret au continu*. Annales de physiques, EDP science, 1999.
- [14] J.M. Eisenberg and W. Greiner. *Nuclear Theory 1: Nuclear Models*. North Holland Publishing Company, 2nd edition edition, 1978.
- [15] David Lawrence Hill and John Archibald Wheeler. Nuclear Constitution and the Interpretation of Fission Phenomena. *Phys. Rev.*, 89:1102–1145, Mar 1953. doi: 10.1103/PhysRev.89.1102. URL:  
<http://link.aps.org/doi/10.1103/PhysRev.89.1102>.
- [16] Aage Niels Bohr. The coupling of nuclear surface oscillations to the motion of individual nucleons. *Dan. Mat. Fys. Medd.*, 26(14):1–40, 1952.
- [17] L. Fortunato. Solutions of the Bohr Hamiltonian, a compendium. *The European Physical Journal A - Hadrons and Nuclei*, 26(1):1–30, 2005. ISSN 1434-6001. doi: 10.1140/epjad/i2005-07-115-8. URL:  
<http://dx.doi.org/10.1140/epjad/i2005-07-115-8>.
- [18] F. Iachello and A. Arima. Boson symmetries in vibrational nuclei. *Physics Letters B*, 53(4):309 – 312, 1974. ISSN 0370-2693. doi: [http://dx.doi.org/10.1016/0370-2693\(74\)90389-X](http://dx.doi.org/10.1016/0370-2693(74)90389-X). URL:  
<http://www.sciencedirect.com/science/article/pii/037026937490389X>.
- [19] Richard F. Casten. *Nuclear Structure from a simpler perspective*. Oxford Studies in nuclear physics, 200.
- [20] Gregoire Henning. *Stability of Transfermium Elements at High Spin : Measuring the Fission Barrier of  $^{254}\text{No}$* . PhD thesis, Universite Paris Sud - Paris XI, 2012.
- [21] Aage Bohr and Ben R. Mottelson. *Nuclear structure: Volume II: Nuclear deformations*. World Scientific, 1998.
- [22] R. F. Casten. Shape phase transitions and critical-point phenomena in atomic nuclei. *Nature Physics*, 2:811–820, 2006. doi: doi:10.1038/nphys451. URL:  
<http://www.nature.com/nphys/journal/v2/n12/pdf/nphys451.pdf>.
- [23] F. Iachello. Dynamic Symmetries at the Critical Point. *Phys. Rev. Lett.*, 85:3580–3583, Oct 2000. doi: 10.1103/PhysRevLett.85.3580. URL:  
<http://link.aps.org/doi/10.1103/PhysRevLett.85.3580>.
- [24] F. Iachello. Analytic Description of Critical Point Nuclei in a Spherical-Axially Deformed Shape Phase Transition. *Phys. Rev. Lett.*, 87:052502, Jul 2001. doi: 10.1103/PhysRevLett.87.052502. URL:  
<http://link.aps.org/doi/10.1103/PhysRevLett.87.052502>.
- [25] N. Pietralla and O. M. Gorbachenko. Evolution of the “ $\beta$  excitation” in axially symmetric transitional nuclei. *Phys. Rev. C*, 70:011304, Jul 2004. doi: 10.1103/PhysRevC.70.011304. URL:  
<http://link.aps.org/doi/10.1103/PhysRevC.70.011304>.
- [26] Dennis Bonatsos, D. Lenis, N. Pietralla, and P. A. Terziev.  $\gamma$ -soft analog of the confined  $\beta$ -soft rotor model. *Phys. Rev. C*, 74:044306, Oct 2006. doi: 10.1103/PhysRevC.74.044306. URL:  
<http://link.aps.org/doi/10.1103/PhysRevC.74.044306>.
- [27] D. Lacroix. Review of mean-field theory. In *International Ecole Joliot Curie school on “Physics at the femtometer scale”*, 2011. URL:  
[http://ejc2011.sciencesconf.org/conference/ejc2011/EJC2011\\_lacroix.pdf](http://ejc2011.sciencesconf.org/conference/ejc2011/EJC2011_lacroix.pdf).
- [28] Claude Cohen-Tannoudji, Bernard Diu, and Franck Laloë. *Quantum Mechanics*, volume II. Willey Interscience, New York, 1992.
- [29] Aage Bohr and Ben R. Mottelson. *Nuclear structure: Volume I: Single particle motion*. World Scientific, 1998.

- [30] L. Grodzins. The uniform behaviour of electric quadrupole transition probabilities from first 2+ states in even-even nuclei. *Physics Letters*, 2(2):88 – 91, 1962. ISSN 0031-9163. doi: [http://dx.doi.org/10.1016/0031-9163\(62\)90162-2](http://dx.doi.org/10.1016/0031-9163(62)90162-2). URL: <http://www.sciencedirect.com/science/article/pii/0031916362901622>.
- [31] R. V. Jolos, P. von Brentano, and N. Pietralla. Generalized Grodzins relation. *Phys. Rev. C*, 71:044305, Apr 2005. doi: 10.1103/PhysRevC.71.044305. URL: <http://link.aps.org/doi/10.1103/PhysRevC.71.044305>.
- [32] R. V. Jolos, P. von Brentano, A. Dewald, and N. Pietralla. Spin dependence of intrinsic and transition quadrupole moments. *Phys. Rev. C*, 72:024310, Aug 2005. doi: 10.1103/PhysRevC.72.024310. URL: <http://link.aps.org/doi/10.1103/PhysRevC.72.024310>.
- [33] Evaluated Nuclear Structure Data File, 03-03-2015. URL: [www.nndc.bnl.gov/ensdf/](http://www.nndc.bnl.gov/ensdf/).
- [34] T. Sumikama, K. Yoshinaga, H. Watanabe, S. Nishimura, Y. Miyashita, K. Yamaguchi, K. Sugimoto, J. Chiba, Z. Li, H. Baba, J. S. Berryman, N. Blasi, A. Bracco, F. Camera, P. Doornenbal, S. Go, T. Hashimoto, S. Hayakawa, C. Hinke, E. Ideguchi, T. Isobe, Y. Ito, D. G. Jenkins, Y. Kawada, N. Kobayashi, Y. Kondo, R. Krücken, S. Kubono, G. Lorusso, T. Nakano, M. Kurata-Nishimura, A. Odahara, H. J. Ong, S. Ota, Zs. Podolyák, H. Sakurai, H. Scheit, K. Steiger, D. Steppenbeck, S. Takano, A. Takashima, K. Tajiri, T. Teranishi, Y. Wakabayashi, P. M. Walker, O. Wieland, and H. Yamaguchi. Structural Evolution in the Neutron-Rich Nuclei  $^{106}\text{Zr}$  and  $^{108}\text{Zr}$ . *Phys. Rev. Lett.*, 106:202501, May 2011. doi: 10.1103/PhysRevLett.106.202501. URL: <http://link.aps.org/doi/10.1103/PhysRevLett.106.202501>.
- [35] F. R. Xu, P. M. Walker, and R. Wyss. Oblate stability of  $A \approx 110$  nuclei near the  $r$ -process path. *Phys. Rev. C*, 65:021303, Jan 2002. doi: 10.1103/PhysRevC.65.021303. URL: <http://link.aps.org/doi/10.1103/PhysRevC.65.021303>.
- [36] N. Schunck, J. Dudek, A. Gózdź, and P. H. Regan. Tetrahedral symmetry in ground and low-lying states of exotic  $A \sim 110$  nuclei. *Phys. Rev. C*, 69:061305, Jun 2004. doi: 10.1103/PhysRevC.69.061305. URL: <http://link.aps.org/doi/10.1103/PhysRevC.69.061305>.
- [37] A. G. Smith, J. L. Durell, W. R. Phillips, W. Urban, P. Sarriguren, and I. Ahmad. Lifetime measurements and nuclear deformation in the  $A \approx 100$  region. *Phys. Rev. C*, 86:014321, Jul 2012. doi: 10.1103/PhysRevC.86.014321. URL: <http://link.aps.org/doi/10.1103/PhysRevC.86.014321>.
- [38] A. M. Bruce, S. Lalkovski, A. M. Denis Bacelar, M. Górska, S. Pietri, Zs. Podolyák, Y. Shi, P. M. Walker, F. R. Xu, P. Bednarczyk, L. Cáceres, E. Casarejos, I. J. Cullen, P. Doornenbal, G. F. Farrelly, A. B. Garnsworthy, H. Geissel, W. Gelletly, J. Gerl, J. Grębosz, C. Hinke, G. Ilie, G. Jaworski, I. Kojouharov, N. Kurz, S. Myalski, M. Palacz, W. Prokopowicz, P. H. Regan, H. Schaffner, S. Steer, S. Tashenov, and H. J. Wollersheim. Shape coexistence and isomeric states in neutron-rich  $^{112}\text{Tc}$  and  $^{113}\text{Tc}$ . *Phys. Rev. C*, 82:044312, Oct 2010. doi: 10.1103/PhysRevC.82.044312. URL: <http://link.aps.org/doi/10.1103/PhysRevC.82.044312>.
- [39] P.-A. Söderström, G. Lorusso, H. Watanabe, S. Nishimura, P. Doornenbal, G. Thiamova, F. Browne, G. Gey, H. S. Jung, T. Sumikama, J. Taprogge, Zs. Vajta, J. Wu, Z. Y. Xu, H. Baba, G. Benzioni, K. Y. Chae, F. C. L. Crespi, N. Fukuda, R. Gernhäuser, N. Inabe, T. Isobe, A. Jungclaus, D. Kameda, G. D. Kim, Y.-K. Kim, I. Kojouharov, F. G. Kondev, T. Kubo, N. Kurz, Y. K. Kwon, G. J. Lane, Z. Li, A. Montaner-Pizá, K. Moschner, F. Naqvi, M. Niikura, H. Nishibata, A. Odahara, R. Orlandi, Z. Patel, Zs. Podolyák, H. Sakurai, H. Schaffner, G. S. Simpson, K. Steiger, H. Suzuki, H. Takeda, A. Wendt, A. Yagi, and K. Yoshinaga. Shape evolution in  $^{116,118}\text{Ru}$ : Triaxiality and transition between the O(6) and U(5) dynamical symmetries. *Phys. Rev. C*, 88:024301, Aug 2013. doi: 10.1103/PhysRevC.88.024301. URL: <http://link.aps.org/doi/10.1103/PhysRevC.88.024301>.
- [40] J. A. Pinston, W. Urban, Ch. Droste, T. Rza a Urban, J. Genevey, G. Simpson, J. L. Durell, A. G. Smith, B. J. Varley, and I. Ahmad. Triaxiality in  $^{105}\text{Mo}$  and  $^{107}\text{Mo}$  from the low to intermediate spin region. *Phys. Rev. C*, 74:064304, Dec 2006. doi: 10.1103/PhysRevC.74.064304. URL: <http://link.aps.org/doi/10.1103/PhysRevC.74.064304>.

- [41] C. Hutter, R. Krücken, A. Aprahamian, C. J. Barton, C. W. Beausang, M. A. Caprio, R. F. Casten, W.-T. Chou, R. M. Clark, D. Cline, J. R. Cooper, M. Cromaz, A. A. Hecht, A. O. Macchiavelli, N. Pietralla, M. Shawcross, M. A. Stoyer, C. Y. Wu, and N. V. Zamfir.  $B(E2)$  values and the search for the critical point symmetry  $X(5)$  in  $^{104}\text{Mo}$  and  $^{106}\text{Mo}$ . *Phys. Rev. C*, 67:054315, May 2003. doi: 10.1103/PhysRevC.67.054315. URL: <http://link.aps.org/doi/10.1103/PhysRevC.67.054315>.
- [42] M. A. Caprio, N. V. Zamfir, R. F. Casten, C. J. Barton, C. W. Beausang, J. R. Cooper, A. A. Hecht, R. Krücken, H. Newman, J. R. Novak, N. Pietralla, A. Wolf, and K. E. Zyromski. Low-spin structure of  $^{156}\text{Dy}$  through  $\gamma$ -ray spectroscopy. *Phys. Rev. C*, 66:054310, Nov 2002. doi: 10.1103/PhysRevC.66.054310. URL: <http://link.aps.org/doi/10.1103/PhysRevC.66.054310>.
- [43] C. Domingo-Pardo, D. Bazzacco, P. Doornenbal, E. Farnea, A. Gadea, J. Gerl, and H.J. Wollersheim. Conceptual design and performance study for the first implementation of AGATA at the in-flight RIB facility of GSI. *Nuclear Instruments and Methods in Physics Research Section A: Accelerators, Spectrometers, Detectors and Associated Equipment*, 694(0):297 – 312, 2012. ISSN 0168-9002. doi: <http://dx.doi.org/10.1016/j.nima.2012.08.039>. URL: <http://www.sciencedirect.com/science/article/pii/S0168900212009102>.
- [44] W. Henning. Physics with SIS/ESR at GSI. *Nuclear Physics A*, 538(0):637 – 648, 1992. ISSN 0375-9474. doi: [http://dx.doi.org/10.1016/0375-9474\(92\)90812-X](http://dx.doi.org/10.1016/0375-9474(92)90812-X). URL: <http://www.sciencedirect.com/science/article/pii/037594749290812X>.
- [45] B. Jurado, K.-H. Schmidt, and K.-H. Behr. Application of a secondary-electron transmission monitor for high-precision intensity measurements of relativistic heavy-ion beams. *Nuclear Instruments and Methods in Physics Research Section A: Accelerators, Spectrometers, Detectors and Associated Equipment*, 483(3):603 – 610, 2002. ISSN 0168-9002. doi: [http://dx.doi.org/10.1016/S0168-9002\(01\)01931-3](http://dx.doi.org/10.1016/S0168-9002(01)01931-3). URL: <http://www.sciencedirect.com/science/article/pii/S0168900201019313>.
- [46] T. Kurtikian Nieto. *Production and  $\beta$  decay half-life of heavy neutron rich nuclei approaching the stellar nucleosynthesis r-process path around  $A=195$* . PhD thesis, Universidade de Santiago de Compostella, 2007.
- [47] H. Wiedemann. *Particle Accelerators Physics*. Springer 3rd Edition, 2007.
- [48] H. Bethe and J. Ashkin. *Experimental Nuclear Physics*. E. Segre, J. Wiley, 1953.
- [49] G. Münzenberg. The separation techniques for secondary beams. *Nuclear Instruments and Methods in Physics Research Section B: Beam Interactions with Materials and Atoms*, 70(1–4):265 – 275, 1992. ISSN 0168-583X. doi: [http://dx.doi.org/10.1016/0168-583X\(92\)95942-K](http://dx.doi.org/10.1016/0168-583X(92)95942-K). URL: <http://www.sciencedirect.com/science/article/pii/0168583X9295942K>.
- [50] H. Weick. FRS settings course. Nov. 2010.
- [51] C. Scheidenberger, T. Stöhlker, W.E Meyerhof, H Geissel, P.H Mokler, and B Blank. Charge states of relativistic heavy ions in matter. *Nuclear Instruments and Methods in Physics Research Section B: Beam Interactions with Materials and Atoms*, 142(4):441 – 462, 1998. ISSN 0168-583X. doi: [http://dx.doi.org/10.1016/S0168-583X\(98\)00244-4](http://dx.doi.org/10.1016/S0168-583X(98)00244-4). URL: <http://www.sciencedirect.com/science/article/pii/S0168583X98002444>.
- [52] V. Hlinka, M. Ivanov, R. Janik, B. Sitar, P. Strmen, I. Szarka, T. Baumann, H. Geissel, and W. Schwab. Time projection chambers for tracking and identification of radioactive beams. *Nuclear Instruments and Methods in Physics Research Section A: Accelerators, Spectrometers, Detectors and Associated Equipment*, 419(23):503 – 510, 1998. ISSN 0168-9002. doi: [http://dx.doi.org/10.1016/S0168-9002\(98\)00827-4](http://dx.doi.org/10.1016/S0168-9002(98)00827-4). URL: <http://www.sciencedirect.com/science/article/pii/S0168900298008274>.
- [53] A. Stolz, T. Fästermann, J. Friese, P. Kienle, H.-J. Körner, M. Münch, R. Schneider, E. Wefers, K. Zeitelhack, K. Sümmerer, H. Geissel, J. Gerl, G. Münzenberg, C. Schlegel, R. S. Simon, H. Weick, M. Hellström, M. N. Mineva, and P. Thirolf. Projectile fragmentation of  $^{112}\text{Sn}$  at  $E_{\text{lab}} = 1\text{A GeV}$ . *Phys. Rev. C*, 65:064603, May 2002. doi: 10.1103/PhysRevC.65.064603. URL: <http://link.aps.org/doi/10.1103/PhysRevC.65.064603>.
- [54] A. Wendt. *Isospin symmetry in the sd shell. Coulomb excitation of  $^{33}\text{Ar}$  at relativistic energies and the new "Lund-York-Cologne-Calorimeter"*. PhD thesis, Köln University, 2013.



- [55] R. Hoischen, S. Pietri, D. Rudolph, W. Prokopowicz, H. Schaffner, S. Emde, P. Golubev, A. Wendt, N. Kurz, H.J. Wollersheim, and J. Gerl. Fast timing with plastic scintillators for in-beam heavy-ion spectroscopy. *Nuclear Instruments and Methods in Physics Research Section A: Accelerators, Spectrometers, Detectors and Associated Equipment*, 654(1):354 – 360, 2011. ISSN 0168-9002. doi: <http://dx.doi.org/10.1016/j.nima.2011.07.013>. URL: <http://www.sciencedirect.com/science/article/pii/S016890021101415X>.
- [56] M. Reese, N. Pietralla, P. Golubev, and D. Rudolph. *Position Sensitivity of LYCCA Time-of-Flight Detectors*, volume 2013-1 of *GSI Report*, page 185. GSI Helmholtzzentrum für Schwerionenforschung, Darmstadt, 2013.
- [57] R. Venturelli and D. Bazzacco. Adaptive Grid Search as Pulse Shape Analysis Algorithm for gamma-Tracking and Results. *LNL Annual Report*, 2004.
- [58] P.-A. Söderström, F. Recchia, J. Nyberg, A. Al-Adili, A. Ataç, S. Aydin, D. Bazzacco, P. Bednarczyk, B. Birkenbach, D. Bortolato, A.J. Boston, H.C. Boston, B. Bruyneel, D. Bucurescu, E. Calore, S. Colosimo, F.C.L. Crespi, N. Dosme, J. Eberth, E. Farnea, F. Filmer, A. Gadea, A. Gottardo, X. Grave, J. Grebosz, R. Griffiths, M. Gulinini, T. Habermann, H. Hess, G. Jaworski, P. Jones, P. Joshi, D.S. Judson, R. Kempley, A. Khaplanov, E. Legay, D. Lersch, J. Ljungvall, A. Lopez-Martens, W. Meczynski, D. Mengoni, C. Michelagnoli, P. Molini, D.R. Napoli, R. Orlandi, G. Pascovici, A. Pullia, P. Reiter, E. Sahin, J.F. Smith, J. Strachan, D. Tonev, C. Unsworth, C.A. Ur, J.J. Valiente-Dobón, C. Veyssiere, and A. Wiens. Interaction position resolution simulations and in-beam measurements of the AGATA HPGe detectors. *Nuclear Instruments and Methods in Physics Research Section A: Accelerators, Spectrometers, Detectors and Associated Equipment*, 638(1):96 – 109, 2011. ISSN 0168-9002. doi: <http://dx.doi.org/10.1016/j.nima.2011.02.089>. URL: <http://www.sciencedirect.com/science/article/pii/S016890021100489X>.
- [59] B. Millon. private communication.
- [60] Glenn F. Knoll. *Radiation detection and measurement*. John Wiley and sons, 1989.
- [61] C. Michelagnoli. *The lifetime of the 6.79MeV state in 15O as a challenge for nuclear astrophysics and gamma-ray spectroscopy*. PhD thesis, Padova University, 2013.
- [62] F. Recchia, D. Bazzacco, E. Farnea, A. Gadea, R. Venturelli, T. Beck, P. Bednarczyk, A. Buerger, A. Dewald, M. Dimmock, G. Duchêne, J. Eberth, T. Faul, J. Gerl, R. Gernhaeuser, K. Hauschild, A. Holler, P. Jones, W. Korten, Th. Kröll, R. Krücken, N. Kurz, J. Ljungvall, S. Lunardi, P. Maierbeck, D. Mengoni, J. Nyberg, L. Nelson, G. Pascovici, P. Reiter, H. Schaffner, M. Schlarb, T. Steinhardt, O. Thelen, C.A. Ur, J.J. Valiente Dobon, and D. Weißhaar. Position resolution of the prototype AGATA triple-cluster detector from an in-beam experiment. *Nuclear Instruments and Methods in Physics Research Section A: Accelerators, Spectrometers, Detectors and Associated Equipment*, 604(3):555 – 562, 2009. ISSN 0168-9002. doi: <http://dx.doi.org/10.1016/j.nima.2009.02.042>. URL: <http://www.sciencedirect.com/science/article/pii/S0168900209004124>.
- [63] M. Descovich, P.J. Nolan, A.J. Boston, J. Dobson, S. Gros, J.R. Cresswell, J. Simpson, I. Lazarus, P.H. Regan, J.J. Valiente-Dobon, P. Sellin, and C.J. Pearson. The position response of a large-volume segmented germanium detector. *Nuclear Instruments and Methods in Physics Research Section A: Accelerators, Spectrometers, Detectors and Associated Equipment*, 553(3):512 – 521, 2005. ISSN 0168-9002. doi: <http://dx.doi.org/10.1016/j.nima.2005.06.052>. URL: <http://www.sciencedirect.com/science/article/pii/S0168900205013331>.
- [64] F.C.L. Crespi, F. Camera, B. Million, M. Sassi, O. Wieland, and A. Bracco. A novel technique for the characterization of a HPGe detector response based on pulse shape comparison. *Nuclear Instruments and Methods in Physics Research Section A: Accelerators, Spectrometers, Detectors and Associated Equipment*, 593(3):440 – 447, 2008. ISSN 0168-9002. doi: <http://dx.doi.org/10.1016/j.nima.2008.05.057>. URL: <http://www.sciencedirect.com/science/article/pii/S0168900208007821>.
- [65] N. Goel, C. Domingo-Pardo, T. Habermann, F. Ameil, T. Engert, J. Gerl, I. Kojouharov, J. Maruhn, N. Pietralla, and H. Schaffner. Characterisation of a symmetric AGATA detector using the imaging scanning technique. *Nuclear Instruments and Methods in Physics Research Section A: Accelerators, Spectrometers, Detectors and Associated Equipment*, 700(0):10 – 21, 2013. ISSN 0168-9002. doi: <http://dx.doi.org/10.1016/j.nima.2012.10.028>. URL: <http://www.sciencedirect.com/science/article/pii/S0168900212011606>.
- [66] B. Bruyneel. *Caraterization of Segmented Large Volume, High purity Germanium Detectors*. PhD thesis, Universität Köln, 2006.



- [67] Dino Bazzacco. The Advanced Gamma Ray Tracking Array AGATA. *Nuclear Physics A*, 746(0):248 – 254, 2004. ISSN 0375-9474. doi: <http://dx.doi.org/10.1016/j.nuclphysa.2004.09.148>. URL: <http://www.sciencedirect.com/science/article/pii/S0375947404009625>. Proceedings of the Sixth International Conference on Radioactive Nuclear Beams (RNB6).
- [68] D. Bazzacco, B. Cederwall, J. Cresswell, G. Duchêne, J. Eberth, W. Gast, J. Gerl, W. Korten, I. Lazarus, R.M. Lieder, J. Simpson, and D. Weisshaar. *AGATA, Technical Proposal for an Advanced Gamma Tracking Array for the European Gamma Spectroscopy Community*. AGATA collaboration, 1991. URL: <https://hal.archives-ouvertes.fr/hal-00729050>.
- [69] H.J. Wollersheim, D.E. Appelbe, A. Banu, R. Bassini, T. Beck, F. Becker, P. Bednarczyk, K.-H. Behr, M.A. Bentley, G. Benzoni, C. Boiano, U. Bonnes, A. Bracco, S. Brambilla, A. Brünle, A. Bürger, K. Burkard, P.A. Butler, F. Camera, D. Curien, J. Devin, P. Doornenbal, C. Fahlander, K. Fayz, H. Geissel, J. Gerl, M. Górská, H. Grawe, J. Grebosz, R. Griffiths, G. Hammond, M. Hellström, J. Hoffmann, H. Hübel, J. Jolie, J.V. Kalben, M. Kmiecik, I. Kojouharov, R. Kulesa, N. Kurz, I. Lazarus, J. Li, J. Leske, R. Lozeva, A. Maj, S. Mandal, W. Meczyński, B. Million, G. Münzenberg, S. Muralithar, M. Mutterer, P.J. Nolan, G. Neyens, J. Nyberg, W. Prokopowicz, V.F.E. Pucknell, P. Reiter, D. Rudolph, N. Saito, T.R. Saito, D. Seddon, H. Schaffner, J. Simpson, K.-H. Speidel, J. Styczeń, K. Sümmerner, N. Warr, H. Weick, C. Wheldon, O. Wieland, M. Winkler, and M. Zieliński. Rare ISotopes INvestigation at GSI (RISING) using gamma-ray spectroscopy at relativistic energies. *Nuclear Instruments and Methods in Physics Research Section A: Accelerators, Spectrometers, Detectors and Associated Equipment*, 537(3):637 – 657, 2005. ISSN 0168-9002. doi: <http://dx.doi.org/10.1016/j.nima.2004.08.072>. URL: <http://www.sciencedirect.com/science/article/pii/S0168900204019588>.
- [70] N. Lalović. Analysis of the response of AGATA Detectors at GSI. *Eur. Phys. J. Web of Conferences (2015)*, 2015.
- [71] C. Stahl. Continuous-Angle DSAM: A new quality of lifetime measurements. Master's thesis, TU- Darmstadt, 2011.
- [72] P. Doornenbal, P. Reiter, H. Grawe, T. Saito, A. Al-Khatib, A. Banu, T. Beck, F. Becker, P. Bednarczyk, G. Benzoni, A. Bracco, A. Bürger, L. Caceres, F. Camera, S. Chmel, F.C.L. Crespi, H. Geissel, J. Gerl, M. Górská, J. Grebosz, H. Hübel, M. Kavatsyuk, O. Kavatsyuk, M. Kmiecik, I. Kojouharov, N. Kurz, R. Lozeva, A. Maj, S. Mandal, W. Meczyński, B. Million, Zs. Podolyák, A. Richard, N. Saito, H. Schaffner, M. Seidlitz, T. Striepling, J. Walker, N. Warr, H. Weick, O. Wieland, M. Winkler, and H.J. Wollersheim. Lifetime effects for high-resolution gamma-ray spectroscopy at relativistic energies and their implications for the {RISING} spectrometer. *Nuclear Instruments and Methods in Physics Research Section A: Accelerators, Spectrometers, Detectors and Associated Equipment*, 613(2):218 – 225, 2010. ISSN 0168-9002. doi: <http://dx.doi.org/10.1016/j.nima.2009.11.017>. URL: <http://www.sciencedirect.com/science/article/pii/S0168900209021676>.
- [73] D. Ralet, S. Pietri, Y. Aubert, M. Bellato, D. Bortolato, S. Brambilla, F. Camera, N. Dosme, A. Gadea, J. Gerl, P. Golubev, X. Grave, H.T. Johansson, N. Karkour, A. Korichi, N. Kurz, X. Lafay, E. Legay, D. Linget, N. Pietralla, D. Rudolph, H. Schaffner, O. Stezowski, B. Travers, and O. Wieland. Data-flow coupling and data-acquisition triggers for the PreSPEC-AGATA campaign at GSI. *Nuclear Instruments and Methods in Physics Research Section A: Accelerators, Spectrometers, Detectors and Associated Equipment*, 786(0):32 – 39, 2015. ISSN 0168-9002. doi: <http://dx.doi.org/10.1016/j.nima.2015.03.025>. URL: <http://www.sciencedirect.com/science/article/pii/S0168900215003332>.
- [74] FAIR. Baseline Technical Report, -. URL: <http://www.fair-center.eu/for-users/publications/fair-publications.html>.
- [75] M. Winkler, H. Geissel, H. Weick, B. Achenbach, K.-H. Behr, D. Boutin, A. Brünle, M. Gleim, W. Hüller, C. Karagiannis, A. Kelic, B. Kindler, E. Kozlova, H. Leibrock, B. Lommel, G. Moritz, C. Mühle, G. Münzenberg, C. Nociforo, W. Plass, C. Scheidenberger, H. Simon, K. Sümmerner, N.A. Tahir, A. Tauschwitz, M. Tomut, J.S. Winfield, and M. Yavor. The status of the Super-FRS in-flight facility at {FAIR}. *Nuclear Instruments and Methods in Physics Research Section B: Beam Interactions with Materials and Atoms*, 266(19-20):4183 – 4187, 2008. ISSN 0168-583X. doi: <http://dx.doi.org/10.1016/j.nimb.2008.05.073>. URL: <http://www.sciencedirect.com/science/article/pii/S0168583X08007015>. Proceedings of the {XVth} International Conference on Electromagnetic Isotope Separators and Techniques Related to their Applications.
- [76] A. Maj, J.J. Gaardhøje, A. Ataç, S. Mitarai, J. Nyberg, A. Virtanen, A. Bracco, F. Camera, B. Million, and M. Pignatelli. Angular distribution of photons from the delay of the GDR in hot and rotating light Yb nuclei from exclusive experiments. *Nuclear Physics A*, 571(1):185 – 220, 1994. ISSN 0375-9474. doi: <http://dx.doi.org/>

- 10.1016/0375-9474(94)90347-6. URL:  
<http://www.sciencedirect.com/science/article/pii/0375947494903476>.
- [77] H.G. Essel, J. Hoffmann, N. Kurz, R. S. Mayer, W. Ott, and D. Schall. The new data acquisition system at GSI. *Nuclear Science, IEEE Transactions on*, 43(1):132–135, Feb 1996. ISSN 0018-9499. doi: 10.1109/23.486018.
- [78] M. Bellato, L. Berti, D. Bortolato, P. J. Coleman-Smith, P. Edelbruck, X. Grave, R. Isocrate, I. Lazarus, D. Linget, P. Medina, C. Oziol, G. Rampazzo, C. Santos, B. Travers, and A. Triossi. Global Trigger and Readout System for the AGATA Experiment. *Nuclear Science, IEEE Transactions on*, 55(1):91–98, Feb 2008. ISSN 0018-9499. doi: 10.1109/TNS.2007.910034.
- [79] X. Grave, R. Canedo, J.-F. Clavelin, S. Du, and E. Legay. NARVAL a modular distributed data acquisition system with Ada 95 and RTAI. In *Real Time Conference, 2005. 14th IEEE-NPSS*, pages 5 pp.–, June 2005. doi: 10.1109/RTC.2005.1547454.
- [80] CES. VME Single Board Computers, -. URL:  
<http://www.ces.ch/board-products/vme-single-board-computers>.
- [81] J.Hoffmann, N.Kurz, and M.Richter. *TRIVA, VME Trigger Module*. GSI, August 2003.
- [82] William R. Leo. *Techniques for nuclear and particle physics experiments: a how-to approach*. Springer, 1994. ISBN 9783540572800.
- [83] Struck-Innovative-System. SIS3301 8 CHANNEL 105 MS/S 14-BIT ADC/DIGITIZER, -. URL:  
<http://www.struck.de/sis3301.htm>.
- [84] F. Ameil, M. Danchev, P. Boutachkov, J. Kurcewicz, S. Pietri, D. Ralet, J. Gerl, N. Pietralla, and the PreSPEC-AGATA collaboration. Time of flight with a segmented plastic finger detector at high particle rate. *GSI scientific report*, 2011.
- [85] D. Beck. Timing System Butis Interface, -. URL:  
<https://www-acc.gsi.de/wiki/Timing/TimingSystemButisInterface>.
- [86] Mesytec. Overview of Mesytec modules, -. URL:  
<http://www.mesytec.com/silicon.htm>.
- [87] H. T. Johansson and Al. TRLO II - flexible FPGA trigger control. *GSI scientific report 2010*, GSI Report-1 IS-EE: 231, 2011. URL:  
<http://www-alt.gsi.de/informationen/wti/library/scientificreport2010/PAPERS/PHN-IS-EE-03.pdf>.
- [88] D. Ralet, S. Pietri, H. T. Jahansson, J. Gerl, N. Pietralla, and the PreSPEC-AGATA collaboration. Test and charectirization of the VULOM with the TRLO firmware. *GSI scientific report*, 2011.
- [89] D. Ralet, N. Pietralla, S. Pietri, and the PreSPEC-AGATA collaboration. Trigger configuration for the PreSPEC-AGATA Campaign at GSI. *GSI scientific report*, 2012.
- [90] VULOM. Vulom Manual, -. URL:  
[http://www.gsi.de/informationen/wti/ee/fertigung/module\\_datempflege\\_e.html](http://www.gsi.de/informationen/wti/ee/fertigung/module_datempflege_e.html).
- [91] A. Georgiev, W. Gast, and R.M. Lieder. An analog-to-digital conversion based on a moving window deconvolution. *Nuclear Science, IEEE Transactions on*, 41(4):1116–1124, Aug 1994. ISSN 0018-9499. doi: 10.1109/23.322868.
- [92] A. Lopez-Martens, K. Hauschild, A. Korichi, J. Roccaz, and J-P. Thibaud. -ray tracking algorithms: a comparison. *Nuclear Instruments and Methods in Physics Research Section A: Accelerators, Spectrometers, Detectors and Associated Equipment*, 533(3):454 – 466, 2004. ISSN 0168-9002. doi: <http://dx.doi.org/10.1016/j.nima.2004.06.154>. URL:  
<http://www.sciencedirect.com/science/article/pii/S0168900204014779>.
- [93] O. Stezowski. GammaWare Head Version for release 0.9, -. URL:  
<http://www.ipnl.in2p3.fr/gammaware/doc/html/>.

- [94] N. Kaffrell, P. Hill, J. Rogowski, H. Tetzlaff, N. Trautmann, E. Jacobs, P. De Gelder, D. De Prenne, K. Heyde, S. Barjesson, G. Skarnemark, S. Alstad, N. Blasi, M.N. Harakeh, W.A. Sterrenburg, and K. Wolfsberg. Levels in  $^{109}\text{Rh}$ . *Nuclear Physics A*, 470(1):141 – 160, 1987. ISSN 0375-9474. doi: [http://dx.doi.org/10.1016/0375-9474\(87\)90125-4](http://dx.doi.org/10.1016/0375-9474(87)90125-4). URL: <http://www.sciencedirect.com/science/article/pii/0375947487901254>.
- [95] F. Farinon, I. Kojouharov, C. Nociforo, S. Pietri, K-H. Behr, A. Brünle, H. Geissel, C. Karagiannis, J. Kurcewicz A. Prochazka, M.V. Ricciardi, C. Scheidenberger, H. Weick, J.S. Winfield, , and M. Winkler. Development and test of Isomer TAGging detector. *GSI scientific report*, 2009.
- [96] J. Genevey, F. Ibrahim, J. Pinston, H. Faust, T. Friedrichs, M. Gross, and S. Oberstedt. Identification of  $\mu\text{s}$  isomers in the fission products of  $^{241}\text{Pu}(n_{\text{th}}, f)$ . *Phys. Rev. C*, 59:82–89, Jan 1999. doi: 10.1103/PhysRevC.59.82. URL: <http://link.aps.org/doi/10.1103/PhysRevC.59.82>.
- [97] S. Pietri. private communication.
- [98] A. Prochazka and et al. *TPC Technical Manual*. GSI, FRS, 2005. URL: <http://www-w2k.gsi.de/frs/technical/FRSsetup/detectors/tpc/tpcmanual.pdf>.
- [99] H. Weick. <https://web-docs.gsi.de/~weick/atima/>.
- [100] M. Reese, J. Gerl, P. Golubev, and N. Pietralla. Automatic intrinsic calibration of double-sided silicon strip detectors. *Nuclear Instruments and Methods in Physics Research Section A: Accelerators, Spectrometers, Detectors and Associated Equipment*, 779(0):63 – 68, 2015. ISSN 0168-9002. doi: <http://dx.doi.org/10.1016/j.nima.2015.01.032>. URL: <http://www.sciencedirect.com/science/article/pii/S0168900215000637>.
- [101] O.B. Tarasov and D. Bazin. LISE++: Radioactive beam production with in-flight separators. *Nuclear Instruments and Methods in Physics Research Section B: Beam Interactions with Materials and Atoms*, 266(19–20):4657 – 4664, 2008. ISSN 0168-583X. doi: <http://dx.doi.org/10.1016/j.nimb.2008.05.110>. URL: <http://www.sciencedirect.com/science/article/pii/S0168583X08007969>. Proceedings of the {XVth} International Conference on Electromagnetic Isotope Separators and Techniques Related to their Applications.
- [102] M.J. Taylor, M.A. Bentley, D. Rudolph, C. Fahlander, P. Golubev, R. Hoischen, P. Reiter, J. Gerl, and M. Górska. A new simulation package to model detector systems with fragmentation reactions and ion separators: Application to the LYCCA-0 system. *Nuclear Instruments and Methods in Physics Research Section A: Accelerators, Spectrometers, Detectors and Associated Equipment*, 606(3):589 – 597, 2009. ISSN 0168-9002. doi: <http://dx.doi.org/10.1016/j.nima.2009.05.003>. URL: <http://www.sciencedirect.com/science/article/pii/S0168900209009103>.
- [103] A.S. Goldhaber. Statistical models of fragmentation processes. *Physics Letters B*, 53(4):306 – 308, 1974. ISSN 0370-2693. doi: [http://dx.doi.org/10.1016/0370-2693\(74\)90388-8](http://dx.doi.org/10.1016/0370-2693(74)90388-8). URL: <http://www.sciencedirect.com/science/article/pii/0370269374903888>.
- [104] Mr. Bayes. An Essay towards solving a Problem in the Doctrine of Chances. *Phil. Trans.*, 53:370–418, 1763. doi: [doi:10.1098/rstl.1763.0053](https://doi.org/10.1098/rstl.1763.0053).
- [105] Jörg Eichler and Thomas Stöhlker. Radiative electron capture in relativistic ion–atom collisions and the photoelectric effect in hydrogen-like high-Z systems. *Physics Reports*, 439(1–2):1 – 99, 2007. ISSN 0370-1573. doi: <http://dx.doi.org/10.1016/j.physrep.2006.11.003>. URL: <http://www.sciencedirect.com/science/article/pii/S037015730600442X>.
- [106] H.J. Wollersheim. private communication.
- [107] J. Goodman and J. Wear. Ensemble samplers with affine invariance. *Comm. App. Math. and Comp. Sci.*, 5, No 1, 2010.
- [108] Daniel Foreman-Mackey, David W. Hogg, Dustin Lang, and Jonathan Goodman. emcee: The MCMC Hammer. *Publications of the Astronomical Society of the Pacific*, 125(925):pp. 306–312, 2013. ISSN 00046280. URL: <http://www.jstor.org/stable/10.1086/670067>.
- [109] D. Bazzacco. private communication.

- 
- [110] C. Michelagnoli. private communication.
- [111] Bart Bruyneel, Peter Reiter, Andreas Wiens, Jürgen Eberth, Herbert Hess, Gheorghe Pascovici, Nigel Warr, and Dirk Weisshaar. Crosstalk properties of 36-fold segmented symmetric hexagonal HPGe detectors. *Nuclear Instruments and Methods in Physics Research Section A: Accelerators, Spectrometers, Detectors and Associated Equipment*, 599(2–3):196 – 208, 2009. ISSN 0168-9002. doi: <http://dx.doi.org/10.1016/j.nima.2008.11.011>. URL: <http://www.sciencedirect.com/science/article/pii/S0168900208015921>.
- [112] Bart Bruyneel, Peter Reiter, Andreas Wiens, Jürgen Eberth, Herbert Hess, Gheorghe Pascovici, Nigel Warr, Sezgin Aydin, Dino Bazzacco, and Francesco Recchia. Crosstalk corrections for improved energy resolution with highly segmented HPGe-detectors. *Nuclear Instruments and Methods in Physics Research Section A: Accelerators, Spectrometers, Detectors and Associated Equipment*, 608(1):99 – 106, 2009. ISSN 0168-9002. doi: <http://dx.doi.org/10.1016/j.nima.2009.06.037>. URL: <http://www.sciencedirect.com/science/article/pii/S0168900209012455>.
- [113] G. Guastalla, D. D. DiJulio, M. Górska, J. Cederkäll, P. Boutachkov, P. Golubev, S. Pietri, H. Grawe, F. Nowacki, K. Sieja, A. Algora, F. Ameil, T. Arici, A. Atac, M. A. Bentley, A. Blazhev, D. Bloor, S. Brambilla, N. Braun, F. Camera, Zs. Dombrádi, C. Domingo Pardo, A. Estrade, F. Farinon, J. Gerl, N. Goel, J. Grębosz, T. Habermann, R. Hoischen, K. Jansson, J. Jolie, A. Jungclauss, I. Kojouharov, R. Knoebel, R. Kumar, J. Kurcewicz, N. Kurz, N. Lalović, E. Merchan, K. Moschner, F. Naqvi, B. S. Nara Singh, J. Nyberg, C. Nociforo, A. Obertelli, M. Pfützner, N. Pietralla, Z. Podolyák, A. Prochazka, D. Ralet, P. Reiter, D. Rudolph, H. Schaffner, F. Schirru, L. Scruton, D. Sohler, T. Swaleh, J. Taprogge, Zs. Vajta, R. Wadsworth, N. Warr, H. Weick, A. Wendt, O. Wieland, J. S. Winfield, and H. J. Wollersheim. Coulomb Excitation of  $^{104}\text{Sn}$  and the Strength of the  $^{100}\text{Sn}$  Shell Closure. *Phys. Rev. Lett.*, 110:172501, Apr 2013. doi: [10.1103/PhysRevLett.110.172501](https://doi.org/10.1103/PhysRevLett.110.172501). URL: <http://link.aps.org/doi/10.1103/PhysRevLett.110.172501>.
- [114] C. Louchart, J.M. Gheller, Ph. Chesny, G. Authelet, J.Y. Rousse, A. Obertelli, P. Boutachkov, S. Pietri, F. Ameil, L. Audirac, A. Corsi, Z. Dombradi, J. Gerl, A. Gillibert, W. Korten, C. Mailleret, E. Merchan, C. Nociforo, N. Pietralla, D. Ralet, M. Reese, and V. Stepanov. The PRESPEC liquid-hydrogen target for in-beam gamma spectroscopy of exotic nuclei at GSI. *Nuclear Instruments and Methods in Physics Research Section A: Accelerators, Spectrometers, Detectors and Associated Equipment*, 736(0):81 – 87, 2014. ISSN 0168-9002. doi: <http://dx.doi.org/10.1016/j.nima.2013.10.035>. URL: <http://www.sciencedirect.com/science/article/pii/S0168900213014150>.
- [115] T. Petrovic, M. Vencelj, M. Lipoglavsek, R. Novak, and D. Savran. Efficient Reduction of Piled-Up Events in Gamma-Ray Spectrometry at High Count Rates. *Nuclear Science, IEEE Transactions on*, 61(1):584–589, Feb 2014. ISSN 0018-9499. doi: [10.1109/TNS.2014.2298552](https://doi.org/10.1109/TNS.2014.2298552).
- [116] A. Lopez-Martens. private communication.
- [117] Juergen Gerl. private communication.
- [118] M. Lettmann. Differential, continuous-angle DSAM for relativistic beam. Master’s thesis, TU- Darmstadt, 2013.
- [119] T. Goigoux. Second year internship report – Monte-Carlo simulation for lineshape analysis. Master’s thesis, Télécom Physique Strasbourg, 2013.
- [120] H. Penttilä, P. Dendooven, A. Honkanen, M. Huhta, G. Lhersonneau, M. Oinonen, J.-M. Parmonen, K. Peräjärvi, J. Äystö, J. Kurpeta, and J. R. Persson. First observation of  $\beta$  decay of  $^{108}\text{Nb}$  to  $^{108}\text{Mo}$ . *Phys. Rev. C*, 54: 2760–2763, Nov 1996. doi: [10.1103/PhysRevC.54.2760](https://doi.org/10.1103/PhysRevC.54.2760). URL: <http://link.aps.org/doi/10.1103/PhysRevC.54.2760>.
- [121] F. Browne, A.M. Bruce, T. Sumikama, I. Nishizuka, S. Nishimura, P. Doornenbal, G. Lorusso, Z. Patel, S. Rice, L. Sinclair, P.-A. Söderström, H. Watanabe, J. Wu, Z.Y. Xu, H. Baba, N. Chiga, R. Carroll, R. Daido, F. Didierjean, Y. Fang, G. Gey, E. Ideguchi, N. Inabe, T. Isobe, D. Kameda, I. Kojouharov, N. Kurz, T. Kubo, S. Lalkovski, Z. Li, R. Lozeva, N. Naoki, H. Nishibata, A. Odahara, Zs. Podolyák, P.H. Regan, O.J. Roberts, H. Sakurai, H. Schaffner, G.S. Simpson, H. Suzuki, H. Takeda, M. Tanaka, J. Taprogge, V. Werner, O. Wieland, and A. Yagi. Gamma-ray Spectroscopy in the Vicinity of  $^{108}\text{Zr}$ . *Acta Physica Polonica B*, 46, 2015. doi: [DOI:10.5506/APhysPolB.46.721](https://doi.org/10.5506/APhysPolB.46.721).

---

## List of publications

Some part of this thesis have been already published or have contributed to scientific articles.

The following list gives the complete record of scientific publications that I have authored:

- **2015:** “Data-flow coupling and data-acquisition triggers for the PreSPEC-AGATA campaign at GSI”, D. Ralet et al., NIMA, .
- **2013:** “Trigger Configuration for the PRESPEC-AGATA Campaign at GSI”, D. Ralet et al., GSI Scientific Report 2012 p.
- **2012:** “Test and characterization of the VULOM with the TRLO firmware for the implementation of the Trigger Logic of the PRESPEC experiments”, D. Ralet et al., GSI Scientific report 2011.

The following list gives the complete record of scientific publications that I have co-authored:

- **2015:** “Isomeric ratios in  $^{206}\text{Hg}$ ”, Alexander et al. , Acta Physica Polonica B, 46, 2015
- **2015:** “Analysis of the response of AGATA Detectors at GSI”, N. Lalović et al., EPJConf, In press.
- **2014:** “On the Road to FAIR: 1st Operation of AGATA in PreSPEC at GSI”, N. Pietralla et al., EPJConf 66, 2014.
- **2014:** “Isospin symmetry in the sd shell: Transition strengths in the neutron-deficient sd shell nucleus  $\text{Ar}^{33}$ ”, A. Wendt et al., Phys. Rev. C 90, 05430, 2014.
- **2013:** “ The PRESPEC liquid-hydrogen target for in-beam gamma spectroscopy of exotic nuclei at GSI ”, C. Louchart-Henning et al., NIMA 736;81-87, 2013.
- **2013:** “Coulomb excitation of  $^{104}\text{Sn}$  and the strength of the  $^{100}\text{Sn}$  shell closure.”, G. Guastalla et al, PRL 110, 2013.
- **2012:** “Coulomb Excitation of  $^{33}\text{Ar}$  - a test of isospin symmetry in the sd shell”, A. Wendt et al., GSI Scientific report 2011 p.152
- **2012:** “Time of flight with a segmented plastic finger detector at high particle rate”, F. Ameil et al., GSI Scientific report 2011 p.
- **2012:** “Development and Commissioning Run of a new Plunger Device for PRESPEC”, M. Hackstein et al., GSI Scientific report 2011 p.154
- **2012:** “In-beam validation of the PRESPEC LH2 target ”, C. Louchart-Henning et al., GSI Scientific report 2012 p.155.



---

## Personal informations

### **Damian Ralet**

Planckstrasse 1,

Darmstadt, Germany 64291

D.Ralet@gsi.de

### **Persönliche Daten**

**Geburtsdatum** : Februar 17, 1988

**Geburstort** : Gérardmer, France

**Staatsanghörigkeit** : Belgien

**Familienstand** : Ledig

### **Schulbildung**

2003 - 2006: Lycée la Haie Griselle, Section Scientific, Gérardmer

### **Studium**

2006-2008: Intensive preparation for competitive exams selection for integrating upper level engineering school - “classes préparatoires aux grandes écoles” - at “Lycée Kleber” (Strasbourg)

2008-2011: Preparation of an Engineer degree from the Superior and National School of Physics of Strasbourg (ENSPS) - “Ecole Nationale Supérieure de Physique de Strasbourg”

2011: Master degree in “subatomic physics and astroparticles” at the University of Strasbourg (France)

2011: Engineer diploma from the Superior and National School of Physics of Strasbourg (ENSPS), Strasbourg (France)